



Predicting metallic nanoparticle morphologies from DFT calculations of surface-ligand interactions

van Bac Nguyen

► To cite this version:

van Bac Nguyen. Predicting metallic nanoparticle morphologies from DFT calculations of surface-ligand interactions. General Physics [physics.gen-ph]. Université Paul Sabatier - Toulouse III, 2016. English. NNT : 2016TOU30299 . tel-01688076

HAL Id: tel-01688076

<https://theses.hal.science/tel-01688076>

Submitted on 19 Jan 2018

HAL is a multi-disciplinary open access archive for the deposit and dissemination of scientific research documents, whether they are published or not. The documents may come from teaching and research institutions in France or abroad, or from public or private research centers.

L'archive ouverte pluridisciplinaire **HAL**, est destinée au dépôt et à la diffusion de documents scientifiques de niveau recherche, publiés ou non, émanant des établissements d'enseignement et de recherche français ou étrangers, des laboratoires publics ou privés.



Université
de Toulouse

THÈSE

En vue de l'obtention du

DOCTORAT DE L'UNIVERSITÉ DE TOULOUSE

Délivré par : l'Université Toulouse 3 Paul Sabatier (UT3 Paul Sabatier)

Présentée et soutenue le 30/11/2016 par :

Van Bac NGUYEN

Prédiction des morphologies de nanoparticules métalliques à partir de calculs DFT des interactions surface-ligand

JURY

Catherine Amiens
Dorothée BERTHOMIEU
Hervé BULOU
Christine MOTTET
Romuald POTEAU
Magali BENOIT
Hao TANG

Professeur de l'université
Directeur de recherche
Chargé de recherche
Directeur de recherche
Professeur de l'université
Chargée de recherche
Chargé de recherche

Examinateur
Examinateur
Rapporteur
Rapporteur
Examinateur
Invitée
Invité

École doctorale et spécialité :

SDM : Physique - COR 02

Unité de Recherche :

Directeur(s) de Thèse :

Magali BENOIT et Hao TANG

Rapporteurs :

Hervé BULOU et Christine MOTTET

Résumé

Les nanoparticules (NPs) sont des matériaux fonctionnels importants du fait de leur taille nanométrique. Cette réduction en taille, associée à la composition, à l'orientation des surfaces et à la morphologie contribue à l'exaltation de nombreuses propriétés importantes telles que les propriétés électroniques, magnétiques, catalytiques, optiques, etc. Pour contrôler la morphologie des NPs, de nombreux efforts ont été consacrés à comprendre leurs mécanismes de formation et l'origine de leur stabilité. Parmi les nanoparticules métalliques, le cobalt, avec sa structure hexagonale compact (hcp), est particulièrement intéressant pour la possibilité d'obtenir des nanocristaux de forme "naturellement" anisotropique. Par synthèse chimique en milieu liquide, des NPs de différentes morphologies telles que des disques, des plaques, des bâtonnets, des fils et des cubes ont été obtenues en contrôlant le type de précurseur, de l'agent réducteur, des ligands stabilisants, ainsi que la concentration de ces ligands, la température ou la vitesse d'injection des précurseurs. Même si ces conditions de synthèse ont été rationalisées, les mécanismes à l'origine de ces différentes morphologies ne sont pas encore bien connus.

Dans ce travail, nous avons développé deux modèles quantitatifs pour la prédiction de la morphologie, l'un est basé sur l'équilibre thermodynamique de l'état final, et l'autre sur un contrôle par l'effet cinétique. Pour appliquer ces modèles, il a été nécessaire de calculer dans un premier temps, avec la théorie de la fonctionnelle de la densité (DFT), les comportements d'adsorption des molécules ligands en fonction du taux de recouvrement sur les facettes de différentes orientations du métal. Pour ce faire, l'adsorption des ligands CH_3NH_2 , CH_3COO , $\text{C}_5\text{H}_{11}\text{COO}$ et $\text{C}_{11}\text{H}_{23}\text{COO}$ a été modélisée sur les différentes surfaces de Co et de Ni. La morphologie des NPs de Co prédite par ces deux modèles a été comparée à celles obtenues expérimentalement et à d'autres résultats théoriques de la littérature. La variété des formes obtenues par le modèle cinétique semblerait mieux correspondre aux NPs synthétisées avec les différentes conditions expérimentales. Ceci confirme que la morphologie des NPs est guidée avant tout par un effet cinétique.

Mots-clés : nanoparticules, morphologie, cinétique, thermodynamique, DFT

Abstract

Nanoparticles are one of the most important families of functional materials due to their nanometric size. This size reduction, associated to their composition, surfaces orientation and morphology has contributed to the emergence of new important properties such as electronic, magnetic, catalytic, optic, etc. To control the morphology of NPs, many efforts have been devoted to understand their formation mechanism and the origin of their stability. Among metallic nanoparticles, cobalt, with its hexagonal closed-packed (hcp) structure, is particularly interesting because of the possibility to grow “naturally” anisotropic shaped nanocrystals. Using chemical synthesis in liquid environment, various morphologies such as disks, plates, rods, wires and cubes have been obtained by controlling the precursor type, the reducing agent, the stabilizing ligands as well as their concentration, the temperature or the rate of precursor injection. Even if these synthesis conditions have been rationalized, few is known concerning the growth mechanisms at the atomic scale.

In this work, we have developed two quantitative morphology prediction models, one based on the final thermodynamic equilibrium state, while another is controlled by the kinetics. These models require the knowledge of the adsorption behaviors of stabilizing molecules as a function of surface coverage on preferential facets of NPs. To this end, density functional theory (DFT) calculations were performed on a series of stabilizing molecules (CH_3NH_2 , CH_3COO $\text{C}_5\text{H}_{11}\text{COO}$ and $\text{C}_{11}\text{H}_{23}\text{COO}$) adsorbed on the different Co and Ni surfaces. The shape of the Co NPs obtained by these two models was compared to experimental morphologies and other theoretical results from the literature. The variety of forms predicted by the kinetic model agrees better with the NPs morphologies obtained under the different synthesis conditions. This confirms that the morphology control of NPs is mostly driven by the kinetics.

Key-word: nanoparticle, morphology, kinetics, thermodynamics, DFT

Remerciements

Je tiens tout d'abord à remercier mes directeurs de thèse Mme Magali Benoit et M Hao Tang chargés de recherche au CEMES pour la confiance qu'ils m'ont accordé pour réaliser ce travail. Je leur dois la disponibilité et la patience pendant tous ces trois ans. J'ai beaucoup apprécié leur qualités professionnelles et scientifiques et la rigueur de leur encadrement. Je leur suis très reconnaissant de m'avoir donné la chance de réaliser cette thèse de doctorat dans d'aussi bonnes soutiens.

Je remercie Catherine Amiens, Professeur de université Paul Sabatier d'avoir accepté de présider le jury de ma soutenance de thèse et pour l'intérêt qu'elle a porté à ce sujet et aux résultats présentés. Je suis très reconnaissant à Christine MOTTET, directrice de recherche de l'université de Marseille et Hervé Bulou, chargé de recherche à l'IPCMS de Strasbourg

d'avoir accepté d'être rapporteurs de ce travail et d'avoir consacré leur temps pour examiner ce manuscrit. Merci également pour toutes ces suggestions constructives autour des résultats présentés. Je tiens à remercier chaleureusement Romual Poteau professeur de l'université Paul Sabatier et Dorothée Berthomieu chargée de recherche à l'ICG de Montpellier pour avoir accepté de participer au jury de ma thèse et avoir examiné soigneusement ce travail.

Je tiens à remercier Je remercie particulièrement Nicolas, pour ses qualités scientifiques, sa disponibilité. Son implication et ses conseils pour le développement du modèle cinétique m'ont permis mieux valoriser, et clarifier mes idées. Un grand merci particulièrement à Marie-Jose, Nathalie, Anne, Joseph les permanents du groupe SINANO pour leur soutien et précieux conseils dans les moment difficile et aussi tout au long de la thèse. Ce fut un plaisir de vous côtoyés, ce qui m'a fait une expérience inoubliable et enrichissante du point de vue scientifique, professionnel et humain. Je remercie aussi mes collègues Xavier, Maxime, Fatah et Mihee pour l'ambiance amicale et enrichissante. Je souhaite également exprimer mes remerciements à tous les membres du CEMES : thésards, chercheurs, enseignants- chercheurs ainsi que les personnels techniques et administratifs qui ont d'une manière ou d'une autre, participé à la réalisation de ce travail.

Je tiens à remercier l'école doctorale de science la matière (EDSM) et Université Paul Sabatier qu'il m'a accordée le financement pour ce travaille. Je remercie aussi le centre de calcul CALMIP ainsi que tous les personnel y travaille qui me permet de réaliser les calcul durant cette thèse.

Je voudrais exprimer mon gratitude à tous mes enseignants, de l'école primaire jusqu'à Master, particulièrement au Pr Trung Don DAM de l'université de Hanoi, qu'il m'a initialisé dans le monde de la recherche scientifique et m'encourager de venir en France.

Je tiens à remercier chaleureusement ma femme Hang pour la grande patience, l'encouragement et la confiance en moi. Je salut son courage de venir en France pour m'accompagner et surtout pour son soutien moral ininterrompu et ses nombreux conseils tout le long de ma thèse.

Finalement, Je tiens à remercier mes parents pour leur amour, leur soutiens, la confiance qu'ils ont toujours eu en moi. Particulièrement je dois à ma mère les premiers leçons de la physique qui me nourrie la passion sur la physique jusqu'au maintenance.

Résumé

0.1 Introduction

Les particules de matière d'une dimension comprise entre un nanomètre (nm) et une centaine de nanomètres sont généralement appelées nanoparticules (NP). Dans ces tailles particulières, les NPs ont attiré beaucoup d'attention non seulement pour leurs propriétés physiques remarquables, mais aussi pour leurs applications industrielles. En même temps, ces particules de taille nanométrique présentent également des dangers potentiels pour la santé et l'environnement. Le manque de connaissances sur les effets de ces NPs sur la santé publique a déjà suscité la crainte du grand public à l'égard de ces nouveaux matériaux.

Pour toutes ces raisons, la connaissance des propriétés physiques des NP est très importante. Outre la taille, la morphologie de ces NP est également un élément clé pour contrôler leurs propriétés. Expérimentalement, la synthèse chimique en solution est l'un des domaines les plus importants pour l'élaboration des NPs. De grands progrès dans l'optimisation du protocole de synthèse pour contrôler la morphologie des NPs ont été atteints au cours des deux dernières décennies. Une grande variété de formes, qui comprennent non seulement la sphère, le cube, le cuboctaèdre, l'octaèdre, le tétraèdre, le dodécaèdre, l'icosaèdre, etc., mais aussi des plaquettes minces triangulaires, hexagonales, des tiges ou des fils avec une croix circulaire, carrée, rectangulaire, pentagonale ou octogonale ont été rapportées dans la littérature [1]. Cependant, il est encore extrêmement difficile de comprendre les mécanismes de formation des NPs pour une morphologie spécifique. Cette difficulté est étroitement liée au grand nombre de paramètres influents dans un protocole de synthèse tels que la nature du précurseur, de l'agent réducteur, du tensioactif, des ligands stabilisants ainsi que leur quantité, leur concentration, leur température, l'ordre d'injection, le temps, etc. Très récemment, on a également découvert que la réaction latérale entre différentes molécules pouvait changer radicalement les conditions de synthèse, et devait donc être considérée [2].

En dépit de ces conditions extrêmement compliquées, la croissance de NPs pourrait être séparée en trois étapes bien identifiées, comme proposé par LaMer et ses collaborateurs au début des années 50 [3].

- (1) La première étape correspond à une augmentation rapide de la concentration en monomère métallique jusqu'à une concentration de saturation. Au cours de cette étape, les précurseurs sont décomposés en atomes métalliques libres ou en monomères.
- (2) La deuxième étape, également appelée étape de nucléation, correspond à la formation de clustrer/noyaux. Lorsque le nombre et/ou la taille des noyaux atteint un nombre donné, la concentration des monomères tombe en dessous de la limite de saturation.
- (3) Au cours de la dernière étape (étape de croissance), les monomères en solution seront incorporés dans des noyaux/graines existants, par différents mécanismes de diffusion. La taille de ces nanocristaux augmente jusqu'à ce que la concentration des monomères diminue jusqu'à une valeur limitée. L'évolution de la morphologie au cours de cette étape de croissance devrait pouvoir être contrôlée.

L'une des idées les plus simples est de stabiliser des facettes d'une NP en utilisant des molécules de ligands. En effet, on sait que la forme d'une NP dans le vide peut être prédite en utilisant la méthode de reconstruction de Wulff, qui est basée sur la minimisation des énergies de surface des facettes. On peut extrapoler que l'adsorption d'une couche de ligands pourrait non seulement modifier sensiblement l'énergie de surface de certaines facettes, mais aussi la cinétique d'incorporation des monomères sur les différentes facettes. En faisant ainsi, l'ordre de stabilité de ces facettes pourrait être modifié, et ainsi induire un changement de morphologie.

Contrairement aux NPs de métaux cubique face centré (fcc), pour lesquels il existe un grand nombre de résultats (expérimentaux et théoriques), il n'existe qu'un nombre limité de travaux sur le contrôle de la morphologie des NPs hexagonales compactes (hcp) dans la littérature [2, 4, 5]. Pourtant, les NPs de cobalt hcp, par exemple, sont particulièrement intéressants en raison de la possibilité de développer "naturellement" des nanocristaux de forme anisotrope. Les propriétés associées à cette anisotropie sont intéressantes pour des applications telles que le stockage d'informations ou des aimants permanents en raison de leur forte magnétisation et de l'énergie d'anisotropie magnéto-cristalline. Les NPs de Co sont également connues comme des catalyseurs efficaces pour de nombreuses réactions [6, 7]. Des nano-disques stables, entièrement métalliques (sans oxyde) de cobalt ont été obtenus par le groupe de C. Amiens en utilisant la rhodamine B (RhB) comme ligand stabilisant [2]. Il était supposé que l'utilisation de RhB pourrait être à l'origine de cette forme de nano-disque. Plus récemment, P. Sautet et ses collaborateurs [5] ont montré que les NPs de Co stabilisées par des ligands carboxylate pouvaient présenter des formes très différentes en fonction de la concentration des ligands en solution: de la forme bâtonnet à faible concentration à la forme d'un disque à forte concentration. L'étude théorique présentée dans l'article [5] a expliqué ce changement de morphologie par une modification des énergies d'interface entre les ligands et les facettes de la NP en fonction de la concentration en ligands. Cependant, cette démonstration était basée uniquement sur des arguments thermodynamiques et ne prenait pas en compte les aspects cinétiques de la croissance du NP.

Afin de comprendre la stabilité de la morphologie des NPs de Co et la raison de cette croissance anisotrope, nous avons d'abord proposé de calculer les énergies d'interface des différentes surfaces de Co recouvertes par les couches moléculaires de carboxylate et de molécules d'amine en fonction du taux de recouvrement, en utilisant des calculs basés sur la Théorie de la Fonctionnelle de la Densité (DFT). En utilisant ces énergies, et en particulier celles obtenues à partir de l'adsorption des molécules de carboxylate, nous avons dérivé différents modèles pour la prédiction de la morphologie des NPs en fonction de la concentration du ligand. Tout d'abord, nous avons utilisé des approches thermodynamiques simples puis nous avons développé un modèle cinétique plus élaboré. Il s'est avéré qu'aucun des modèles thermodynamiques ne pouvait reproduire la grande variété de morphologies observées expérimentalement alors que, en tenant compte de la cinétique, la diversité des morphologies pouvait être obtenue.

Le manuscrit contient 5 chapitres en plus de l'introduction et de la conclusion. Dans ce résumé, les chapitres 3, 4 et 5 qui regroupent les résultats principaux de cette thèse seront détaillés dans la suite. Les deux premiers chapitres concernent des synthèses bibliographiques qui ne seront pas présentés ici.

Dans le premier chapitre, je présente d'abord un bref compte rendu des travaux expérimentaux récents sur les différentes étapes des mécanismes de croissance lors de la synthèse des NPs de métaux fcc et hcp. Ce compte rendu révèle la complexité de chaque étape de synthèse «en solution» des NPs. Cette complexité pourrait cependant être réduite dans certains cas spécifiques en modifiant seulement un ou deux paramètres choisis. Dans un second temps, les méthodes théoriques de prédiction de la morphologie des NPs selon une approche thermodynamique sont présentées incluant :

- (i) le modèle de reconstruction de Wulff [8],

- (ii) le modèle d'énergie d'interface le plus faible
- (iii) le modèle d'isotherme d'adsorption, en fonction du taux de recouvrement de ligands sur la surface.

En ce qui concerne les approches cinétiques, la théorie classique de la nucléation et de la croissance est brièvement présentée, ainsi que la théorie de Lifshitz-Slyozov-Wagner [9] avant une simple description du temps moyen du premier passage (MFPT) [10] et les méthodes de surface limitée (SAL) [11].

Comme les énergies d'adsorption et de surface/interface ont été calculées en utilisant des calculs de DFT, le deuxième chapitre est consacré à la description des principes de la DFT et des approximations standards pour l'évaluation de l'énergie de corrélation et d'échange. Ce chapitre se termine par une présentation rapide des méthodes de correction de dispersion, des calculs en base d'ondes planes et des pseudopotentiels de type PAW (Projector augmented wave method), tels que mis en œuvre dans code de simulation VASP.

Le troisième chapitre détaille l'optimisation des conditions de simulation telles que le maillage de points k de la zone de Brillouin dans l'espace réciproque, l'énergie de coupure et le paramètre de «smearing» σ qui sont nécessaires au calcul des systèmes métalliques. Le reste du chapitre est consacré à la présentation des résultats pour les propriétés des systèmes massifs et des surfaces libres de Co et Ni.

Dans le quatrième chapitre, les configurations de simulation utilisées pour l'adsorption des ligands du groupe carboxylate avec différentes longueurs de chaîne (CH_3COO , $\text{C}_5\text{H}_{11}\text{COO}$ et $\text{C}_{11}\text{H}_{23}\text{COO}$) et du groupe amine (NH_2CH_3) au lieu de la rhodamine B sont détaillées. A la fin de ce chapitre, les énergies d'adsorption en fonction du taux de recouvrement des ligands sur les surfaces et du transfert de charge lors de l'adsorption sont présentées pour chaque configuration molécule-surface.

Dans le cinquième chapitre, les prédictions de la morphologie des NPs issues des différents modèles étudiés sont testées en utilisant les quantités précédemment calculées pour la plus petite molécule de ligand CH_3COO et les NPs de Co pour lesquelles une comparaison expérimentale est possible. La première partie est consacrée à la présentation des modèles thermodynamiques, c'est-à-dire le modèle de minimisation de l'énergie d'interface et les modèles d'isotherme d'adsorption, et les morphologies prédites en fonction de la concentration des ligands sont présentées et discutées. Dans la deuxième partie, nous proposons un nouveau modèle cinétique qui comprend une compétition entre les vitesses d'incorporation des atomes de cobalt et les vitesses d'adsorption des molécules de ligand. L'évolution de la morphologie en fonction de la concentration des ligands et des différents taux d'adsorption est présentée et discutée à la fin du chapitre.

Enfin, une conclusion générale est donnée à la fin du manuscrit.
récents dans la modélisation et la prédiction de la morphologie de ces NP.

0.2 Calculs des propriétés des métaux et des énergies de surface

L'objectif de cette première partie de travail est de modéliser l'interaction entre les surfaces métalliques (Co, Ni) et les molécules adsorbées (ligands) afin d'en déduire l'énergie des interfaces métal-ligands. Pour commencer, il est nécessaire d'étudier les systèmes de référence, c'est-à-dire la surface métallique et le ligand isolé, puis comparer avec le système de surface-ligand. Dans ce chapitre 3, j'ai présenté les détails des simulations utilisées pour la surface métallique, et j'ai décrit la façon dont nous avons obtenu ses propriétés géométriques, physiques et mécaniques. J'ai présenté également la méthodologie utilisée pour prendre en compte les

effets des interactions de dispersion de van der Waals (vdW) et finalement donner nos choix finaux de paramètres et de fonctionnelles pour les calculs supplémentaires. Contrairement aux interactions molécule/surface, pour lesquelles les interactions de dispersion vdW doivent être prises en compte, la présence ou non de ces interactions dans les systèmes métalliques est encore un sujet à discussion [12]. Dans ce travail, nous comparons l'efficacité des deux méthodes de correction de dispersion en DFT les populaires: la méthode DFTD [13] et la fonctionnelle opt86B [14, 15] à la fonctionnelle PBE [16] où aucune correction n'a été prise en compte.

Je me suis d'abord concentré sur les systèmes métalliques: j'ai commencé par les atomes isolés de Co et de Ni dans le vide. Ensuite, j'ai optimisé leur structure cristalline et enfin j'ai construit des modèles de leurs surfaces cristallines. Les propriétés physiques déduites de ces modèles ont été comparées aux résultats expérimentaux et d'autres calculs existants dans la littérature pour obtenir les meilleurs paramètres pour l'étape suivante. Tous les calculs DFT ont été effectués à l'aide du programme VASP [17, 18, 19, 20], un code DFT pour les systèmes périodiques. Les cellules unitaires de Co (hcp) et Ni (fcc) massifs ont été utilisées pour optimiser la convergence des calculs par rapport à l'énergie de coupure, au "smearing" et au nombre de points k dans la première zone de Brillouin. Pour obtenir une précision de 1 meV par atome sur l'énergie totale par cellule, les paramètres optimaux pour la grille de points k sont 19x19x19 pour Ni et 21x21x21 pour Co. L'énergie de coupure optimale pour Co est de 650 eV et pour Ni, elle est de 600 eV. Les valeurs de "smearing" de 0,01 à 0,1 sont toutes acceptables, mais la convergence peut être difficile avec une valeur trop petite de σ . Par conséquent, tous les calculs sont effectués d'abord avec une valeur de 0,1 eV puis recalculés avec la valeur conservatrice de 0,01 eV. Dans les calculs du métal massif, les trois fonctionnelles PBE, PBE+DFTD et opt86B donnent des résultats en bon accord avec les expériences pour les paramètres de maille et le "bulk modulus", mais des écarts sont significatifs pour les énergies de cohésion (environ 20-25% pour les trois méthodes). Au final, les résultats obtenus par PBE apparaissent meilleurs que ceux obtenus par les 2 autres fonctionnelles (opt86B est cependant meilleure que DFTD).

Pour les surfaces, les calculs utilisant ces trois fonctionnelles donnent des résultats contrastés en fonction de la propriété recherchée. Pour les énergies de surface, la fonctionnelle DFTD donne le meilleur accord avec les expériences pour Co(0001) et Ni(111). Pour la relaxation des plans inter-atomiques (de surface), même s'il n'existe pas de valeurs expérimentales très précises, toutes les 3 méthodes donnent une contraction (relaxation vers l'intérieur) de la première couche et une expansion (relaxation vers l'extérieur) de la seconde couche qui reproduisent bien le comportement observé dans les expériences. Quantitativement, la fonctionnelle opt86B donne les résultats les plus proches des valeurs expérimentales. Pour le travail de sortie, PBE et DFTD donnent approximativement les mêmes résultats, qui sont en meilleur accord avec les expériences que ceux obtenus par opt86B. Enfin, pour le moment magnétique de surface, PBE semble être le meilleur choix pour Co et opt86B est le mieux pour Ni. Compte tenu de la disparité des résultats, nous avons décidé de modéliser les surfaces métalliques avec la fonctionnelle PBE et d'inclure les forces de dispersion uniquement entre les atomes de surface et les molécules en utilisant la méthode DFTD.

Après avoir défini tous les paramètres pour les calculs de surface, nous avons calculé les propriétés de surface de 7 orientations cristallographiques pour Co et 2 pour Ni (tables 2 et 1). Les énergies de surface ainsi obtenues seront utilisées dans la suite pour construire nos modèles pour les interactions surface/molécule. En outre, la morphologie des nanoparticules sans ligands est présentée dans ce chapitre en utilisant le modèle de construction de Wulff et le modèle d'énergie d'attachement. Les surfaces dominantes pour le modèle de Wulff sont les (0001), (01-11) et (10-10) tandis que dans le modèle d'énergie d'attachement, ce sont les surfaces (01-11) qui sont prédominantes. Les autres facettes ayant également une contribution non négligeable (Figure 1).

En résumé, les résultats de ces calculs pour les métaux Co et Ni massifs et pour leurs surfaces

Surface	γ [eV/ \AA^2]	γ [J/m ²]	DFT [J/m ²] [21]	exp [J/m ²] [22]
(0001)	0.132	2.115	2.11	
(1-100)	0.140	2.243	2.25	
(10-10)	0.173	2.783		
(01-11)	0.149	2.397	2.40	
(1-102)	0.157	2.526		
(10-12)	0.158	2.542	2.54	
(2-1-10)	0.156	2.510	2.46	

Table 1: Energies de surface de Co en eV/ \AA^2 et en J/m².

Surface	γ [eV/ \AA^2]	γ [J/m ²]	DFT [J/m ²] [21]	exp [J/m ²] [22]
(111)	0.119	1.906	1.92	
(100)	0.136	2.178	2.19	

Table 2: Energies de surface de Ni en eV/ \AA^2 et en J/m².

ont été présentés dans ce chapitre. Ceci est la première étape avant de modéliser l'interaction entre un substrat métallique et une molécule.

0.3 Adsorption de ligands sur des surfaces métalliques

Dans ce chapitre, j'ai présenté les principaux résultats de calculs DFT de ce travail: l'interaction entre les molécules et les surfaces métalliques. Dans ce travail, j'ai étudié la topologie et le mode d'adsorption de plusieurs molécules stabilisatrices sur les surfaces métalliques de Co(0001), Co(10-10), Co(01611) et Ni(111), Ni(001) décrites dans le chapitre précédent. L'interaction de ces molécules avec ces différentes surfaces et la dépendance des propriétés énergétiques de ces ligands avec le taux de recouvrement seront la clé pour comprendre l'effet des ligands sur la morphologie des NPs. Je commence d'abord par présenter les calculs DFT sur les molécules isolées, qui sont nécessaires pour évaluer les énergies d'adsorption. Ensuite, la construction de la cellule de simulation est décrite et la formulation des propriétés physiques qui seront extraites de ces calculs est donnée. Ceci est suivi par une présentation de l'analyse d'adsorption de ces molécules au cas par cas. Ces données seront utilisées dans le chapitre suivant dans nos modèles de prédiction de la morphologie. Dans un article récent, il a été montré que différentes morphologies des NPs de Co peuvent être obtenues en utilisant des ligands du type amine ($R-\text{NH}_2^-$) ou du type carboxylate de différentes longueurs de chaîne d'hydrocarbone ($R-\text{COO}$ avec $R=\text{C}_n\text{H}_{2n+1}\text{COO}^-$)[5]. Pour modéliser ces ligands, nous aurions besoin d'ajouter un électron à une localisation spécifique dans la molécule. Ceci n'est malheureusement pas possible avec VASP qui utilise des bases en ondes planes. Nous avons donc choisi de modéliser la forme radicalaire de ces molécules plutôt que sa forme ionique. Nous avons donc décidé d'étudier l'adsorption de ligands simples CH_3COO^- et CH_3NH_2^- sur les surfaces métalliques et ensuite de

généraliser à des chaînes hydrocarbonées plus longues.

Dans ce travail, nous avons ainsi optimisé les propriétés structurales de CH_3NH_2 , CH_3COO , $\text{C}_5\text{H}_{11}\text{COO}$ et $\text{C}_{11}\text{H}_{23}\text{COO}$. Nous n'avons pas calculé l'adsorption de $\text{R}-\text{NH}_2$ de longueur plus grande car les premiers résultats ont montré que les énergies d'adsorption de CH_3NH_2 étaient beaucoup plus petites que celles de CH_3COO . Dans ce chapitre, j'ai détaillé la géométrie optimisée de ces ligands et l'énergie de ces ligands dans une grande cellule qui est nécessaire pour modéliser une molécule isolée avec des conditions aux limites périodiques.

Pour les calculs de l'interaction molécule-surface, nous décrivons tout d'abord les détails de simulation utilisés pour calculer l'adsorption des molécules de ligand sur les surfaces métalliques

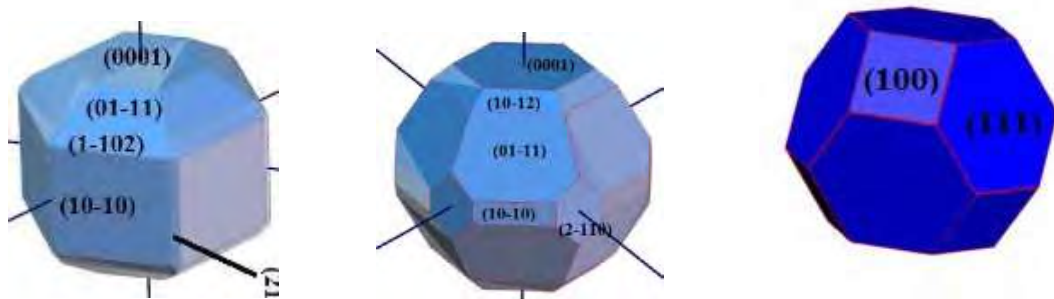


Figure 1: Formes des NPs déterminées par le modèle de construction de Wulff et le modèle de l'énergie d'attachement. De gauche à droite: forme d'équilibre de la NP de Co, forme de la NP de Co par le modèle de l'énergie d'attachement et forme d'équilibre de la NP de Ni.

étudiées, puis nous montrons les résultats en termes de (i) les géométries d'adsorption et (ii) les énergies d'adsorption.

Comme présenté dans le chapitre 3, les surfaces Co et Ni ont été calculées avec la fonctionnelle PBE sans correction vdW. La prise en compte de l'interaction de dispersion entre la surface et la molécule adsorbée est en revanche importante, comme cela a été discuté dans de nombreuses références dans la littérature. Un des exemples récents est celui de Tkatchenko et al. [23] sur la structure et l'énergie d'adsorption du benzène sur les surfaces des métaux de transition. Nous avons donc décidé d'inclure ces forces de dispersion uniquement entre les atomes de la surface et les atomes des molécules, en utilisant les paramètres proposés par Grimme dans la méthode DFT-D2 [13].

Pour les calculs avec les molécules de ligand, la taille du substrat dans la direction perpendiculaire à la surface est limitée à 4 couches atomiques pour réduire le coût de calcul. Les atomes dans les 2 couches à la base du substrat ont été fixés à leurs positions dans le massif. Les cellules de simulation (les supercellules), multiples de la cellule unitaire dans les directions x et y, ont ensuite été construites pour décrire les différents taux de recouvrement étudiés et le nombre de points k a été diminué en conséquence.

Quatre types de ligands ont été étudiés sur les surfaces de cobalt: CH_3NH_2 , CH_3COO , $\text{C}_5\text{H}_{11}\text{COO}$ et $\text{C}_{11}\text{H}_{23}\text{COO}$. Les tailles des cellules correspondantes dans la direction z sont respectivement de 20.25 Å, 20.25 Å, 30 Å et 43 Å afin d'éviter les interactions entre les molécules et l'image périodique du substrat. Les distances de vide sont au minimum de l'ordre de 12 Å. Ensuite, j'ai présenté les résultats des calculs DFT pour les différentes molécules étudiées et leur adsorption sur certaines surfaces de Co et Ni pour des taux de recouvrement choisis. Pour les molécules, deux types de terminaisons, -COO et -NH₂ ont été étudiées. Les énergies d'adsorption des molécules terminant par -COO sont plus grande que celles des molécules terminant par -NH₂ sur les deux métaux.

Parmi les 3 longueurs de chaîne différentes pour les molécules R-COO, les calculs de CH_3COO étaient les plus légers et nous ont permis d'obtenir une variation continue des énergies d'adsorption en fonction du taux de recouvrement pour les trois surfaces de Co étudiées. Les fonctions d'ajustement de ces énergies d'adsorption seront utilisées ensuite pour construire des modèles de croissance de NPs en présence de ligands. Dans le chapitre qui suit, plusieurs modèles seront donc testés à l'aide de ces résultats.

L'adsorption de CH_3COO sur la surface de Co sera donc étudiée par la suite en raison de son adsorption d'énergie beaucoup plus grande que la méthylamine. En outre, la structure de cette molécule est assez simple pour avoir un temps raisonnable de calcul en comparaison avec les autres carboxylates. L'influence de la longueur de la chaîne hydrocarbonée sur l'énergie d'adsorption sera discutée plus loin. Dans ce résumé, je vais présenter en détail la géométrie

d'adsorption, le mode d'adsorption et la variation de l'énergie d'adsorption en fonction du taux de recouvrement de CH_3COO , car il joue un rôle important dans nos modèles décrits au chapitre 5.

La surface (0001) a la plus petite surface de cellule unitaire avec une aire de $5,37 \text{ \AA}^2$. La molécule adsorbée a ses 2 atomes d'oxygène en position "top" quelque soit le taux de recouvrement. Une analyse des charges de Bader nous a permis de montrer que, lorsque le taux de recouvrement est de $0,031 \text{ \AA}^{-2}$, une charge nette de $0,67 \text{ e}$ (électron) est transférée de la surface vers la molécule.

Les deux surfaces (10-10) et (01-11) ont une aire de cellule unitaire de $10,10 \text{ \AA}^2$ et de $11,49 \text{ \AA}^2$ respectivement. Dans la cellule unitaire, il n'y a qu'un Co dans la couche de surface. Pour tous les taux de recouvrement inférieur à $1/2$ (c'est-à-dire $\theta = 0,049 \text{ \AA}^{-2}$ pour (10-10) et $\theta = 0,043 \text{ \AA}^{-2}$ pour (01-11)), tous les atomes d'oxygène se positionnent en position "top". Lorsque toutes les positions "top" sont occupées, leur taux de recouvrement sont encore inférieurs à celui de la surface (0001). Il est donc possible d'augmenter la densité de recouvrement de ces surfaces en prenant en compte les autres sites d'adsorption. Les figures 4.7-c et d du Chapitre 3 montrent les configurations optimisées de 4 molécules sur la surface 2×3 de Co(10-10). Deux molécules sont adsorbées avec leurs atomes d'oxygène en position "top" tandis que les 2 autres molécules sont adsorbées avec un atome O sur le site "top" et l'autre dans un site "hollow". L'énergie d'adsorption est de $-3,233 \text{ eV}$ pour $\theta = 0,066 \text{ \AA}^{-2}$, ce qui n'est pas trop éloigné de l'énergie d'adsorption sur la surface (0001) pour un taux de recouvrement similaire ($3,431 \text{ eV}$ à $\theta = 0,062 \text{ \AA}^{-2}$).

L'analyse de charge de Bader de la molécule dans la configuration avec 2 sites "top" donne une valeur similaire de transfert de charge par rapport au cas de la surface Co(0001) pour une recouvrement similaire: $0,64 \text{ e}$. En revanche, l'analyse de charge de Bader pour la molécule avec un O sur la position "top" et l'autre sur la position "hollow" donne un transfert de charge de seulement $0,49 \text{ e}$. Cette différence est due à un transfert de charge différent pour l'atome O₁ en position "hollow". On trouve des résultats similaires pour la surface Co(01-11).

Les énergies d'adsorption et les transferts de charge sont présentés dans le tableau 4.5 pour les différents taux de recouvrement par unité de surface θ avec la taille de la supercellule (multiple de la cellule unitaire), le nombre de ligands par supercellule et les taux de recouvrement correspondants.

L'énergie d'adsorption de CH_3COO varie fortement avec θ , l'énergie minimale étant obtenue pour un taux de recouvrement de $1/4$ dans le cas de la surface (01-11). Pour les autres surfaces, l'énergie minimale est obtenue pour un taux de recouvrement de $1/3$ pour la surface (10-10) et pour un taux de recouvrement de $2/3$ pour la surface (0001). La variation de E_{ads} en fonction de θ est l'élément le plus important pour l'évaluation de l'énergie des interfaces. Pour construire un modèle de croissance des NPs à partir de ces énergies d'adsorption, nous devons extraire une dépendance continue de E^{ads} en fonction de θ . Comme l'énergie d'adsorption d'une molécule sur la surface peut être calculée seulement pour un nombre limité de valeurs de taux de recouvrement, il est donc nécessaire d'ajuster ("fitter") E^{ads} en fonction de θ par une fonction continue.

Pour choisir la forme de la fonction d'ajustement pour $E^{\text{ads}} = f(\theta)$, nous notons que le transfert de charge et la distance des liaisons Co-O sont très similaires pour presque toutes les configurations. Par conséquent, nous supposons que la variation de l'énergie d'adsorption est principalement due à l'interaction entre les molécules lorsque les distances inter-moléculaires varient avec la densité de recouvrement. Par conséquent, nous proposons de modéliser l'interaction inter-moléculaire par un potentiel de type Lennard-Jones [24]:

$$V_{LJ} \propto \frac{a_1}{r^6} - \frac{a_2}{r^{12}} \quad (1)$$

où r est la distance entre les molécules adsorbées à la surface, a_1 et a_2 sont des paramètres. Le

surface	supercellule taille	nombre de ligands	taux de recouvrement	θ [\AA^{-2}]	E^{ads} [eV]	δQ_m [e]
(0001)	4x2	4	1	0.093	-2.036	0.67
	2x3	2	2/3	0.062	-3.431	0.67
	2x2	1	1/2	0.046	-3.363	0.67
	2x3	1	1/3	0.031	-3.328	0.67
(10-10)	2x2	4	1	0.099	-1.993	0.49
	2x3	4	2/3	0.066	-3.233	0.49-0.64
	4x2	4	1/2	0.050	-3.644	0.64
	2x3	1	1/3	0.033	-3.692	0.64
	2x2	1	1/4	0.025	-3.651	0.64
(01-11)	2x2	4	1	0.087	-1.396	0.42
	2x3	4	2/3	0.058	-2.901	0.42 -0.63
	2x2	2	1/2	0.043	-3.567	0.63
	2x3	1	1/3	0.029	-3.574	0.63
	2x4	1	1/4	0.023	-3.717	0.63

Table 3: Les énergies d'adsorption et les transferts de charge de CH_3COO sur les différentes surfaces de Co à différents taux de recouvrement. Le transfert de charge est une valeur moyenne calculée avec toutes les molécules dans la supercellule. Lorsque deux valeurs sont présentes, elles correspondent aux deux modes d'adsorption.

taux de recouvrement θ est inversement proportionnel au carré de la distance moyenne entre les molécules. Ainsi, dans une première approximation, la forme polynomiale suivante a été choisie pour la fonction d'ajustement:

$$E^{\text{ads}} = a + b \times \theta^3 + c \times \theta^6 \quad (2)$$

Les énergies d'adsorption sur la surface (0001) sont bien représentées par cette fonction polynomiale. Pour cette surface, l'augmentation de l'énergie d'adsorption a lieu à une densité de recouvrement plus élevée. On peut remarquer une faible diminution de l'énergie d'adsorption de CH_3COO sur cette surface pour des valeurs intermédiaires de θ qui pourraient correspondre à une stabilisation de la couche des ligands en raison des interactions à longue portée. Pour cette surface, même pour la couche la plus dense, les atomes O sont toujours en positions "top".

Pour les 2 autres surfaces, les fonctions de lissage montrent un écart plus important avec les énergies d'adsorption. Les énergies d'adsorption augmentent fortement pour les $\theta \geq 0.05 \text{ \AA}^{-2}$. Cette augmentation de l'énergie d'adsorption vient du fait que, pour ces deux surfaces, il n'est pas possible de maintenir l'adsorption du carboxylate en position "top" pour les deux atomes d'oxygène tout en augmentant le taux de recouvrement. Le mode d'adsorption est donc moins favorable et l'énergie d'adsorption devient plus faible. Néanmoins, nous avons considéré que les valeurs données par ces fonctions polynomiales sont suffisamment précises pour être utilisées dans les modèles de croissance.

Afin d'étudier l'effet de la longueur de la molécule de carboxylate sur la morphologie des NPs de Co, les mêmes calculs ont été effectués avec deux autres longueurs de chaîne: $\text{C}_5\text{H}_{11}\text{COO}$, $\text{C}_{11}\text{H}_{23}\text{COO}$ pour quelques valeurs de θ .

Cette limitation à seulement quelques configurations d'adsorption a été imposée par le temps CPU dont nous disposons auprès des centres de calculs. Néanmoins, nous avons pu constater que pour la molécule $\text{C}_{11}\text{H}_{23}\text{COO}$, les énergies d'adsorption ont diminué de plus de 1 eV pour chaque surface par rapport aux 2 autres molécules (CH_3COO et $\text{C}_5\text{H}_{11}\text{COO}$). Tantdis que

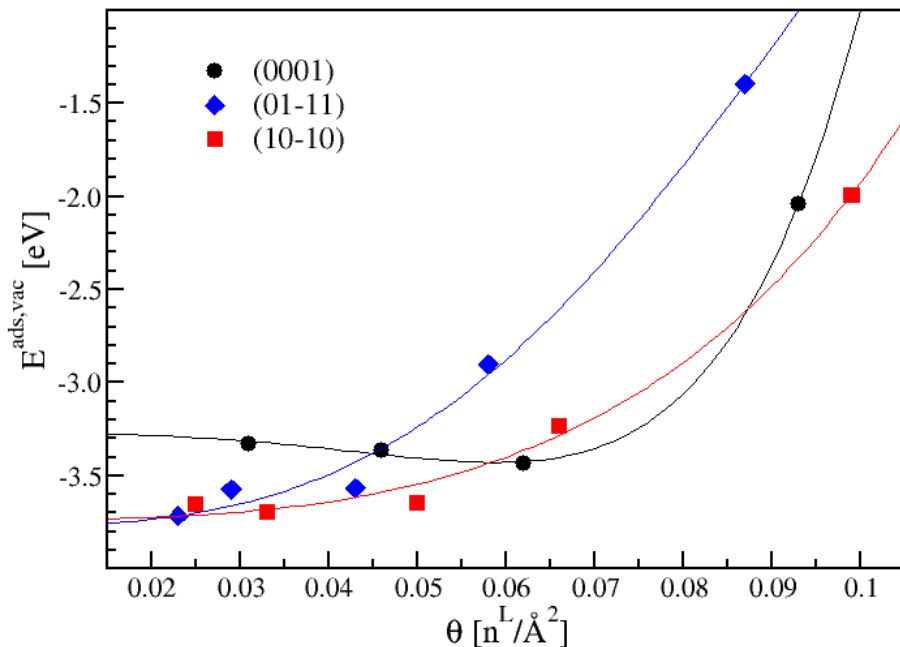


Figure 2: Energies d'adsorption de CH_3COO en fonction de θ pour les 3 surfaces étudiées. Les lignes correspondent aux fonctions polynomiales de la forme $a + b \times \theta^3 + c \times \theta^6$ pour chacune de ces 3 surfaces.

celles de la molécule $\text{C}_5\text{H}_{11}\text{COO}$ sont assez proches de la molécule CH_3COO . La dépendance de l'énergie d'adsorption en fonction de la longueur de chaîne n'est donc pas facilement prévisible.

En bref, j'ai présenté dans ce chapitre 4 les résultats des calculs DFT pour les différentes molécules étudiées et leur adsorption sur certaines surfaces de Co et Ni pour des taux de recouvrement choisis. Deux types de molécules ont été étudiés, les carboxylates et une amine, et les résultats ont révélé que l'adsorption des molécules terminées par le groupe -COO est plus favorable que l'amine sur les deux métaux. Parmi les 3 longueurs de chaîne différentes pour les molécules R-COO, les calculs pour CH_3COO étaient les plus légers et nous ont permis d'obtenir une variation continue des énergies d'adsorption en fonction du taux de recouvrement pour les trois surfaces étudiées. Cette fonction d'ajustement de l'énergie d'adsorption sera utilisée comme base pour construire des modèles de croissance de la nanoparticule en présence de ligands. Dans le chapitre qui suit, plusieurs modèles seront donc testés à l'aide de ces résultats.

0.4 Prédiction de la morphologie des nanoparticules de Co en présence de ligands

Dans ce chapitre, je présente les modèles utilisés pour prédire la morphologie des NPs de Co hcp en présence du ligand CH_3COO et les principaux résultats obtenus. Ces modèles peuvent être classés en deux catégories: thermodynamique et cinétique, basés respectivement sur des arguments thermodynamiques ou sur des arguments cinétiques. Comme précisé dans le chapitre précédent, les énergies d'adsorption de la molécule sur les 3 surfaces de Co, (0001), (10-10) et (0-110), obtenues en fonction du taux de recouvrement servent de base à ces modèles.

0.4.1 Modèles thermodynamiques

0.4.1.1 Modèle de minimisation de l'énergie d'interface

Le premier modèle thermodynamique est celui dit de "minimisation de l'énergie d'interface". Ce modèle suppose que la forme équilibre d'une NP à un volume donné est celle qui minimise les énergies de surface de la NP. En présence du ligand, on extrapole les énergies de surface par celles des interfaces métal-molécule. A partir de ces énergies d'interface, on peut construire le polyèdre représentant la morphologie de la NP en utilisant la méthode de Wulff. L'énergie d'une interface (hkl) est définie comme :

$$\gamma_{hkl}^{int} = \gamma_{hkl} + \theta_{hkl} \times E_{hkl}^{\text{ads}}(\theta_{hkl}) - \theta_{hkl} \times \Delta\mu \quad (3)$$

où γ_{hkl} est l'énergie de la surface Co (hkl) sans ligand, θ_{hkl} est le taux de recouvrement de ligands sur la surface (hkl), E_{hkl}^{ads} est l'énergie d'adsorption d'un ligand sur la surface (hkl) au taux de recouvrement θ_{hkl} dans le vide, et $\Delta\mu = \mu(c, T)$ est la différence de potentiel chimique du ligand dans la solution à la concentration c et la température T et du ligand dans le vide. Dans ce qui suit, plutôt que d'utiliser le taux de recouvrement θ_{hkl} exprimé par l'aire de surface occupé par une molécule, nous définissons Θ comme :

$$\Theta_{hkl} = \frac{\theta_{hkl}}{\theta_{hkl}^{\max}} \quad (4)$$

où θ_{hkl}^{\max} est le maximum de taux de recouvrement sur la surface (hkl). Θ_{hkl} varie de 0 à 1.

Dans le modèle de minimisation de l'énergie d'interface, nous supposons d'abord que les effets du solvant sur l'énergie d'adsorption de la molécule sur la surface métallique sont négligeables. Ensuite, on suppose que la tempéraure est à 0 K (comme celle des calculs DFT). Dans ce cas, les énergies d'interface peuvent être obtenues à partir des énergies d'adsorption et de la différence de potentiel chimique $\Delta\mu$. Comme cette quantité est inconnue, nous l'exprimons par la suite comme un paramètre ajustable.

L'évolution des énergies des interfaces en fonction de $\Delta\mu$ est montrée dans le figure 3. Pour $\Delta\mu < -4,0$ eV, les énergies d'interface les plus faibles pour les 3 surfaces sont les surfaces sans ligands. Nous obtenons alors une forme proche de celle présentée dans le chapitre 3. Pour $-3,45$ eV $< \Delta\mu < -3,31$ eV, les énergies d'interface les plus faibles sont (10-10) avec $\Theta = 1/2$, (0-110) avec $\Theta = 1/2$ et (0001) avec $\Theta = 2/3$. Pour $\Delta\mu > -3,31$ eV, les surfaces les plus stables sont (0001) avec $\Theta = 2/3$, les énergies d'interface les plus faibles sont (0001) avec $\Theta = 2/3$, (10-10) avec $\Theta = 1/2$, (0-110) avec $\Theta = 1/2$ et (0001) avec $\Theta = 2/3$.

Par rapport au travail de Atmane et collaborateurs [5], dans lequel seule la surface prédominante était présentée en fonction de la concentration du ligand ($\Delta\mu$), nous présentons ici une variation de la morphologie sous la forme de construction Wulff. La figure 4 montre ces polyèdres pour $\Delta\mu = -4,0$ eV, $\Delta\mu = -3,43$ eV, $\Delta\mu = -3,0$ eV et $\Delta\mu = -2,0$ eV. Ces formes ne permettent clairement pas d'expliquer les différentes morphologies des NPs de Co présentées dans la figure 10 de [5].

0.4.1.2 Modèle de l'isotherme d'adsorption

Pour prendre en compte explicitement la dépendance en concentration des ligands dans le solvant et la température dans l'expression du taux de recouvrement à l'équilibre, C. Bealing et al. ont proposé une approche similaire au calcul de l'isotherme de Langmuir [25]. Dans son modèle, Θ_{hkl}^{eq} pour la facette (hkl) est dérivé des probabilités d'adsorption et de désorption

d'une molécule de ligand sur la surface (hkl) donnée comme :

$$\Theta_{hkl}^{\text{eq}} = \frac{e^{(-E_{hkl}^{\text{ads}}(\Theta_{hkl}^{\text{eq}}) + \Delta\mu)/k_B T}}{\text{ads eq}} \quad (5)$$

0.4. PRÉDICTION DE LA MORPHOLOGIE DES NANOPARTICULES DE CO EN PRÉSENCE DE LIG

$$1 + e^{(-E_{hkl}(\Theta_{hkl}) + \Delta\mu)/k_B T}$$

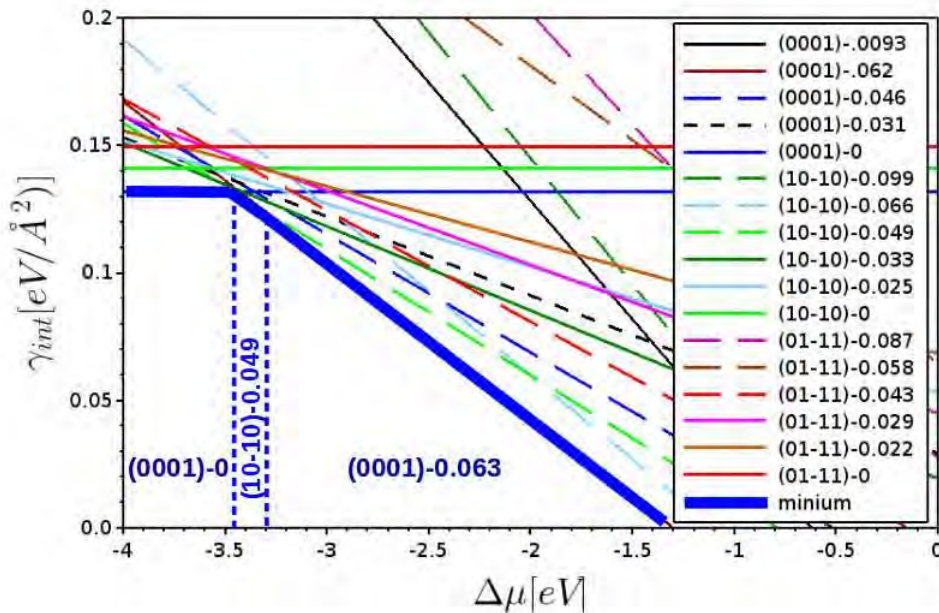


Figure 3: Évolution de l'énergie d'interfaces pour les différentes facettes et couvertures en fonction du potentiel chimique du ligand dans la solution. Pour chaque courbe, la légende indique le nom de la facette et la couverture de surface. La ligne verte en gras représente l'énergie d'interface la plus faible pour toute la couverture à chaque potentiel chimique. Les interfaces correspond à l'énergie d'interface minimale sont indiquées dans chaque région. (0001) dominant la surface correspondent à une forme de disque, (10-10) la surface dominante correspond à la forme de bâtonnet.

Dans notre cas, nous remplaçons les courbes $E_{hkl}^{\text{ads}}(\Theta_{hkl})$ par les fonctions polynomiales obtenues au chapitre 4 pour les 3 principales surfaces de cobalt, et nous obtenons Θ_{hkl}^{eq} en fonction de

$\Delta\mu$ comme le montre la figure 5, en résolvant numériquement l'équation 5 pour chacune de ces 3 surfaces et à chaque valeur de $\Delta\mu$. Notez que, physiquement, $\Delta\mu$ est reliée à la concentration de ligands en solution par:

$$\Delta\mu = \Delta\mu_0 + k_B T \ln \frac{c}{c_{\text{ref}}} \quad (6)$$

où $\Delta\mu_0 = \mu(T, c_{\text{ref}}) - \mu^{\text{vac}}$ est la différence entre le potentiel chimique du ligand dans le vide et dans la solution à la concentration de référence c_{ref} . Par conséquent, dans ce qui suit, nous considérerons qu'un changement de $\Delta\mu$ correspondra à un changement de la concentration du ligand en solution. Pour ces trois surfaces, le taux de recouvrement d'équilibre est nul pour de petites valeurs de $\Delta\mu$, puis augmente jusqu'à la valeur maximale de $\Theta_{hkl}^{\text{eq}} = 1$.

A partir de ces Θ_{hkl}^{eq} , nous pouvons alors calculer les énergies d'interface pour chaque facette (hkl) comme montré dans la figure 6. Les formes de Wulff construites à partir de ces énergies sont semblables à celles obtenues en utilisant le modèle de minimisation de l'énergie d'interface. Aucun de ces deux modèles ne semble capable d'expliquer les différentes morphologies expérimentales des NPs de Co stabilisées par des ligands (les formes de bâtonnet et disque, présentant un rapport d'aspect très différent de l'unité).

0.4.1.3 Conclusion

Nous avons vu, dans cette première partie, que les deux modèles thermodynamiques ne permettent pas d'obtenir les morphologies de type bâtonnet et disque pour les NPs de Co. Comme ces deux modèles supposent que les NPs sont en équilibre thermodynamique, l'aspect cinétique de

0.4. PRÉDICTION DE LA MORPHOLOGIE DES NANOPARTICULES DE CO EN PRÉSENCE DE LIG

la croissance ne joue aucun rôle dans les morphologies finales. Afin de tester cette hypothèse,

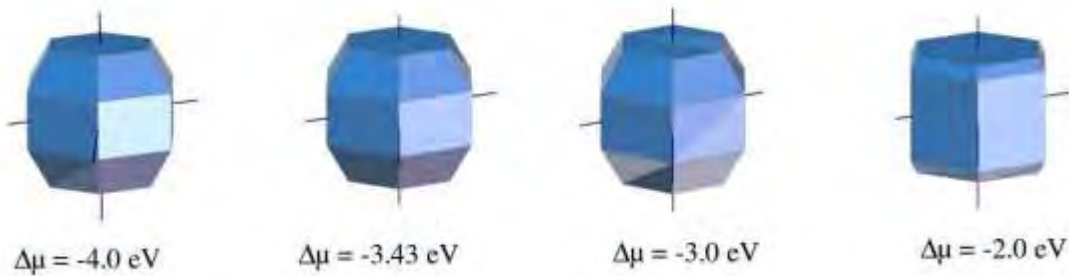


Figure 4: Polyèdres de Wulff construits pour différentes valeurs de $\Delta\mu$ en utilisant les énergies d'interface minimales.

nous avons développé un modèle cinétique pour la croissance des NPs de Co en présence de ligands.

0.4.2 Modèle cinétique

Dans ce modèle, nous décrivons la croissance d'une NP en tenant compte des taux d'incorporation des atomes de Co et le taux d'adsorption des ligands sur les différentes facettes de la NP. Comme pour les modèles thermodynamiques, nous nous limitons à trois facettes principales : (0001), (10-10) et (01-11) et la molécule de ligand $\text{CH}_3 \text{COO}$. Nous décrivons la forme de la NP en utilisant L_{hkl} , les distances du centre de la NP à la surface des facettes (hkl) et S_{hkl} les surfaces des facettes (hkl). Ensuite, nous déduisons le taux d'adsorption de Co et des ligands. Enfin, l'ensemble des équations obtenues sera résolu simultanément en considérant également la conservation des atomes de Co.

0.4.2.1 Aspects théoriques

Incorporation de Co, Pour une surface (hkl) donnée, nous supposons que la vitesse d'adsorption et de désorption des atomes de Co dépend linéairement du nombre de sites disponibles, c'est-à-dire le nombre de sites non recouverts par des ligands. Le rapport de la probabilité d'adsorption $p_{hkl}^{\text{Co,ads}}$ et désorption $p_{hkl}^{\text{Co,des}}$ à un instant t est défini comme :

$$\frac{p_{hkl}^{\text{Co,des}}}{p_{hkl}^{\text{Co,ads}}} = e^{(\mu^{\text{NP}}_{\text{Co}}(T) - \mu^{\text{sol}}(T, c_{\text{Co}}(t))) / k_B T} \quad (7)$$

où $\mu^{\text{NP}}(T)$ et $\mu^{\text{sol}}(T, c_{\text{Co}}(t))$ sont les potentiels chimiques de Co à la température T dans la NP et dans la solution de concentration $c_{\text{Co}}(t)$. Nous retrouvons la vitesse de croissance de Co comme:

$$\frac{dL_{hkl}}{dt} = p_{hkl}^{\text{Co,ads}} \left(1 - \frac{c_1}{c_{\text{Co}}(t)} \right) (1 - \Theta_{hkl}(t)) d_{hkl} \quad (8)$$

où d_{hkl} est la distance inter-planaire de la surface (hkl) considérée, c_1 est la concentration d'équilibre du ligand dans la solution. Elle est supposée beaucoup plus petite que la concentration initiale c_0 . On considère que la croissance s'arrête à l'équilibre, quand $c_1 = c_{\text{Co}}(t)$ ou quand il n'y a plus de sites d'adsorption disponibles ($\Theta_{hkl}(t) = 1$). La croissance de la facette diminue lorsque la concentration de Co dans la solution diminue. Enfin, le nombre total des atomes de Co présents dans le système (solution + NP) doit être conservé pendant la croissance de la NP :

$$\sum_{hkl} N_{hkl} + N^{\text{tot}} = 0 \quad (9)$$

0.4. PRÉDICTION DE LA MORPHOLOGIE DES NANOPARTICULES DE CO EN PRÉSENCE DE LIG

$$_{hkl} \overline{\frac{dt}{dt}} = c_0 \times c_0 dt - c_1$$

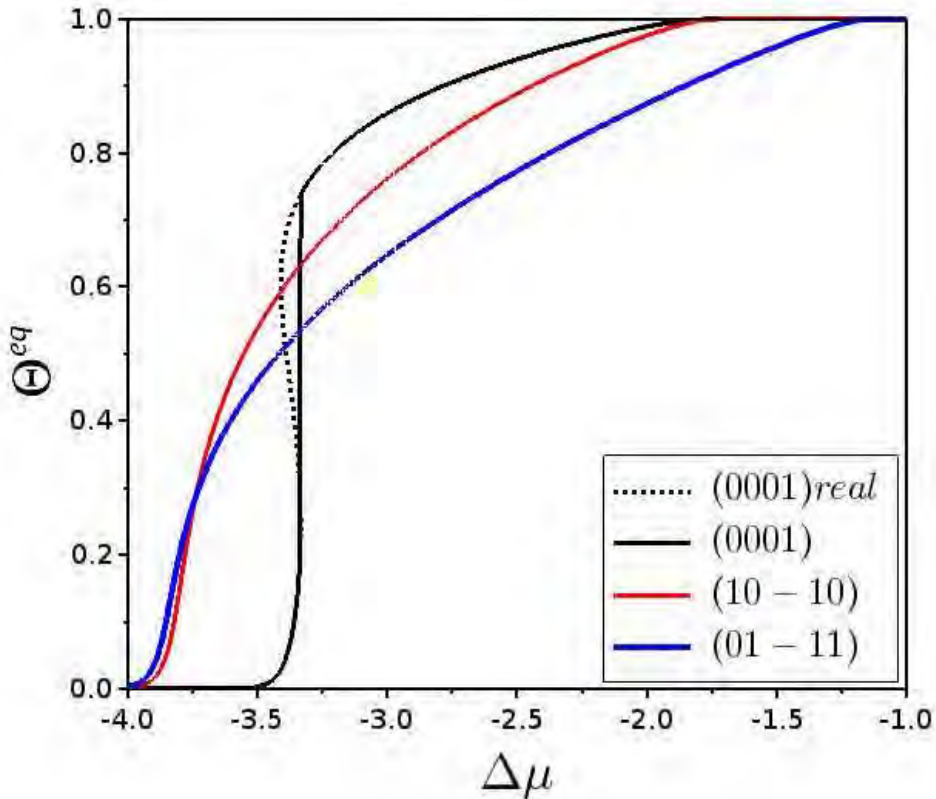


Figure 5: Évolution du Θ^{eq} en fonction du $\Delta\mu$ pour les trois facettes étudiées.

Pour l'adsorption des ligands Comme pour les atomes de Co, nous définissons le rapport de la probabilité d'adsorption $p_{hkl}^{L,ads}$ et la probabilité de désorption $p_{hkl}^{L,des}$ des ligands comme :

$$\frac{p_{hkl}^{L,ads}}{p_{hkl}^{L,des}} = \exp \left[(-E_{hkl}^{ads}(\Theta_{hkl}) + \Delta\mu)/k_B T \right] \quad (10)$$

où $E_{hkl}^{ads}(\Theta_{hkl})$ est donnée par la fonction polynomiale obtenue à par des calculs DFT (chapitre 4).

Nous supposons que la concentration c des ligands dans la solution ne change pas pendant la croissance, puisque seule une petite fraction de ligands dans la solution peuvent être adsorbés sur les surfaces de NP. La variation du nombre de ligands dans la surface est donc:

$$\frac{d\Theta_{hkl}(t)}{dt} = p_{hkl}^{L,ads} \frac{\text{f}_{hkl}}{hkl} \frac{\text{f}_{hkl}}{hkl} \frac{\text{f}_{ads}}{ads} \quad (11)$$

A l'équilibre, le nombre de ligands sur les facettes ne varie plus, $d(\Theta_{hkl}(t)N_{hkl}^{tot})/dt = 0$, et nous retrouvons l'isotherme d'adsorption donné par l'équation 5. La résolution des 3 équations 8 11 et 9 nous permet alors de suivre l'évolution de la morphologie de NPs. Pour chaque facette, nous initialisons $\Theta_{hkl} = 0$. Les dimensions L_{0001} , L_{10-10} et L_{01-11} sont initialisées afin de définir le volume et la taille des facettes de la NP juste après l'étape de nucléation. La compétition entre l'adsorption des ligands et l'incorporation des atomes de Co est prise en compte par le paramètre λ :

$$\lambda = \frac{p_{hkl}^{L,ads}}{p_{Co,ads}^{Co,ads} \left(1 - \frac{c_1}{c} \right)}$$

0.4. PRÉDICTION DE LA MORPHOLOGIE DES NANOPARTICULES DE CO EN PRÉSENCE DE LIG

$$hkl \quad c_0 \quad (12)$$

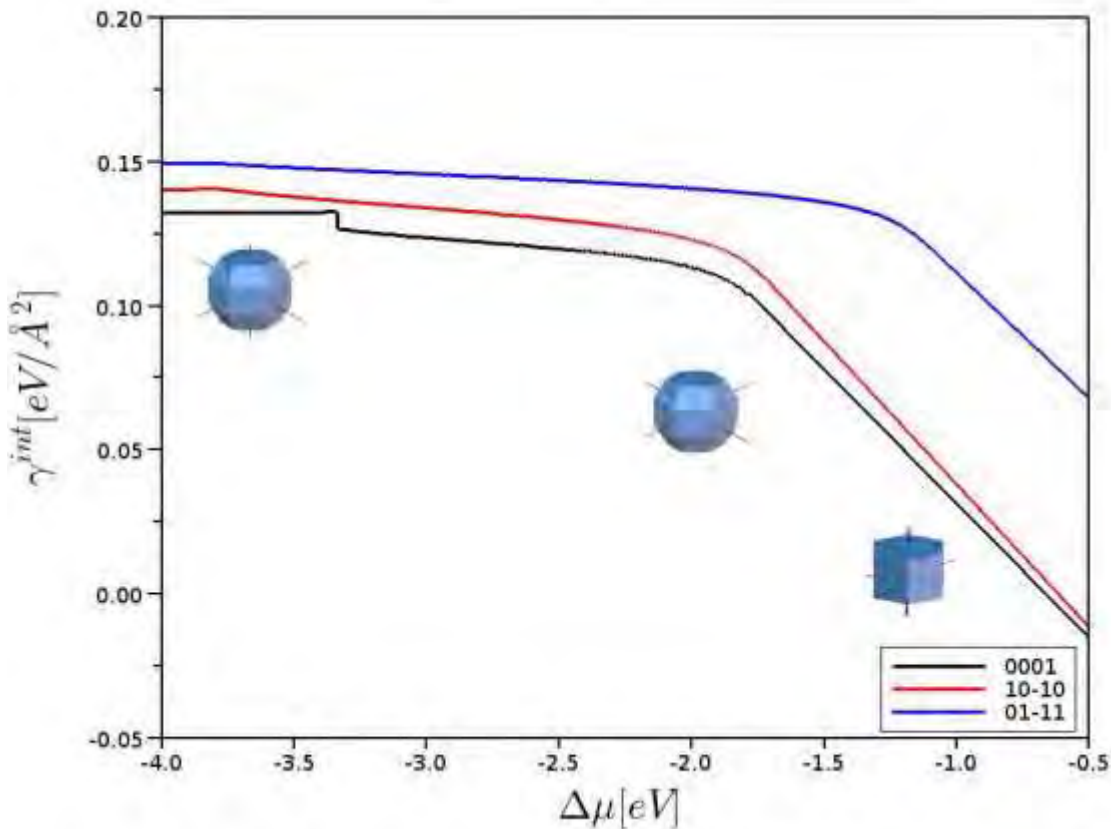


Figure 6: Evolution de l'énergie de l'interface en fonction de $\Delta\mu$ pour les trois facettes considérées, en utilisant le modèle basé sur l'isotherme de Langmuir, et les polyèdres de Wulff de morphologies choisies.

L'équation 11 devient

$$\frac{d\Theta_{hkl}(t)}{dt} = \lambda \times p_{hkl}^{Co,ads} \left(\frac{c_1}{c_0} \right)^f \frac{1 - \Theta_{hkl}(t)}{1 - \Theta_{hkl}(t)[1 + e^{(E_{hkl}^{ads}(\Theta_{hkl}) - \Delta\mu)/k_B T}]^f} \quad (13)$$

Les autres paramètres nécessaires pour la modélisation sont $\Delta\mu$; $\frac{c_0}{c_1}$ et le nombre total de Co dans le système (solution + NP) N . Dans notre cas, nous avons fixé $\frac{c_0}{c_1} = 100$ et N_{Co}^{tot} pour que la NP se termine vers 200 \AA . L'évolution de la morphologie est discutée en fonction des paramètres λ et $\Delta\mu$ pour 2 cas suivants :

- le modèle isotrope, dans lequel $p_{hkl}^{Co,ads}$ et d_{hkl} ne dépendent pas de l'orientation de la facette (hkl) ce qui se traduit par une croissance isotrope des facettes quelque soit l'orientation.
- le modèle d'énergie d'attachement, où $p_{hkl}^{Co,ads}$ et d_{hkl} dépendent de l'énergie d'attachement qui varie en fonction de l'orientation des facettes (chapitre 3).

0.4.2.2 Prédiction des morphologies

L'effet du facteur de compétition λ entre l'incorporation des atomes de Co et l'adsorption des ligands peut être divisé en trois régimes. Pour chacun de ces régimes, la morphologie est

0.4. PRÉDICTION DE LA MORPHOLOGIE DES NANOPARTICULES DE CO EN PRÉSENCE DE LIGAND

contrôlée par $\Delta\mu$ (ou la concentration du ligand dans la solution, voir la figure 7) :

- Lorsque $\lambda = 10^{-3}$, l'incorporation de Co est très rapide par rapport à l'adsorption des ligands. Dans ce cas, le rapport d'aspect ne change pas avec $\Delta\mu$. Ce régime correspond à la situation où la croissance de la NP ne dépend pas de la présence des ligands. La morphologie est proche d'une forme "sphérique".
- Lorsque $\lambda > 0,1$, l'adsorption des ligands est très rapide par rapport à l'incorporation des atomes de Co. la forme de la NP est sphérique pour $\Delta\mu$ petit, allongée pour des valeurs intermédiaires et disque pour des valeurs plus grandes.
- Lorsque $0,1 > \lambda > 0,001$, les temps caractéristiques de l'incorporation des atomes de Co et de l'adsorption des ligands sont proches. le rapport d'aspect maximal est plus faible pour des valeurs de $\Delta\mu$ intermédiaires mais la tendance générale ne change pas par rapport au cas précédent.

Pour les deux derniers régimes, le rapport d'aspect maximal se situe à une valeur de $\Delta\mu$ où la surface (0001) n'est pas recouverte par des ligands mais les 2 autres surfaces sont partiellement recouvertes. Ce maximum est le même pour toutes les valeurs de λ , mais les taux de croissance des deux autres surfaces dépendent du recouvrement des ligands. Plus le taux de recouvrement des ligands est important, plus le taux de croissance est faible. Ainsi, lorsque λ diminue, les ligands n'ont pas assez de temps pour atteindre la recouvrement d'équilibre et le rapport entre ces taux de croissance diminue.

La variation du rapport d'aspect en fonction de $\Delta\mu$ pour différent λ est présentée dans la figure 7 pour le cas du modèle "isotrope". Le comportement est similaire pour le modèle de l'énergie d'attachement.

Lorsque $\lambda \gg 1$ Les ligands s'adsorbent et se désorbent plus rapidement que le monomère de cobalt. La forme finale peut être prédite en utilisant le rapport entre les taux de croissance de ces surfaces et le taux de recouvrement à l'équilibre. La morphologie des NP dépend uniquement de $\Delta\mu$. C'est aussi dans ce cas que les rapports d'aspect extrêmes sont trouvés. La figure 8 montre ces formes correspondant à certaines valeurs particulières de $\Delta\mu$.

Il est intéressant de noter que, contrairement aux modèles thermodynamiques, on observe ici une modification significative de la morphologie en fonction de $\Delta\mu$, qui est liée à la concentration de ligands en solution: la NP passe d'une forme polyèdre sphérique à une forme allongée et puis à une forme de disque. Même si la forme allongée obtenue ne ressemble pas exactement à la forme bâtonnet observée dans les expériences, ce modèle cinétique apporte une amélioration réelle par rapport aux modèles thermodynamiques puisque les morphologies changent considérablement avec la concentration de ligands ($\Delta\mu$) comme observé dans les expériences.

0.4.2.3 Discussion

Dans le modèle de croissance cinétique proposé ici, la morphologie dépend de la vitesse de croissance des facettes dans les trois principales orientations de surface du cobalt hcp. Pour chaque orientation, la vitesse de croissance résulte de la compétition entre la vitesse d'incorporation des atomes de cobalt et la vitesse de recouvrement de surface par l'adsorption de ligands (jusqu'à une monocouche). Pour une facette donnée, la vitesse d'incorporation de Co a été définie comme la vitesse de l'augmentation de l'épaisseur (lorsqu'une couche atomique complète d'atomes de cobalt a été incorporée). Ce taux d'épaissement dépend de deux quantités. Le premier est le nombre de sites disponibles sur la surface du cobalt (non couverts par des ligands). La seconde quantité est le rapport de concentration des monomères de cobalt en solution à l'instant t et celui à l'équilibre (lorsque la croissance de NP s'arrête). Le taux de recouvrement de surface dépend également du nombre de sites disponibles sur la surface ($1 - \Theta_{hkl}(t)$) avec $\Theta_{hkl}(t)$ variant de 0 à 1. A l'équilibre, Θ_{hkl}^{eq} peut être défini par le même isotherme d'adsorption que celui décrit dans

le modèle thermodynamique. Cette croissance cinétique est considérée comme arrêtée lorsque

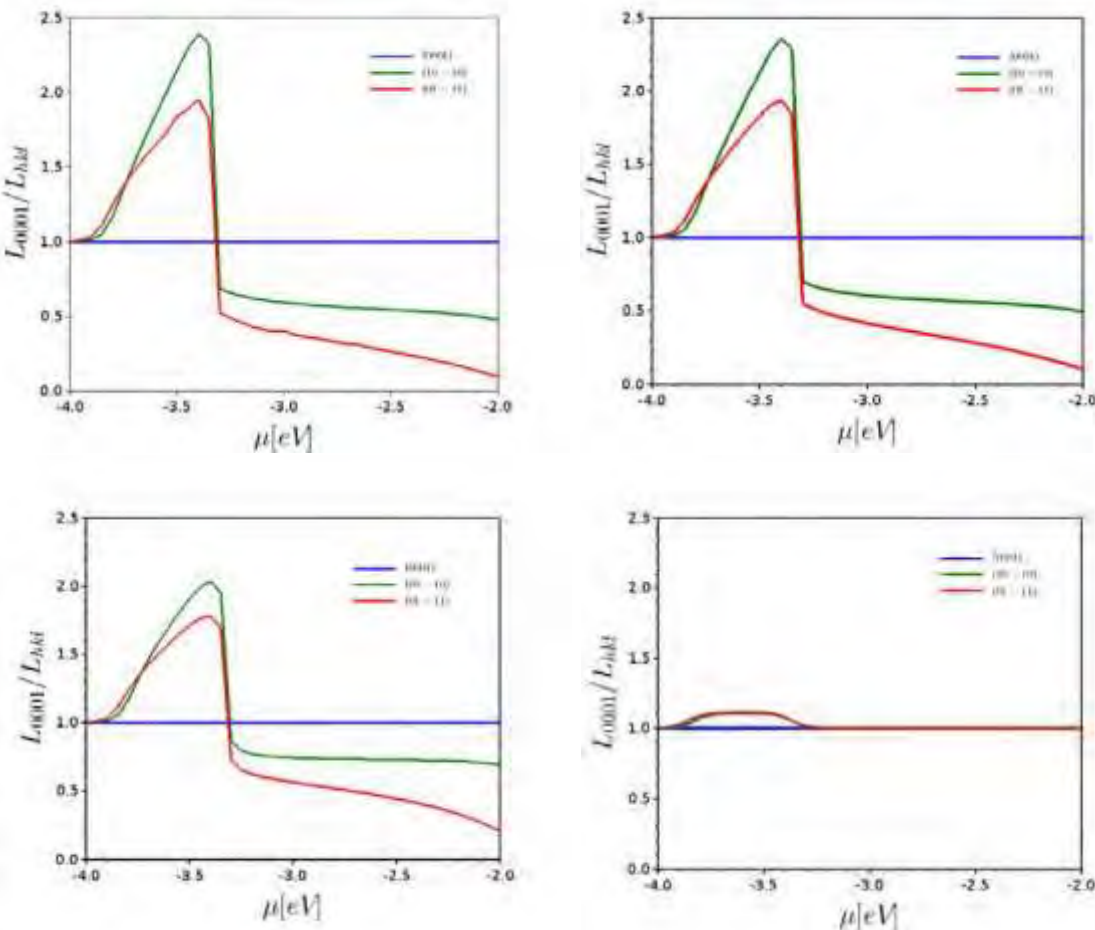


Figure 7: Evolution du rapport d'aspect de la NP en fonction de $\Delta\mu$ pour le modèle "isotrope".
Haut: Gauche : $\lambda = 1$; Droite : $\lambda = 0.1$ - **Bas** Gauche: $\lambda = 0.01$; Droite: $\lambda = 0.001$

la concentration de cobalt dans la solution $c_{Co}(t)$ atteint la concentration d'équilibre c_1 . La compétition (entre l'incorporation de cobalt et l'adsorption de ligands) a été caractérisée par λ . Lorsque λ est proche de 0,1, le temps pour que les monomères de cobalt soient incorporés dans le NP est similaire au temps pour que les surfaces du NP soient recouvertes par des ligands au taux de recouvrement d'équilibre Θ_{hkl}^{eq} . Lorsque $\lambda \gg 1$, les surfaces seront recouvertes bien avant que la concentration de cobalt en solution atteigne c_1 . Inversement, pour λ petit ($\lambda = 0,001$ par exemple), lorsque les atomes de cobalt sont complètement incorporés dans le NP, les taux de recouvrement des ligands sont encore loin d'atteindre l'équilibre.

Lorsque la croissance s'arrête, les morphologies prédites par l'utilisation de ce modèle cinétique dépendent essentiellement de la différence de potentiel chimique $\Delta\mu$, qui reflète la concentration initiale de ligands dans la solution, ceci à l'exception de λ très faible (ex: $\lambda = 0,001$). La morphologie des NPs passe d'une forme sphérique dans le cas où aucun ligand n'est adsorbé sur les surfaces ($\Delta\mu < -3,8$ eV) à une forme allongée pour des valeurs intermédiaires ($-3,8$ eV $< \Delta\mu < -3,3$ eV) et ensuite change en une forme de disque pour des valeurs plus grandes du potentiel chimique ($\Delta\mu > -3,3$ eV). Avec λ petit ($\lambda = 0,001$), comme la NP est le plus souvent découverte, la morphologie est très proche de la forme sphérique.

Pour l'application de ce modèle cinétique, nous avons limité la taille du NP à environ 200 Å (environ 100 couches dans la direction [0001]) et le rapport de concentration à $\frac{c_0}{c_1} = 100$.

Tant le modèle "isotrope" que le modèle de l'énergie d'attachement donnent des résultats similaires. La seule différence (en dimension) est due à la différence de croissance entre les facettes

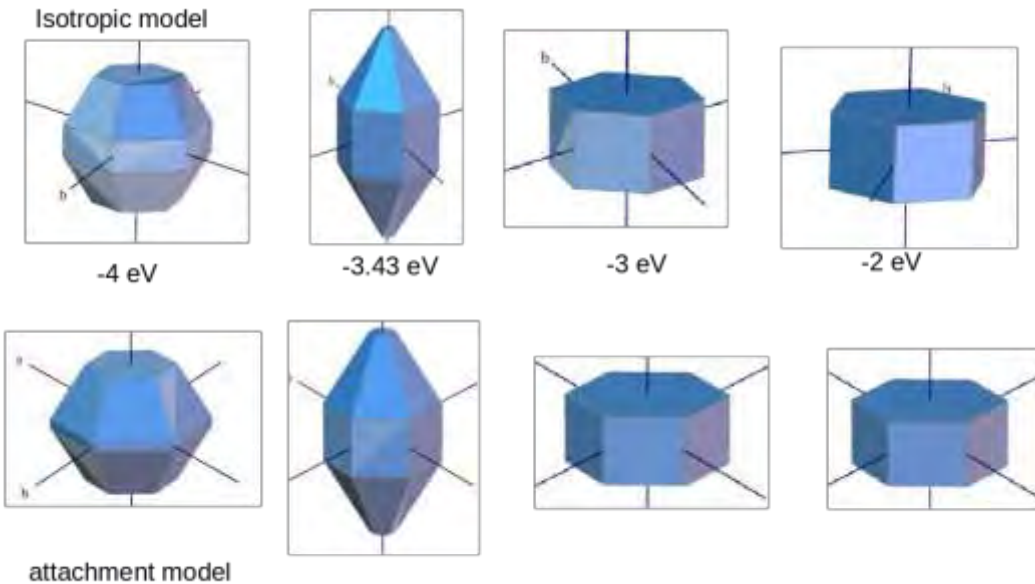


Figure 8: Formes des NPs pour différentes valeurs de $\Delta\mu$: -4 eV; -3,43 eV; -3 eV; -2 eV à $\lambda = 1$ avec le modèle "isotrope" et le modèle de l'énergie d'attachement.

de différentes orientations. Même relativement simple, l'application de ce modèle a montré plusieurs aspects cinétiques importants non présents dans les modèles thermodynamiques:

1. l'évolution de la forme anisotrope (de forme sphérique, en forme allongée à la forme d'une disque) en fonction de la concentration des ligands,
2. la cinétique de croissance (temps pour qu'une NP atteigne sa taille maximale) en fonction de λ ,
3. l'évolution de la taille en fonction de la concentration initiale de cobalt c_0 .

Bien entendu, les morphologies prédites ne sont pas en parfait accord avec celles observées dans les expériences. Ces différences pourraient être attribuées pour partie à la différence entre les conditions utilisées en simulation et en synthèse. Il faut également noter que les hypothèses que nous avons utilisées ont imposé certaines restrictions telles que:

- les effets du solvant sur les énergies d'adsorption sont négligés,
- λ utilisé est identique pour toutes les facettes,
- λ ne dépend pas du taux de recouvrement $\Theta_{hkl}(t)$,
- les ligands sont considérés comme toujours en excès.
- le taux d'adsorption/incorporation (des ligands et des atomes de Co) est supposé être constant pendant la croissance,
- la diffusion des ligands et des atomes de cobalt entre les différentes facettes et avec la solution n'a pas été prise en compte explicitement.

Certains de ces facteurs pourraient être facilement introduits dans notre modèle et pourraient aider à améliorer l'accord entre les morphologies prédites et les résultats expérimentaux.

0.4.3 Conclusion

Dans ce chapitre, j'ai présenté différents modèles de prédiction de la morphologie des NPs de Co en présence du ligand CH_3COO . Dans la première partie, deux modèles thermodynamiques ont été étudiés: le modèle de minimisation d'énergie d'interface et le modèle d'isotherme d'adsorption. Les applications de ces deux modèles ont montré une évolution de la morphologie NP en fonction de la concentration des ligands. Cependant, ces formes d'équilibre thermodynamique n'expliquent pas la formation des bâtonnets observés dans les expériences. Afin de prendre en compte les effets cinétiques sur la morphologie des NPs de Co, nous avons dérivé un modèle basé sur la compétition entre la vitesse d'adsorption des ligands et la vitesse d'incorporation des atomes de cobalt. Ce modèle, à la fois sous sa forme simplifiée ou sous

sa forme générale, a la capacité de prédire non seulement une forme allongée, mais aussi les formes sphériques et de disque en fonction de la concentration des ligands en solution. Cette anisotropie de forme est clairement due aux effets cinétiques. Notre modèle cinétique, encore relativement simple, semble être une méthode prometteuse pour expliquer la variété des formes de nanoparticules de Co synthétisées en solution.

0.5 Conclusion

La connaissance de la relation entre la structure et les propriétés des matériaux est la clé pour comprendre et améliorer leurs propriétés fonctionnelles. Des nanoparticules de qualité avec une distribution de taille étroite et une morphologie bien définie seraient nécessaires à cette fin. Parmi les procédés de fabrication, la synthèse chimique présente l'avantage d'un faible coût et d'une grande flexibilité. Cependant, dans ce procédé, la nature des précurseurs, des agents réducteurs et des ligands stabilisateurs, ainsi que leurs concentrations, la température, les conditions chimiques et les paramètres cinétiques jouent un rôle important dans le contrôle morphologique. Cependant, l'utilisation de ces conditions spécifiques rend les mécanismes de croissance complexes et difficiles à expliquer par une théorie unifiée. Les efforts existants pour prédire les morphologies des nanoparticules ne peuvent qu'étudier les systèmes au cas par cas.

Dans le cas particulier des nanoparticules de Co hcp, les propriétés magnétiques anisotropes sont particulièrement intéressantes pour des applications grâce à leurs morphologies comme dans le cas des nano-disques. Récemment, il a été montré expérimentalement que le contrôle de morphologie des NPs de Co est possible en utilisant des ligands tels que la rhodamine, l'hexadecylamine[2, 26] (avec une terminaison amine) ou des carboxylates comme $C_{11}H_{23}COO$ [5]. Cependant, les mécanismes impliqués pour obtenir ces formes particulières ne sont pas bien compris.

La motivation de mon travail était donc d'utiliser les calculs DFT pour étudier l'effet de ces ligands adsorbés sur les surfaces métalliques avec pour objectif final de construire un modèle capable de prédire la morphologie d'une nanoparticule en fonction de la concentration des ligands adsorbés. Tous nos calculs de DFT ont été effectués en utilisant le logiciel VASP [18, 20, 17, 19], un programme DFT périodique avec une base d'ondes planes.

Dans la modélisation de l'interaction entre les surfaces et les ligands, la première étape consiste à décrire les substrats métalliques (les propriétés dans le massif et à la surface) et

les molécules isolées. À cette fin, le choix d'une fonctionnelle d'échange et de corrélation est important. De plus, il est nécessaire de prendre en compte les interactions de van der Waals (vdW) dans ces systèmes (molécule-surface). Contrairement au cas des molécules, l'utilisation de l'interaction de dispersion vdW dans des systèmes métalliques n'est pas toujours justifiée. Nous avons alors comparé l'efficacité des fonctionnelles PBE, PBE+DFTD et opt86B pour tenir compte des effets de l'interaction vdW sur les propriétés de surface et du massif de Ni fcc et Co hcp. Au final, nous avons trouvé que les paramètres de maille, l'énergie de cohésion et

le "bulk modulus" calculés avec la fonctionnelle PBE sont en meilleur accord avec les valeurs expérimentales pour les 2 métaux. Pour la surface Co(0001), c'est aussi la fonctionnelle PBE qui donne un meilleur accord pour les propriétés de surface. En revanche, pour la surface Ni(111), la fonctionnelle opt86B semblerait mieux adaptée. Mais la fonctionnelle PBE donne des valeurs assez proches.

Avec les énergies de surfaces calculées avec la fonctionnelle PBE, nous avons construit les polyèdres en utilisant la méthode de Wulff pour représenter la morphologie des nanoparticules de Co hcp et de Ni fcc non recouvertes par les ligands. Dans le cas de Co, les orientations principales sont les facettes (0001), (01-11) et (10-10). Dans le cas de Ni, seules les facettes (111) et (001) existent.

Compte tenu de la taille de la molécule de rhodamine, nous nous sommes concentrés uniquement sur les calculs des carboxylates et d'une amine : CH_3COO , $\text{C}_5\text{H}_{11}\text{COO}$, $\text{C}_{11}\text{H}_{23}\text{COO}$ et CH_3NH_2 . Toujours à cause de la taille des systèmes ($\text{C}_{11}\text{H}_{23}\text{COO}$ par exemple), après avoir discuté sur l'influence des longueurs de chaînes hydrocarbonées et sur le rôle du groupe de terminaison sur l'énergie d'adsorption, nous avons calculé toutes les énergies d'adsorption de CH_3COO sur Co(0001), Co(01-10) et Co(10-10) avec des taux de recouvrement variant de 1/4 jusqu'à 1. A partir de ces énergies, nous avons présenté la variation de l'énergie d'adsorption en fonction du taux de recouvrement θ de façon continue par une fonction polynomiale pour les 3 surfaces. Ces fonctions sont ensuite utilisées pour prédire la morphologie des NPs de Co stabilisées par les ligands CH_3COO .

Pour construire les polyèdres représentant la morphologie des NPs de Co, nous avons d'abord testé deux modèles thermodynamiques (le modèle de minimisation d'énergie d'interface et le modèle de l'isotherme d'adsorption). Les 2 modèles thermodynamiques ont montré une évolution de la morphologie de NPs en fonction de la concentration des ligands (représenté sous forme de potentiel chimique) assez similaire. Mais aucun de ces deux modèles n'a pu prédire la forme bâtonnet observée expérimentalement. Nous avons ensuite proposé un modèle cinétique pour pouvoir prendre en compte la compétition entre le taux d'incorporation des atomes de Co et la vitesse de recouvrement des facettes de la NP lors d'une synthèse. Pour ce faire, nous avons émis plusieurs hypothèses importantes: (1) le nombre total d'atomes de Co dans le système (solution +NP) est fixe, (2) la concentration des ligands dans la solution ne varie pas en cours de croissance, (3) la croissance de la NP s'arrête lorsqu'une des ces conditions est atteinte: (a) la concentration de Co est égale à la concentration d'équilibre ou (b) les facettes sont entièrement recouvertes par une couche dense de ligands ($\Theta = 1$). Sous ces conditions, nous avons introduit un facteur de compétition λ sous la forme d'un rapport de probabilité $p_{hkl}^{\text{L,ads}} / p_{hkl}^{\text{Co,ads}}$ en fonction de Θ . A partir de ce modèle cinétique, nous avons obtenu une plus grande variété de morphologies comme des formes allongées, sphériques et disques en fonction du potentiel chimique (concentration initiale des ligands dans la solution) et du facteur λ .

Ce modèle pourrait encore être amélioré et nous devons compléter cette étude par une analyse systématique de l'influence de chacun des paramètres clés. Par exemple, changer la valeur de λ pourrait être interprété comme l'utilisation d'un type de ligand différent (amine, TOPO ou RhB par exemple). Nous devons également améliorer la fonction d'ajustement pour l'énergie d'adsorption en fonction du taux de recouvrement pour mieux prendre en compte l'inhomogénéité des facettes (01-10) et (10-10). Nous pouvons par la suite inclure d'autres facteurs qui ne sont pas encore pris en compte dans ce modèle comme les effets du solvant sur les énergies d'adsorption, la dépendance de λ sur le potentiel chimique de la solution, sur la couverture de surface $\Theta_{hkl}(t)$ et sur l'orientation des facettes, ou encore la diffusion de ligands et de monomères en surface et en solution. Ces paramètres supplémentaires pourraient contribuer à améliorer l'accord entre les morphologies prédictes et les résultats expérimentaux. Avec ces améliorations, ce modèle pourrait être généralisé pour prédire une variété de morphologies de différentes nanoparticules.

Contents

Résumé	v
0.1 Introduction	v
0.2 Calculs des propriétés des métaux et des énergies de surface	vii
0.3 Adsorption de ligands sur des surfaces métalliques	ix
0.4 Prédiction de la morphologie des nanoparticules de Co en présence de ligands	xiii
0.4.1 Modèles thermodynamiques	xiv
0.4.2 Modèle cinétique	xvi
0.4.3 Conclusion	xxii
0.5 Conclusion	xxii
Introduction	1
1 Controlling and predicting the NP morphology	5
1.1 Controlling the NP morphology	5
1.1.1 Precursor decomposition and nucleation	7
1.1.2 Formation of nuclei/seeds	8
1.1.3 From seeds to nanocrystals	9
1.1.4 The case of cobalt nanocrystals	12
1.2 Predicting the NP morphology	14
1.2.1 Thermodynamics prediction	14
1.2.2 Kinetics prediction	22
1.3 Conclusion	25
2 Density Functional Theory	27
2.1 The Schrödinger Equation	28
2.1.1 Born-Oppenheimer approximation	28
2.1.2 Variational Principle and ground state	28
2.2 Hartree Fock approximation	29
2.3 Density functional approach	30
2.3.1 Electron density function	30
2.3.2 The Thomas Fermi model	30
2.3.3 Hohenberg and Kohn theorems	30
2.3.4 Kohn Sham Equation	31
2.4 Exchange-correlation energy	31
2.4.1 The local density approximation (LDA)	33
2.4.2 The generalized gradient approximation (GGA)	33
2.4.3 Hybrid functional	33
2.5 Van der Waals dispersion	34
2.5.1 Including empirical corrections DFT-D	34
2.5.2 Non Local dispersion density functional (vdW-DF)	35
2.6 DFT in periodical system	35

2.6.1 Plane Wave basis	35
2.6.2 Pseudopotentials	36
2.7 Conclusion	36
3 Metal surfaces and bulk calculations	37
3.1 Introduction	37
3.2 Preliminary calculations	38
3.2.1 The number of k-points	38
3.2.2 Cutoff energy	39
3.2.3 Smearing	40
3.3 Bulk properties	41
3.3.1 State equation	41
3.3.2 Isolated Atom	41
3.3.3 Cohesive energy and structural parameters	42
3.3.4 Summary	44
3.4 Surface optimization and choice of vdW dispersion	44
3.4.1 Surface models	44
3.4.2 Preliminary calculations of Co(0001) and Ni(111) surfaces	46
3.4.3 Surface properties of Co(0001) and Ni(111) with vdW dispersion	48
3.4.4 Summary	53
3.5 Surface energies of Co and Ni	53
3.5.1 Co surfaces	53
3.5.2 Ni surfaces	54
3.6 The <i>attachment energy</i> model	56
3.7 Conclusion	58
4 Adsorption of ligands on metallic surfaces	61
4.1 Molecules	61
4.1.1 Computational details	62
4.1.2 Geometry and charges	62
4.2 Ligand adsorption on the metallic surfaces	63
4.2.1 Modelling aspects	63
4.2.2 Adsorption of CH ₃ COO ⁻ on the Co surfaces	66
4.2.3 Adsorption of C ₅ H ₁₁ COO ⁻ and C ₁₁ H ₂₃ COO ⁻ on the Co surfaces	71
4.2.4 Adsorption of CH ₃ COO ⁻ on the Ni surfaces	72
4.2.5 Adsorption of CH ₃ NH ₂ on the surfaces of Co and Ni	72
4.3 Conclusion	74
5 Morphology prediction of Co NPs	77
5.1 Thermodynamic model	77
5.1.1 Lowest interface energy model	78
5.1.2 Adsorption isotherm model	80
5.1.3 Conclusion	82
5.2 Kinetic model	83
5.2.1 Theoretical aspects	83
5.2.2 Results	87
5.2.3 Discussion	95
5.3 Conclusion	96
Conclusion	97

CONTENTS

xxvii

A Atomics position of Co surfaces	99
B Diffusion of adatom and ligands molecule on the Co surfaces	103

Introduction

Particles of matter with a size ranging from 1 nanometer (nm) to hundreds of nm are generally called nanoparticles (NPs). Within these particular sizes, NPs have attracted much attention not only for their remarkable physical properties from a scientific point of view, but also for their industrial applications from an economical point of view. At the same time, this nanometer sized particles present also potential dangers for the health and the environment. The lack of knowledge on the effects of these NPs on public health has already aroused general public fear on these new materials.

In any case, the knowledge of the physical properties of NPs is highly important. Besides the size, the morphology of these NPs is also a key element to control their properties. Experimentally, the chemical synthesis in solution is one of the most important fields for NPs elaboration. Great progress in the optimization of the synthesis protocol to control the morphology of NPs has been achieved in the past two decades. The obtention of a large variety of shapes which include not only sphere, cube, cuboctahedron, octahedron, tetrahedron, dodecahedron, icosahedron, etc. but also triangular, hexagonal thin plats, rods or wires with circular, square, rectangular, pentagonal or octagonal cross-section have been reported in the literature [1]. However, it is still extremely difficult to understand the formation mechanisms of NPs with a specific morphology. This difficulty is closely linked to the large number of influent parameters in a synthesis protocol such as the nature of precursor, reducing agent, surfactant, stabilizing ligands, their quantity, concentration, temperature, injection order, time, etc. Very recently, it was also discovered that the side reaction between different molecules could drastically change the synthesis conditions, and thus must be considered [2].

In spite of these extremely complicated conditions, the NP growth could be separated in three well identified steps, as proposed by LaMer and coworkers at the beginning of 50s [3]. (1) The first step corresponds to a rapid increase of the concentration of metal monomer up to a saturation concentration. During this step, the precursors are decomposed into free metallic atoms or monomers. (2) The second step, also called nucleation step, corresponds to the formation of clusters/nuclei. When the number and/or the size of the nuclei reaches a given number, the concentration of monomers drops below the saturation limit. (3) During the last step (growth step), the monomers in solution will be incorporated into existing nuclei/seed through different diffusion mechanisms. The size of these nanocrystals increases until the concentration of monomers decreased to a limited value. The morphology evolution during this growth step should be possible to control. One of the simplest idea is to control the stability of facets of a given NP by using molecular capping agents. Indeed, as the shape of a NP in vacuum could be predicted by using the Wulff construction method, which is based on the surface energy of the facets. One can extrapolate that the adsorption of a capping layer could not only modify significantly the surface energy of some facets but also the kinetics of incorporation of the monomers on the different facets. By doing so, the stability order of these facets could be modified, and thus induce a morphology change.

Unlike metallic face centered cubic (fcc) NPs, for which a huge number of results (both experimental and theoretical) exist, only limited works on the morphology control of hexagonal closed-packed (hcp) NPs could be found [2, 4, 5]. Yet, the hcp cobalt NPs, for instance,

are particularly interesting because of the possibility to grow “naturally” anisotropic shape nanocrystals. The properties associated to this anisotropy are interesting for applications such as information storage or permanent magnets due to their high magnetization and magneto-crystalline anisotropy energy. It is also known as efficient catalysts for many reactions [6, 7]. Stable, fully metallic (without oxide) cobalt nanodisks were obtained by the group of C. Amiens by using the rhodamine B (RhB) as stabilizing ligand [2]. It was supposed that the use of RhB could be at the origin of this nanodisk shape. More recently, it has been shown by P. Sautet and coworkers [5], that Co NPs stabilized by carboxylate ligands exhibited very different shapes depending on the concentration of ligands in solution: from rod-like shape at low concentration to disk-like shape at high concentration. The theoretical investigation presented in Ref. [5] explained this morphology change by a modification of the interface energies between the ligands and the Co NP facets as a function of the ligand concentration. However, this demonstration was based on thermodynamic arguments only and did not take into account the kinetics aspects of the NP growth.

In order to understand the stability of the Co NP morphology and the reason of this anisotropic growth, we have first proposed to calculate the interface energies of the different Co surfaces covered by RhB, carboxylate and amine molecular layers as a function of the coverage, by using density functional density (DFT) calculations. Using these energies, and in particular the ones obtained from the adsorption of the carboxylate molecules, we have derived different models for the prediction of the NP morphology as a function of the ligand concentration, from the simple thermodynamic approaches to a more elaborated kinetics model. It turned out that none of the thermodynamics models could reproduce the large variety of morphologies observed experimentally whereas, by taking into account the kinetics, the diversity of morphologies could be obtained.

In the first chapter, I first present a brief review on recent experimental works on the different steps of the growth mechanism on the shape-controlled synthesis of fcc metals and hcp cobalt. This review reveals the complexity of each step of “in solution” synthesis of NPs. This complexity could however be reduced in some specific cases by modifying only one or two selected parameters. In a second time, the NP morphology prediction methods according to a thermodynamic approach including (i) the Wulff reconstruction model [8], (ii) the lowest interface energy model and (iii) the adsorption isotherm model, as a function of the surface coverage. Within the kinetics approach, the classical nucleation and growth theory, as well as the Lifshitz-Slyozov-Wagner theory [9] are briefly presented before a simple description of the mean first passage time (MFPT) [10] and the surface area limited (SAL) methods [11].

As the precise adsorption and surface/interface energies were calculated by using DFT calculations, the second chapter is devoted to the description of the principles of DFT and of the standard approximations for the exchange-correlation energy evaluation. This chapter terminates by a rapid presentation of the dispersion correction methods, the plane wave basis set and the projector augmented wave (PAW) pseudopotentials as implemented in the Vienna ab-initio simulation package (VASP).

The third chapter details the optimization of the simulation conditions such as the k-points mesh for the reciprocal space Brillouin zone sampling, the cut-off energy and the smearing, needed for the computation of metallic systems. The rest of the chapter is devoted to the presentation of the results for Co and Ni bulk and surface properties.

In the fourth chapter, the simulation setups used for the adsorption of organic ligands on different surfaces of hcp Co and fcc Ni are detailed. The reason for using carboxylate with different chain lengths (CH_3COO , $\text{C}_5\text{H}_{11}\text{COO}$ and $\text{C}_{11}\text{H}_{23}\text{COO}$) and amine (NH_2CH_3) instead of rhodamine B is also explained. At the end of this chapter, the adsorption energies as a function of the surface coverage and the charge transfer upon adsorption are shown for each molecule-surface configuration.

In the fifth chapter, the Co NPs morphology prediction models are tested using the previously computed quantities for the smallest ligand molecule CH_3COO and the Co NPs for which experimental comparison is possible. The first part is devoted to the presentation of the thermodynamic models, i.e. the lowest interface energy model and the adsorption isotherm models, and the predicted morphologies as a function of the ligand concentration are presented and discussed. In the second part, we propose a new kinetic model which includes a competition between the cobalt atom incorporation and the molecular ligand adsorption. The morphology evolution as a function of the ligand concentration and for different rates of adsorption is shown and discussed at the end of the chapter.

Finally, a general conclusion is given at the end of the manuscript.

Chapter 1

Controlling and predicting the nanoparticle morphology

Contents

1.1 Controlling the NP morphology	5
1.1.1 Precursor decomposition and nucleation	7
1.1.2 Formation of nuclei/seeds	8
1.1.3 From seeds to nanocrystals	9
1.1.4 The case of cobalt nanocrystals	12
1.2 Predicting the NP morphology	14
1.2.1 Thermodynamics prediction	14
1.2.2 Kinetics prediction	22
1.3 Conclusion	25

Nanoparticles (NPs) can present different morphologies such as spheres, cubes, polyhedron and even nanorods. These morphologies have a great impact on the NPs properties and in particular on reactivity, magnetic or optical properties. Controlling the NP morphology is thus one of the key factor for mastering and exploiting their properties. However, since now, the mechanisms leading to a specific morphology remain poorly understood, except for the equilibrium shape of nanocrystals under vacuum. The large variety of experimental parameters involved at different steps of nucleation and growth is a barrier in the development of a robust theory able to predict the NP morphology whatever the synthesis conditions. In this chapter, I would like to present the recent methods of synthesis of metallic NPs, focusing on the essential parameters controlling their morphology. I also summarize the recent theoretical efforts in modelling and predicting the morphology of these NPs.

1.1 Controlling the NP morphology

Nanoparticles are one of the most important families of functional materials which are characterized by their nanometric size. Compared to other materials, the electronic confinement due to this size reduction, when associated to their composition, surface orientations, morphology and environment has contributed to the emergence of important new properties in many different fields (electronics, magnetism, catalysis, optics...) and has opened a boulevard to their applications in information storage, medical imaging, catalysts, to name a few examples [27].

These functionalities depend also on the nature of these NPs, which can be insulator, semiconductor, or metallic. The techniques to obtain NPs range from mechanical milling (top-down approach), vaporisation-condensation (CVD, magnetron sputtering, etc.), spray pyrolysis, sol-gel... to chemical synthesis in solution (bottom-top approaches). However, in order to improve the functional properties of these materials, it is important to understand the close connection between the structure and the properties. To this end, one of the first conditions is to obtain NPs with a well crystallized single domain, a narrow size distribution and a single morphology. The fabrication of such high quality NPs requires very specific conditions with controlled environment (vacuum), growth temperature, annealing steps...for what concerns the NP synthesis by CVD (chemical vapor deposition) or PVD (physical vapor deposition as magnetron sputtering, pulsed laser deposition or thermal evaporation) methods. For the chemical synthesis in solution, one needs to use specially selected precursors, reducing agents and stabilizing ligands and to control temperature, (injection) kinetics and reaction time. Compared to the fabrication in ultra high vacuum (UHV)conditions, chemical synthesis has the advantage to be more accessible because of its lower cost and enhanced flexibility. In addition, large amounts of NPs can be synthesized and easily functionalized or just directly protected against oxidation by the stabilizing ligands (Figure 1.1). In a controlled atmosphere (inert gas or vacuum), NPs

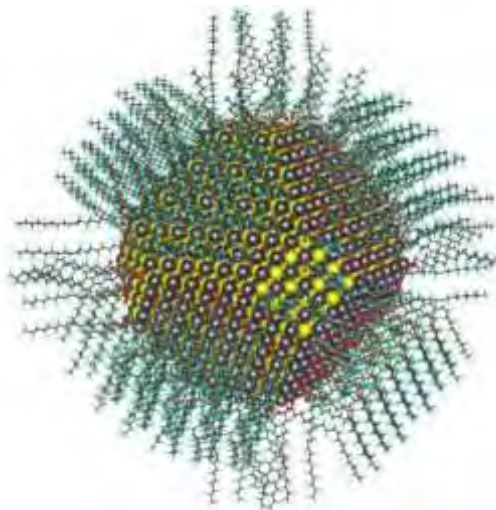


Figure 1.1: Calculated atomic structure of a 5nm diameter PbS nanocrystal passivated with oleate and hydroxyl ligands (from [28]).

can adopt the well-known thermodynamic equilibrium shape minimizing their surface Gibbs free energy, predicted by the Wulff theorem [8]. In solution, as the equilibrium conditions are drastically deviated due to the presence of solvents, precursors, reducing agents, surfactants... at different reaction temperatures and times, the Wulff theorem can no longer be used to predict the NP morphology. However, in spite of the dependence of the NP shape on a large number of reaction parameters, the success of the chemical synthesis to obtain a wide variety of morphologies for metallic NPs is among the most important progresses in this field during the two last decades. This success is due to progress reached lastly in the methods of synthesis (including new precursors/reducing agents/stabilizers) and in the identification of reaction intermediates (nuclei, seeds etc), as well as in atomistic modeling and theoretical prediction methods. As summarized in a recent review of Y. Xie et al. [1], the degree of understanding is already reasonably good for the shape control of some metallic NPs, which is proven by the reproducibility and controllability of optimized synthetic protocols. Nevertheless, the mechanisms at the origin of this morphology are very complicated, and still not fully understood (more particularly at the atomic scale). The first example of intentional synthesis of metallic NPs was attributed to Faraday in 1850's. In this synthesis, gold colloids were prepared by the

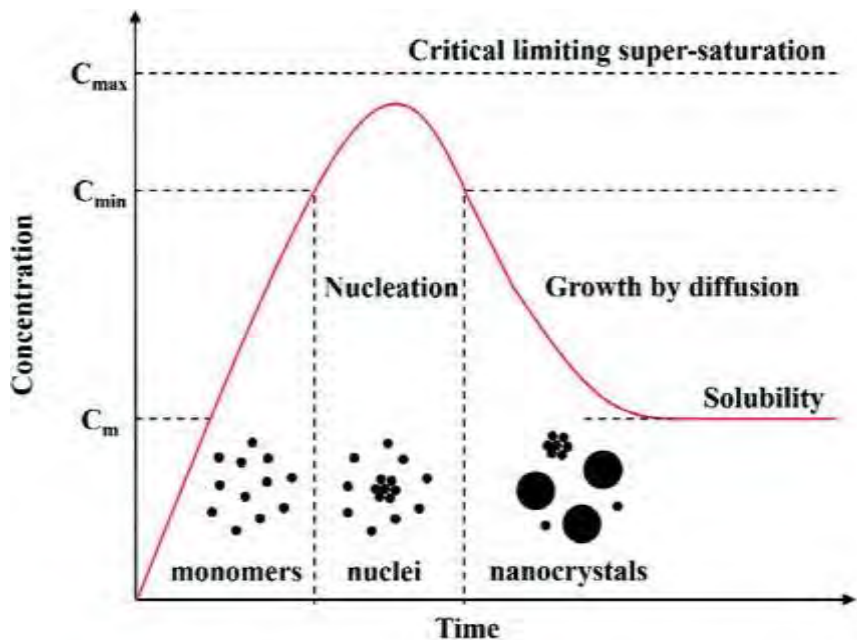


Figure 1.2: LaMer diagram showing the growth steps of nanoparticle in the solution (from [29]).

reduction of gold chloride in water with the presence of phosphorus [30]. The first simplified growth mechanism was proposed by LaMer et al. in 1950's [3] during their work on the synthesis of mono-dispersed sulfur colloids in solution. This diagram (also called LaMer diagram) divided the whole mechanism into 3 steps:

1. decomposition of the precursor and generation of metal atoms with the increase of the concentration.
2. when the concentration of metal atoms reach the supersaturation condition, nucleation starts and continues to the formation of small clusters or seeds. At the same time, the concentration decreases.
3. when the concentration has decreased below the saturation condition, seeds formation stops and the growth of nanocrystals starts.

However, the second step should be separated into 2 sub-steps:

- 2a nucleation starts when the concentration of metal atoms reach the supersaturation condition.
- 2b stop of nucleation and formation of seeds (growth, Oswald ripening or aggregation).

Ideally, a systematic in-situ characterization at each of these steps could contribute greatly to the understanding of the formation mechanisms with controlled synthesis parameters. However, these characterizations are difficult, specially for the early stages of nucleation. In the following, I try to make a brief summary on the present knowledge of the growth mechanisms from the experimental point of view.

1.1.1 Precursor decomposition and nucleation

Before the nucleation step, precursor salts are decomposed and supposed to be reduced to metal atoms in order to constitute a reservoir of building blocks for the growth of nanocrystals. During this step, the concentration of atoms will increase up to the supersaturation condition

at which the nucleation starts. However, it is unclear whether the precursors are reduced into zero-valent atoms first and then aggregate into nuclei to form nanocrystals, or if the precursors aggregate first to form nuclei before the reduction and the detachment of ligands. These different mechanisms could conduct to different nanoclusters and/or seeds, and could influence the final shapes of NPs. One example was emphasized by the first-principles molecular dynamics simulation on the platinum cluster nucleation and growth in solution [31]. Indeed, it was shown that Pt-Pt bonds could be formed between dissolved Pt(II) complexes. Moreover, $[\text{PtCl}_2(\text{H}_2\text{O})_2]$ complexes (the hydrolysis product of a precursor $(\text{PtCl}_4)^{2-}$) for Pt NPs synthesis) could be directly added to small clusters according to the autocatalytic growth mechanism. Partially reduced Pt dimers and trimers could thus be considered as early stage intermediates of Pt nucleation. In an experimental investigation on the formation of nanoplates of Ag, it was confirmed by using mass spectrometry that about 27% of the total Ag in AgNO_3 precursor solution are trimeric clusters [32]. These examples confirm that it is necessary to characterize species in the solution at the decomposition/early nucleation stage to understand a particular shape of nanocrystals (and to ensure reproducibility).

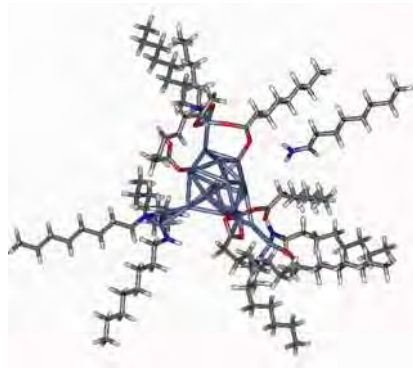


Figure 1.3: Example of an early stage Co cluster with carboxylate and amine as ligands (calculated with MOPAC2012.)

1.1.2 Formation of nuclei/seeds

1.1.2.1 Nucleation

Starting from the early intermediates described here above, small clusters (nuclei) are formed, and play the most important role in driving the assembly of atoms into nanocrystals. Due to their small sizes, very little is known about these nuclei during a synthesis. Experimental techniques such as electrospray mass spectrometry could be used to estimate the population of clusters with different masses [33], while electrospray photoelectron spectroscopy could eventually reach the geometric information by comparing recorded absorption/emission spectra with characteristic signals at known wavelengths [34]. At this step, the kinetic effect is already important as illustrated in the burst nucleation mechanism [3]. The control of this explosive growth of nucleated clusters is considered as the key factor for obtaining reproducible narrow size distributed NPs. Indeed, this fast nucleation step will stop as soon as the concentration of metal atoms in solution becomes undersaturated. Experimentally, it is ensured by modulating the precursor injection rate into a hot stock solution [35]. In the case of Co nanocrystals, as a result of precursor injection rate, huge variation of morphology can be observed by transmission electron microscopy (TEM), as shown in figure 1.4. [4]

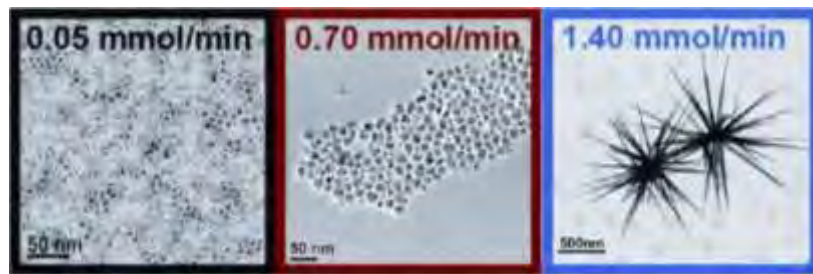


Figure 1.4: TEM images with precursor injection rate in a synthesis of Co NPs: (a) slow addition; (b) intermediate addition; (c) fast addition. [4].

1.1.2.2 From nuclei to seeds

When a cluster reaches a critical size, its structure can be stabilized. This critical point marks the formation of a single crystal seed. Within a thermodynamic approach, the most stable seed should have the greatest population among all products. When large enough, the shape of this most stable seed can be predicted through the Wulff construction, as a truncated octahedron with mainly (111) and (100) facets for face-centered cubic (fcc) metals for instance. At smaller size, metastable full shell clusters with “magic number” of atoms and high degree of symmetry [36, 37] such as icosahedra, decahedra are preferred. If the undersaturated condition is achieved before the nuclei reach the critical size (no supplementary nucleus will be formed), nuclei will aggregate in order to form larger, stable seeds with single or multiple twinned structure. These seeds will compensate the strain energy due to twins by maximizing the surface of the low energy (111) facets. When their size increases, the gain due to the lower surface energy of (111) facets can not sufficiently compensate the excess of strain energy so that the twinned seeds will be transformed into single crystals [38, 39, 40]. Experimentally, This indicates that twinned seeds need to be confined to relatively small sizes to be stable. This condition can be obtained experimentally by slowing down the kinetics of precursor decomposition/reduction to facilitate the formation of stacking faults [41, 42] and lead to the formation of a plate-like seed. This kinetically controlled geometry could never be obtained under thermodynamic equilibrium conditions owing to the required defect energy. Another consequence of slowing the precursor decomposition/reduction kinetics is the enlargement of size distribution. This renders the population control of different seeds more difficult than in the case of burst nucleation. The control of seeds formation is thus a rather critical stage for the morphology control of NPs. As shown in Figure 1.5, these seeds are the important intermediates between the nuclei and the nanocrystals [43]. Obtaining only one nanocrystal shape requires a very precise control over the population of seeds with different internal structures. This task is almost impossible in real conditions of chemical synthesis.

1.1.3 From seeds to nanocrystals

When the concentration of metal atoms in the solution decreases down to the nucleation limit, seeds will grow in size by the addition of metal atoms. When atoms arrive on the seed surface, the adatoms will diffuse until they reach a stable position (step edge, kink, defects) to be incorporated in the surface. By using transmission electron microscopy, structures and shapes of seeds and nanocrystals can be analysed at different stages of the growth. From these investigations, correlations between the initial seeds and the final nanocrystals have been established for a number of noble metals [44, 45, 43]. However, these observations are performed on *ex situ* prepared samples deposited on TEM grids (usually covered by a carbon film) and they may not precisely reflect the effective *in situ* evolution of the morphology during the growth process.

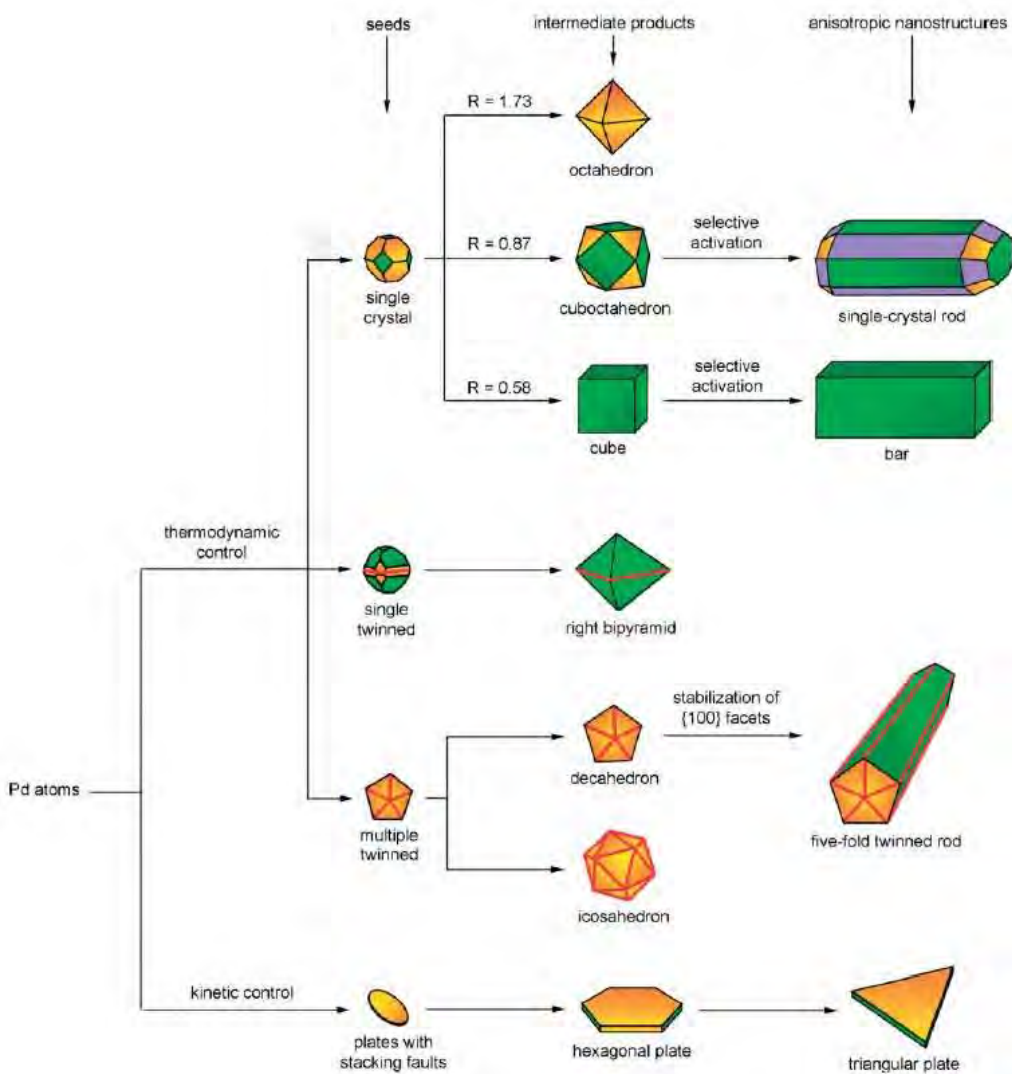


Figure 1.5: A schematic illustration of the reaction pathways that lead to Pd nanostructures with different shapes. The green, orange, and purple colors represent the (100), (111), and (110) facets, respectively. R is the ratio between the growth rates along the [100] and [111] axes.(Adapted from [43])

1.1.3.1 Seed mediated crystal growth

The final nanocrystals' morphology can still be modulated even when starting with a same seed. As most syntheses of NPs use a one-pot approach, it is extremely difficult to identify which kind of seeds is at the origin of the observed NPs morphology, especially when the comparison between two syntheses with different conditions is required. In order to disambiguate this uncertainty, efforts are made to separate the growth step from the nucleation and seed formation step. To this end, colloidal nanocrystals were synthesized, starting from a same type of single crystal seed. By this seed mediated growth, it was supposed to be possible to focus only on the thermodynamic or/and kinetic effects on the evolution of nanocrystals morphologies.

1.1.3.2 Surface capping (thermodynamic control)

It is well known in heterogeneous catalysis that depending on the chemisorbed gas molecules, the surface energy of specific facets can be modified differently. As a consequence, by alternating the gas under which Pt nanocrystals were annealed, Wang et al. have shown that it was possible to [46] reversibly change the morphology of these nanocrystals. This control of surface

energy by adsorbed selected molecules is generally considered as a thermodynamic effect on the morphology evolution. In solution, molecules such as carboxylate, amine, trioctylphosphine oxide (TOPO)... are commonly used as capping agents to stabilize the facets of nanocrystals. The binding energy of a capping agent varies from one crystal facet to another. The preferential capping of a given facet is one of the means to control its growth. The capping agent can be introduced or directly liberated during the synthesis. By adsorbing these stabilizing molecules, the facet modifies its surface energy and this may change the morphology of nanocrystals. As shown by Axet et al. [47] on the synthesis of platinum NPs, long alkyl amines ligands favor the formation of multipodal NPs which transform into cubic, truncated cubic or cubooctahedral shape, while as diamine ligands favor the formation of desert-rose like shape with the growth of (111) facets. This approach is also called thermodynamic approach. Experimentally, the presence of a capping layer on the surface has been confirmed by spectroscopy techniques such as X-ray photoelectron spectroscopy (XPS), energy dispersive X-ray spectroscopy (EDS) Fourier Transform Raman spectroscopy(FTIR) and Raman [48, 49, 50, 51], whereas scanning probe microscopies (AFM, STM) were used for investigating the surface coverage [52]. Concerning the comparison between surface energies, first-principles calculations seem the most suitable approach to investigate the charge transfer between a molecule and the surface. For example, by using DFT calculations, G. Fischer et al. precisely described the morphology evolution of colloidal iron NPs in different chemical environment (H_2 , Cl, HCl, NH_3 , NH_4Cl and CH_3COOH) [53].

1.1.3.3 Kinetic control

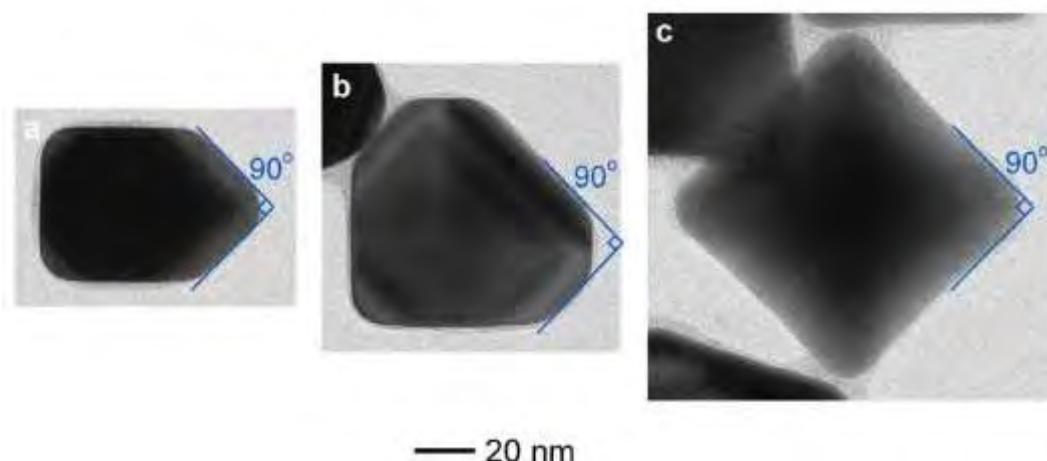


Figure 1.6: Shape of Ag NPs obtained by selectively deposited Ag atoms on a) one, 2) two and c) six faces of a Ag 40 nm side cube seed (Adapted from [54])

In a kinetic approach proposed by Y. Xia et al [55], the ratio between the rate of atom deposition ($V_{deposition}$) and the rate of surface diffusion ($V_{diffusion}$) is considered as the main factor to achieve a given morphology. The deposition rate is directly related to the rate of metal atoms generation (concentration variation). For a given precursor/reducing agent couple, one of the easiest ways to control this concentration is the modulation of the injection rate of the precursor by using a syringe pump. On the opposite side, the diffusion rate can be modulated by adjusting the reaction temperature. Such a kinetic control has been demonstrated in different experiments. [54, 56]. In these examples, asymmetric growth on symmetric fcc metal seeds was achieved by controlling the $V_{deposition}/V_{diffusion}$ ratio. As the deposition rate is directly linked to the concentration of metal monomers in solution, it can be controlled by the injection quantity and rate. Figure 1.6 shows how, by adjusting the precursor's injection rate, three

fully different Ag nanocrystals can be formed by overgrowth on (a) one, (b) three adjacent, and (c) six faces of a silver cubic seed with 40 nm of side length [54]. This injection rate can be improved as suggested by H.S. Peng et al [56], who proposed a cyclic dropwise addition of the precursor. By controlling the size of the droplets and/or the time interval of addition, one can control rather precisely the quantity of metal atoms in solution, and avoid the nucleation induced by newly introduced atoms.

1.1.4 The case of cobalt nanocrystals

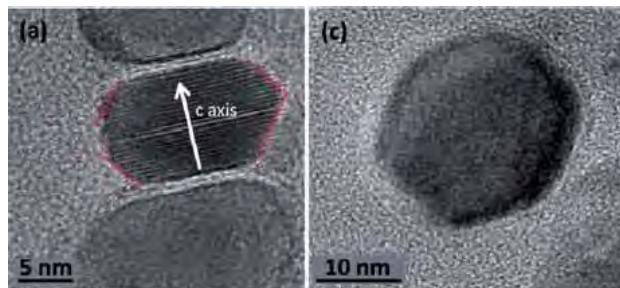


Figure 1.7: High resolution TEM images of hcp-Co nanodisks with (a) c-axis parallel to the substrate, (c) with c-axis perpendicular to the substrate. (Adapted from ref. [2])

Cobalt is well known to display very interesting ferromagnetic properties[57]. Its hexagonal close packed (hcp) structure is particularly interesting provides a “natural” crystalline anisotropy which favors the formation of single domain nanodisks with an easy axis of magnetization perpendicular to their basis. This induces a magnetic anisotropy which makes it a good candidate for high density magnetic data storage devices [2]. However, maintaining the stability of nanodisks is a huge challenge (phase stability, avoiding aggregation and oxidation). One of the first hcp-Co nanodisks was reported by Puntes et al. in 2001 [26]. In that synthesis, by decomposing a cobalt carbonyl in a hot mixture of solvent and surfactants (oleic acid, amines and TOPO), a mixture of hcp-Co disks and e-Co spheres was obtained. But, nanodisks were redissolved if the reaction was not quenched.

More stable hcp Co disks with the easy axis of magnetization perpendicular to its basis were obtained by C. Amiens et al. [2] (see figure1.7). These nanodisks were obtained by hydrogenation of $[\text{Co}(\eta^3\text{-C}_8\text{H}_{13})(\eta^4\text{-C}_8\text{H}_{12})]$ (as precursor) in a mixture of rhodamine B (RhB) and hexadecylamine (HDA) (as stabilizing agent). This mixture is the necessary condition for obtaining disk shape NPs. It was supposed that the HDA preferentially attached to the (0001) surface, while RhB occupied the truncated lateral facets. In a complementary study focused on the formation mechanisms of hcp Co nanodisks, C. Amien et al. [2] emphasized a possible role of side reaction between RhB and HDA which results in a cyclization of RhB, and conducted to the deactivation of carboxylic function in RhB, and thus could favor the formation of defected seeds (stacking faults).

In 2014, Atmane et al. have also obtained more robust hcp Co nanocrystals with shapes ranging from nanorods to nanoplates by using polyols as both solvent and reducing agent [5]. $\text{Co}(\text{C}_n\text{H}_{2n+1}\text{COO})_2$ was used as precursor and $\text{RuCl}_3\cdot x\text{H}_2\text{O}$ as a nucleating agent. In order to investigate the influence of concentration of the carboxylate ligand on the size and shape of NPs, a supplementary amount of sodium dodecanoate ($\text{NaC}_{11}\text{H}_{23}\text{COO}$) was added in the solution with respectively 0, 0.5, 1.5 and 2 equivalent to $\text{Co}(\text{C}_{11}\text{H}_{23}\text{COO})_2$. The consequence of this addition is a drastic change of morphology of NPs (figure 1.8). The direction of this variation (decrease of length/diameter ratio of the nanorods as the increase of carboxylate concentration was explained by the stability diagram in figure 1.9. This diagram was constructed by plotting

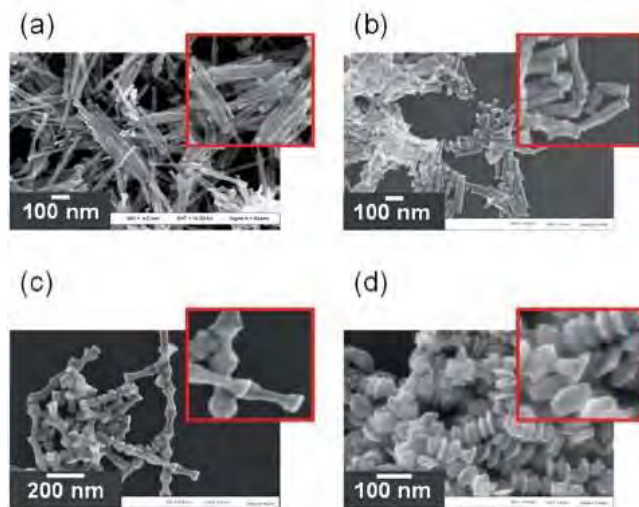


Figure 1.8: TEM images of Co nanoparticles obtained with an addition of different $\text{Na}(\text{C}_1\text{H}_2\text{COO})$ equivalents relative to $\text{Co}(\text{II})$: (a) 0 equiv.; (b) 0.5 equiv.; (c) 1.5 equiv. and (d) 2 equiv. (Adapted from [5]).

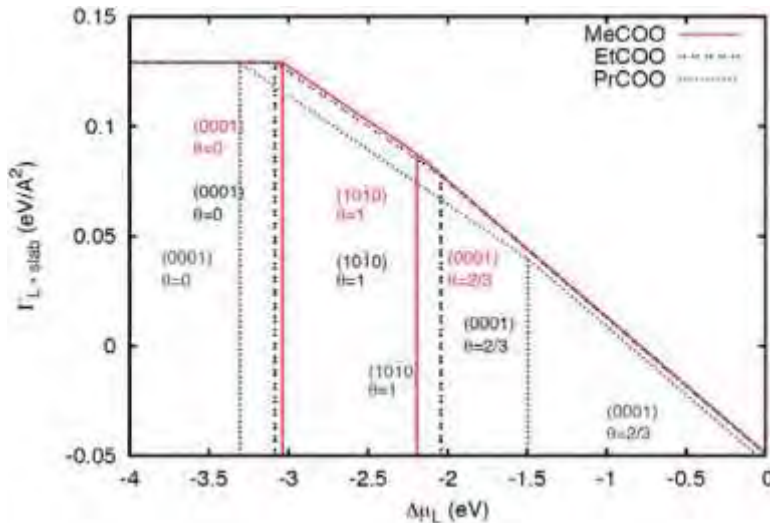


Figure 1.9: Stability diagrams for the Co (0001) and (10-10) surfaces with different ligands: in red, CH_3COO ; in black, $\text{C}_2\text{H}_5\text{COO}$; in blue, $\text{C}_3\text{H}_7\text{COO}$. (Adapted from [5])

the surface energy of $\text{Co}(0001)$ and $\text{Co}(10-10)$ covered with carboxylate ligands with different density (coverage). The surface energy γ was expressed as in Sec 1.2.1.2. The adsorption energies were deduced from DFT calculations. The chemical potential difference was defined by comparing the ligand molecule in a solution of concentration c with the same molecule in vacuum.

1.2 Predicting the NP morphology

In the previous section, we have seen that the growth mechanisms of metal NPs during chemical synthesis depend on many parameters and are extremely difficult to elucidate. Very few is known experimentally on the first steps of growth (nucleation and formation of seeds) and the effects of the precursors, reducing agents, solvent, temperature etc. are still largely unknown. Therefore, most of the effort devoted to understand the NP growth has been focused on the study of the third step, i.e. the growth of the nanocrystals once the seeds have nucleated, using simple models in which only one or two of these experimental parameters can vary. The methods for predicting the NP morphology are very diverse and can be considered either as methods looking for the equilibrium shape (thermodynamics shape) or for the stationary shape (stationary kinetics shape), or even a mix between these two. In this section, I present the methodology of these two different approaches and the previous models of the literature that are used to predict the NP morphology.

1.2.1 Thermodynamics prediction

The thermodynamics predictions are based on finding the equilibrium shape of the NP in different environment conditions. In other words, it is a method to find the configuration in which the energy of the system is the lowest with respect to some pre-fixed conditions. The system can be a free NP in vacuum, a NP with adsorbates on its surface or a NP in a solution or a gaze of ligands. Here, I present the most popular thermodynamic models used to predict the NP morphologies.

1.2.1.1 Nanoparticle of clean metal

In the case of a clean metal, the energy of a polyhedral NP is :

$$E_{np} = nE_{bulk} + \sum_{hkl} \gamma_{hkl} S_{hkl} + \sum_i e_i^e l_i + \sum_j e_j^c \quad (1.1)$$

where n is the number of metal atoms, E_{bulk} is the bulk energy of the metal, γ_{hkl} is the surface energy of the (hkl) facet and S_{hkl} is the total surface of all (hkl) facets ; e_i^e is the energy of the i -th edge; l_i is the length of the i -th edge and e_j^c is the energy of j -th corner of the polyhedron. In the case of nanoclusters, the edge and corner energies are very important and they really affect the shape of the nanocluster. But in the case of nanoparticles, where surfaces and volumes are large and the action of adding one atom or one layer does not change their physical properties, we normally neglect the energy of corners and edges of these polyhedra. Thus the NP energy can be reduced to :

$$E_{np} = nE_{bulk} + \sum_{hkl} \gamma_{hkl} S_{hkl} \quad (1.2)$$

where E_{bulk} and γ_{hkl} depend on the crystalline structure of the NP and on the temperature whereas n and S_{hkl} depend on its size and on its shape. We will focus only on NPs with perfect crystalline structure. In the following, we will not concentrate on the competition between the different structures but rather investigate only the most stable equilibrium structure in our models and calculations.

Wulff construction The Wulff construction [8] is a model that was developed to predict the equilibrium shape of a fixed volume crystal with polyhedral shape. The equilibrium shape corresponds to the one with lower energy and must satisfy the following condition:

$$\frac{\gamma_{hkl}}{L_{hkl}} = const \quad (1.3)$$

where L_{hkl} is the distance from the (hkl) surface to the polyhedron center.

Wulff construction proof We recall that the energy of the polyhedron droplet is :

$$E_{np} = nE^{bulk} + \sum_{hkl} \gamma_{hkl} S_{hkl} \quad (1.4)$$

where n is fixed by its volume, E^{bulk} is fixed by its crystalline structure and the γ_{hkl} do not depend on the size of the droplet. The variation of the total energy must be zero at equilibrium:

$$\delta E_{np} = \sum_{hkl} \gamma_{hkl} \delta S_{hkl} = 0 \quad (1.5)$$

We look for the shape having the lower energy at fixed volume V :

$$V = \sum_{hkl} \frac{1}{3} S_{hkl} L_{hkl} \quad (1.6)$$

where d_{hkl} is the distance from the polyhedron center to the (hkl) surface. Therefore, for any variation of the S_{hkl} surfaces, the variation of the volume is :

$$\delta V = \sum_{hkl} \frac{1}{3} \delta S_{hkl} d_{hkl} + \sum_{hkl} \frac{1}{3} S_{hkl} \delta L_{hkl} = 0 \quad (1.7)$$

The second term represents the augmentation of the NP volume in each direction and must be equal to 0. The first term is :

$$\sum_{hkl} \delta S_{hkl} L_{hkl} = 0 \quad (1.8)$$

Equations 1.5 and 1.8 being valid for any arbitrary variation of δS_{hkl} , we have the relation:

$$\frac{\gamma_{hkl}}{L_{hkl}} = \text{const} \quad (1.9)$$

1.2.1.2 Nanoparticles in presence of ligands

In the presence of ligands, both the interactions of adsorbates at the surface and in the solution affect the energy of the system. The equilibrium shape must therefore take into account these conditions when minimizing the total energy of the system.

Interface energy When ligands are adsorbed on a NP surface, it is possible to define an "interface energy" between the nanoparticle and the ligands. Generally, γ_{int} , the interface energy of a metallic surface on which $n_{\text{ligand}}^{\text{surf}}$ ligand molecules are adsorbed is given by:

$$\gamma_{hkl}^{int} = \gamma_{hkl} + \theta_{hkl} \times E_{hkl}(\theta_{hkl}) \quad (1.10)$$

where, γ_{hkl} is the surface energy of the pure metal (hkl) facet before adsorption of the ligands, $E_{hkl}(\theta_{hkl})$ is defined as the adsorption energy of a ligand molecule on the metal (hkl) facet in vacuum, for a given θ_{hkl} coverage per surface unit. This coverage is defined as $\theta_{hkl} = n_{\text{ligand}}^{\text{surf}} / S_{hkl}$.

This interface energy is accessible from DFT calculations of a slab surface and of a molecule in vacuum. The adsorption energy for each molecule on a given surface is given by:

$$E_{hkl}^{\text{ads}} = \frac{1}{n^{\text{ligand}}} \times (E_{hkl}^{\text{metal+ligand}} - E_{hkl}^{\text{metal}} - n^{\text{ligand}} \times E^{\text{ligand}}) \quad (1.11)$$

where n^{ligand} is the number of ligands (on the metal surface), $E_{hkl}^{\text{metal+ligand}}$ is the total energy of the system formed by the metal slab and the adsorbed ligands, E_{hkl}^{metal} is the total energy of the relaxed, bare metal slab and E^{ligand} is the energy of a ligand molecule in vacuum. When the metallic NPs are in solution, the ligand molecules are not in vacuum but in the solvent. Therefore, a term representing the chemical potential difference between the solution and the vacuum $\Delta\mu = \mu(T, c) - \mu^{\text{vacuum}}$, where c is the concentration of ligands in the solution, should be added in:

$$\gamma_{hkl}^{\text{int}} = \gamma_{hkl} + \theta_{hkl} \times E_{hkl}^{\text{ads}}(\theta_{hkl}) - \theta_{hkl} \times \Delta\mu \quad (1.12)$$

1.2.1.3 Wulff construction in the presence of ligands

The Wulff construction method was developed for pure metallic systems under vacuum. In the presence of ligands, the shape of the nanoparticles can be modified due to the modification of the surface energies after adsorption of the ligand molecule. Considering these surface energy modifications, it is possible to derive a Wulff construction type model using the interface energies between the metallic surface and the ligands instead of the metallic surface energies.

Let us consider a system containing a constant number n^M of metal atoms and a constant number of ligand molecules n^L which are distributed in the solvent n_{sol}^L and on the surface of the nanoparticle n_{hkl}^L . The total energy of this system is:

$$E_{\text{tot}} = n^M \times E^{\text{bulk}} + \sum_{hkl} S_{hkl} \times \gamma_{hkl} + \sum_{hkl} n_{hkl}^L \times \mu(T, \text{ads}) + n^L \times \mu(T, c)$$

where S_{hkl} is the area of the (hkl) facet, γ_{hkl} is the surface energy of the (hkl) facet, $\mu(T, \text{ads})$ is the energy of the adsorbed ligands on the (hkl) facet and $\mu(T, c)$ is the chemical potential of the ligands in the solution at temperature T and concentration c . We will now examine how the total energy changes due to a small variation of the facet surfaces S_{hkl} for fixed coverages. In this case, if the surface changes, then the number of ligands adsorbed on the facets will change accordingly. So the variation of the total energy due to a small variation of the antiparticle surface reduces to:

$$\delta E_{\text{tot}} = \sum_{hkl} \delta S_{hkl} \times \gamma_{hkl} + \sum_{hkl} \delta n_{hkl}^L \times \mu(T, \text{ads}) + \delta n_{\text{sol}}^L \times \mu(T, c) \quad (1.13)$$

Here we assume that a small change of the number of ligands at the surface does not change the concentration in the solution. Therefore, $\mu(T, c)$ is kept fixed. Besides, the total number of ligands in the system $n_{\text{tot}}^L = \sum_{hkl} n_{hkl}^L + n_{\text{sol}}^L$ is fixed, so $\delta n_{\text{tot}}^L = \sum_{hkl} \delta n_{hkl}^L + \delta n_{\text{sol}}^L = 0$. It follows that:

$$\begin{aligned} \delta E_{\text{tot}} &= \sum_{hkl} \delta S_{hkl} \times \gamma_{hkl} + \sum_{hkl} \delta n_{hkl}^L (\mu(T, \text{ads}) - \mu(T, c)) \\ &= \sum_{hkl} \delta S_{hkl} [\gamma_{hkl} + \theta_{hkl}(\mu(T, \text{ads}) - \mu(T, c))] \end{aligned} \quad (1.14)$$

The chemical potential of the adsorbed ligand can be related to the adsorption energy, for each

facet and each coverage:

$$E^{\text{ads}} = \mu(T, \text{ads}) - \mu(T, c) \quad (1.15)$$

Since $\delta n_{\text{hkl}}^L = \delta S_{\text{hkl}} \times \theta_{\text{hkl}}$ at fixed coverage, one obtains:

$$\delta E_{\text{tot}} = \sum_{\text{hkl}} \delta S_{\text{hkl}} \left[\gamma_{\text{hkl}} + \theta_{\text{hkl}} E^{\text{ads}}(\theta_{\text{hkl}}) \right] \quad (1.16)$$

Using Eq. 1.12, we finally find that E_{tot} is minimum for :

$$\delta E_{\text{tot}} = \sum_{hkl} \delta S_{hkl} \gamma_{hkl}^{\text{int}} = 0 \quad (1.17)$$

For a constant number of metal atoms, the volume V of the nanoparticle is fixed and we have $\delta V = \sum_{hkl} \delta S_{hkl} \times d_{hkl} = 0$ where d_{hkl} is the distance between the center of the polyhedron and the (hkl) surface. We thus obtain the modified Wulff relation:

$$\frac{\gamma_{hkl}^{\text{int}}}{L_{hkl}} = \text{const} \quad (1.18)$$

This shows that, in the case of a NP covered by ligands, one can simply adapt the Wulff construction method by using the interface energies as defined in Eq. 1.12 instead of the surface energies. In our work, we will use this result for different models that give the interface energies at equilibrium.

1.2.1.4 Prediction models

As we just saw, the Wulff construction can be extended to the case of a NP with adsorbed ligands on its surface. The prediction of these NPs shapes requires of course the knowledge of the equilibrium coverage of ligands on their surface. In the following, I present some methods used to find this equilibrium coverage, and to compute the corresponding interface energies.

Lowest interface energy model For a given fixed surface S which is in contact with a solution of ligands, the equilibrium coverage of adsorbates on this surface is the one having the lowest interface energy (see the proof below). For each facet of the nanoparticle, an equilibrium coverage will be found as a function of its interface energy. The interface energy given by Eq. 1.12 shows the possibility to find the optimum coverage of the lowest interface energy as a function of the chemical potential of the solution. The only problem is that each coverage requires a separate calculation. Only some rational numbers of coverages can be calculated. Finally, overall, the equilibrium coverage of each surface can be deduced for each value of the chemical potential $\mu(T, c)$ by taking the lowest value of the interface energy from all calculated values or by fitting the dependency of the adsorption energy on the coverage.

Proof of the lowest energy model Let us consider a clean metal surface of area S in contact with a solution made of N molecules with chemical potential $\mu(N)$. Now, we find the number n_{ads} of adsorbed molecules which minimizes the total energy of this system. The total energy of the system in this case is:

$$E_{\text{tot}} = n \times E^{\text{bulk}} + S \times \gamma^{\text{int}} + n_{\text{ads}} \times \mu(T, c) + (N - n_{\text{ads}}) \times \mu(T, c) \quad (1.19)$$

Thus,

$$E_{\text{tot}} = n \times E^{\text{bulk}} + N \times \mu(T, c) + S \times \gamma^{\text{int}} \quad (1.20)$$

When the numbers of metal atoms and of adsorbent molecules are fixed, the total energy depends only on the interface energy. It is believed that, by comparing the interface energies of these facets, one can determine the dominant surface of the NP. The enlargement of the facet with the lowest interface energy must be quicker than the ones of higher energy. It should be noted that there is nevertheless no explicit demonstration of this hypothesis.

An example of these model for cobalt NP can be found in Ref. [5] where it is predicted that the domination of the (0001) surface will lead to disk shaped NPs while the domination of the (10-10) surface will lead to rod-like NPs (Fig. 1.10). The authors of Ref.[5] show that

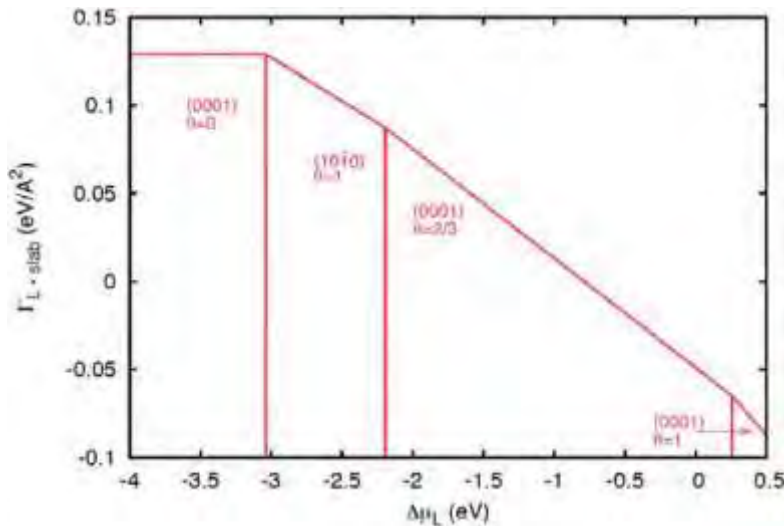


Figure 1.10: Stability of Co NP facets as a function of the chemical potential in the solution[5].

the tendency of the NP morphology matches the change of the ligands chemical potential in the solution. The dependency of the chemical potential can be related to the concentration of ligands in the solution, the pH of the solution, the temperature etc. However these types of prediction give only the tendency of the NP growth. The Wulff constructions from the interface energies derived from this model, in the same conditions, are not always in good agreement with experiments.

Adsorption isotherms Another way to find the equilibrium coverage of adsorbents on the NP surface is to use the isotherm of adsorption. At present, there are many existing isotherms in the literature, but the most common one is the Langmuir isotherm in the case of chemisorption.

Langmuir isotherm The Langmuir isotherm is the first one derived from a theoretical basis. It can be derived from both a kinetics equation and statistical mechanics. It is based on the following four assumptions:

- The adsorption surface is flat and homogeneous,
- The coverage does not change the adsorption energy of molecules,
- The adsorbate is immobile,
- at the adsorption site, only one molecule can be adsorbed which means that the maximum adsorption is a mono layer.

The Langmuir isotherm states that the equilibrium fraction of coverage on the surface is :

$$\Theta^{eq} = \frac{pK^{eq}}{1 + pK^{eq}} \quad (1.21)$$

where, p is the pressure of the adsorption gaze, K^{eq} is the equilibrium rate of the adsorption reaction between the adsorbent (A) and the surface (S) to form a AS complex:



This constant can be derived as:

$$K^{eq} = \exp \frac{\delta G}{k_B T} \quad (1.23)$$

where δG is the activation energy of the reaction. Figure 1.11 present an example of Langmuir isotherm for the case $K^{eq} = 1$ and $K^{eq} = 2$. There exist many isotherms which derive from

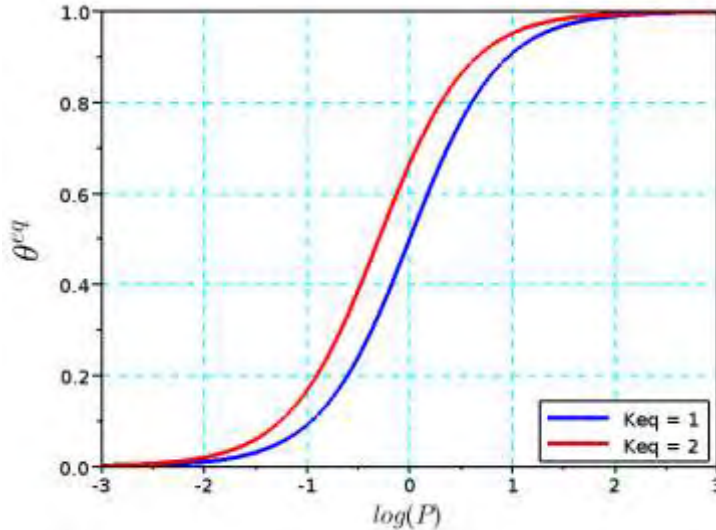


Figure 1.11: Example of Langmuir isotherm.

the Langmuir isotherm. The three most important ones are the Freundlich Isotherm [58], the BET isotherm [59] and the Temkin isotherm [60]. While the Freundlich isotherm describes the roughness of the surface, the BET isotherm is the modification of the Langmuir's one in the case of multi-layer adsorption. The Temkin isotherm describes the interaction between adsorbed molecules by replacing the constant activation energy of adsorption by a linear one that depends on the coverage. In practice, the activation energy is not linear with the adsorbent coverage. It is common to replace the constant activation energy by a fitted function of the activation energy depending on the coverage.

In their work, Bealing et al. [25] used the fitted adsorption energy of adsorbent molecules on the

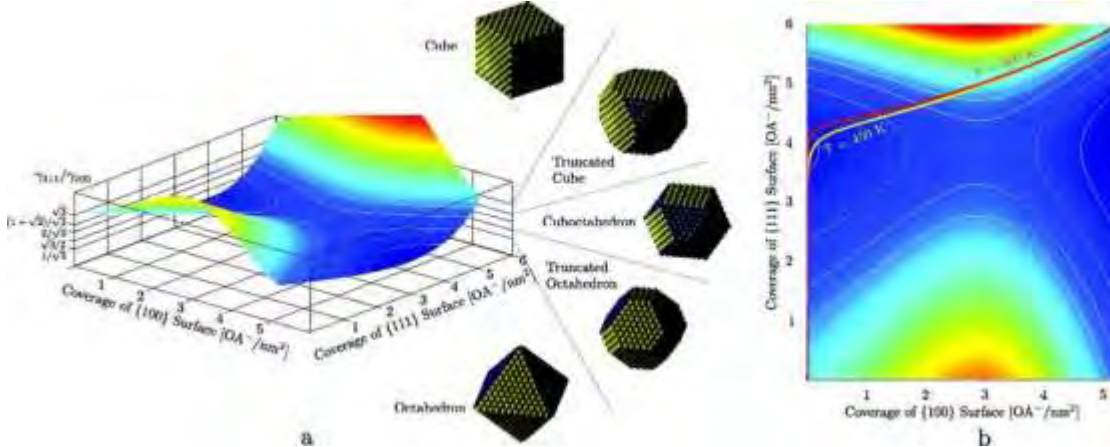


Figure 1.12: Prediction of PbSn NP shape using adsorption isotherm. **left:** Interface energy ratio as a function of an arbitrary coverage of the two facets and morphology prediction in each region; **right:** Isotherm lines at different temperatures linking the surface coverage of 2 facets in the same gaze pressure conditions. [25]

different facets of a PbSn nanoparticle and used the interface energy to predict the morphology of these NPs with the change of the adsorbent gaze pressure and temperature. Figure 1.12 shows the ratio between the interface energies and the Wulff reconstructions derived from these interface energies. The red line and yellow line in the left panel of Fig. 1.12 show the evolution of the coverage, and thus the morphology, as a function of the gaze pressure variation.

Vibrations of the adsorbents on the metal surface Equation (1.12) does not take into account the change of thermodynamical energy of the ligand molecule in the solution and on the metal surface. In their work on Fe NPs stabilized by ligands, Fisher *et al.* [53] have shown that it is possible to take into account the temperature effects on adsorption energies, and that the main contribution comes from the difference in translation, rotational and vibrational energies of the molecules in the solution and adsorbed on the surface. The three terms are all included in the heat capacity of molecules in the gaze or in the solution while, on the surface, the first 2 terms are zero. The vibrational energy corresponding to this part has the form:

$$E_v(T) = \sum_v 1v \frac{1}{2} + \frac{1}{\exp(\frac{1v}{k_B T}) - 1} \quad (1.24)$$

The difference of vibrational energy has an important contribution to the change of surface energy if the highest vibrational frequencies of the molecule change when it is adsorbed. Using this method, Fisher *et al.* [53] computed the Wulff form of Fe NPs at different conditions of temperature and gaze activity of H_2 (figure 1.13). Although these results show important differences on the NP shape induced by these conditions, the obtained morphologies do not correspond to the experimental ones in similar conditions (cubic shape).

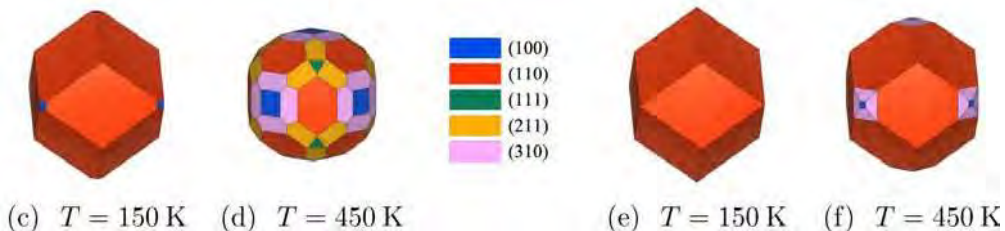


Figure 1.13: Wulff polyhedra of Fe NPs for different temperatures and gaze activity of H_2 (10^{-7} for the first two ones and 1 for the last two), adapted from [53].

Population balance Some experiments show the coexistence of several NP morphologies in the same conditions of synthesis. This fact can be explained by the population balance model which is based principally on statistical mechanics. The probability to find a nanoparticle with a specified morphology (n) belonging to a set of N morphologies is obtained using the Boltzmann distribution.

$$p_{(n|N)} = \frac{\exp \left(\frac{-G_n(D, T)}{k_B T} \right)}{\sum_n^N \exp \left(\frac{-G_n(D, T)}{k_B T} \right)} \quad (1.25)$$

Where $-G_n(D, T)$ is the average free energy of the metal atom in the n configuration corresponding to diameter D and temperature T . The relative stability of these configurations is defined as :

$$p_n = \exp \left(\frac{-G_n(D, T)}{k_B T} \right) \quad (1.26)$$

A. Barnard showed in her work on several metals (Ag, Au, Pd and Pt) [61] that the relative population between these configurations converges to the same value at large size and high temperature (see Fig. 1.14). A polydispersity of the NP morphologies is expected in this case.

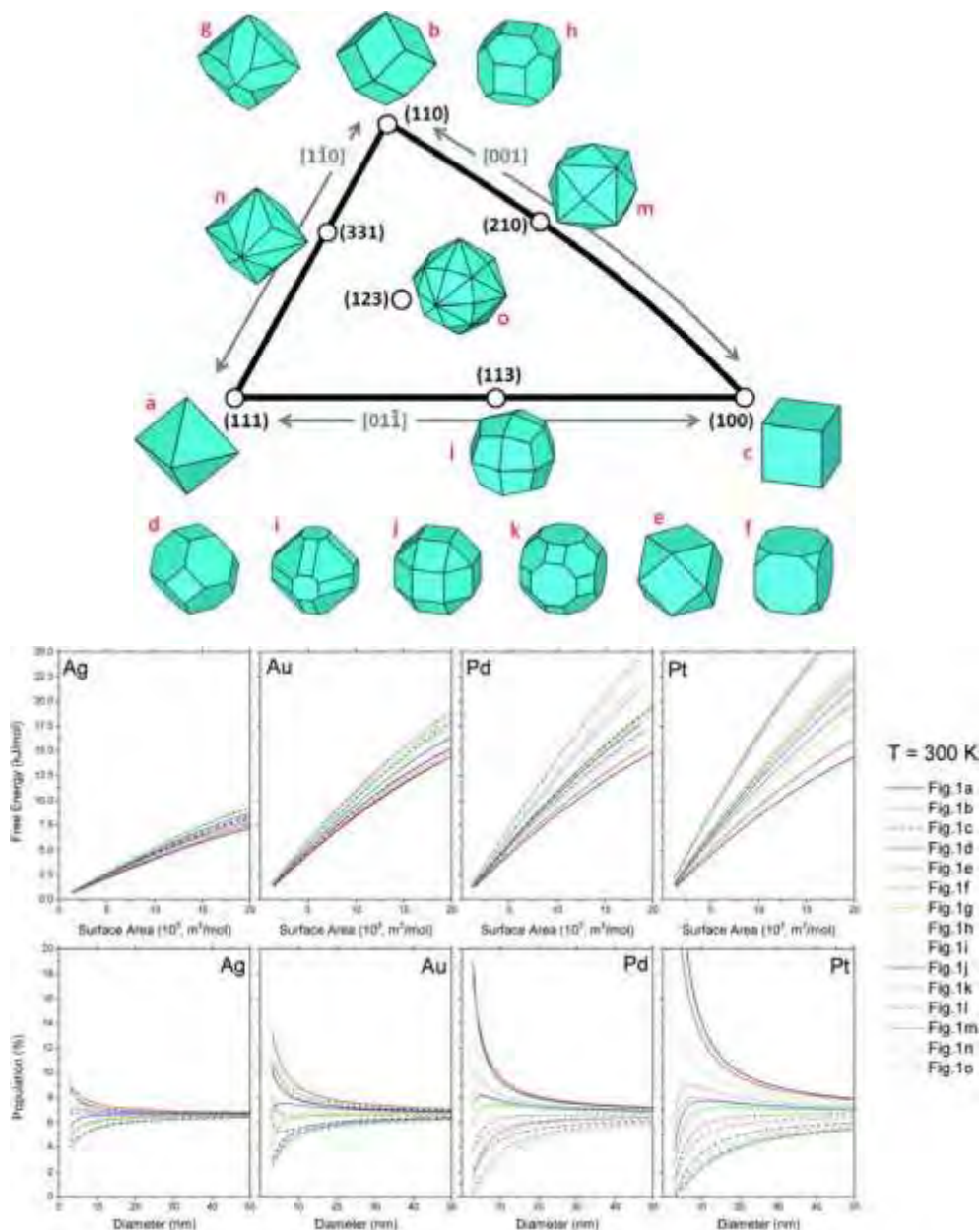


Figure 1.14: **Top:** Nanoparticle shape. **Bottom** Free energy as a function of the surface area of the NP and the relative population of NPs as a function of their diameter. [11]

1.2.2 Kinetics prediction

In the kinetics prediction of the NP morphology, it is assumed that the morphologies observed in experiments are not necessarily the equilibrium shapes but rather result from the kinetic growth of the NP. If the kinetics simulation can give the NP final dimensions or the relation between these dimensions, the most important aspect here is to clarify the mechanisms dominating the processes of NP formation and the mathematical formulation corresponding to these processes. In the following, I only summarize the main ideas describing the mechanisms of formation and give some examples of models which are closed to ours.

1.2.2.1 Classical nucleation and growth theory

Classical nucleation Nucleation is the process in which seeds act as templates for crystal growth. The main driving force of this process is the supersaturation of the monomer in the liquid solution. The formulation of this process can be derived from thermodynamics using macroscopic quantities.

For a seed of spherical shape, the free energy of a seed of radius r is :

$$\Delta G = 4\pi r^2 \gamma + \frac{4\pi}{3} r^3 \Delta G_v \quad (1.27)$$

where γ is the surface energy which is positive and ΔG_v is the free energy change of the bulk metal per volume unit:

$$\Delta G_v = -\frac{k_B T \ln S}{v} \quad (1.28)$$

with S the supersaturation and v the volume of a monomer in the bulk. In nucleation process, ΔG_v is negative. Thus, this equation has a solution for a critical radius R_c :

$$R_c = \frac{2\gamma v}{k_B T \ln S} \quad (1.29)$$

The nucleation rate can be described with an Arrhenius form:

$$\frac{dN}{dt} = A \exp \left(-\frac{\delta G_c^c}{k_B T} \right) = A \exp \left(-\frac{16\pi\gamma^3 v^2}{3(k_B T)^3 (\ln S)^2} \right) \quad (1.30)$$

where A is a pre-factor.

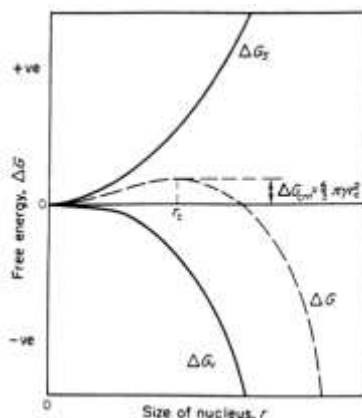


Figure 1.15: Free energy diagram for nucleation as the variation of nucleus size (extracted from [62])

Classical growth In classical growth, the growth of the particle can be controlled by two mechanisms: the diffusion control and the surface reaction control. In the diffusion control, the flux of monomer going from the solution of concentration C_s to the particle of radius r , and with a concentration at the interface metal-solution C_i , can be described by the Fick's first law:

$$J_d = 4\pi r D(C_s - C_i) \quad (1.31)$$

where D is the diffusion constant.

A similar formulation can be derived for the case of the surface reaction control:

$$J_r = 4\pi r^2 k(C_s - C_r) \quad (1.32)$$

where k is a constant independent of the radius r and C_r is the concentration at which the equilibrium radius of the particle is r .

Thus the growth rate of particle radius is:

$$\frac{dr}{dt} = \frac{Dv(C_b - C_r)}{1 + \frac{D}{k}} \quad (1.33)$$

The ratio $\frac{D}{k}$ determines whether the growth process is governed by reaction or diffusion characteristics.

1.2.2.2 Growth and nucleation theories

LaMer nucleation and growth As we have seen in Section 1.1, the NP formation phenomena in solution can be divided in 3 steps. Figure 1.2 shows the typical LaMer diagram for this case. The first step is the chemical reaction of free metallic atoms from the precursor, the second step is the nucleation of metal atoms, and the last step is the NP growth by diffusion. The first 2 steps are difficult to control experimentally and there does not exist a clear theory which describes this process. The models used for the prediction the NP growth in solution are normally developed for the third step of growth.

Ostwald ripening Ostwald described in 1900 the mechanism of growth caused by the change in solubility of nanoparticle depending on their size. In 1961, Lifshitz and Slyozov [9] gave the mathematical formulation of Ostwald ripening:

$$\frac{d(\langle R \rangle^3 - \langle R \rangle_0^3)}{dt} = \frac{8\gamma C_\infty v^2 D}{9k_B T} \quad (1.34)$$

where $\langle R \rangle$ is the average NP radius and $\langle R \rangle_0$ is the equilibrium NP radius; C_∞ is the monomer solubility in the solution. v is the molar mass, γ is the surface energy. In 1975, Kahlweit [63] combined the previous works of Lifshitz and Slyozov with the one of Wagner, which is a similar work, independent of the first two, into the Lifshitz-Slyozov-Wagner (LSW) theory of Ostwald ripening. In the case of detachment and attachment governing the growth process, the growth rate becomes :

$$\frac{d \langle R \rangle^2}{dt} = \frac{64\gamma C_\infty v^2 k_s}{81k_B T} \quad (1.35)$$

where k_s is the attachment rate of length per time constant.

Other mechanisms Fasolka and Wulff [64] propose the particle can be controlled by nucleation and growth happen simultaneously. The first step, a slow continuous nucleation, is similar to classical nucleation but the second step is not diffusion controlled but an auto-catalytic surface growth.

The coalescence and the orientated attachment both describe the attachment of small clusters to a large nanoparticle. The difference between the two is the preference of attachment in the crystallographic alignment in the case of orientated attachment whereas it does not exist in the case of coalescence. One of the most studied case was the work of Li et al [65] where the orientated attachment of iron oxyhydroxide are seen in real time using a liquid cell within a high resolution transmission electron microscope (HRTEM). However, the formulation of the mechanism for this process is not too developed.

Peng et al. [66] describe in their work another mechanism where there is no net diffusion to the NP but monomer can diffuse from one surface to another and thus change the shape of the NP. This process can explain the change of morphology in aging solutions.

1.2.2.3 Morphology in the presence of adsorbates

These previous theories were adapted to the kinetics morphology prediction models for nanoparticles without the presence of adsorbates. The present of adsorbates is believed to have an important impact on the stability of the NP surface and on the NP morphology. The effect of the ligands can be treated in many cases only as a change of the diffusion constant in the solution. However, the presence of adsorbates on the surface of the NP obviously changes the effect of diffusion and reaction of attachment of the monomer on the surface. The real effect on this attachment is still difficult to model. In the section below, I present only the most recent kinetics model that takes into account the effect of adsorbates coverage on the NP growth.

Stationary prediction In this method, the morphology will be predicted by the stationary growth rate G_{hkl} of the surfaces using the Wulff construction in the kinetics framework:

$$\frac{G_{hkl}}{L_{hkl}} = \text{const} \quad (1.36)$$

where L_{hkl} is the distance from the (hkl) surface to the center of the Wulff polyhedron.

As an example of this method, Xin Qi et al [10], in their work on the Ag nanocube shape, used molecular dynamics to determine the mean first passage time (MFPT) of the monomer through a mono layer of ligands for different surfaces. The MFPT of a Ag atom from a distance z (from the surface) to a distance z_f is characterized by:

$$t_m(z, z_f) = \int_{z_0}^{z_f} \exp \left(-\frac{W(z)}{k_B T} \right) dz \frac{\exp \left(-\frac{W(z_f)}{k_B T} \right)}{D(z^{\text{II}})} \quad (1.37)$$

where $W(z^{\text{II}})$ is the potential mean force of the Ag atom at distance z^{II} pre-calculated by the umbrella sampling method. $D(z^{\text{II}})$ is the diffusion coefficient. z_0 is the distance from the surface to the boundary of surface neighborhood and bulk solution. Instead of calculating the MPFT from equation 1.37, the authors used molecular dynamics simulations and then estimated this MFPT by means of the reaction time t_R and the diffusion time t_D from the solution to z_0 :

$$t_m = \frac{p}{1-p} t_R + T_D \quad (1.38)$$

where p is the reaction probability. Then, the morphology will be predicted by the Wulff construction (Eq.1.36) using the stationary growth rate determined by the inverse ratio of MFPT. Figure 1.16 shows the prediction morphology with different chain lengths and different adsorbent coverages.

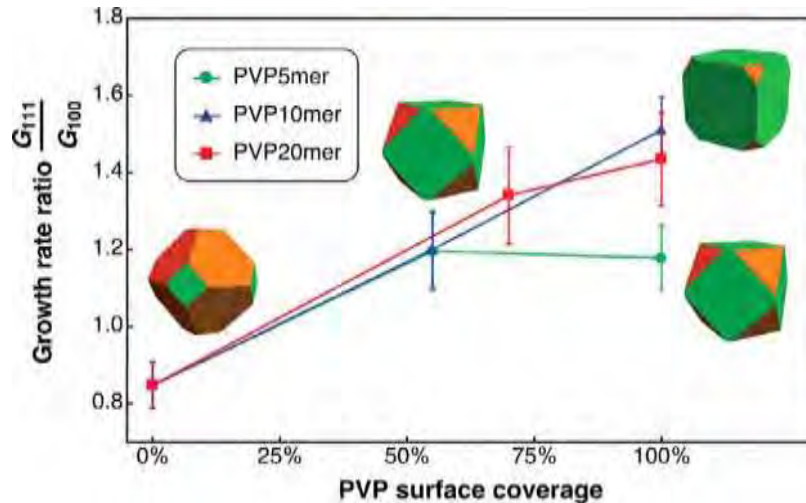


Figure 1.16: The morphology prediction of Ag nanoparticles with adsorbent of different chain lengths, as a function of coverage. [10]

Final morphology prediction The final morphology prediction using the simulation of growth rate depends on the time used to calculate the final dimension of the nanoparticle. The particle final size is given by:

$$L(\infty) = \int_0^{\infty} G(t) dt \quad (1.39)$$

where $G(t)$ is the growth rate at time t .

The work of A. Barnard et al, [67, 11] on the prediction of Au NP morphology is based on the LSW theory. Unlike the spherical approximation in previous works, the authors enable the possibility to explore the evolution of faceted nanostructures. By adding the effective fraction of total sites of the nanoparticle, the effect of adsorption of ligands on the surfaces was introduced in the growth rate of the nanoparticles by the formulation:

$$G(t) = \frac{dL}{dt} = \frac{-X dV_m}{N_{ef,f,i}} \frac{v \exp\left(\frac{E_{diff,i}}{k_B T}\right) k_B T \ln\left(\frac{C_{eq,i}(t)}{C_0(t)}\right)}{\exp\left(\frac{E_{ad,i}-E_{des,i}}{k_B T}\right)} \quad (1.40)$$

where V_m is the molar volume of the monomer, X is the number of mono layers of interlayer distance d ; v is the sum of the vibrational frequencies of the monomer on the surface, E_{diff} is the activation energies required for diffusion, E_{ad} and E_{des} are the activation energies of adsorption and desorption, respectively; $C_0(t)$ and $C_{eq}(t)$ are the concentrations of the solution and the concentration of monomers participating in the coarsening around the surface; i is the surface index. In this model, Barnard et al. showed the possibility to investigate the impacts of seed size, monomer concentration, and temperature in the evolution of the relative ratio of the NP dimensions and the surface area between the different surfaces.

1.3 Conclusion

In this chapter, I have presented the possible ways to control the morphology of NPs synthesized in solution and their essential parameters. The concentration of the solution, the nature of the adsorbates (or ligands), the temperature, the chemical conditions and the kinetics parameters play an important role in the morphological control, which renders the rationalization

of this phenomena particularly difficult. The mechanisms which govern the formation of NPs are rich and therefore difficult to explain in an unified theory. The efforts made to predict

the NP morphology using thermodynamics and/or kinetics correspond only to case by case investigations. The unified theory to explain all the aspects of the morphology prediction is still an open question.

Chapter 2

Density Functional Theory

Contents

2.1	The Schrödinger Equation	28
2.1.1	Born-Oppenheimer approximation	28
2.1.2	Variational Principle and ground state	28
2.2	Hartree Fock approximation	29
2.3	Density functional approach	30
2.3.1	Electron density function	30
2.3.2	The Thomas Fermi model	30
2.3.3	Hohenberg and Kohn theorems	30
2.3.4	Kohn Sham Equation	31
2.4	Exchange-correlation energy	31
2.4.1	The local density approximation (LDA)	33
2.4.2	The generalized gradient approximation (GGA)	33
2.4.3	Hybrid functional	33
2.5	Van der Waals dispersion	34
2.5.1	Including empirical corrections DFT-D	34
2.5.2	Non Local dispersion density functional (vdW-DF)	35
2.6	DFT in periodical system	35
2.6.1	Plane Wave basis	35
2.6.2	Pseudopotentials	36
2.7	Conclusion	36

The Density functional theory (DFT), initially proposed by Hohenberg, Kohn and Sham [68], [69] was progressively developed in the last 50 years. It is nowadays a leading methodology for modeling varied systems such as molecules or solid structures. DFT provides access to many properties including structures, vibrational frequencies, cohesion energies, ionization energies, electric-magnetic properties, reaction paths ...

The motivation of my work is to use DFT to investigate the effect of ligand adsorption on metallic surfaces stability, with as final objective the building of a model able to predict the morphology of a nanoparticle as a function of the ligands. In this chapter theoretical descriptions of the DFT method and of the approximations used in my calculations will be given.

2.1 The Schrödinger Equation

In solid state physics and quantum chemistry, the target is to find a solution of the time-independent, non-relativistic Schrödinger equation. The Schrödinger equation for a system of N electrons and M nuclei can be written as :

$$\hat{H}\psi(\mathbf{r}_1, \mathbf{r}_2, \dots, \mathbf{r}_N, \mathbf{R}_1, \mathbf{R}_2, \dots, \mathbf{R}_M) = E\psi(\mathbf{r}_1, \mathbf{r}_2, \dots, \mathbf{r}_N, \mathbf{R}_1, \mathbf{R}_2, \dots, \mathbf{R}_M) \quad (2.1)$$

where \hat{H} is the Hamiltonian of the system, ψ is the wave functions of electrons and nuclei, \mathbf{r}, \mathbf{R}

are the coordinates of electrons and nuclei. E is the system energy corresponding to the wave function ψ . Finding the solution of equation (2.1) is equivalent to find the eigenvalues E and the eigenvectors ψ of the operator \hat{H} in the Hilbert space. The Hamiltonian of this system can be divided in five terms:

$$\hat{H} = -\frac{1}{2} \sum_{i=1}^N \nabla_i^2 - \frac{1}{2} \sum_{a=1}^M \frac{\nabla_a^2}{m^a} - \frac{1}{2} \sum_{i=1}^N \sum_{a=1}^M \frac{Z_a}{|\mathbf{r}_i - \mathbf{R}_a|} + \sum_{i=1}^N \sum_{j>i}^N \frac{1}{|\mathbf{r}_i - \mathbf{r}_j|} + \sum_{a=1}^M \sum_{b>a}^M \frac{Z_a Z_b}{|\mathbf{R}_a - \mathbf{R}_b|} \quad (2.2)$$

Here, i and j denote the electrons index; a and b denote the nuclei index. The first two terms are the kinetic energy of electrons and nuclei, the last three terms are the interaction energies between the nuclei - electrons, electrons - electrons and nuclei - nuclei. The equation can only be resolved analytically in the case of the hydrogen atom and the He^+ ion with one nucleus and one electron. For all other cases, approximations are required.

2.1.1 Born-Oppenheimer approximation

The mass of one proton or one neutron is some 1836 times larger than the mass of electrons. The nuclei's kinetic energy is then very small with respect to the ones of electrons. The Born-Oppenheimer approximation considers that the kinetic energy of nuclei is zero and its potential is constant. So, the Hamiltonian in equation (2.2) can be reduced to that of electrons moving in an external electrical field generated by the ions:

$$\hat{H}_e\psi_e = E_e\psi_e \quad (2.3)$$

Here

$$\hat{H}_e = -\frac{1}{2} \sum_{i=1}^N \nabla_i^2 - \frac{1}{2} \sum_{a=1}^M \frac{Z_a}{|\mathbf{r}_i - \mathbf{R}_a|} + \sum_{i=1}^N \sum_{j>i}^N \frac{1}{|\mathbf{r}_i - \mathbf{r}_j|} = T_e + V_{N-e} + V_{e-e} \quad (2.4)$$

The solution of equation (2.1) is the product of two wave functions : ψ_e of electrons and χ_n - the Dirac function at position \mathbf{R}_a of nuclei.

$$\psi(\mathbf{r}_1, \mathbf{r}_2, \dots, \mathbf{r}_m, \mathbf{R}_1, \mathbf{R}_2, \dots, \mathbf{R}_n) = \chi_n(\mathbf{R}_1, \mathbf{R}_2, \dots, \mathbf{R}_n)\psi_e(\mathbf{r}_1, \mathbf{r}_2, \dots, \mathbf{r}_m) \quad (2.5)$$

The energy of the system is the sum of the electronic energy and nuclei energy: $E_{tot} = E_e + E_n$.

2.1.2 Variational Principe and ground state

When the system is in the state ψ , the expectation value of its energy is given by :

$$E_\psi = \frac{\langle \psi | \hat{H} | \psi \rangle}{\langle \psi | \psi \rangle} \quad (2.6)$$

The variational principle states that the energy E_ψ is an upper bound of the energy E_0 of ground state ψ_0 .

$$E_\psi = \frac{\langle \psi | \hat{H} | \psi \rangle}{\langle \psi | \psi \rangle} \geq \frac{\langle \psi_0 | \hat{H} | \psi_0 \rangle}{\langle \psi_0 | \psi_0 \rangle} = E_0 \quad (2.7)$$

Variational principle defines a process to calculate the ground state ψ_0 and its properties through the ground state energy E_0 . The ground state is the state that possesses the minimal energy among all the state ψ_N of N electrons.

$$E_0 = \min_{|\psi_N\rangle} \frac{\langle \psi_N | \hat{H} | \psi_N \rangle}{\langle \psi_N | \psi_N \rangle} = \min_{|\psi_N\rangle} \frac{\langle \psi_N | T_e + V_{N-e} + V_{e-e} | \psi_N \rangle}{\langle \psi_N | \psi_N \rangle} \quad (2.8)$$

The ground state energy is a function of the number of electrons and the external potential V_{N-e} of nuclei.

2.2 Hartree Fock approximation

The Hartree Fock (HF) approximation assumes that variational solution ψ_0 of the Schrodinger equation can be approximated by a Slater determinant ψ_{HF} .

$$\psi_0 \approx \psi_{HF} = \sqrt{\frac{1}{N!}} \begin{vmatrix} \psi_1(\mathbf{r}_1, \mathbf{s}_1) & \psi_2(\mathbf{r}_1, \mathbf{s}_1) & \dots & \psi_N(\mathbf{r}_1, \mathbf{s}_1) \\ \psi_1(\mathbf{r}_2, \mathbf{s}_2) & \psi_2(\mathbf{r}_2, \mathbf{s}_2) & \dots & \psi_N(\mathbf{r}_2, \mathbf{s}_2) \\ \dots & \dots & \dots & \dots \\ \psi_1(\mathbf{r}_N, \mathbf{s}_N) & \psi_2(\mathbf{r}_N, \mathbf{s}_N) & \dots & \psi_N(\mathbf{r}_N, \mathbf{s}_N) \end{vmatrix} \quad (2.9)$$

in which the orthogonal orbitals $\psi_i(r_i, s_i)$ are solution of a series of independent equations :

$$\hat{F}\psi_i(\mathbf{r}_i, \mathbf{s}_i) = E_i\psi_i(\mathbf{r}_i, \mathbf{s}_i) \quad (2.10)$$

where \hat{F} is the Fock operator :

$$\hat{F} = -\frac{1}{2}\nabla^2 - \frac{1}{2} \sum_{a=1}^{Z_a} \frac{Z_a}{|\mathbf{r}_i - \mathbf{R}_a|} + V_{H-F}(i, i) = T(i, i) + V_e(i, i) + V_{ext}(i, i) + V_{H-F}(i, i) \quad (2.11)$$

The first term is the kinetic energy of electron, the second term is the attractive electron-nucleus potential energy. $V_{H-F}(ri, si)$ is the Hartree-Fock potential, the average potential due to all other electrons to the i^{th} electrons. The expression of $V_{H-F}(i)$ is :

$$\begin{aligned} V_{H-F}(\mathbf{r}_i, \mathbf{s}_i) &= \sum_{j=1}^N |\psi_j(\mathbf{r}_j, \mathbf{s}_j)|^2 \frac{d\mathbf{r}_j d\mathbf{s}_j}{r_{ij}} - \sum_{j=1}^N \psi_j^*(\mathbf{r}_j, \mathbf{s}_j) \frac{1}{r_{ij}} \psi_i(\mathbf{r}_j, \mathbf{s}_j) d\mathbf{r}_j d\mathbf{s}_j \\ &= \sum_{j=1}^N |J_j - K_j| \end{aligned} \quad (2.12)$$

Here, the first term J_j is coulomb interaction and the second term K_j is the exchange contrib-

bution. The total energy of the systems is the sum of the energies of the filled orbitals minus the double counting of Coulomb repulsion and exchange energy :

$$E_{total} = \sum_{i=1} T_e(\mathbf{r}_i, \mathbf{s}_i) + V_{ext}(\mathbf{r}_i, \mathbf{s}_i) + \frac{1}{2}(J_i - K_i) = T_e + V_{ext} + \frac{1}{2}(J - K) \quad (2.13)$$

Note that this total energy is an overestimation of the energy of the system because the Hartree Fock method fail to describe the electronic correlation.

2.3 Density functional approach

2.3.1 Electron density function

The key quantity in DFT is the electron density :

$$\rho(\mathbf{r}) = N \int \psi_i(\mathbf{r}_1, \mathbf{r}_2, \dots, \mathbf{r}_N, \mathbf{s}_1, \mathbf{s}_2, \dots, \mathbf{s}_N)^2 d\mathbf{s}_i \prod_{j=1}^N d\mathbf{r}_j \quad (2.14)$$

$\rho(\mathbf{r})$ is the probability to find one of N electrons within the $d\mathbf{r}$ volume element. The $\rho(\mathbf{r})$ function has only four variables (three spatial and the spin), it integrates to the total number of electrons and vanishes at infinity. The electron density is an observable which can be experimentally measured.

2.3.2 The Thomas Fermi model

Using the kinetic energy of the uniform electron gas, Thomas and Fermi proposed the kinetic energy functional :

$$T_{TF}[\rho(\mathbf{r})] = \frac{3}{10} (3\pi^2)^{2/3} \rho(\mathbf{r})^{5/3} dr \quad (2.15)$$

In the case of one atom with nuclei charge Z , the total atom energy in equation (2.4) can now be expressed as a function of the electron density:

$$E_{TF} = T_{TF} + V_{N-e} + V_{e-e} = \frac{3}{10} (3\pi^2)^{2/3} \rho(\mathbf{r})^{5/3} dr - \frac{Z\rho(\mathbf{r})}{|\mathbf{r} - \mathbf{r}_a|} dr + \underbrace{\frac{\rho(\mathbf{r})\rho(\mathbf{r}')}{|\mathbf{r} - \mathbf{r}'|}}_{drdr'} \quad (2.16)$$

2.3.3 Hohenberg and Kohn theorems

The Hohenberg and Kohn theorems [69] relate to any system of electrons moving in an external potential $V_{ext}(\mathbf{r})$. They are as follows: *First Hohenberg and Kohn theorem* "The external potential $V_{ext}(\mathbf{r})$, and hence the total energy, is uniquely determined by the electron density $\rho(\mathbf{r})$ " [69]. Equation (2.4) can be rewrite as functional of $\rho(\mathbf{r})$:

$$E_e[\rho] = V_{N-e}[\rho] + T_e[\rho] + V_{e-e}[\rho] = \rho(\mathbf{r})V_{ext}d\mathbf{r} + F_{H-K}[\rho] \quad (2.17)$$

Where $F_{H-K}[\rho] = T_e[\rho] + V_{e-e}[\rho]$ is an universal function that depends only on the number of electrons and not on the external potential V_{ext} of nuclei. The major problem is that the F_{H-K} has two terms, one for kinetic energy of electrons and one for electron-electron interaction energy, but none of them are mathematically known. The second term V_{e-e} can be expressed as :

$$V_{e-e} = \frac{\rho_1(\mathbf{r})\rho_2(\mathbf{r}')}{2|\mathbf{r} - \mathbf{r}'|} drdr' + E_{N \text{ on-classical}} = J[\rho] + E_{N \text{ on-classical}} \quad (2.18)$$

Where the first terms is the classical interaction energy, the second term represents all the others non-classical effect.

Second Hohenberg and Kohn theorem : "The functional $F_{H-K}(\rho)$ delivers the true ground state density and ground state energy of the system if and only if the input density is the true ground state density." In others words, the second theorem is nothing more than the variational

principle : the density that minimizes the total energy E_0 is the exact ground state density . The two Hohenberg and Kohn theorems give us an efficient tool to find the ground state of many body system.

2.3.4 Kohn Sham Equation

The main challenge is to find the best form of F_{H-K} , in other words, the form of T_e and $E_{non-classical}$. Kohn and Sham [69] proposed the following expression for the kinetic energy and the density functional:

$$T_s = -\frac{1}{2} \sum_{i=1}^N \langle \varphi_i | \nabla^2 | \varphi_i \rangle \quad (2.19)$$

$$\rho_s = \sum_{i=1}^N |\varphi_i|^2 \quad (2.20)$$

Where φ_i is the orbital wave function for non-interacting system. Thus, the F_{H-K} functional is now written as :

$$F_{H-K}[\rho] = T_s[\rho] + J[\rho] + E_{XC}[\rho] \quad (2.21)$$

where J is the classical term of electrons interactions (defined in equation (2.18), the E_{XC} exchange and correlation energy represents all the unknown terms :

$$E_{XC}[\rho] = T_s[\rho] - T_e[\rho] + V_{e-e}[\rho] - J[\rho] \quad (2.22)$$

By substituting these terms in equation (2.17) we obtain the following expression for the system total energy :

$$E_e[\rho] = T_s[\rho] + J[\rho] + E_{XC}[\rho] + V_{N-e}[\rho] \quad (2.23)$$

$$E_e(\rho) = -\frac{1}{2} \sum_{i=1}^N \sum_{j=1, j>i}^N \langle \varphi_i | \nabla^2 | \varphi_j \rangle + \sum_{i=1}^N \sum_{j=1}^M \frac{|\varphi_i(\mathbf{r})|^2 |\varphi_j(\mathbf{r}')|^2}{|\mathbf{r} - \mathbf{r}'|} d\mathbf{r} d\mathbf{r}' + E_{XC}[\rho]$$

$$-\frac{1}{2} \sum_{i=1}^N \sum_{a=1}^M \frac{|\varphi_i(\mathbf{r})|^2 Z_a}{|\mathbf{r}_i - \mathbf{R}_a|} d\mathbf{r} \quad (2.24)$$

Here only E_{XC} , the exchange and correlation energy, is unknown and its explicit form is the main challenge in DFT. Using $V_{XC} = \frac{\delta E_{XC}}{\delta \rho}$ and the normalization constraint $\langle \varphi_i | \varphi_j \rangle = \delta_{ij}$,

we obtain the Kohn-Sham equations :

$$-\frac{1}{2} \nabla^2 + \frac{\rho(\mathbf{r}_2)}{|\mathbf{r}_1 - \mathbf{r}_2|} d\mathbf{r}_2 + V_{XC} - \sum_{a=1}^M \frac{Z_a}{|\mathbf{r}_i - \mathbf{R}_a|} \varphi_i = -\frac{1}{2} \nabla^2 + V_s \quad \varphi_i = E_i \varphi_i \quad (2.25)$$

With V_s being the effective potential

$$V_s = \frac{\rho(\mathbf{r}_2)}{|\mathbf{r}_1 - \mathbf{r}_2|} d\mathbf{r}_2 + V_{XC} - \sum_{a=1}^M \frac{Z_a}{|\mathbf{r}_i - \mathbf{R}_a|}$$

Note that the solution of equation (2.25) have no physical significance, except the highest occupied orbital (HOMO) which is equal to the opposite of the ionization energy. The Kohn Sham equations give us an algorithm to find self-consistently the electrons density functional (figure 2.1).

2.4 Exchange-correlation energy

As presented in the previous section, E_{XC} is unknown and needs approximations. In this section, two of them will be presented: the Local Density Approximation (LDA) and Generalized Gradient Approximation (GGA).

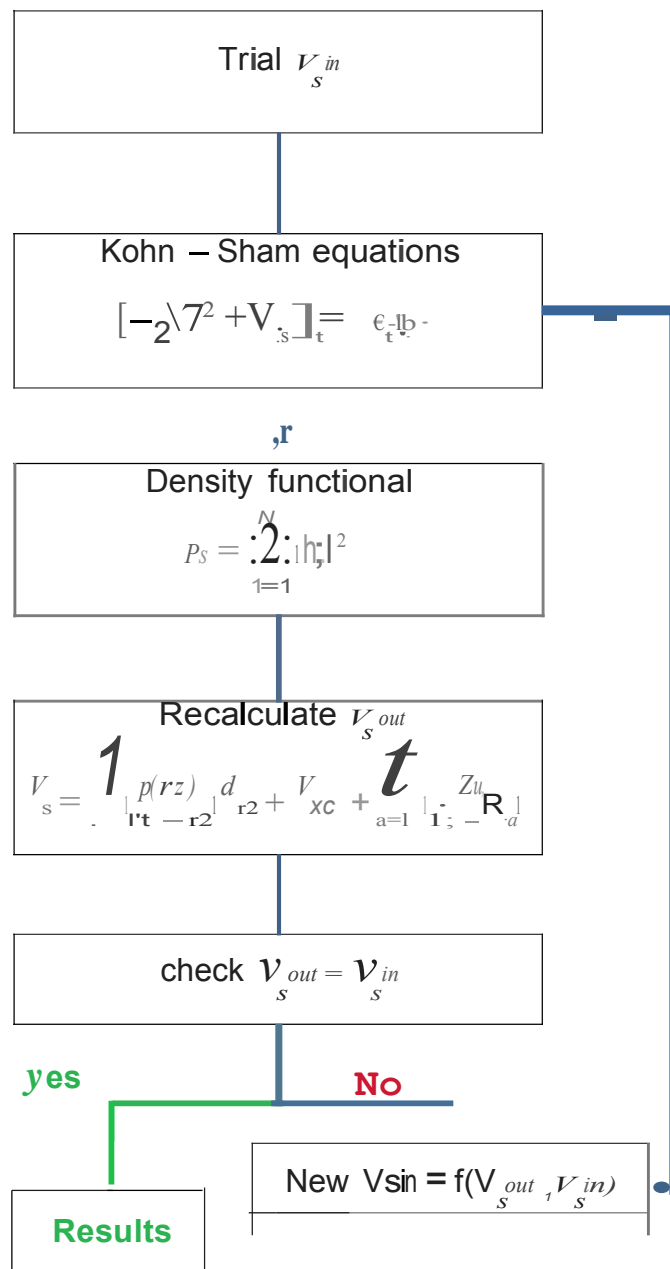


Figure 2.1: Self-consistency scheme: from an initial guessed $V_{:in}$, we solve the Kohn Sham equations. Then, we find the electron density functional. Afterwards, V_{ext} , V_{xc} and the coulomb potential of electron are recalculated to compose $V_{:out}$. If $V_{:out} = V_{:in}$ the problem is solved, if not, an other new $V_{:in}$ will be introduced in function of $V_{:out}$ and $V_{:in}$ then restart a new iteration.

2.4.1 The local density approximation (LDA)

The local density approximation is the simplest method and also the origin of all DFT methods. This method considers the system as a system of free electrons moving in a positive background of nuclei. So the E_{XC} energy can be written as :

$$E_{XC}[\rho] = \int E_{XC}(\rho) \rho(\mathbf{r}) d\mathbf{r} \quad (2.26)$$

Where E_{XC} is the exchange-correlation energy per particle of an uniform electron gas of density $\rho(\mathbf{r})$. E_{XC} can be expressed in 2 terms:

$$E_{XC} = E_X + E_C = -\frac{3}{4} \left(\frac{3\rho(\mathbf{r})}{\pi} \right)^{\frac{1}{3}} + E_C \quad (2.27)$$

The first term is the exchange energy of an electron in an uniform electron gas, derived by Bloch and Dirac[70]. The second term is unknown, but could be estimated using Monte-Carlo simulations of the homogeneous electron gas [Alder, P-B [71]].

LDA has an accuracy of typically 10-20 % in the calculation of ionization energies of atoms, dissociation energies of molecules and cohesive energies. However, it gives a very good accuracy of bond lengths of molecules and solids (less than 2%). LDA can not be applied in systems where the electron-electron interaction effect is dominant (for example in heavy fermions).

2.4.2 The generalized gradient approximation (GGA)

The generalized gradient approximation is a method approximating the exchange-correlation energy not only as a functional of the electron density but as a functional of its gradient. In this purpose, the E_{XC} is rewritten as:

$$E_{XC}^{GGA}(\rho_\alpha, \rho_\beta) = \int f(\rho_\alpha, \rho_\beta, \nabla \rho_\alpha, \nabla \rho_\beta) d\mathbf{r} \quad (2.28)$$

In this framework, a simple Taylor expansion, tested in the early 70s by Sham and Herman et al [72], appears disappointing and give even less satisfactory results than those obtained with LDA. Since, significant progresses have been made and have allowed to determine functions satisfying a large number of the criteria audited by the $E_{XC}(\rho)$ functional. The first GGA functional was proposed in 1986 by Becke[73], then Perdew and Wang [74] for the exchange (designated PW86) and Perdew (P)[74] for the correlations. Besides the later, the most popular ones are those of Becke (B) [73] for the exchange energy, Lee, Yang and Parr (LYP) [75] for the correlation energy, and the functional PW91 of Perdew and Wang [76] for the exchange and correlation energy. The functional developed by Perdew, Burke and Ernzerhof (PBE) [16] and its successor (RPBE)[77] are also among the most popular GGA functional at present. Most of these functional contain a GGA functional or more parameters which derived from experimental measurements. Recently the meta GGA method, containing the second derivative of ρ , was developed. Filatov et Thiel (1998) [78] build a functional whose performance is comparable in terms of quality to those provided by the best GGA functional, but costing twice the GGA computational time. Until now, none of such functional is widely used.

2.4.3 Hybrid functional

In another approach, many hybrid functionals were proposed by mixing the previous methods. The first method was proposed by A. Becke [79]:

$$E_{xc}^{B3PW91} = E_{xc}^{LDA} + a(E_{X}^{exact} - E_{X}^{LDA}) + b\Delta E_X + c\Delta E_C \quad (2.29)$$

Where $a = 0.20, b = 0.72, c = 0.81$ are fitted parameters. ΔE_X^{B88} [80] is B88 gradient correction and ΔE_C^{PW91} [76] is the PW91 gradient correction. Since then, more complex formulations were developed, and the most popular functional is the B3LYP[81] suggested by Stevens et al :

$$E_{xc}^{B3LYP} = (1 - a)E_X^{LDA} + aE_X^{H-F} + bE_X^B + (1 - c)E_C^{LDA} + cE_C^{LYP} \quad (2.30)$$

The B3LYP functional uses three fitted parameters a, b, c which control the contribution of LDA, H-F and B ([73]) for exchange energy and LYP [75] and LDA for the correlation part. The use of GGA and hybrid approximations reduces errors of atomization energies 2 -3 times with respect to the LDA approximations. Thus, GGA and GGA hybrid functional are more convincing in both quantum chemistry and quantum physics.

2.5 Van der Waals dispersion

Standard DFT exchange correlation functionals do not include the Van Der Waals forces. These latter are very important in weak bonded materials or in the framework of the adsorption/desorption of molecules on surfaces. Discovered since a long time, the dispersion interaction, originating from the instantaneous interaction between dipoles induced by charge fluctuations, decreases with a $1/r^6$ decay. As the main interest of this work is the study of the effect of adsorption of ligands on metallic surfaces, I have evaluated and compared the advantage and inconvenient of two popular methods which take into account the vdW dispersion : the DFT Grimme D2 correction and vdW-DF functional. In the following section, the essential details of these two methods are presented.

2.5.1 Including empirical corrections DFT-D

One of the simplest way to take into account the vdW interactions consists in adding an empirical correction to the DFT total energy. The method of Grimme [13] proposes the following form for the dispersion energy :

$$E_{disp} = -S_6 \sum_{i=1}^{M-1} \sum_{j>i}^M \frac{C_6^{ij}}{R^{ij}} f_{damp}(R^{ij}) \quad (2.31)$$

where S_6 is a global factor depending on the functional (for PBE, $S_6 = 0.75$), M is the number of atoms, C_6^{ij} is the couple interaction between atom i and atom j . R^{ij} is the distance between atom i and atom j . f_{damp} is the damping function decreasing with the inter-atomics distance. The version used in this work was DFT Grimme D2 [13], in which f_{damp} have the following form :

$$f_{damp}(R^{ij}) = \frac{1}{1 + e^{-d[(R^{ij}/R_i + R_j) - 1]}} \quad (2.32)$$

where d is a damping parameter, R^{ij} the distance between the atoms i and j and R_0 the Van der Waals radius of atom i . The C_6^{ij} factor for 2 atoms of the same type is derived from dipole oscillator strength distributions [13]. For two different atoms, C_6^{ij} was chosen as :

$$C_6^{ij} = -\frac{C_6^i C_6^j}{C_6^i C_6^j}$$

The C_6 factor and R_0 of all elements used in this works are given in table (2.1). Note that all

elements from Zn to Cr (for which Co and Ni belong to) take the same average value.

Element	O	C	N	H	P	Co	Ni
C_6 [J nm ⁶ mol ⁻¹]	0.70	1.75	1.23	0.14	7.84	10.8	10.8
R_0 [Å]	1.342	1.452	1.397	1.101	1.705	1.562	1.562

Table 2.1: C_6 coefficients and Van der Waals radii R_0 used in the DFT-D2 method[13]

2.5.2 Non Local dispersion density functional (vdW-DF)

Originally proposed by Langreth and Lundqvist and co-workers [14], this method consists in adding a non-local correction to the E_{XC} term which was calculated by the LDA and the GGA methods :

$$E_{XC} = E_X^{GGA} + E_C^{GGA/LDA} + E_C^{nl} \quad (2.33)$$

The non-local part E_C^{nl} has the form:

$$E_C^{nl} = \frac{1}{2\pi} \int_0^\infty \frac{du}{u} \text{Re}[Tr(\ln(E^{-1} \nabla E \nabla \mathbf{G}))] \quad (2.34)$$

where \mathbf{G} is the Coulomb Green's function, E is the dielectric function, u is wave number. Several proposed versions of the method were developed from the original vdW-DF such as optPBE-vdW, optB88-vdW, and optB86b-vdW [82].

2.6 DFT in periodical system

In this section, the basic aspects of the DFT calculations with periodic boundary conditions used in work is presented.

2.6.1 Plane Wave basis

In general, Kohn-Sham equations (equations 2.25) can be solved by developing the ψ_i orbitals on set of adequate orthogonal basis functions φ_j .

$$\psi_i = \sum_j \varphi_j \quad (2.35)$$

The problem now reduces to the diagonalization of the Kohn Sham Hamiltonian H_{KS} . The choice of orthogonal basis sets is really convenient. There are two types of popular basis sets : plane waves and localized orbitals. The localized basis sets are particularly used in quantum chemistry. These basis sets use localized functions in real space, which are centered on the atoms. Many basis sets have been developed to ensure a fast convergence. The most common ones are the linear combination of atomic orbitals (LCAO). This approach is adapted to the study of small and non-periodical systems such as atoms or molecules. The plane wave basis sets, widely used in solid state physics, are well adapted to study periodical systems. These bases are easily linked to the Fourier transform, allowing the use of fast transform algorithms. In the following paragraph, I will focus on the plane wave basis set which is implemented in the VASP code that I used in all my calculations. A plane wave basis is defined by a set of wave vectors \mathbf{G}

$$\psi_{\mathbf{G}} = \frac{1}{V} e^{i\mathbf{G} \cdot \mathbf{r}} \quad (2.36)$$

here V is the crystal volume. For the periodic systems, the Bloch theorem allows to write the Kohn-Sham orbitals ψ_i as:

$$\psi_{n,\mathbf{k}} = u_{n,\mathbf{k}}(\mathbf{r}) e^{i\mathbf{k}\cdot\mathbf{r}} \quad (2.37)$$

where $u_n, k(\mathbf{r})$ is a periodic function with the same periodicity as the crystal, \mathbf{k} is a vector of real numbers in the first Brillouin zone, n is band index. $u_n, k(\mathbf{r})$ can be decomposed in Fourier series on the basis of plane waves in reciprocal lattice , which leads to the following decomposition of $\psi_{n,k}$:

$$u_{n,\mathbf{k}}(\mathbf{r}) = \sum_{\mathbf{G}} C_{n,\mathbf{k}+\mathbf{G}} e^{i(\mathbf{k}+\mathbf{G}) \cdot \mathbf{r}} \quad (2.38)$$

The Kohn Sham equations now written in reciprocal space:

$$\sum_{\mathbf{G}} \frac{1}{2} |\mathbf{k} + \mathbf{G}|^2 \delta(\mathbf{G}, \mathbf{G}') + V s(\mathbf{G} - \mathbf{G}') C_{i,\mathbf{k}+\mathbf{G}} = E_i C_{i,\mathbf{k}+\mathbf{G}} \quad (2.39)$$

The first term are diagonalized, and the second term can be obtained by simple Fourier transformation. It is very simple for any calculation on both real space and reciprocal space. In general, computed quantities can only be exact in an infinity basic set of wave numbers \mathbf{G} . In practical computation, the convergence quality can be controlled by imposing an cut-off energy $E_{cut-off}$ such as:

$$\frac{1}{2} |\mathbf{k} + \mathbf{G}|^2 \leq E_{cut-off} \quad (2.40)$$

2.6.2 Pseudopotentials

The Schrödinger equation can be simplified if we divide electrons in two groups: valence electrons and core electrons. The electrons in the inner shells are strongly attached to the nuclei and are not involved in the chemical bonding of atoms. In the framework of a pseudopotential, only the chemically active valence electrons are dealt with explicitly, while the core electrons are pre-calculated in an atomic environment and kept 'frozen'. Several pseudopotential methods were proposed including, among others, the norm-conserving pseudopotentials, the ultra-soft pseudopotentials and the PAW (Projector augmented wave) potentials used in my calculation (PAW are implemented in VASP[83]). The PAW method contains the numerical advantages of pseudopotential calculations while retaining the physics of all-electron calculations, including the correct nodal behavior of the valence-electron wave functions .

2.7 Conclusion

I have presented in this chapter the formalism of periodic Density Functional Theory. The computational cost of such methods is cheaper compared to traditional methods based on the wave function. The choice of the functional, parameters and the way to control the errors will be discussed in the next chapter.

Chapter 3

Metal surfaces and bulk calculations

Contents

3.1	Introduction	37
3.2	Preliminary calculations	38
3.2.1	The number of k-points	38
3.2.2	Cutoff energy	39
3.2.3	Smearing	40
3.3	Bulk properties	41
3.3.1	State equation	41
3.3.2	Isolated Atom	41
3.3.3	Cohesive energy and structural parameters	42
3.3.4	Summary	44
3.4	Surface optimization and choice of vdW dispersion	44
3.4.1	Surface models	44
3.4.2	Preliminary calculations of Co(0001) and Ni(111) surfaces	46
3.4.3	Surface properties of Co(0001) and Ni(111) with vdW dispersion	48
3.4.4	Summary	53
3.5	Surface energies of Co and Ni	53
3.5.1	Co surfaces	53
3.5.2	Ni surfaces	54
3.6	The attachment energy model	56
3.7	Conclusion	58

3.1 Introduction

The ultimate goal of this work is to model the interaction between the metallic surfaces (Co, Ni) and the adsorbed molecule (ligand). For the beginning, it is necessary to investigate the reference systems, i.e. the metallic surface and the isolated ligand, then to compare with the system of the surface and the ligand in interaction. In this chapter, I would like not only to present the simulation details employed for the metallic surface, but also to describe the way we obtained its geometrical, physical and mechanical properties. I will also present the

methodology used to take into account the effects the van der Waals (vdW) dispersion interactions and finally give our final choices of parameters and functionals for further calculations. Unlike for the molecule/surface interactions, for which the vdW dispersion interactions must be taken into account, the presence of vdW interactions in metallic systems is a subject of debate [12]. In this work, I investigate the efficiency of two popular dispersion functionals: the DFTD method [13] and the opt86B functional [14], [15] and compare them to the PBE functional [16] where no vdW dispersion interactions are taken into account.

I have concentrated firstly on metallic systems: I started by the isolated atoms of Co and of Ni in vacuum. Then, I optimized their crystalline structure and finally I built models of their crystalline surfaces. The physical properties deduced from these models have been compared to experimental results and others existing calculations in the literature to get the best parameters for the next step. All of the DFT calculations have been performed using the VASP package [17, 18, 19, 20], a DFT code for periodical systems. The bulk systems have been used to optimize the convergence of the calculations with respect to the cut-off energy, the smearing and the number of k-points in the first Brillouin zone.

3.2 Preliminary calculations

We expect to model the interaction between the metallic surface and the molecule. An energy difference of some decades of meV is essential, this is the reason why we wish to get bulk and surface energies with an error of less than a few meV. The three most important parameters to be optimized at first are the number of k-points in the first Brillouin zone, the cutoff energy and the smearing. We use the primitive cell of each metal for the calculations because of its simplicity and the short computing time. The Co bulk crystalline structure is the hexagonal compact (HCP) structure. The primitive cell is modeled by a cell of 2 atoms in a tetrahedral box (figure 3.1 (c)) with the three lattice vectors a, b, c with the following formula:

$$\begin{aligned} \square & a \quad \square \quad \square & 1 & 0 & 0 & \square \square \quad a \times i & \square \\ & & & & & & \\ \square & b \square = \square & -1 & \frac{-3}{2} & \square \square \quad a \times j & \square & (3.1) \\ & & & & & & \\ c & & 0^2 & 0 & 1 & a \times \frac{c}{a} \times & \\ & & & & & & \\ & & & & & & k \end{aligned}$$

where i, j, k are the unitary orthogonal vectors in space.

The Ni metal crystallizes in the face centered cubic (FCC) structure. The primitive cell for Ni is a triclinic cell with one atom (figure 3.1 (a)). Its lattice vectors were defined using the following formula:

$$\begin{aligned} \square & a \quad \square \quad \square & \frac{1}{2} & \frac{1}{2} & 0 & \square \square \quad a \times i & \square \\ & & & & & & \\ \square & b \square = \square & 0 & 1 & \frac{1}{2} & \square \square \quad a \times j & \square & (3.2) \\ & & & & & & \\ c & & \frac{1}{2} & 0 & \frac{2}{2} & a \times k & \end{aligned}$$

3.2.1 The number of k-points

The number of k-points in the first Brillouin zone has a great influence on the accuracy and also the computation time. The wave-functions in reciprocal space are defined with an infinite number of k-points. In numerical calculations, the infinity number is impossible, so we must

approximate the electron density by using a limited number of k-points. Therefore we generate a grid of k-points in the reciprocal space. In this work, I use only the method of Monkhorst-Pack (MP)[84] to get a grid of special k-points of high symmetry (except for the case of the calculation of the band structure for which a selected path in k-space is used). In the case that the dimension of the simulation cells is large, such as for the isolated atom, the approximation of

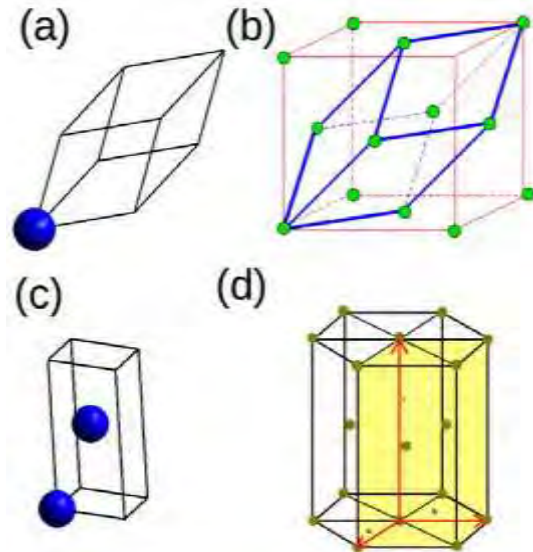


Figure 3.1: Primitive and unity cells of HCP and FCC structures. (a) triclinic cell of Ni, (b) FCC primitive cell in the unit cell, (c) tetragonal primitive cell of Co, (d) HCP primitive cell in the unit cell.

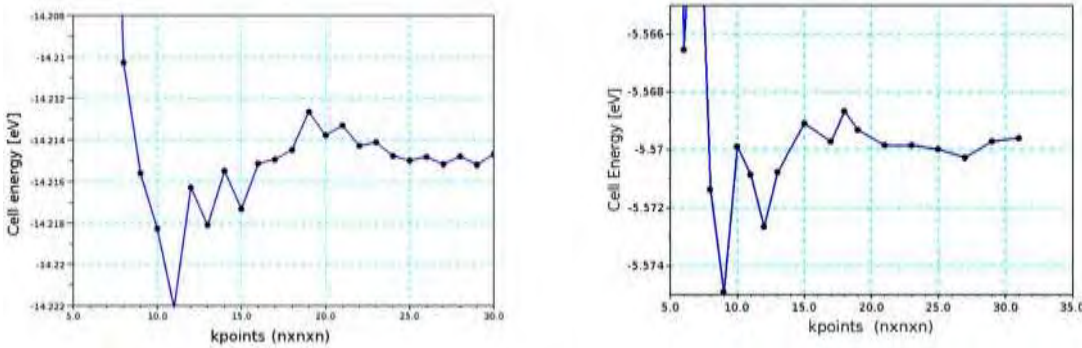


Figure 3.2: Left: Co primitive cell energy as a function of the k-points number. Right: Ni primitive cell energy as a function of the k-points number.

the Γ point gives reasonable results for acceptable computation time. However, the calculations of the metal bulk and surface require a suitable number of points in the reciprocal to get a good representation of the electronic structure. In order to get the most accurate results for the lowest computational time, it is necessary to optimize the number of k-points. Figure 3.2 represents the dependency of the total energy of the primitive cell of Co and Ni as a function of the k-points grid. The calculations were performed with a smearing $\sigma = 0.01$ and a cutoff energy of 600 eV for Ni and 650 eV for Co. It is clearly showed in these figures that the total energy exhibits large fluctuations with a small k-points grid and then converges with a large number of k-points. In order to get results with a maximum error of 1 meV on the total energy per atom, the truncated error generated by the limited number of k-points can not exceed 0.5 eV. So the optimal number of k-points for the bulk calculations is 19x19x19 in the case of Ni and 21x21x21 in the case of Co.

3.2.2 Cutoff energy

As showed in the previous chapter, in general, the computed quantities can only be exact in an infinite basis of wave vectors \mathbf{G} . In practical computations, the convergent quality can be

controlled by imposing a cutoff energy E_{cutoff} that truncates the sum over the \mathbf{G} vectors. Only the wave vectors \mathbf{G} that satisfy the following condition will be taken into account:

$$|\mathbf{k} + \mathbf{G}|^2 \leq E_{\text{cutoff}} \quad (3.3)$$

It is clearly showed that the chosen cutoff energy influences the accuracy of the calculation but

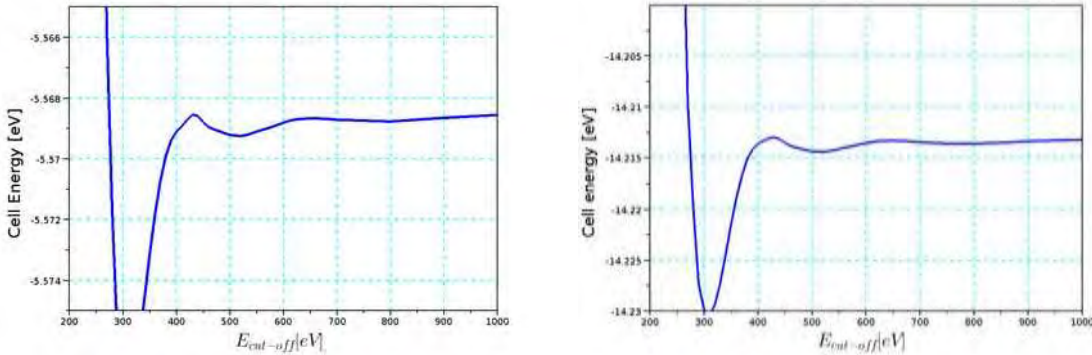


Figure 3.3: Ni (left) and Co (right) cell energy as a function of the cutoff energy.

also the computation time. A compromise between the two must be found. VASP recommends a cutoff energy of 400 eV for both Co and Ni with an accuracy on the total energy per atom of about 10 meV. To obtain the limited 1 meV error we expect, we must optimize this cutoff energy. Figure 3.3 shows the variation of the total energy of a primitive cell of Ni with 1 atom. The fluctuations are in the limit of 1 meV from $E_{\text{cutoff}} = 600$ eV - shows the variation of the total energy of a primitive cell of Co with 2 atoms. The fluctuations are in the limit of 1 eV per atom from $E_{\text{cutoff}} = 650$ eV . The two calculations were performed with an optimized k-point grid. So, in all following metallic calculations in this chapter, we will use $E_{\text{cutoff}} = 600$ eV for Ni and $E_{\text{cutoff}} = 650$ eV for Co.

3.2.3 Smearing

Figures 3.4 shows the variation of the total energy as a function of the smearing value σ for the Co and Ni cells, respectively, using the PBE functional. We find that the total energy is converged with an error of 1 meV at $\sigma = 0.2$ eV but a more accurate convergence of 0.1 meV can be reached for a value of $\sigma = 0.05$ eV. We chose the conservative value of $\sigma = 0.01$ eV for further calculations on the properties of metal bulk and surfaces.

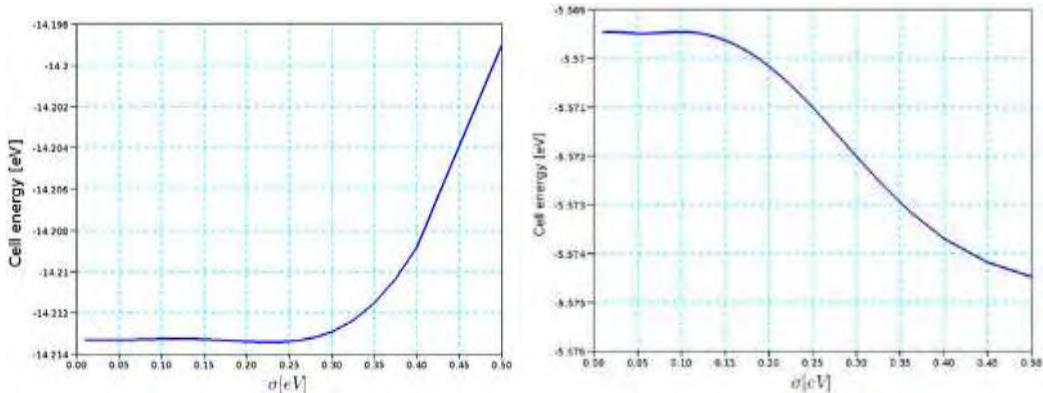


Figure 3.4: Co (left) and Ni (right) cell energy as a function of the smearing σ .

3.3 Bulk properties

In this section, I present our studies on the equilibrium bulk structure and the magnetic properties. The structural parameters must be evaluated with a good accuracy since they will serve as basis for all the following studies carried out on the surface and adsorption properties. Additionally, the bulk equilibrium structure has been thoroughly studied both experimentally and theoretically and we can compare our results with the literature.

3.3.1 State equation

The equilibrium bulk structure is the one that minimizes the total energy with respect to the unit cell volume. The total energy of the system depends on the unit cell volume following the Murnaghan equation:

$$E(V) = E(V_0) + \frac{B'}{B^t} \times \frac{(1 - V/V_0)^{B' - 1}}{B^t - 1} + V_0 \frac{1 - V/V_0}{B^t - 1} \quad (3.4)$$

where $E(V_0)$ is the minimum energy of the system corresponding to unit cell volume V_0 of the system at zero temperature. B is the bulk modulus defined as:

$$B(T, V) = V \left. \frac{\partial P}{\partial V} \right|_T \quad (3.5)$$

and B' is the pressure derivative of the bulk modulus at zero pressure and zero temperature:

$$B'(T, V) = \left. \frac{\partial}{\partial V} V \frac{\partial p(T, V)}{\partial V} \right|_{T=0, p=0} \quad (3.6)$$

From the knowledge of the minimum energy $E(V_0)$, one can obtain the cohesive energy E_0 which is the energy required to break the atoms of the solid into isolated atomic species. The cohesive energy can be compared with experiments. It is defined as:

$$E_0 = \frac{E(V_0)}{N} - E_{atom} \quad (3.7)$$

where E_{atom} is energy of an isolated atom, N is the number of atom in the primitive cell. It requires the knowledge of the isolated atom energy.

3.3.2 Isolated Atom

For the calculation of isolated atoms, we use a large super-cell of 18 Å x 19 Å x 20 Å so that the atom does not interact with its periodic image. The calculations are performed with the γ point only for the mesh of the first Brillouin zone. For consistency, the energy of the isolated atom should be calculated in the same conditions of cutoff energy and smearing than the ones used for the bulk calculations: $\sigma = 0.01$ eV and $E_{cutoff} = 600$ eV for Ni and 650 eV for Co. The calculated energies of isolated Co and Ni are given in Tab. 3.1 for different E_{xc} functionals. Note that in DFT with pseudo-potentials the values of the isolated atom energy has no physical meaning. These calculations will serve only in order to compute cohesive energies and work

functions.

Functional	PBE/PBE+DFTD	opt86B
Co	-1.696 eV	0.241 eV
Ni	-0.812 eV	1.543 eV

Table 3.1: Energies of isolated atoms. The size of the box is larger than the cutoff distance of the Grimme dispersion term so that PBE and PBE+DFTD give the same results.

3.3.3 Cohesive energy and structural parameters

The Murnagan equation (Eq 3.4) of solid state is complex to use and, for small variations of unit cell volume, can be approximated to an order 2 polynomial function with a good accuracy around the minimum energy volume V_0 :

$$E(V) = a_0 + a_1 V + a_2 V^2 \quad (3.8)$$

By fitting the result with this function, one obtains the bulk modulus B , the equilibrium cell volume $V_0 = \frac{-a_1}{2a_2}$ and the minimum energy of the system $E_0 = \frac{a_1^2}{4a_0a_2}$.

3.3.3.1 Case of Ni

Ni has a FCC structure and the three lattice vectors have the same norm a . The lattice parameter a , bulk modulus B are presented in Table 3.2 and in Figure 3.5. For the lattice

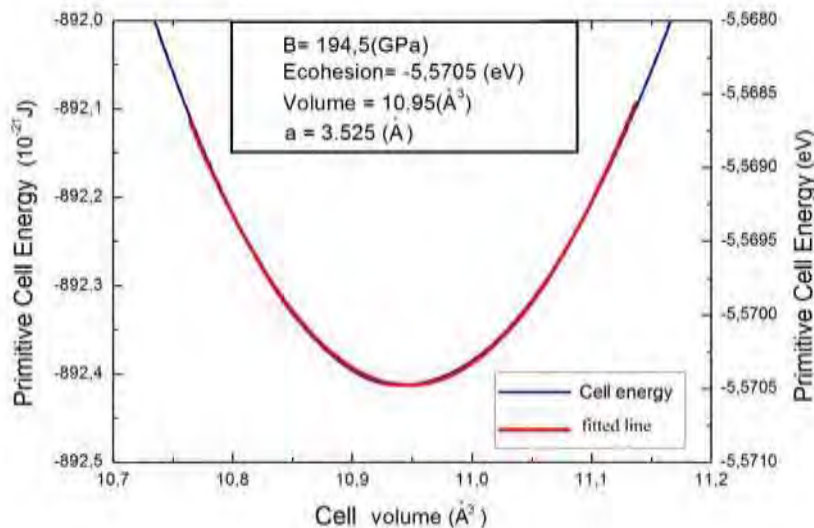


Figure 3.5: Cell energy as a function of the primitive cell volume for Ni with the PBE functional. The results of the fit are given in the inset: lattice parameter a , bulk modulus B and cohesive energy (before isolated atom correction).

parameter, the agreement between the three methods and experiments are very good: +0.14 % for PBE, -0.74% for Opt86B and -1.59% for DFTD. The bulk modulus is estimated with a reasonable error for PBE (+4.82%), but a larger one for DFTD (+17.74%) and Opt86B (+12.36%). The optimized cohesive energy gives a considerable error around +9.68% for PBE, -20.49% for Opt86B and -14.41 % for DFTD. Finally, the magnetic moment per atom is found in very good agreement with the experimental value for all functionals.

Functional	a [Å]	B [GPa]	E_0 [eV]	magnetic moment [$\mu_B/\text{at.}$]
PBE	3.525	195	-4.87	0.65
PBE+DFTD	3.464	219	-5.35	0.59
Opt86B	3.494	209	-5.08	0.58
Experimental [22]	3.52	186	-4.44	0.61

Table 3.2: Lattice parameter a , bulk modulus B , cohesive energy and atomic magnetic moment for Ni with different functionals.

3.3.3.2 Case of Co

Cobalt has a HCP symmetry and 2 cell parameters to optimize : a and c/a . The equilibrium lattice parameters are the ones that minimize the energy of the unit cell at each volume. Therefore, only the the unit cell with the smallest energy among all the unit cells with the same volume must be used to fit the equation of state. These corresponds to the red points in Figure 3.6. The results of the fit are shown in Table 3.3. For the lattice parameter a , the agreement with experimental data is very good for the three methods: -0.36 % for PBE, -1.12% for Opt86B and -1.48% for DFTD. The bulk modulus is obtained with a fairly good agreement with experiments : +5.23% for PBE, +10.47% for DFTD and +8.90% for Opt86B. The optimized cohesive energy gives a considerable error around -19.16% for PBE, -22.03% for Opt86B and -29.74 % for DFTD. Note that the atomic magnetic moment are computed with a reasonable error for PBE (-6.34%), but are less accurate for Opt86B (-9.30%) and DFTD (-9.88%).

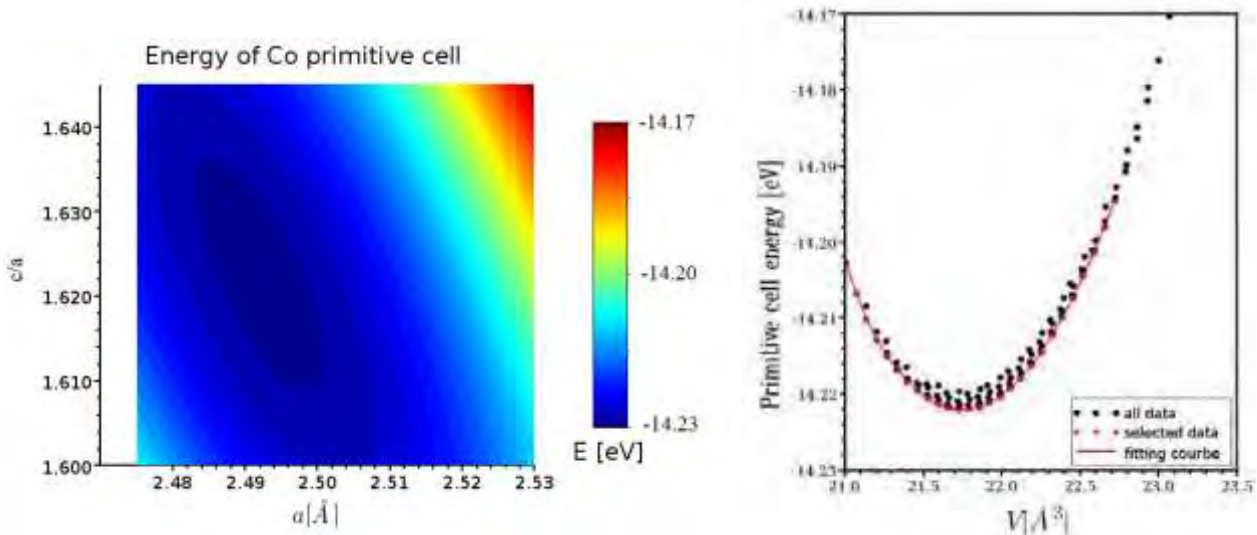


Figure 3.6: Energy of the Co primitive cell as a function of the lattice parameters (left) and of the volume cell (right). Only the red points are taken into account in the fitting curve.

Functional	a [Å]	c/a	B [GPa]	E_0 [eV]	magnetic moment [$\mu_B/\text{at.}$]
PBE	2.491	1.625	201	-5.41	1.61
PBE+DFTD	2.463	1.600	211	-5.89	1.55
Opt86B	2.472	1.616	208	-5.54	1.56
Experimental [22]	2.50	1.623	191	-4.39	1.72

Table 3.3: Lattice parameters a and c/a , bulk modulus B , cohesive energy E_0 and magnetic moment of Cobalt with different functionals.

3.3.4 Summary

In summary, the two optimized lattice parameters of these two metals are computed with a very good accuracy. All of the functionals give values with an error of less than 2%. Among the three functionals, the ordering of the lattice parameter is:

$$a^{PBE} > a^{opt86B} > a^{PBE+DFTD}$$

The estimated value for the bulk modulus is acceptable with an error around 5-10 % depending on the method. All methods overestimate the value of B , and the same ordering as the one observed for the lattice parameters is found:

$$B^{PBE} > B^{opt86B} > B^{PBE+DFTD}$$

However the estimation of the cohesive energy exhibits an error greater than 10%. All methods overestimate the value of E_0 and have also the same ordering:

$$|E_0^{PBE}| > |E_0^{opt86B}| > |E_0^{PBE+DFTD}|$$

In all cases, the PBE functional gives the best agreement to experimental results. Taking into account the van der Waals dispersion for the calculation of bulk Co and Ni do not present any improvement with respect to PBE. A thorough study carried out on several metals (Al, Cu, Fe, Au, Co and Ni) [12] lead to the same conclusion.

3.4 Surface optimization and choice of vdW dispersion

In this section, I would like to present the conditions used to model the surface properties. In the progress of optimization and comparing the computed quantities with the experimental results, I will also explain the choice of the vdW dispersion in our surface calculations.

3.4.1 Surface models

All our models are built using periodical boundary conditions. The model cell will be a large cell with many successive layers of metal (slab) and will respect the symmetry, periodicity and the orientation of the studied surface. The slab must be thick enough to represent the bulk properties of the materials. The periodicity of the 2 directions parallel to the studying surface generate a surface infinite ensure to product good surface properties of metal in the slab center. However, in the direction perpendicular to the studied surface, a vacuum is introduced to generate the free surface. In order to prevent interactions between the surface and the image slab, a large enough distance between the slab and its image must be chosen. Therefore, there are two parameters to optimize in slab simulations: the number of layers and the vacuum distance. The initial structure of the slab is the bulk geometry. By introducing vacuum in the direction perpendicular to the studied crystalline surface, one creates two identical surfaces. It is necessary to model a slab with a sufficiently large number of layers to ensure the convergence of the surface energy and to reproduce the bulk structure in the center of the slab. To compute the surface energy, two different methods of slab construction can be used, presented in Fig. 3.7: the "symmetric" and "asymmetric" configurations. These configurations are built in the aim of modeling an infinite number of layers. In the symmetric configuration, the atoms at the center of the slab are kept fixed at the positions of the bulk and the atoms of all other layers are free to relax. This way, the model exhibits two identical surfaces. The energy needed to create one surface is given by:

$$E_{surf}^{sym} = \lim_{n \rightarrow \infty} \frac{1}{2} (E_{slab} - n \times E_b) \quad (3.9)$$

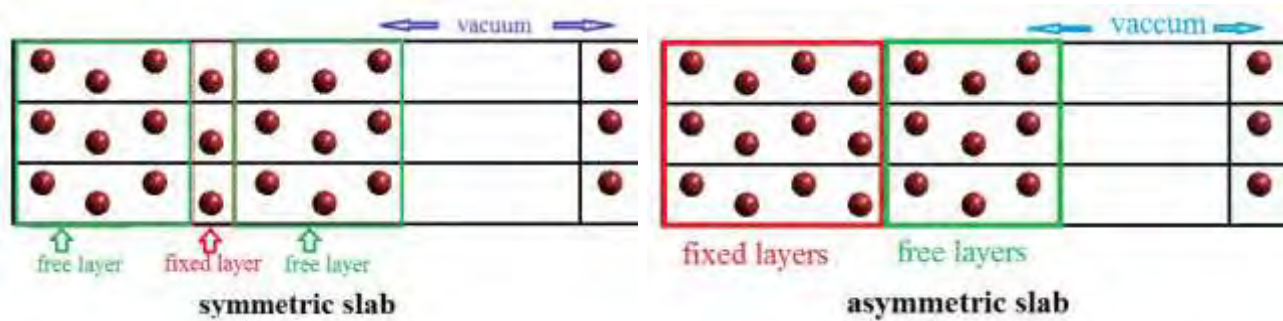


Figure 3.7: Top: Symmetric configuration. Bottom: asymmetric configuration of a slab.

where E_{slab} is the energy of the slab after relaxation, n is the number of layers in the slab and E_b is the energy of one layer in the bulk. Thus, the surface energy is:

$$\gamma = E_{\text{surf}}^{\text{sym}} / A \quad (3.10)$$

where A is the surface area of the studied surface. It is necessary to study the convergence of γ as the function of the number of layers in the slab. In order to do that, one usually performs a linear fit of the total energy of the slab as a function of n :

$$E_{\text{slab}}(n) = 2E_{\text{surf}}^{\text{sym}} + nE_b \quad (3.11)$$

In the asymmetric configuration (Fig. 3.7), the atoms of some layers on one side of the slab are kept fixed at their positions in the bulk. Only the atoms belonging to the layers close to the surface are free to relax. This way, the two surfaces are not equivalent, one will be relaxed whereas the other will remain unrelaxed. The energy of the unrelaxed and relaxed surfaces are given by:

$$\begin{aligned} E_{\text{slab}}^{\text{ur}} &= 2E_{\text{surf}}^{\text{ur}} + nE_b \\ E_{\text{slab}}^r &= E_{\text{surf}}^r + E_{\text{surf}}^{\text{ur}} + nE_b \end{aligned}$$

where $E_{\text{slab}}^{\text{ur}}$ and E_{slab}^r are the unrelaxed and relaxed slab energies, respectively and E^{ur} and E^r

E_{surf}^r are the unrelaxed and relaxed surface energies, respectively. So one obtains the relaxed surface energy in the asymmetric case with:

$$E_{\text{surf}}^{\text{asym}} = E_{\text{slab}}^r - \frac{1}{2} (E_{\text{slab}}^{\text{ur}} + nE_b) \quad (3.12)$$

and

$$\gamma = E_{\text{surf}}^{\text{asym}} / A \quad (3.13)$$

In the following, We chose the symmetric configuration to compute the surface energies. Due to difference in kpoints number in the z direction, the value of E_b is not given by the bulk value but a linear fit of slab energy as functions of the number layer. We note that the linear fits give the same value for the E_b as the bulk value derived from the cohesive energy with an error of less than 1 meV. Therefore, the cohesive energy was used to compute γ . The relaxation of the surface is described by the variation of the interlayer distances:

$$\Delta d_{i,i+1} = \frac{d_{i,i+1} - d_{i,i+1}^{\text{bulk}}}{d_{i,i+1}^{\text{bulk}}} \times 100\% \quad (3.14)$$

where $d_{i,i+1}$ is the distance between the layer i and the successive layer $i+1$, compared to that found in the bulk. As stated before, the slab must be chosen with a number of layers sufficient so that $\Delta d_{i,i+1} = 0$ in the center of the slab.

A solid surface is also defined by its work function which is the energy necessary to extract one electron from the surface to the vacuum. The work function Φ is calculated as:

$$\Phi = \Phi_\infty - E_f \quad (3.15)$$

where Φ_∞ is the electrostatic potential in the vacuum, E_f is the Fermi level of the metallic surface. Φ_∞ can be obtained from DFT calculations by plotting the electrostatic potential in the direction perpendicular to the studied surface. The electrostatic potential exhibits a plateau in the vacuum which height gives the value of Φ_∞ .

3.4.2 Preliminary calculations of Co(0001) and Ni(111) surfaces

The most stable surfaces of each metal (Co(0001) and Ni(111)) have been chosen in order to test the parameters that will be used hereafter for all the surface simulations. In these calculations, we chose the symmetric configuration for the surface models for its simplicity in convergence conditions.

In the following and for all surface calculations, the z-direction will always be defined as the direction perpendicular to the studied surface. For the Co(0001) surface, each layer of Co contains a single atom and is replicated in the surface by two lattice vectors (v_1, v_2) and by v_3 in the z-direction.

$$\begin{array}{ccccccccc}
 & v_1 & & 1 & 0 & 0 & a_i & \\
 & v_2 & = & -1/2 & -3 & 0 & a_j & \\
 v_3 & & 0 & 0^2 & 1/2 & c_k &
 \end{array} \quad (3.16)$$

where a and c are the lattice parameters of Co and i, j, k are the orthogonal unit vectors in the space. The position of each atom of Co is given by equation 3.17:

$$\begin{array}{ccccccc}
 \square & \square & \square & 1/3 & 2/3 & 1/2 & \square \\
 p_1 & & & & & & \\
 \square & \square & \square & 2/3 & 1/3 & 1 & \square \\
 p_2 & & & & & & v_1 \\
 \\
 \square & \square & \square & = & \square & \square & \square \\
 \square & \dots & \square & \square & \dots & \square & \square \\
 \square & & \square & & & \square & \square \\
 \square & & \square & & & \square & \square \\
 p_{2n-1} & & \square & & & \square & \square \\
 & & \square & & & \square & \square \\
 & & & 1/3 & 2/3 & n - 1/2 & \square \\
 & & & & & & v_3 \\
 \\
 p_{2n} & & & 2/3 & 1/3 & n &
 \end{array} \tag{3.17}$$

where n is a positive integer. v_1, v_2, v_3 are the replication vectors of the surface given by Eq. 3.16. For the Ni(111) surface, each layer of Ni contains a single atom and is replicated in the surface by two lattice vectors (v_1, v_2) and by v_3 in the z-direction.

$$\begin{array}{ccccccccc} \square & v_1 & \boxed{} & \boxed{} & \frac{\sqrt{-2}}{2} & 0 & 0 & \boxed{} & a i \\ \square & v_2 & = & \boxed{} & \frac{\sqrt{2}}{4} & \frac{\sqrt{6}}{4} & 0 & \boxed{} & a j \\ & v_3 & & & \boxed{} & 0 & 0 & \sqrt{-3} & a k \end{array} \quad (3.18)$$

where a is the lattice parameter of Ni, i, j, k are the orthogonal unit vectors in the space. The position of each atom of Ni is given by Eq. 3.19:

$$\begin{array}{cccccc} & \square & \square & \square & 0 & 0 & 0 \\ & p_1 & & & & & \end{array}$$

$$\begin{array}{ccccccccc}
 & p_2 & & \square & 1/3 & 2/3 & 1/3 & & \\
 & p_3 & & \square & 2/3 & 1/3 & 2/3 & & \\
 & & & & & & & v_1 & \square \\
 & & & & & & & & \\
 & & & & & & & & \\
 & & & & & & & & \\
 & \cdots & & \square & \cdots & \cdots & \cdots & & \\
 & & & \square & & & & v_2 & \square \\
 & & & \square & & & & & v_3 \\
 & p_{3n-2} & & \square & 0 & 0 & n-1 & & \\
 & & & \square & & & & & \\
 & & & \square & 1/3 & 2/3 & n-2/3 & & \\
 & p_{3n-1} & & \square & & & & & \\
 & & & \square & 2/3 & 1/3 & n-1/3 & & \\
 & p_{3n} & & & & & & &
 \end{array} \tag{3.19}$$

where n is a positive integer. v_1, v_2, v_3 are the replication vectors of the surface given by Eq. 3.18.

To ensure the accuracy of all the calculated energies within an error of 1 meV per atom, all the calculations bulk and surfaces have been performed in the same conditions of cutoff energy (650 eV for Co, 600 eV for Ni) and of k-points grid ($21 \times 21 \times 21$ for the Co primitive cell, $19 \times 19 \times 19$ for the Ni primitive cell). The smearing parameter σ was fixed at 0.01 eV. The energy difference between the 2 last electronic iteration is below 1×10^{-6} eV and the ions are relaxed until forces are less than 0.01 [eV/Å]. Tests of convergence were performed with the PBE functionals, except when specified.

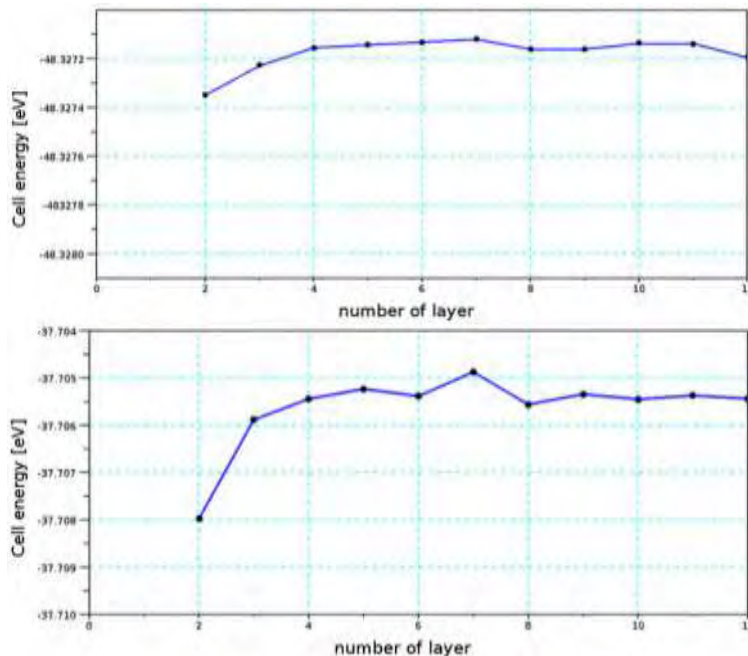


Figure 3.8: Total energy of 7 Co layers (top) and 7 Ni layers (bottom) as a function of the number of vacuum layers, calculated with the PBE functional.

First, we wish to optimize the vacuum distance. We set up the surface model with 7 layers of metal (Co and Ni) where 1 fixed layer in the center of the slab and 3 free layers on each side. The number of vacuum layers has then been increased from 1 to 12 to test the convergence of the total energy of the system. The total energies as a function of vacuum size are shown in Figure 3.8 for Co and Ni.

It is clearly shown that from 3 vacuum layers of Co (about 6 Å between top layers and the bottom layer of next images), the fluctuations of the total energy are smaller than 0.2 meV. For Ni, the cell energy is converged, since the fluctuations are less than 0.2 meV, when the number of vacuum layers is greater than 8 (about 16 Å). For an error of approx 1 meV per atom on the total energy, 3 vacuum layers for Co and 3 vacuum layers for Ni would be sufficient. Once the size of the vacuum needed for the surface calculations has been optimized, it is necessary to evaluate the convergence of the surface properties with the number of layers included in the slab. The simulation cell in the z-direction was fixed at 30 layers for Co and Ni in order to ensure that the vacuum distance is at least of 8 layers. Figure 3.9 shows the surface energies of Co and Ni, computed as in Eq. 3.10, as a function of the number of atomic layers in the slabs. The surface energies of Co and Ni fluctuate with the number of layers. The fluctuations limit of 0.5 meV/Å² can be obtained from 15 layers of Co and Ni. However, for maximum fluctuations of ≈ 1 meV/Å², 6 layers for Co and 7 for Ni could be used.

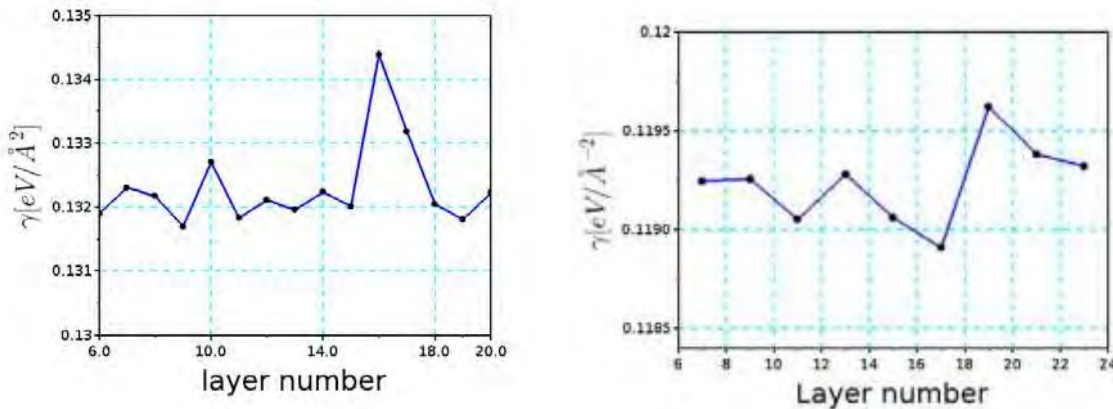


Figure 3.9: Surface energy of Co(0001) (left) and Ni(111) (right) as a function of the number of layers calculated with the PBE functional.

3.4.3 Surface properties of Co(0001) and Ni(111) with vdW dispersion

Comparing properties of surface such as surface energy, interlayer distances, surface work-function and the magnetization are the best way to see the efficient of the vdW dispersion on surface calculation. For this comparison, we chose the parameters that ensure the best convergence, as defined in the previous section (8 layers of vacuum and 15 layers of metal). The surface energies of Co(0001) and Ni(111) computed this way for the three different methods, PBE, DFTD and Opt86B, are shown in Table 3.4. For both Co (0001) and Ni(111), the functional opt86B gives the closest value to experimental surface energy (0.94% for Co and 5.02 % for Ni). While PBE underestimated surface energy +16.74 % for Co, -21.63% for Ni. DFTD overestimated the surface energy 17.4% for Co and +13.14% for Ni. Taking into account dispersion forces decreases the lattice parameter, therefore the surface area also decreased, the cohesive energy (in absolute value) are increased. Thus, surface energy observed in dispersion corrected DFT greater than PBE can be explained by bulk properties. In the middle of the

	PBE	Opt86B	DFTD	Experimental [22]
$\gamma(\text{Co}(0001))$ [eV/Å ²]	0.132	0.160	0.186	0.159
$\gamma(\text{Ni}(111))$ [eV/Å ²]	0.119	0.146	0.173	0.153

Table 3.4: surface energy of Co (0001) and Ni(111) calculated by different functionals.

slabs, the interlayer distance should converge to its value in the bulk. In Figs. 3.10, the deviation of the interlayer distances Δd_{ij} as defined in Eq. 3.14 are presented for the two systems and for the three functionals. One can notice that the interlayer distances converge to their bulk values for Ni(111) whatever the calculation method used. For Co(0001), the interlayer distances converge to the bulk value in the middle of the slab with an uncertainty of less than $\pm 1\%$. It is interesting to notice that the surface relaxations, measured by the Δd_{12} and Δd_{23} deviations of the interlayer distances, can be very different from one method to the other for a given metal. These surface relaxations are reported in Tab. 3.5. Some experimental studies in the literature have shown that for most of the fcc metals, the surface relaxation is inward, i.e. the distance between the two topmost atomic layers decreases when compared to this distance in the bulk. Since experimental values are difficult to obtain with a reasonable uncertainty, the prediction of this opposite behavior could be considered to evaluate the performance of the dispersion corrected approaches. The Ni(111) surface shows experimentally an inward relaxation, which

is reproduced by the three methods. However, the optB86b value (-1.31%) agrees better with the $-1.2\% \pm 1.2\%$ estimated by Lahtinen et al [85]. For the Co(0001) surface, all methods reproduce the inward relaxation. For the two metals, the agreement with experiment is difficult to evaluate because of the dispersion of the experimental values. Globally, we note that for the Δd_{12} variation, the PBE and optB86b functional show the same trends whereas DFT-D2 has a different behavior.

surfaces	Deviation	PBE	DFTD	opt86B	experimental
Co(0001)	Δd_{12}	-3.24	-1.18	-2.81	-2.1 ± 1.3 [85]
	Δd_{23}	+1.41	+2.02	+2.30	+1.3 [85]
Ni (111)	Δd_{12}	-0.82	-0.11	-1.31	$+1.2 \pm 1.2$ [85]
	Δd_{23}	+0.14	-0.05	-0.35	?

Table 3.5: Calculated and experimental deviation of the interlayer distances Δd_{12} , Δd_{23} , and Δd_{34} , from the corresponding bulk values (in %).

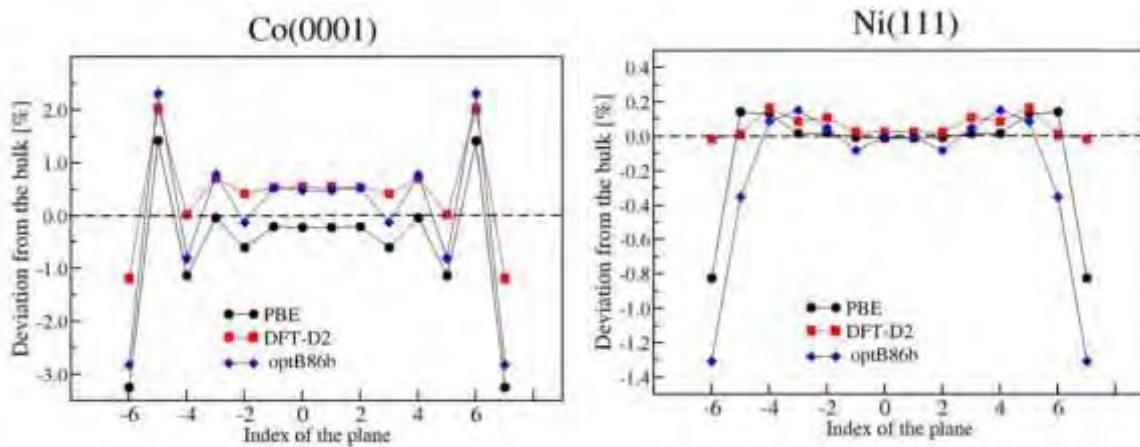


Figure 3.10: Deviation of the calculated interlayer distances from the interlayer distance in the bulk (in %).

For Co(0001) and Ni(111), the magnetic moment of atoms belonging to the different layers shows a similar variation for the three methods (Fig. 3.11). The green line are experimental values of the magnetic moment in the bulk. We can see that the two dispersion methods give good results for Ni(111) (less than 2 % error) while PBE overestimates the magnetic moment of around 8.2%. On the contrary, all the three methods give bad values for bulk Co: They all underestimate the value of the Co magnetic moment by 5.8% for PBE, 6.7% for opt86B and 8.7 % for DFTD. Similarly to what was observed in the bulk, the decrease of the lattice parameter when the dispersive forces are included induces a decrease of the atomic magnetic moment in the middle of the slabs. At the surface, due to the lack of neighboring atoms, the magnetic moment of the surface atoms is exalted. This exaltation is obtained with the three functionals and the differences between the obtained values are simply due to the change in bulk atomic moments. As different vdW corrections significantly modify the bulk properties and the surface energies, we expect to find noticeable differences for the work function from one method to the other. For the two investigated metallic surfaces, figures 3.12 and 3.13 show the variation of the electrostatic potential in the direction perpendicular to the surface, for the three methods. The work functions are computed by subtracting the Fermi energy (green line) to the value of the potential in vacuum (the plateau). The obtained work functions are presented in Table 3.6. The general variation trend here is PBE < DFTD < optB86b. The PBE and DFT-D2

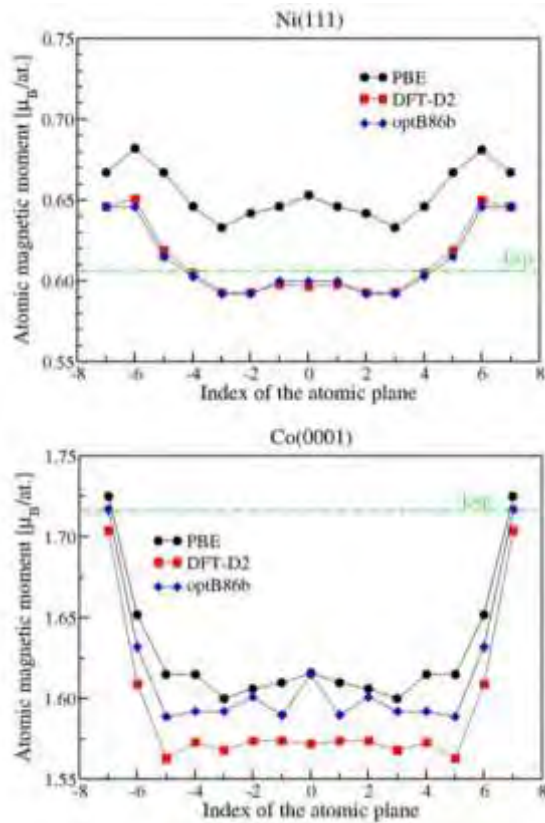


Figure 3.11: Atomic magnetic moments in each layer for Ni (111) (upper graph) and Co(0001) (lower graph) computed with the three different methods.

methods give similar results and the best agreement with experiment for the Co(0001) surface whereas the optB86b functional describes better the Ni(111) surface. Tkatchenko *et al.* also noticed an increase of the work function for the (111) surface of Cu, Rh and Au when applying the self-consistent PBE+vdW correction [86]. This variation is indeed linked to the change in the surface electronic density description.

surfaces	PBE	DFTD	opt86B	exp
Co(0001)	4.91	4.91	5.17	5.0 [22]
Ni (111)	5.09	5.11	5.27	5.35 [22]

Table 3.6: Calculated and experimental work functions Φ in eV.

Figure 3.12: Average electrostatic potential in the z-direction for the Co(0001) calculated by different functionals. From top to bottom: PBE, DFTD, opt86B.

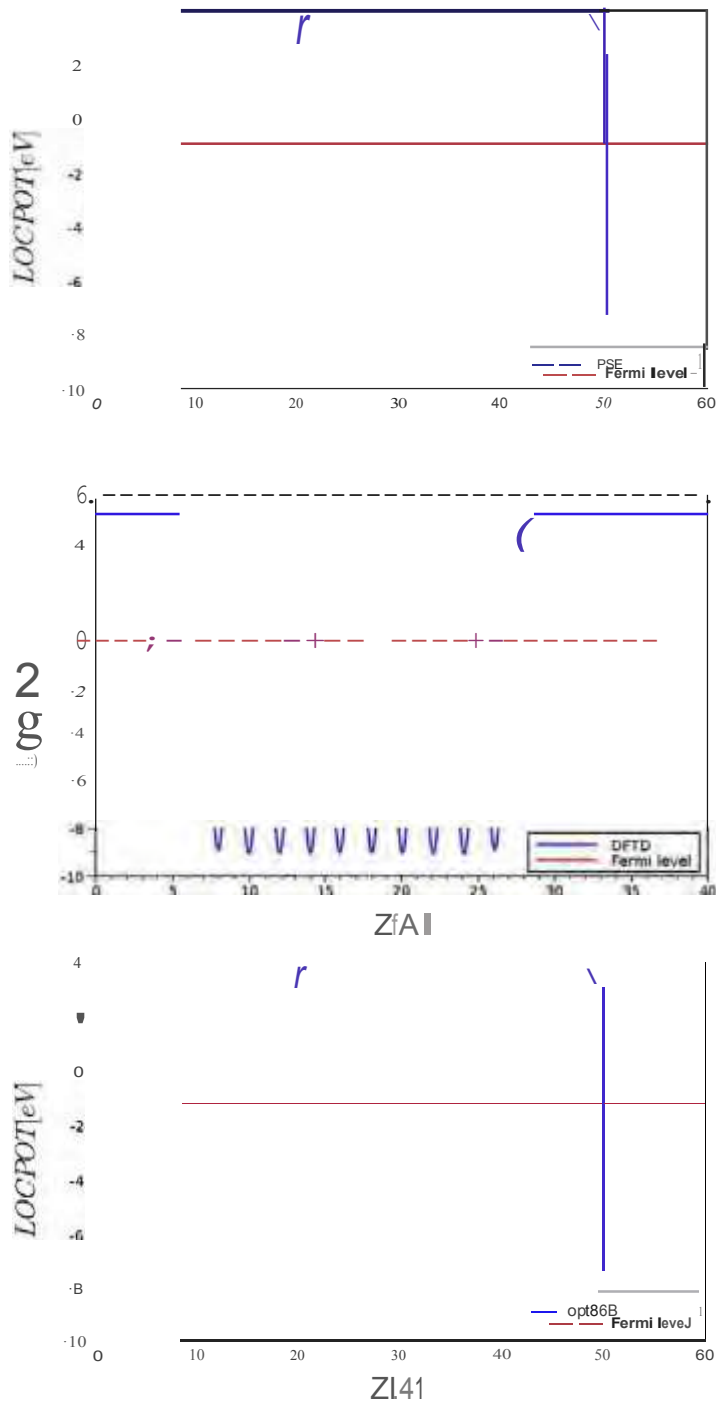


Figure 3.13: Average electrostatic potential in the z-direction for the Ni(III) calculated by different functionals. From top to bottom: PBE,DFTD,opt86B.

3.4.4 Summary

To conclude, we observed a systematic decrease of the lattice parameter compared to the PBE value which is directly related to the inclusion of the attractive dispersion forces in the metal. For the same reasons, the cohesive energy is systematically increased in absolute value and the magnetic moment is decreased when vdW corrected functionals are used, with respect to PBE. However, for the bulk moduli which is linked to the elastic properties of the materials, no general trend could be found. A variation trend was underlined for the surface energy: $PBE < opt86b < DFTD$, which can be attributed to the changes in the bulk properties. Concerning the work function, the ordering is different and the trend is: $PBE < DFTD < opt86b$. For surface relaxations, the DFTD correction tends to increase the distance between the two topmost layers compared to the very similar behavior found with PBE and the optB86b functionals. A proper description of molecule/surface systems implies to take into account London dispersion forces which is not done in standard GGA–DFT calculations. The state-of-the-art vdW corrected functionals are now routinely used to overcome this failure of DFT. Care should be taken regarding the effects induced by these forces on the metal properties. In this work, we have observed that the use of vdW corrected functionals strongly affects the bulk and surface properties of the investigated metals. In order to avoid this effect, for semi-empirical corrections based on pairwise additive interactions, one could introduce the corrections between the atoms of the molecule and of the surface only [12]. This strategy can not be used for non-local vdW corrected functionals. In the present work, we have decided to use the strategy of [12], i.e. not to introduce any dispersion corrections in the metal slab, rather to add dispersion interactions between the atoms of the adsorbed molecules and the atoms of the metal surface only. Details on this method and on the parameters used will be presented in chapter 5: adsorption of ligands on metallic surfaces.

3.5 Surface energies of Co and Ni

After having determined and compared the effect of vdW dispersions on the surfaces properties for Co(0001) and Ni(111), we decided to calculate the properties of all studied surfaces with the PBE functional only. The results are presented in the following paragraphs.

3.5.1 Co surfaces

7 surfaces of Co have been investigated: (0001), (1-100), (10-10), (01-11), (2110), (1-102) and (0-112). The replication vectors of these surfaces and the atomics position in the layer are shown in Annexe A. The surface energy of all the surfaces have been computed with a number of layers from 6 to 20. The results are presented in Fig. 3.14 (for the (0001) surface, see Fig.3.9). The fluctuations of the surface energy is less than $0.5 \text{ meV}/\text{\AA}^2$ from 12-13 layers in the slabs. The converged surface energies are presented in Tab. 3.7. From these values, we can conclude that, in vacuum and at 0K, the most stable surface is (0001), followed by (10-10) and (01-11). These surface energies allows us to predict the equilibrium morphology of clean Co np from the Wulff relation:

$$\frac{\gamma_{hkl}}{L_{hkl}} = \text{const} \quad (3.20)$$

where L_{hkl} is the distance from the surface to the center of the NP. Figure 3.15 shows the Wulff reconstruction form of a clean Co NP obtained from the computed surface energies. The dominating surfaces are (0001),(10-10) and (01-11).

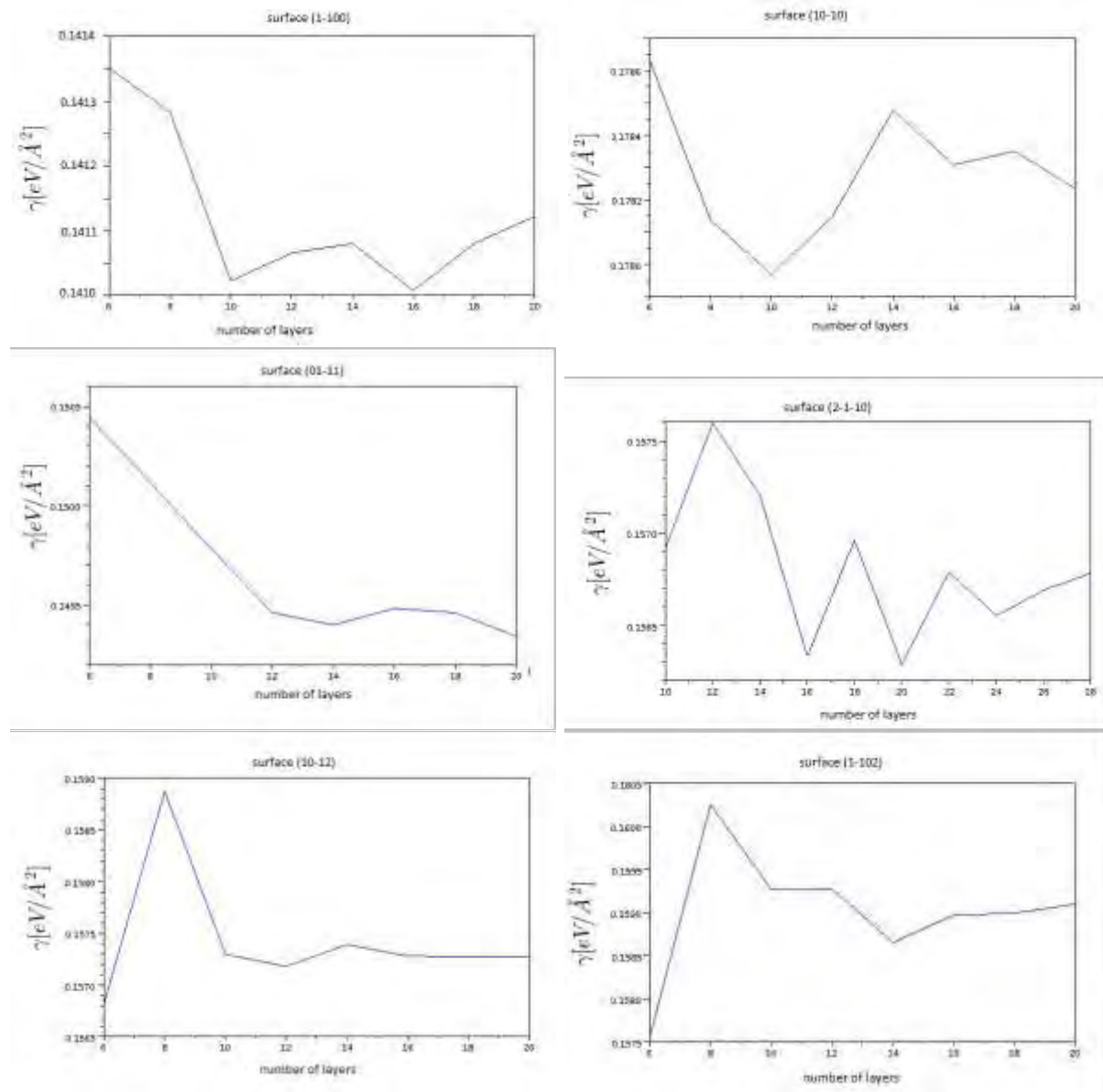


Figure 3.14: Surface energies of Co surfaces (1-100), (10-10), (0-111), (2-1-10), (10-12) and (1-102) as a function of the number of layers in the slab, computed with the PBE functional.

3.5.2 Ni surfaces

For Ni, only two surfaces were studied: the (111) and (100) crystallographic orientations. The replication vectors and atomic positions of Ni(111) were shown in Eqs. 3.19 and 3.18 respectively. For the (100), the replication vectors are given by Eq. 3.21:

$$\begin{array}{ccccccccc}
 \square & v_1 & \square & \square & 0.5 & 0.5 & 0 & \square & a_i \\
 \square & v_2 & \square & = \square & -0.5 & 0.5 & 0 & \square & a_j \\
 v_3 & & & & 0 & 0 & 1 & & a_k
 \end{array} \quad (3.21)$$

Surface	γ [eV/ \AA^2]	γ [J/m^2]	DFT [J/m^2] [21]	exp [J/m^2] [22]
(0001)	0.132	2.115	2.11	2.55
(10-10)	0.140	2.243	2.25	
(1-100)	0.173	2.783		
(01-11)	0.149	2.397	2.40	
(1-102)	0.157	2.526		
(10-12)	0.158	2.542	2.54	
(2-1-10)	0.156	2.510	2.46	

Table 3.7: Surface energies of all the investigated Co surfaces computed with the PBE functional, in eV/ \AA^2 and in J/m^2 .

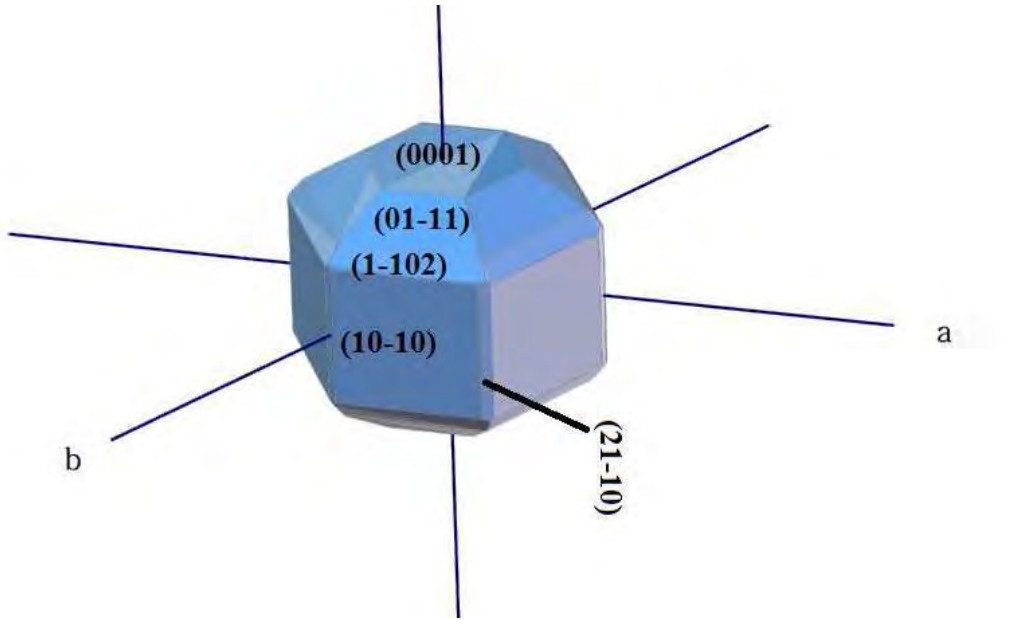


Figure 3.15: Equilibrium form of a Co NP using the Wulff reconstruction model.

where a is the lattice parameter of Ni and i, j, k are the orthogonal unit vectors in the space. The atomic positions for this surface are given by Eq. 3.22:

$$\begin{array}{ccccccc}
 & p_1 & & 0 & 0 & 0 & \\
 & p_2 & & 0 & 0.5 & 1/2 & v_1 \\
 & \dots & = & \dots & \dots & \dots & v_2 \\
 & p_{2,i-1} & & 0 & 0 & n-1 & v_3 \\
 & p_{2n} & & 0 & 0 & n-1/2 &
 \end{array} \quad (3.22)$$

The Ni(100) surface energy as a function of the number of layers inside the slab is shown in the upper graph of Fig. 3.16. Even for 18 layers, the surface energy does not seem to be fully converged, however fluctuations are less than 0.5 meV/ \AA^2 from ≈ 10 layers. In order to check that the calculations are well converged for this slab with 10 to 12 layers, we examined the interlayer distance in the center of the slab (next to the fixed layers). The evolution of the deviation of the interlayer distance with respect to the bulk one is presented as a function of the number of layers, in the lower graph of Fig. 3.16. One can see that the interlayer distance in the slab center is fully converged from 9 layers, thus validating our calculation. The surface energies for these two surfaces are presented in the Tab. 3.8. The (100) surface is less stable than the (111) surface, in vacuum and at 0K. the Wulff reconstruction from these 2 surfaces are presented in figure 3.17.

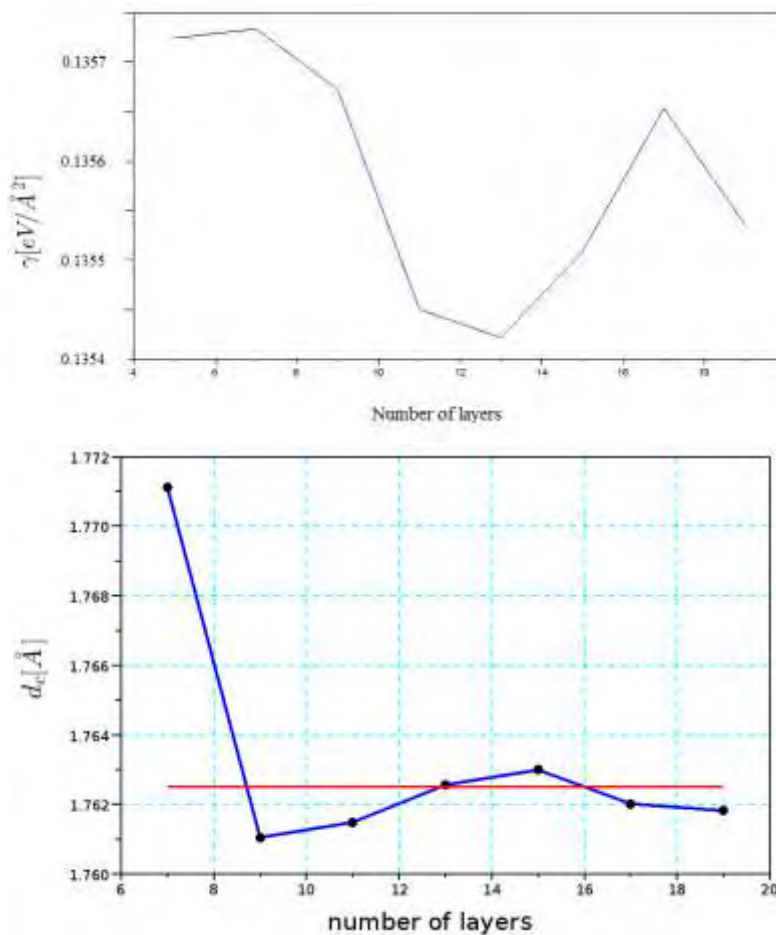


Figure 3.16: Surface energy (left) and center interlayer distances deviation (right) for Ni(100) as a function of the layer number in the slab, computed with the PBE functional. the red line in the lower graph present the bulk distance.

3.6 The attachment energy model

The "attachment energy" is the energy needed to add one atomic layer of metal on the same metal surface. The attachment energy per atom for a given (hkl) surface can be calculated as :

$$E_{hkl}^{\text{att}} = \frac{E_{n+1}^{\text{slab}} - E_n^{\text{slab}} - E^{\text{monolayer}}}{N} \quad (3.23)$$

where E_{n+1}^{slab} and E_n^{slab} are respectively the energy of a (hkl) slab with $n + 1$ and n layers.

$E^{\text{monolayer}}$ is the energy of one layer and N is the number of atoms per layer. The attachment energy model states that the time needed to add a new atomic layer is inversely proportional to E_{hkl}^{att} [87] and thus proportional to the growth rate of this surface:

$$R_{hkl} = \alpha E_{hkl}^{\text{att}} \quad (3.24)$$

where α is a constant. For the case of Co, in certain directions such as the [0001] and the [2-1-10], the interlayer distance is always the same. The growth velocity in the [hkl] direction takes the form:

$$V_{hkl} = d_{hkl} R_{hkl} = \alpha d_{hkl} E_{hkl}^{\text{att}} \quad (3.25)$$

where d_{hkl} is the interlayer distance.

However, in other directions (such as the [10-10] and the [1-100] ones, see Fig. 3.18), there are different interlayer distances and E_{hkl}^{att} depends on the surface termination. The layers will

Surface	γ [eV/ \AA^2]	γ [J/m ²]	DFT [J/m ²][21]	exp [J/m ²] [22]
(111)	0.119	1.906	1.92	2.45
(100)	0.136	2.178	2.19	

Table 3.8: Surface energies of Ni surfaces computed with the PBE functional, in eV/ \AA^2 and in J/m².

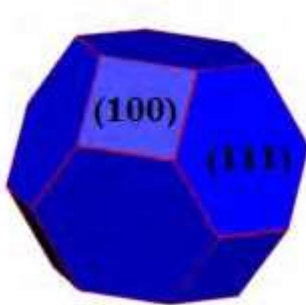


Figure 3.17: Equilibrium form of a Ni NP using the Wulff construction model.

be added one after the others with different growth rates. Therefore, one has to determine an average velocity in the $[hkI]$ direction which is calculated as :

$$V_{hkI} = \frac{\sum_i d_i}{\sum_i 1/R_i} \quad (3.26)$$

where i denotes a set of surface terminations in the same direction, d_i is the distance from the top layer of surface i to the additional layer and R_i is the growth rate (layer per time unit) of the surface i . Thus $1/R_i$ is the time needed to add one layer at the top of surface i . Replacing the growth rate R_i from Eq. 3.24, we have:

$$V_{hkI} = \frac{\sum_i d_i}{\sum_i 1/R_i} = \alpha \sum_i \frac{1}{d_i} \times \frac{1}{E_i^{\text{att}}} \quad (3.27)$$

where E_i^{att} is the corresponding attachment energy for the surface termination i . Table 3.9

presents the attachment energies of the investigated Co surfaces and the ratio between their corresponding growth velocity with respect to the slowest surface (0001). The couple (1-100) | (10-10) have the same direction but different terminations. The same is true for the couple (1-102) and (10-12). So in these cases, the replication vectors on the surface are the same, so

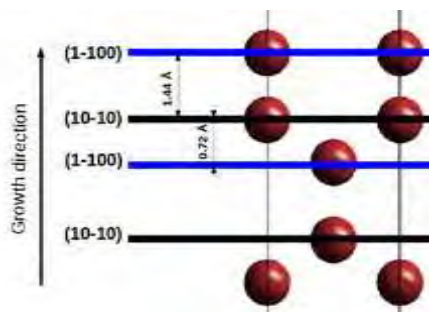


Figure 3.18: (1-100) and (10-10) surface terminations and the corresponding interlayer distances.

surface	(0001)	(1-100) (10-10)	(01-11)	(1-102) (10-12)	(2-1-10)
$E^{\text{monolayer}}$ [eV]	-5.587	-3.798	-3.803	-3.656	-2.450
E^{att} [eV]	-1.520	-3.648 -2.968	-2.174	-3.450 -3.450	-4.657
$V^{(hkl)}/V_{(0001)}$	1	1.15	1.03	1.12	1.17

Table 3.9: Attachment energies and relative growth velocities of Co surfaces in the attachment energy model. Note that the surfaces (1-100)— (10-10) have the same directions but different terminations, so only average velocities are presented for these surfaces. The same is true for (1-102) — (10-12).

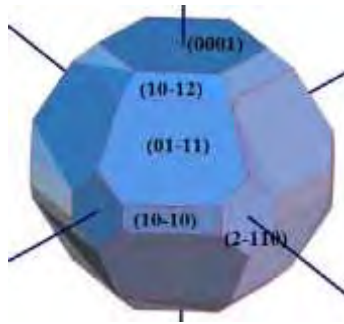


Figure 3.19: Visual form of a Co NP obtained from the attachment energy model.

the monolayers energy per atom are the same, but the attachment energy are different due to the arrangement in the z direction (see Fig. 3.18). The morphology can be predicted by the growth velocity V_{hkl} of the surfaces using the Wulff reconstruction in the kinetics framework [87]:

$$\frac{V_{hkl}}{L_{hkl}} = \text{const} \quad (3.28)$$

where L_{hkl} is the distance from the (hkl) surface to the center of the Wulff polyhedron. The reconstruction form of a Co NP from the attachment model is shown in Fig.3.19. All the surfaces having a non-negligible contribution but the dominating surface is the (01-11) one.

3.7 Conclusion

In this chapter, I have presented the results of for pure Co and Ni regarding their bulk and surface properties. This is the first step before modeling the interaction between a metallic substrate and a molecule. I also discussed the efficiency of PBE, PBE+DFTD and opt86B functionals in taking account the effect of Van der Waals interaction in these systems. In order to have an accuracy of 1 meV per atom in our calculations, the optimal parameters for the k-point grid are 19x19x19 for Ni and 21x21x21 for Co. The optimal cutoff energy for Co is 650 eV and for Ni, it is 600 eV. Values of smearing from 0.01 to 0.1 are all acceptable but convergence can be difficult with a too small value of σ , therefore in the following all the calculations are carried out firstly with a value of 0.1 eV and then recalculated with the Conservative value 0.01 eV.

In bulk calculations, the three functionals PBE, PBE+DFTD, opt86B give results in good agreement with experiments for the lattice parameters and the bulk modulus but significant discrepancies for the cohesive energies (around 20-25% for the three methods). In many aspects, PBE shows a clear advantage over the 2 other functionals (opt86B is still better than DFTD).

In surface calculations, the results of the three investigated functionals give contrasted results

depending on the studied property. For surface energies, the DFTD functional gives the best agreement with experiments for Co(0001) and Ni(111). For relaxations, even if there are no very precise experimental values, all methods give an inward relaxation of the 1st surface layer and an outward relaxation of the second layer which agrees well with experimental results. Quantitatively, the opt86B functional gives the closest results to the experimental ones. For work functions, both PBE and DFTD give about the same results, which are in better agreement with experiments than opt86B. Finally, for the surface magnetic moment, PBE seems to be the best choice for Co and opt86B is the one for Ni. Given the disparity of the results, we decided to model the metallic surfaces with the PBE functional and to add dispersion forces between the surface atoms and the molecules only.

Finally, after having defined all the parameters for the surface calculations, the surface properties of 7 crystallographic orientations for Co and 2 for Ni have been computed. The surface energies thus obtained will be used in the following to build our models for the surface/molecule interactions. In addition, the morphology of nanoparticle without ligands are presented in this chapter using the Wulff reconstruction model and the attachment energy model. The dominating surfaces for the Wulff model are the (0001),(01-11) and (10-10) ones whereas in the attachment energy model, the (01-11) surface dominates, the other surfaces having non-negligible contributions.

Chapter 4

Adsorption of ligands on metallic surfaces

Contents

4.1 Molecules	61
4.1.1 Computational details	62
4.1.2 Geometry and charges	62
4.2 Ligand adsorption on the metallic surfaces	63
4.2.1 Modelling aspects	63
4.2.2 Adsorption of CH ₃ COO ⁻ on the Co surfaces	66
4.2.3 Adsorption of C ₅ H ₁₁ COO and C ₁₁ H ₂₃ COO on the Co surfaces	71
4.2.4 Adsorption of CH ₃ COO ⁻ on the Ni surfaces	72
4.2.5 Adsorption of CH ₃ NH ₂ on the surfaces of Co and Ni	72
4.3 Conclusion	74

In this chapter, I would like to present the main DFT results of this work: The interaction between the molecules and the metallic surfaces. In this work, I investigated the topology and the mode of adsorption of several molecules on the Co and Ni metal surfaces described in the previous Chapter. The interaction of these molecules with different surfaces and the dependency of the energetical properties of these ligands with the coverage will be the key to understand the effect of the ligands on the NP morphology. I begin by presenting the DFT calculations on isolated molecules, which will be necessary to compute the adsorption energies. Then the construction of the simulation cell is described and the formulation of the physical quantities which will be extracted from these calculations are given. This is followed by a presentation of the adsorption analysis of the molecules case by case. Finally, these data will be used in our prediction model of the NP the morphology.

4.1 Molecules

In recent experiments, it has been shown that the morphology control of Co NP could be obtained by using ligands of the R-NH₂ type or carboxylate ions such as C₁₁H₂₃COO⁻ [5]. For modeling these ligands by DFT calculation, we need to add one electron to a specific location of a molecule which is not possible in plan wave basis. So, we chose to modelize the radical form of these molecules rather than its ionic form. Therefore we have decided to investigate the adsorption of simple ligands CH₃COO⁻ and CH₃NH₂ on the metallic surfaces

and then to generalize to longer hydrocarbon chains. In this work, we have thus optimized the structural properties of CH_3COO^- , $\text{C}_5\text{H}_{11}\text{COO}^-$, $\text{C}_{11}\text{H}_{23}\text{COO}^-$ and CH_3NH_2 . We did not compute the adsorption of R-NH_2 with longer length because the first results showed that the adsorption energies of CH_3COOH and CH_3NH_2 were much smaller than the one of CH_3COO^- . The discussion of this choice will be detailed in the following section. In this section, I present only the optimized geometry of these ligands and the energy of these ligands in a large simulation cell which is necessary to model an isolated molecule with periodic boundary conditions.

4.1.1 Computational details

These calculations are intended to give access to the optimized molecular structures and to their energy in vacuum, which will be used afterwards to compute adsorption properties. The modelling cell includes only the molecule in a large box. For all calculations, we used a k-point grid in reciprocal space containing only the Γ point. To be consistent with the molecule/surface calculations, we decided to use the DFT-D2 method for the vdW dispersion [13]. The cut-off energy and the size of the box have been optimized to reach convergence of the total energy of the system.

Figure 4.1 left shows the dependency of the total energy of the CH_3COO molecule as a function of the size of the simulation cell. For an error less than 1 meV per atom (i.e. an error of ≈ 7 meV on the total energy), the box size must be large than 12 Å. For the simulation cell used when the molecule is adsorbed on a surface, the vacuum distance between the molecule and the periodic image of the slab will be kept around this value. Figure 4.1 right shows the

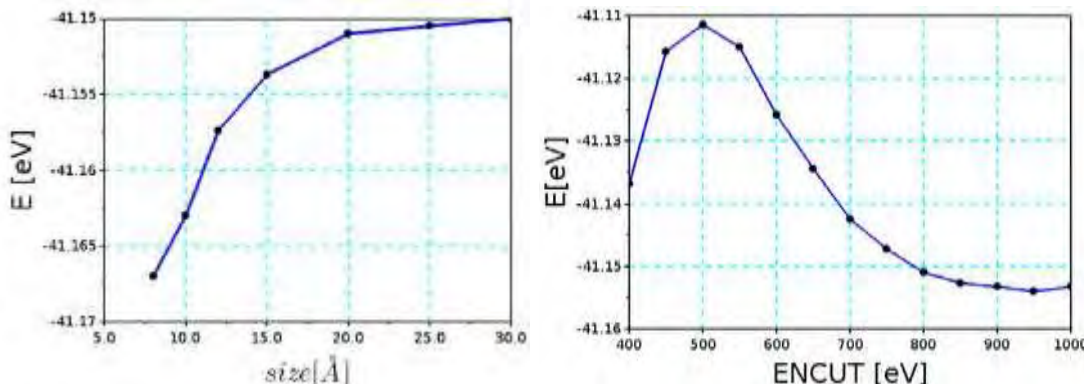


Figure 4.1: **Left:** Total energy of the CH_3COO^- molecule as a function of the size of the simulation cell. **Right:** Total energy of the CH_3COO^- molecule as a function of the cut-off energy.

dependency of the total energy of the CH_3COO^- molecule as a function of the cut-off energy. We can see that the total energy is converged from a cut-off energy of about 800 eV. For all the calculations from here, the cut-off energy will be kept at 800 eV.

4.1.2 Geometry and charges

The relaxed geometries of all ligands investigated in our work, CH_3COO^- , $\text{C}_5\text{H}_{11}\text{COO}^-$, $\text{C}_{11}\text{H}_{23}\text{COO}^-$ and CH_3NH_2 , are shown in Figure 4.2. The energy of these molecules are shown in Table 4.1. These energies are the total energies without subtracting the energy of isolated atoms. The main geometrical characteristics in terms of bond lengths are also given. Overall, the agreement with the experimental data is very good with an error below 1 %.

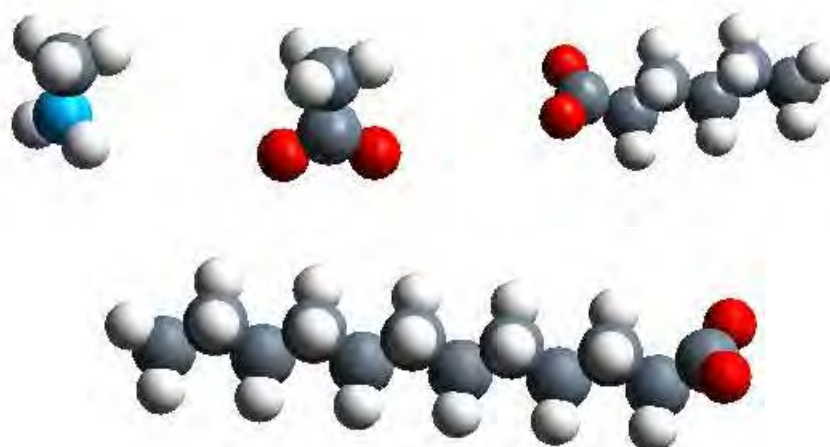


Figure 4.2: Relaxed geometry of the investigated molecules. **Top** from left to right: CH_3NH_2 , CH_3COO , $\text{C}_5\text{H}_{11}\text{COO}$. **Bottom** $\text{C}_{11}\text{H}_{23}\text{COO}$. H: white; C: grey; O: red; N: blue.

Molecules	CH_3COO	$\text{C}_5\text{H}_{11}\text{COO}$	$\text{C}_{11}\text{H}_{23}\text{COO}$	CH_3NH_2	Exp [88]
Energy [eV]	-41.156	-107.589	-206.417	-35.500	-
C-C bond [\AA]	1.52	1.53	1.53		1.53
C-O bond [\AA]	1.23	1.23	1.23		1.23
C-N bond [\AA]				1.47	1.47

Table 4.1: Energy of the computed molecules in vacuum and covalent bond lengths. The experimental values are taken from the corresponding average bond length. C-C distance was the value of $\text{CH}_2\text{-CH}_2$ bond for $\text{C}_5\text{H}_{11}\text{COO}$ and $\text{C}_{11}\text{H}_{23}\text{COO}$.

4.2 Ligand adsorption on the metallic surfaces

In this section, we first describe the simulation details that were used to compute the adsorption of the ligand molecules on the investigated metallic surfaces, then we show the results in terms of (i) adsorption geometries and (ii) adsorption energies.

4.2.1 Modelling aspects

4.2.1.1 Interface construction

For calculations with the ligand molecules, the size of the slabs in the direction perpendicular to the surface were reduced to 4 layers in order to reduce the computational cost, and the 2 bottom layers were then fixed at the bulk positions. Supercells, made of multiples of the unit cell in the x and y directions, were then constructed in order to describe the different studied coverages and the number of k-points was decreased accordingly.

Four ligands have been studied on the cobalt surfaces: CH_3NH_2 , CH_3COO , $\text{C}_5\text{H}_{11}\text{COO}$ and $\text{C}_{11}\text{H}_{23}\text{COO}$. The corresponding cell sizes in the z-direction have been taken equal to 20.25 Å, 20.25 Å, 30 Å and 43 Å, respectively, in order to avoid interactions between the molecules and the periodic image of the slab. The vacuum distances are at least 12 Å.

Figure 4.3 shows an example of interface between Co(0001) and the $\text{C}_{11}\text{H}_{23}\text{COO}$ molecule. The simulation cell contains 2 molecules in contact with the surface of 4 atomic layers.

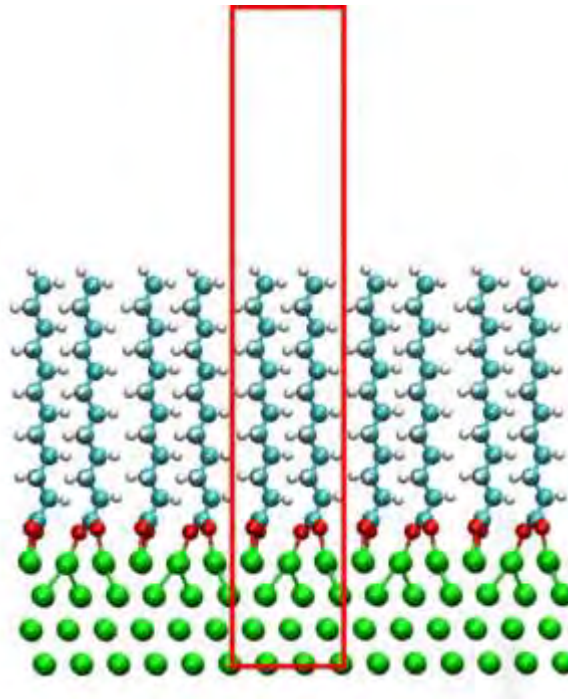


Figure 4.3: Red rectangle: simulation cell of the interface between Co(0001) and the $\text{C}_{11}\text{H}_{23}\text{COO}^-$.

4.2.1.2 Adsorption quantities

The surface coverage θ of the ligands on the surface is defined as :

$$\theta = \frac{n_L}{A} \quad (4.1)$$

where n_L is the number of ligands in the simulation cell and A is the surface area of the simulation cell. Using this definition, the coverage is in units of \AA^{-2} . The ligand adsorption energy per molecule is given by:

$$E^{\text{ads}} = \frac{1}{n_L} (E_{\text{tot}}^{\text{slab-ligand}} - E^{\text{relaxed-slab}} - n_L E^{\text{ligand-vac}}) \quad (4.2)$$

where $E_{\text{tot}}^{\text{slab-ligand}}$ is the total energy of the simulation cell of the metal-molecule interface, $E^{\text{relaxed-slab}}$ is the energy of the relaxed metallic slab without molecules and $E^{\text{ligand-vac}}$ is the energy of the molecule in the vacuum.

The net charge transfer between the surfaces and the molecule upon adsorption is defined as:

$$\delta Q_m = Q_m^{\text{ads}} - Q_m^{\text{vac}} \quad (4.3)$$

where Q_m^{ads} is the net charge of all atoms in the molecule in its adsorption state and Q_m^{vac} is the net charge of all atoms in the molecule in vacuum.

4.2.1.3 Coverage

As presented in Eq.4.1, the ligand surface coverage depends on the number of ligands in the simulation cell and on the surface area of the simulation cell. Due to the use of periodic boundary conditions, only some limited value of θ can be computed since n_L is an integer and A must be a multiple of the surface unit cell in the x and y directions. Moreover, due to the size of the ligands, it is not possible to go beyond a maximum value of θ on a given (hkl) facet.

It is therefore impossible to have continuous values of θ and only a selected number of θ is accessible.

In the case of Co, the maximum surface coverage for the (0001), (10-10) and (01-11) surfaces are respectively: 0.093 \AA^{-2} , 0.099 \AA^{-2} and 0.087 \AA^{-2} which correspond to 2 molecules per unit cell for the Co(0001) surface and 4 molecules per unit cell for the 2 other surfaces.

4.2.1.4 Adsorption sites

The adsorption site of the molecule depends on the topology of the surface and on the molecule of interest. Figure 4.4 shows the possible adsorption sites on the Co(0001) surface. As we will see later, the adsorption sites will depend on the type of studied molecule and can be modified in the case of a large coverage. All possible adsorption configuration have been tested but only the most favorable ones are presented in the following.

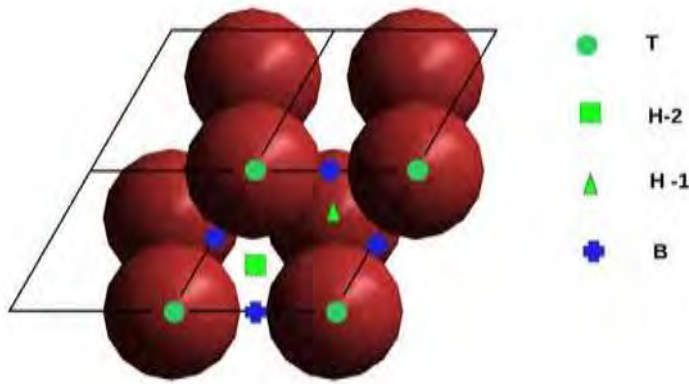


Figure 4.4: Possible adsorption sites on the Co(0001) surface: T = Top ; H = hollow; B = bridge. The 2 hollow sites H1 and H2 are not equivalent.

4.2.1.5 Van der Waals interactions

As presented in Chapter 3, the Co and Ni surfaces were computed with the PBE functional without any vdW corrections. However, the inclusion of the dispersion forces induce modifications of the bulk properties of Co that are not favorable. Interaction between surface and adsorbed molecule is important as discussed in many references in the literature. One example is the recent works of Tkatchenko et al. [23] in structure and energetics of benzene adsorbed on transition-metal surfaces. Therefore, we decided to include these dispersion forces only between the Co atoms of the surface and the atoms of the molecules, using the parameters given by Grimme [13]. The results are presented in Tab. 4.2 where the adsorption energy of the CH_3COO molecule computed with different methods is given together with the Co-O bond length. The DFT-D corresponds to the method of Grimme [13], the AAS method consists in including dispersion interactions between atoms of the molecule and between atoms of the molecule and the Co atoms of the surface, the DFT-D for CHO consists in including the dispersion interactions between atoms of the molecule only. In absence of experimental data for this specific adsorption, it is difficult to conclude. However, the AAS method gives an adsorption energy and a Co-O distance in between the PBE functional in which no dispersion interactions are included, and the DFT-D functional in which the dispersion interactions inside the Co slab deteriorates the bulk properties. This method appears therefore as a good compromise to include dispersion interactions for adsorption properties and will be used hereafter.

	DFT-D	AAS	DFT-D for CHO only	PBE
E_{ads} [eV]	-3.64	-3.36	-2.98	-2.72
Co-O distance [\AA]	2.00	1.97	1.95	1.95

Table 4.2: Adsorption energy of the CH_3COO^- molecule and Co-O distance calculated with different functionals.

4.2.2 Adsorption of CH_3COO^- on the Co surfaces

The adsorption of CH_3COO^- on the surface of Co are intensively studied due to its adsorption energy much larger (in absolute value) than the methyl amine one. That give an important impact in our models of morphology prediction. In addition, the structure of this molecule is simple enough to have a reasonable time of calculation in comparing with the other R-COO. In additional, the influence of hydrocarbon chain length on the adsorption energy will be discussed later. In this section i will present in detailed the adsorption mode adsorption geometry and the variation of adsorption energy as a function of coverage of ligands.

4.2.2.1 Adsorption modes

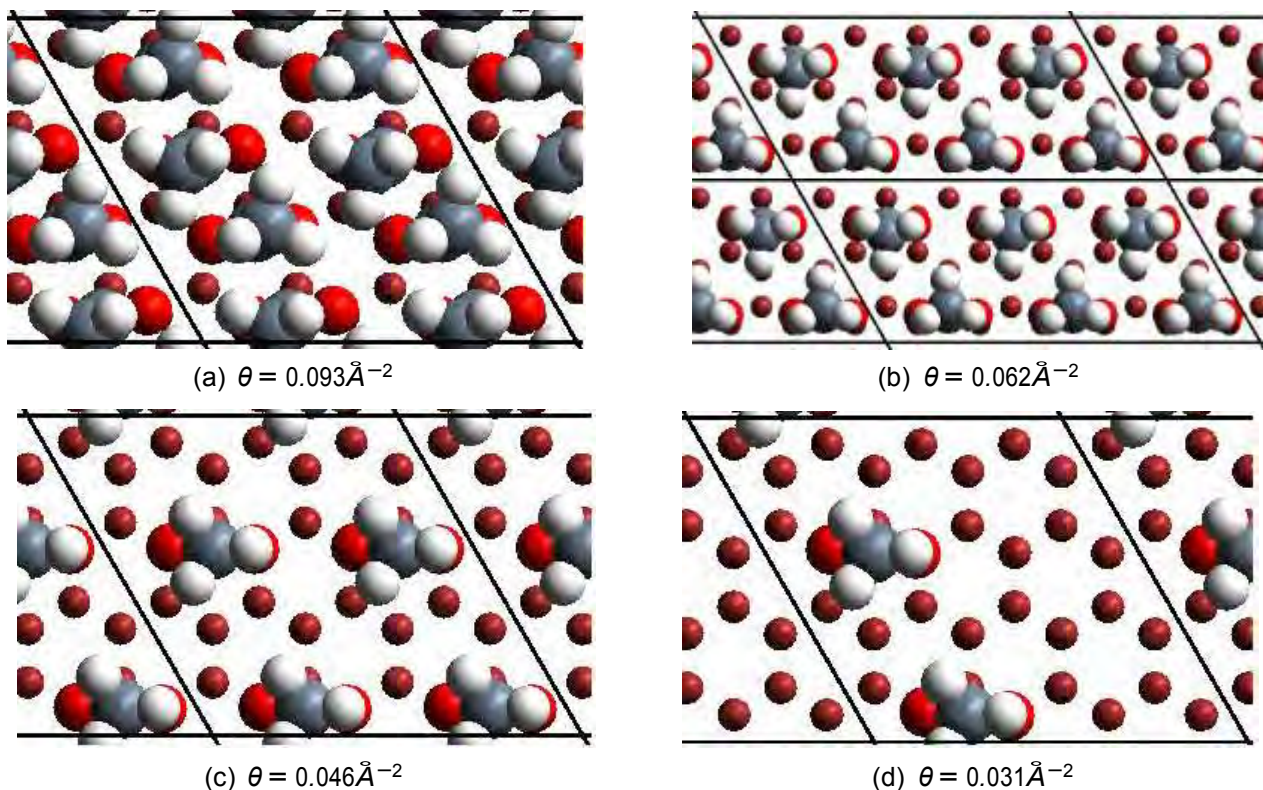


Figure 4.5: Adsorption of CH_3COO^- on Co(0001) at different coverages. The oxygen atoms are in always in the "Top" position.

(0001) surface The (0001) surface has the smallest unit cell surface with a surface area of 5.37\AA^2 , with one "Top" position per surface cell. Therefore it is necessary to use 2 surface cells for each top molecule. The adsorbed molecule has the 2 oxygen atoms in the "Top" configuration. Figure 4.5 shows the coverage of ligands on the Co(0001) surface. An example of the Bader charge analysis is shown in Table 4.3 when the coverage is $0.031 [\text{\AA}^{-2}]$. The net

charge of 0.67 e were transferred from the surfaces to the molecule upon adsorption indicates the chemisorption mode of the molecule on this surface.

Atom	Q_a^{vac} [e]	Q_a^{ads} [e]	δQ [e]
O ₁	7.42	7.76	0.33
O ₂	7.41	7.75	0.34
C ₁	1.30	1.27	-0.02
C ₂	4.01	3.95	-0.06
H ₁	0.94	0.97	0.03
H ₂	0.93	0.96	0.02
H ₃	0.93	0.95	0.02
total	22.96	23.63	0.67

Table 4.3: Bader charge analysis of the CH₃COO molecule adsorbed on Co(0001) for a surface coverage of 0.031 Å⁻² and in vacuum.

(10-10) and (01-11) surfaces The two surfaces (10-10) and (01-11) have a surface area of the unit cell respectively equal to 10.10 Å and 11.49 Å. In the unit cell, there is only one Co in the top layer. For all coverages below 1/2 i.e. $\theta = 0.049\text{Å}^{-2}$ for (10-10) and $\theta = 0.043\text{Å}^{-2}$ for (01-11), all the oxygen atoms are found in "Top" position. However, when all the Top positions are occupied, the coverage is still much lower than the one on the (0001) surface. It is possible to increase the coverage of these surfaces by considering other adsorption sites. Figure 4.6-c and d show the optimized configurations of 4 molecules on the 2x3 Co(10-10) surface. 2 molecules are adsorbed on "Top" sites of Co (0001), while the 2 other molecules are adsorbed with one O atom on the "Top" site and the other in the "Hollow" site. The adsorption energy is still equal to -3.233 [eV] for $\theta = 0.066\text{Å}^{-2}$ which is not too far from the adsorption energy on the (0001) surface for a similar coverage (-3.431 [eV] for $\theta = 0.062\text{Å}^{-2}$). The Bader charge analysis of the molecule in the configuration with 2 top sites gives similar values of charge transfer than in the case of the Co(0001) surface for a similar coverage: 0.64 e from the surface to the molecule upon adsorption. Conversely, the Bader charge analysis for the molecule with one O on the Top position and the other on the Hollow position gives a net charge transfer of only 0.49 e from the surface to the molecule upon adsorption. The details are given in Table 4.4. The major difference comes from the charge variation of atom O₁ which is the one in the "Hollow" position. Similar results are found for the Co(01-11) surface. All the adsorption energies and charge transfers are summarized in Table 4.5.

Atom	Q_a^{vac} [e]	Q_a^{ads} [e]	δQ [e]
O ₁	7.42	7.56	0.14
O ₂	7.41	7.76	0.35
C ₁	1.30	1.23	-0.07
C ₂	4.01	3.92	-0.09
H ₁	0.94	0.99	0.05
H ₂	0.93	1.00	0.07
H ₃	0.94	0.98	0.04
total	22.96	23.45	0.49

Table 4.4: Bader charge analysis of the CH₃COO molecule with one O atom in Top position and one in Hollow H1 position on Co(10-10) for a surface coverage of 0.66 Å⁻² and in vacuum.

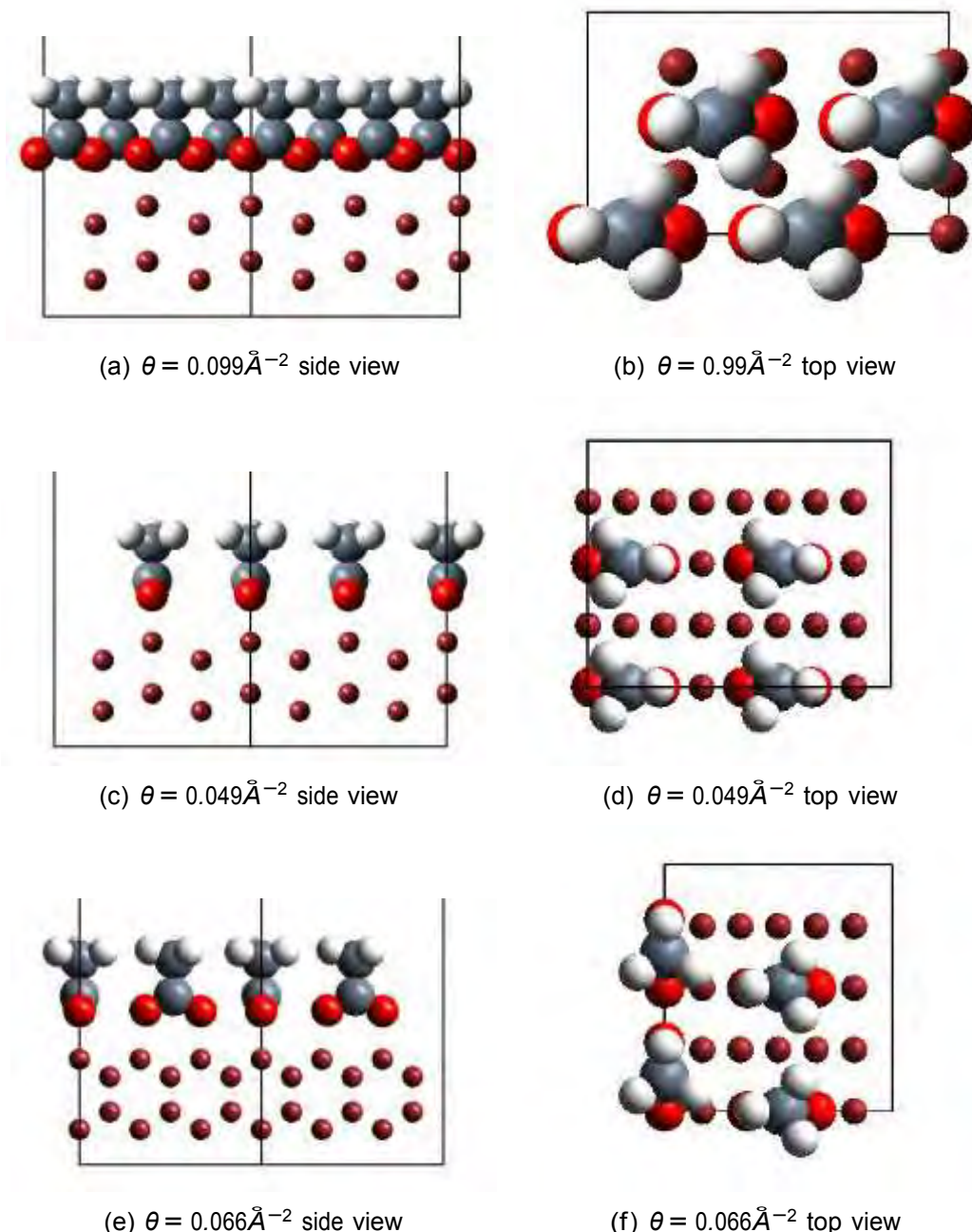


Figure 4.6: Adsorption of CH_3COO^- on $\text{Co}(10-10)$ surface at different coverages: (a& b) $\theta = 0.099 \text{\AA}^{-2}$ with one O atom in Top position and one in Hollow H1 position; (c&d) $\theta = 0.049 \text{\AA}^{-2}$ with all O atoms in Top positions. (e & f) $\theta = 0.066 \text{\AA}^{-2}$ Mix of the 2 configurations.

4.2.2.2 Adsorption energies

The adsorption energies are shown in Table 3 for the different coverages per surface unit θ with the corresponding size of the supercell, number of ligands per supercell and corresponding coverages. The adsorption energy of CH_3COO strongly varies with the coverage, the minimum

surface	supercell size	number of ligands	coverage	$\theta [^\circ]$	E^{ads} [eV]	δQ_m [e]
(0001)	4x2	4	1	0.093	-2.036	0.67
	2x3	2	2/3	0.062	-3.431	0.67
	2x2	1	1/2	0.046	-3.363	0.67
	2x3	1	1/3	0.031	-3.328	0.67
(10-10)	2x2	4	1	0.099	-1.993	0.49
	2x3	4	2/3	0.066	-3.233	0.49-0.64
	4x2	4	1/2	0.050	-3.644	0.64
	2x3	1	1/3	0.033	-3.692	0.64
	2x2	1	1/4	0.025	-3.651	0.64
(01-11)	2x2	4	1	0.087	-1.396	0.42
	2x3	4	2/3	0.058	-2.901	0.42 -0.63
	2x2	2	1/2	0.043	-3.567	0.63
	2x3	1	1/3	0.029	-3.574	0.63
	2x4	1	1/4	0.023	-3.717	0.63

Table 4.5: Adsorption energies and net charge transfer of CH_3COO on the different surfaces of Co at different coverages. The charge transfer is averaged over the ones of the different molecules in the supercell. When two values are present, they correspond to the two adsorption modes.

energy being obtained for the lowest coverage (1/4) monolayer in the case of the (01-11) surfaces. For the 2 other surfaces, the minimum energy is obtained for a coverage of 1/3 monolayer for the (10-10) surface and for a coverage of 2/3 monolayer for the (0001) one. The variation of E^{ads} as a function of θ is the key factor for the variation of interface energy and also for the kinetics aspects of the ligands adsorption on the surface. In order to build the growth models from these adsorption energies, we need to extract a continuous dependency of E^{ads} as a function of θ . Since the adsorption energy of a molecule on the surface can be calculated only for a limited number of coverage values, due to the periodical constraints of DFT calculation, it is necessary to fit E^{ads} as a function of the θ by a continuous function.

In order to choose the form of the fit function for $E^{\text{ads}} = f(\theta)$, we note that the charge transfer and the distance of Co-O bonds are very similar for almost the adsorption configurations. Therefore we assume that the variation of the adsorption energy is mainly due to the interaction between molecules when the inter-molecular distances vary with the coverage. Let us suppose that the inter-molecular interaction is mainly electrostatic and can be modelled by a Lennard-Jones potential [24]:

$$V_{LJ} \propto \frac{a_1}{r^6} - \frac{a_2}{r^{12}} \quad (4.4)$$

where r is the distance between the molecules adsorbed on the surface, a_1 and a_2 are fitting parameters. The coverage θ is inversely proportional to the square of the average distance between the molecules. Thus, in a first approximation, the following polynomial form was chosen for the fit function:

$$E^{\text{ads}} = a + b \times \theta^3 + c \times \theta^6 \quad (4.5)$$

Figure 4.7 shows the variation of E^{ads} as a function of the coverage θ per surface unit, for each studied surfaces. The adsorption energies on the basal surface (0001) can be fitted with a good

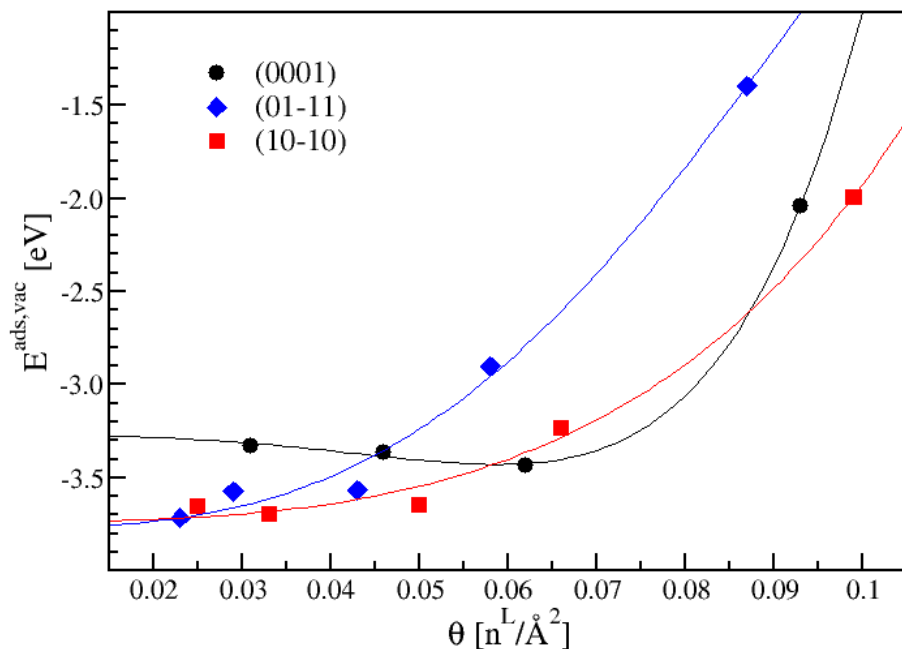


Figure 4.7: Adsorption energies of CH_3COO as a function of the coverage per surface unit, for each studied facet. The lines correspond to polynomial fits of the form $a + b \times \theta^3 + c \times \theta^6$.

accuracy with this polynomial function. For the (0001) facet, the increase in adsorption energy takes place at a higher coverage. One can even notice a small decrease of the adsorption energy of CH_3COO on this facet for intermediate values of θ which might correspond to a stabilization of the ligands on the basal surface due to long range interactions. For this facet, even for the highest coverage, the adsorption takes place on the Top sites. The polynomial fit is not as satisfactory for the 2 other surfaces. The adsorption energies on the (10-10) and (01-11) facets show a strong increase for $\theta \geq 0.05 \text{ \AA}^{-2}$. This increase comes from the fact that, for these two facets, it is not possible to maintain the adsorption of the carboxylate on the Top sites while increasing the coverage. The adsorption mode is therefore less favorable and the adsorption energy is increased. Nevertheless, we considered that the fitted functions are close enough to the calculated values to be used in the growth models (see CHAPTER 5:Prediction morphology).

Parameters of the fit for (0001):

$$E^{ads} = -3.27155 - 1549.99 \times \theta^3 + 382723 \times \theta^6$$

$$E^{ads} = -3.27155 - 1.2467 \times \frac{\theta}{\theta_{0001}^{max}} + 2.476182 \times \frac{\theta}{\theta_{0001}^{max}}$$

with $\theta_{0001}^{max} = 0.093 \text{ \AA}^{-2}$ is the maximum coverage of CH_3COO on the (0001) surface.

Parameters of the fit for (10-10):

$$E^{ads} = -3.735447 + 1478.66 \times \theta^3 + 329787 \times \theta^6$$

$$E^{ads} = -3.735447 + 1.43474 \times \frac{\theta}{\theta_{10-10}^{max}} + 0.31048 \times \frac{\theta}{\theta_{10-10}^{max}}$$

with $\theta_{10-10}^{max} = 0.099 \text{ \AA}^{-2}$ is the maximum coverage of CH_3COO on the (10-10) surface.

Parameters of the fit for (01-11):

$$E^{\text{ads}} = -3.76863 + 4390.28 \times \theta^3 - 188849 \times \theta^6$$

$$E^{\text{ads}} = -3.76863 + 2.891012 \times \frac{\theta}{\theta_{01-11}^{max}}^3 - 0.5153604 \times \frac{\theta}{\theta_{01-11}^{max}}^6$$

with $\theta_{01-11}^{max} = 0.87 \text{ \AA}^{-2}$ is the maximum coverage of CH_3COO on the (01-11) surface.

4.2.3 Adsorption of $\text{C}_5\text{H}_{11}\text{COO}$ and $\text{C}_{11}\text{H}_{23}\text{COO}$ on the Co surfaces

In order to study the effect of the hydrocarbonne length of the carboxylate molecules on the morphology of the Co NP, the same calculations have been carried out with two other chain lengths: $\text{C}_5\text{H}_{11}\text{COO}$ and $\text{C}_{11}\text{H}_{23}\text{COO}$. The same protocol has been followed than for the CH_3COO molecule: calculations of the adsorption energies on the different facets and for different coverages. However, we realized the computer time was too long for getting a sufficiently large number of coverages needed to fit the $E^{\text{ads}} = f(\theta)$ function. Therefore, we decided to compute the adsorption of these molecules only for selected configurations and to use these values only in the aim to discuss the variation of the adsorption energies as a function of the chain length. Table 4.6 presents the results obtained in the case of the $\text{C}_5\text{H}_{11}\text{COO}$ molecule. For the (0001) facet, we chose only the coverage of 2/3 monolayer at which the adsorption energy of the CH_3COO molecule reaches its smallest value. The adsorption energy of the $\text{C}_5\text{H}_{11}\text{COO}$ molecule for that coverage is 27 meV higher than that of the CH_3COO molecule. For the (10-10) surface, we limited our calculations to the case of the adsorption on the Top sites of the surface. The adsorption energy of the $\text{C}_5\text{H}_{11}\text{COO}$ molecule at coverage 1/2 is 125 meV smaller than that of the CH_3COO molecule for the same coverage. For the (01-10) surface, the value at the lower coverage of 1/4 monolayer is not too much changed (-6 meV) whereas the maximum value now turns to the one at coverage of 1/2 monolayer. In Tab. 4.7, the adsorption energies

surface	Fraction of monolayer	E^{ads} (eV)
(0001)	2/3	-3.404
(10-10)	1/2	-3.817
	1/4	-3.607
(01-11)	1/2	-3.839
	1/4	-3.711

Table 4.6: Adsorption energies of $\text{C}_5\text{H}_{11}\text{COO}$ on the different surfaces of Co at different coverages.

surface	Fraction of monolayer	E_{ads} (eV)
(0001)	2/3	-4.435
(10-10)	1/2	-4.775
(01-11)	1/2	-5.019

Table 4.7: Energy adsorption of $\text{C}_{11}\text{H}_{23}\text{COO}$ on the different surfaces of Co at different coverages.

are presented for the $\text{C}_{11}\text{H}_{23}\text{COO}$ molecule, but only for one coverage for each facet. We see

clearly that the adsorption energy is decreased of more than 1 eV for each surface comparing

to the 2 other molecules. The dependency of the adsorption energy which the chain length is therefore not easily predictable. Due to the computer time cost of these calculations, we were unfortunately not able to compute additional coverages for these molecules. However, given the difference in adsorption energies and the fact that the $C_{11}H_{23}COO$ molecules are the ones used in experiments, it would be very interesting to further investigate this system in the future.

4.2.4 Adsorption of CH_3COO on the Ni surfaces

The adsorption of ligands on the surface of Ni have also been calculated. The results of the adsorption energies are presented in Table 4.8. In this case, the strongest adsorption of the

surface	cell	n_L	$\theta [^\circ]$	E^{ads} [eV]
111	2x2	1	0.046	-3.268
111	2x2	2	0.093	-0.841
100	2x2	1	0.040	-3.428
100	2x2	2	0.080	-3.147
110	2x2	1	0.029	-3.693
110	2x2	2	0.058	-3.748

Table 4.8: Adsorption energies of CH_3COO on different surfaces of Ni at different coverages.

CH_3COO molecule is on the (110) surface, then on the (100) and then on the (111) one. As for the Co surfaces, the ligand adsorption decreases (i.e. the adsorption energy increases) when the coverage increases for the (111) and (100) facets but this is the opposite for the (110) facet. This result together with the fact that the adsorption energies on the (110) facet is much larger than on the other facets might have important implications for the NP growth. However, due to the lack of time, we did not obtain enough coverage values to be able to fit $E^{ads} = f(\theta)$ for the case of Ni surfaces. The growth models will therefore only be test for the Co NP growth in the following.

4.2.5 Adsorption of CH_3NH_2 on the surfaces of Co and Ni

Alkyl amine [26], hexadecylamine (HDA) [2] and Rhodamin(RHB)[2] have shown to be efficient to control the crystalline morphology of nanoparticles. We therefore dedicated to compute also the adsorption energy of the simplest molecule in amine group: CH_3NH_2 .

surface	cell	n_L	$\theta [^\circ]$	E^{ads} [eV]
0001	2x3	2	0.063	-1.099
10-10	2x2	1	0.025	-1.450
	2x2	2	0.049	-1.353
0111	2x4	1	0.022	-1.525
	2x2	1	0.043	-1.400

Table 4.9: Adsorption energies of CH_3NH_2 on the different surfaces of Co for different coverages.

On the Co surfaces The N atom is found to be favored to make the bonding with the surface on the Top site, while the C atom is in the Bridge position. Figure 4.8 shows the adsorption configuration of CH_3NH_2 on the (0001), (10-10) and (01-11) surfaces. The value of the corresponding adsorption energies are shown in Tab. 4.9. These energies are much smaller in absolute value than the adsorption energies of CH_3COO . The effect of the adsorption

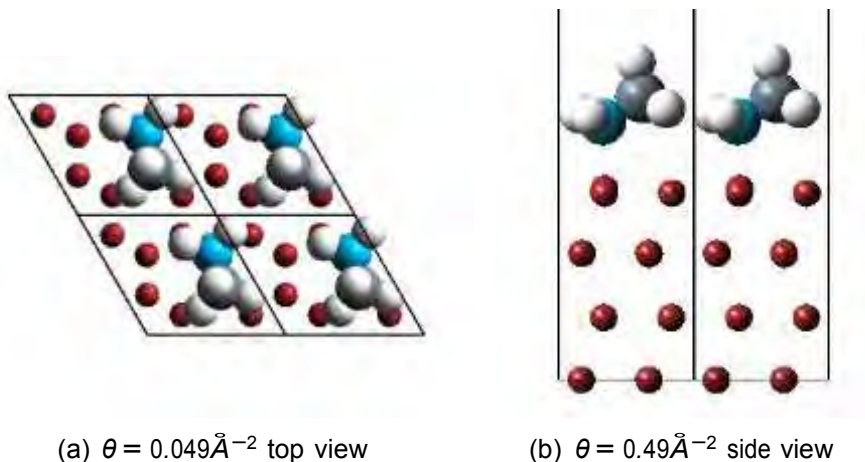


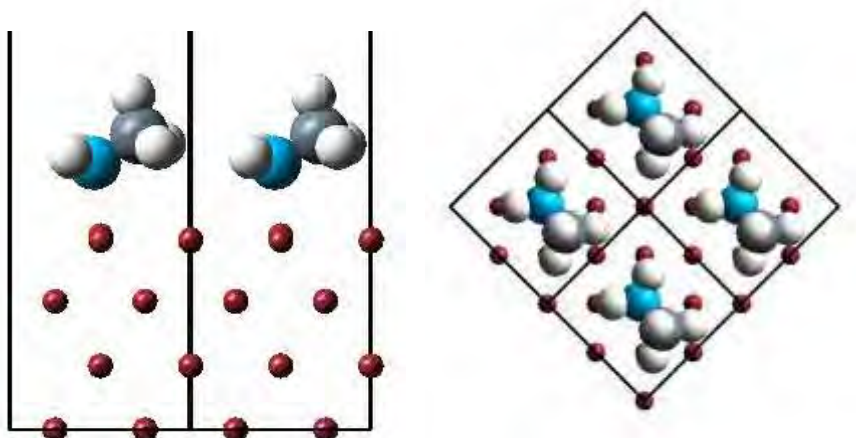
Figure 4.8: Top and side views of the adsorption of CH_3NH_2 on the $\text{Co}(0001)$ surface.

of the amine group on the surface is small compared to that of the carboxylate group at thermodynamics equilibrium. Regarding kinetics aspects, the effect of the ligands on the surface should be dominated by the adsorption of the carboxylate group due to the difference of nearly 2 eV in adsorption energies and to the fact that the mass and the size of the 2 molecules are not much different.

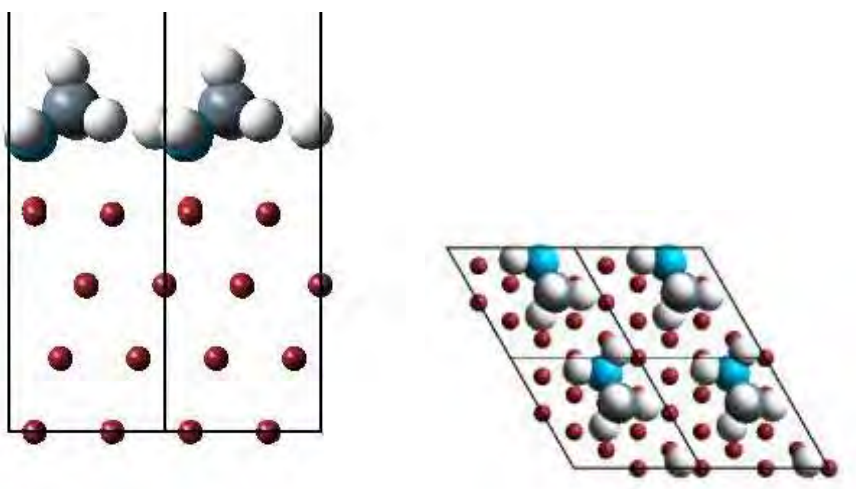
On the Ni surfaces The geometries of adsorption are shown in the figure 4.9 The adsorption energies of the CH_3NH_2 molecule on the Ni surfaces are also far smaller in absolute value than the ones of CH_3COO for the similar coverages. As for the case of Co, the domination of the effect of carboxylate group is also expected.

surface	cell	n_L	$\theta[\circ]$	$E_{\text{ads}}(\text{eV})$
111	2x2	1	0.046	-1.384
	2x4	1	0.023	-1.566
100	2x2	1	0.040	-1.499
110	2x2	1	0.028	-1.566
	2x2	2	0.057	-1.504

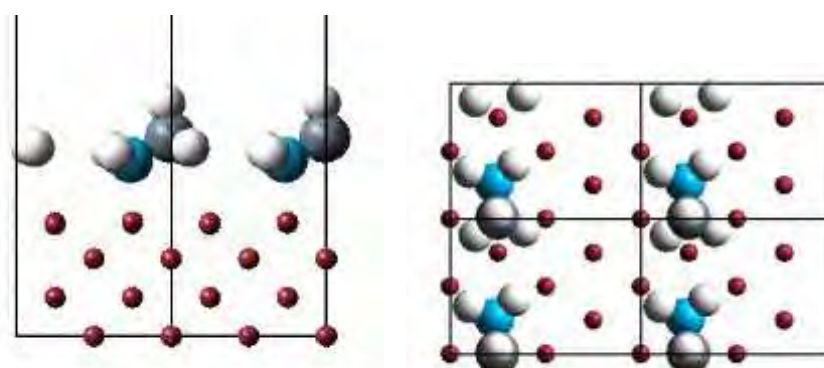
Table 4.10: Adsorption energies of CH_3NH_2 on the different surfaces of Ni for different coverages.



(a) Amine CH_3NH_3^+ on Ni (100) side (b) Amine CH_3NH_3^+ on Ni (100) top view



(c) Amine CH_3NH_3^+ on Ni (111) side (d) Amine CH_3NH_3^+ on Ni (111) top view



(e) Amine CH_3NH_3^+ on Ni (110) side (f) Amine CH_3NH_3^+ on Ni (110) top view

Figure 4.9: Top and side views of the adsorption of CH_3NH_2 on the Ni surfaces.

4.3 Conclusion

In this chapter, I have presented the results of DFT calculations for the different investigated molecules and their adsorption on some Co and Ni surfaces for selected coverages. Two types

of molecules were studied, R-COO or R-NH₂ terminated, and the results revealed that the adsorption of the R-COO terminated molecules are more favorable than the R-NH₂ ones on both metals. Among the 3 different chain lengths for the R-COO molecules, the calculations for CH₃COO were the lightest ones and allowed us to obtain a continuous variation of the adsorption energies as a function of the coverage for the three investigated surfaces. This fitted function of the adsorption energy will be key ingredient to build growth models of the nanoparticle in presence of ligands. In the following Chapter, several models will therefore be tested using the DFT results obtained for the adsorption of CH₃COO on Cobalt.

Chapter 5

Morphology prediction of Co nanoparticles in presence of ligands

Contents

5.1 Thermodynamic model	77
5.1.1 Lowest interface energy model	78
5.1.2 Adsorption isotherm model	80
5.1.3 Conclusion	82
5.2 Kinetic model	83
5.2.1 Theoretical aspects	83
5.2.2 Results	87
5.2.3 Discussion	95
5.3 Conclusion	96

In this chapter, I present the results and a detailed discussion of the different models that predict the morphologies of the grown NP. These models can be classified in two categories: thermodynamics and kinetics models, respectively based on thermodynamics or kinetic arguments. These models have been already presented in Sec. 1.2.1 of Chapter 1 and will thus not be presented again here. Below, I provide the prediction of these different models to the case of Co NPs stabilized by CH_3COO molecule where I use the results of the DFT calculations carried out on the bare Co surfaces and on the adsorption energies of the CH_3COO molecules on the different Co facets. Since the results obtained with the existing models were not satisfactory to explain the experimental results, therefore I have developed a new kinetics model which is described in the second part of this chapter. Application of this model to the case of Co NP stabilized by CH_3COO are then presented and extended to the case of molecules with different chain lengths.

5.1 Thermodynamic model

In order to predict the shape of the NPs, the thermodynamics model assumes that this shape minimizes the interface energies of the NPs. The Wulff construction relates the morphology to the interfaces energies. However, the interface energies depend on the ligands coverage. The ligands coverage can be determined either by minimization of the interface energy giving rise to the *lowest interface energy model* or by using a Langmuir type approach giving rise to a *adsorption isotherm* model.

5.1.1 Lowest interface energy model

As already seen in Eq. 1.12 of Sect.1.2.1, the interface energy as a function of the ligand surface coverage and the chemical potential of the ligand in solution reads :

$$\gamma_{hkl}^{int} = \gamma_{hkl} + \theta_{hkl} \times E_{hkl}^{\text{ads}}(\theta_{hkl}) - \theta_{hkl} \times \Delta\mu \quad (5.1)$$

where γ_{hkl} is the surface energy of the clean (without ligand) (hkl) Co surface, θ_{hkl} is the surface ligand coverage on the (hkl) surface, E_{hkl}^{ads} is the adsorption energy of one ligand on the (hkl) surface at surface coverage θ_{hkl} in vacuum, and $\Delta\mu = \mu(c, T) - \mu^{\text{vac}}$ is the chemical potential difference of the ligand in the solution at concentration c and temperature T and in vacuum.

Within this model, the surface coverage of the ligands is obtained by the minimization of the interface energy.

In our evaluation of adsorption energies E_{hkl}^{ads} and of surface energies γ_{hkl} , several important assumptions are made. The first one is that the solvent effects on the adsorption energy of the molecule on the metallic surface are neglected.

The second one is that the temperature effects are not taken into account: the adsorption of the ligand molecule takes place at a finite temperature whereas, in DFT calculations, the adsorption energy is computed at 0 K. In their work on Fe NPs stabilized by ligands, Gerber *et al.* [53] have shown that it is possible to take into account the temperature effects on adsorption energies, and that the main contribution comes from the vibrational entropy of the molecules adsorbed on the surfaces. This entropy contribution can be approximated by considering the highest vibrational frequencies of the molecules. In the present case, the vibrational frequencies of the CH_3COO molecules adsorbed on the different facets of interest have been evaluated using a finite difference calculations. The highest frequency corresponds to the C=C stretching mode (3360cm^{-1}) and its value is the same for adsorption on the different facets. We therefore considered that this entropy term could be neglected when comparing the different facets interface energies at a constant temperate, i.e. 450 K .

The interface energies can be obtained from the knowledge of the adsorption energies using Eq. 5.1 and of the difference of chemical potential $\Delta\mu$. This last quantity being unknown, it will be used in the following as a varying parameter.

5.1.1.1 Predominant surfaces as a function of the chemical potential

In the following, rather than using the surface coverage, we define the coverage as

$$\Theta_{hkl} = \frac{\theta_{hkl}}{\theta_{hkl}^{\max}} \quad (5.2)$$

where θ_{hkl}^{\max} is the maximum surface coverage on the (hkl) facet. Θ_{hkl} simply denotes the number of ligands adsorbed on the surface divided by the total number of ligand adsorption sites; it thus ranges between 0 and 1. We denote $E_{hkl}^{\text{ads}}(\Theta_{hkl})$ the adsorption energy of ligands as a function of the coverage Θ_{hkl} .

Figure 5.1 reports the evolution of the interface energies as a function of $\Delta\mu$ for each facet and for different coverages Θ_{hkl} . These interface energies are calculated using Eq. 5.1 and the adsorption energies evaluated from Table.4.5. As already mentioned in Sec 4.2.2 of Chapter 4, the adsorption energies of CH_3COO have only been computed on the three crystalline facets that dominate the Wulff polyhedron of a clean Co NP. In the following, the NP morphology will be therefore determined from the relative areas of these three facets. These three facets are the (0001), (10-10) and (01-11). In Fig. 5.1, for each of these facets, the interface energy is reported for 6 different surface coverages 0, 1/4, 1/3, 1/2, 2/3 and 1.

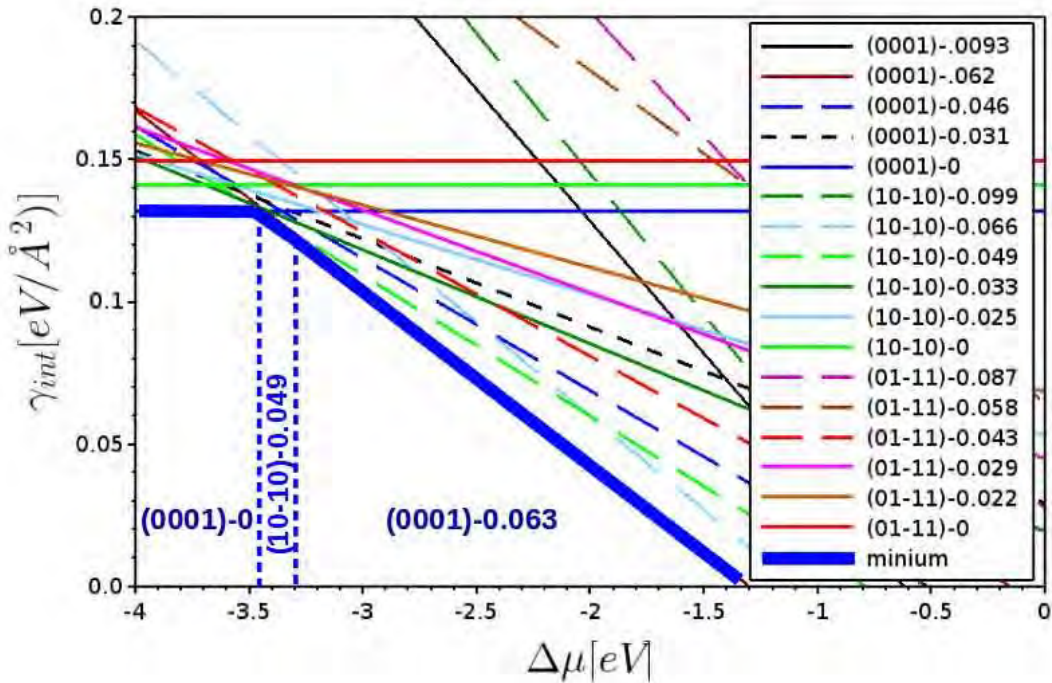


Figure 5.1: Evolution of the interface energies for the different facets and coverages as a function of the chemical potential in the solution. For each curve, the legend reports the facet name and the coverage of ligands (molecules/ \AA^2). The bold blue line represents the lowest interface energy for all coverage at each chemical potential. The interfaces with the smallest interface energy are indicated in each region. (0001) surface dominating correspond to a disk-like form, (10-10) dominating surface correspond to rod-like form.

From Fig. 5.1, the lowest interface energies are the clean (0001) facet for $\Delta\mu < -3.45$ eV, the (10-10) facet with coverage 1/2 for $-3.45 \text{ eV} < \Delta\mu < -3.1$ eV and the (0001) facet with coverage 2/3 for $\Delta\mu > -3.1$ eV.

In the work of Ref. [5], similar results were found except that the $\Delta\mu$ boundaries slightly differ. This is mainly due to the fact that the vdW interactions between the ligands and the surface are not equivalently evaluated in their calculations.

5.1.1.2 Morphology as a function of the ligand concentration

Some attempts have been made to conclude that the facet with the minimum interface energy would be the predominant one and would therefore control the NP morphology [5].

We propose in this section to go beyond this qualitative argument and to calculate the NP morphology using the Wulff construction. For a faceted particle, the Wulff construction imposes:

$$\frac{\gamma_{hkI}^{int}}{L_{hkI}} = \text{const} \quad (5.3)$$

Where L_{hkI} is the distance between the facet plane and the NP center. From results of Fig. 5.1, for each value of $\Delta\mu$, the optimum coverage Θ_{hkI} of a (hkI) facet is determined by minimizing the interface energy. From the minimum interface energies, we construct the NP morphology using the Wulff construction. Figure 5.2 reports these Wulff polyhedra for $\Delta\mu = -4.0$ eV, $\Delta\mu = -3.43$ eV, $\Delta\mu = -3.0$ eV and $\Delta\mu = -2.0$ eV.

For $-4\text{eV} < \Delta\mu < -3\text{eV}$, these polyhedra are similar to the polyhedra of the clean Co NP i.e. without ligands which also corresponds to the one at $\Delta\mu = -4.0$ eV. Note that this latter

shape is slightly different from the Wulff polyhedron presented in Fig.3.15 of Sec.3.5.1 Chapter 3 because only three facets are considered here compared to the seven ones used for Fig.5.2.

For $\Delta\mu = -2\text{eV}$, the NP has a almost prismatic shape with an aspect ratio of 0.92 i.e. slightly smaller than 1.

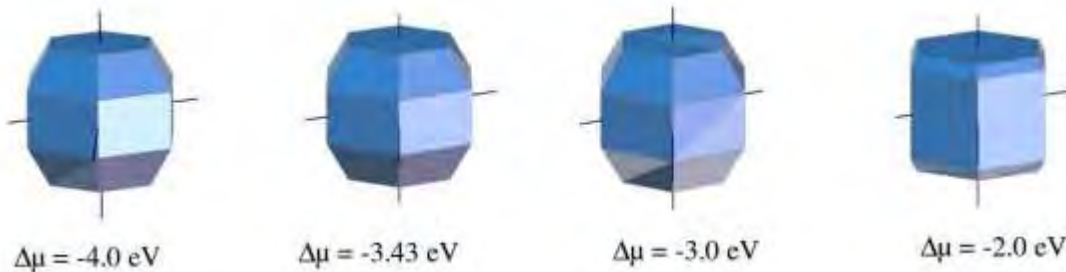


Figure 5.2: Wulff polyhedra built for different values of $\Delta\mu$ using the lowest interface energies of Fig. 5.1.

The lowest interface energy model is therefore not able to explain the different experimental shapes of Co NP stabilized by ligands, i.e. the rod-like and disk-like shapes (exhibiting aspect ratio very different from unity).

5.1.2 Adsorption isotherm model

In the previous model, the coverage of ligands was determined by minimizing the interface energies regardless the concentration of ligands in the solution and/or the temperature. In order to take into account these terms, C. Bealing and *al.* [25] have proposed that the equilibrium coverage for each facet is controlled by the concentration of the ligands in the solvent and the reaction temperature: this approach is very similar to the Langmuir isotherm calculation. This equilibrium coverage Θ_{hkl}^{eq} for the (hkl) facet is derived from the probability rate of adsorbing

one ligand molecule on a (hkl) surface.

I will now present the model proposed by C. Bealing *al.* and then apply it to our specific system. Let us consider the free enthalpy difference between the adsorbed ligand and in the solution :

$$\Delta G_{hkl} = \mu^{\text{ads}}(T, \Theta_{hkl}) - \mu(T, c) \quad (5.4)$$

where $\mu^{\text{ads}}(T, \Theta_{hkl})$ and $\mu(T, c)$ are respectively the chemical potential of the adsorbed ligand (depending on the coverage Θ_{hkl} and the temperature) and $\mu(T, c)$ its chemical potential in the solution at temperature T and concentration c. From DFT calculations, we have access to the adsorption energy of the ligand on the (hkl) facet:

$$E_{hkl}^{\text{ads}}(\Theta_{hkl}) = \mu^{\text{ads}}(T, \Theta_{hkl}) - \mu^{\text{vac}} \quad (5.5)$$

where μ^{vac} is the ligand chemical potential in vacuum. Thus,

$$\Delta G_{hkl} = E_{hkl}^{\text{ads}}(\Theta_{hkl}) - \mu(T, c) + \mu^{\text{vac}} = E_{hkl}^{\text{ads}}(\Theta_{hkl}) - \Delta\mu \quad (5.6)$$

Where $\Delta\mu = \mu(T, c) - \mu^{\text{vac}}$. Here we have again assumed that solvent effects are negligible, so that the chemical potential of the adsorbed ligand is the same in presence of the solution or in vacuum.

The equilibrium coverage Θ_{hkl}^{eq} for the (hkl) facet is then given by (see Sec.1.2.1 of Chapter 1):

$$\Theta_{hkl}^{\text{eq}} = \frac{e^{(-E_{hkl}^{\text{ads}}(\Theta^{\text{eq}}) + \Delta\mu)/k_B T}}{e^{hkl_{\text{ads}}} + e^{hkl_{\text{eq}}}} \quad (5.7)$$

$$1 + e^{(-E_{hkl}(\Theta_{hkl}) + \Delta\mu)/k_B T}$$

Eq.5.7 reduces to the Langmuir's isotherm when E_{hkl}^{ads} does not depend on Θ_{hkl} .

Using a polynomial fit for the $E_{hkl}^{\text{ads}}(\Theta_{hkl})$ curves (Fig. 2 in Sec.4.2.2 of Chapter 4) for the three considered facets, we numerically solve Eq. 5.7 to find the equilibrium coverage for each facet and each value of $\Delta\mu$.

$$\Delta\mu = E_{hkl}^{\text{ads}}(\Theta_{hkl}) + k_B T \ln \frac{\Theta_{hkl}^{\text{eq}}}{1 - \Theta_{hkl}^{\text{eq}}} \quad (5.8)$$

note that physically, $\Delta\mu$ is related to the concentration of ligands in solution by:

$$\Delta\mu = \Delta\mu_0 + k_B T \ln \frac{c}{c_{\text{ref}}} \quad (5.9)$$

where $\Delta\mu_0 = \mu(T, c_{\text{ref}}) - \mu^{\text{vac}}$ is the difference between the chemical potential of the ligand in vacuum and in the solution at the reference concentration c_{ref} . Therefore, in the following, we will consider that a change of $\Delta\mu$ will correspond to a change of the ligand concentration in solution.

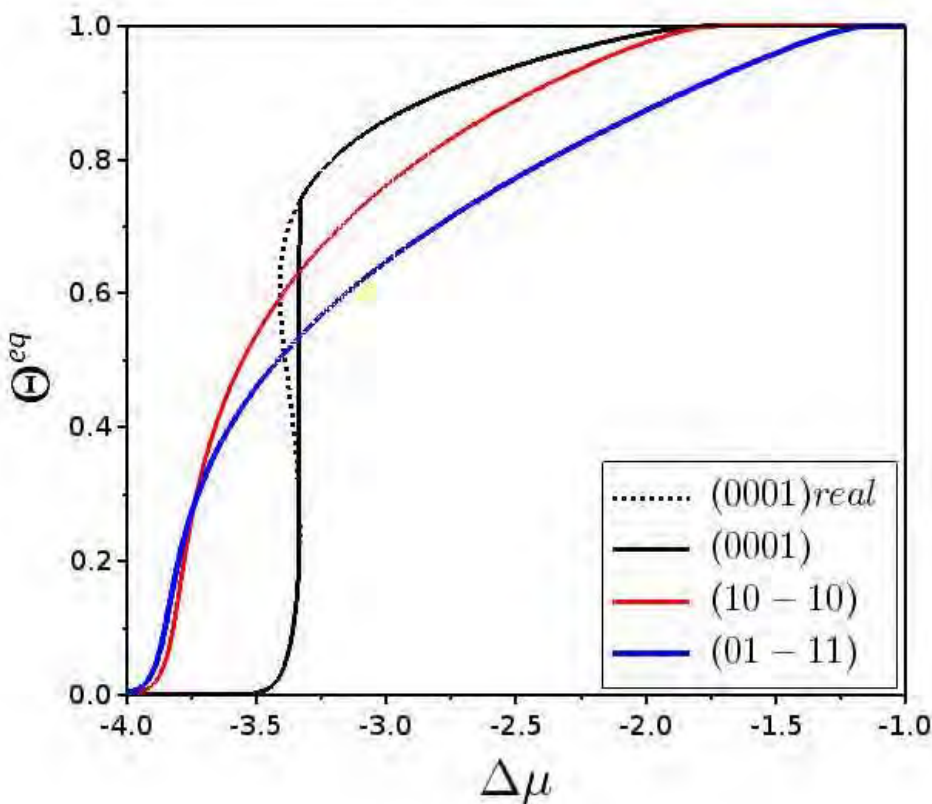


Figure 5.3: Evolution of Θ^{eq} as a function of $\Delta\mu$ for the three considered facets.

From Eq. 5.7 or 5.8, the equilibrium coverage for each facet is calculated as a function of $\Delta\mu$. Figure 5.3 presents Θ_{hkl}^{eq} as a function of $\Delta\mu$ for the three considered facets. In the three cases, the equilibrium coverage is zero for small values of $\Delta\mu$ and then increases until it reaches the maximum value of $\Theta_{hkl}^{\text{eq}} = 1$. The two (10-11) and (01-11) facets (red and blue lines) behave similarly and are monotonous functions of $\Delta\mu$ but the (10-10) facet is fully recovered by ligands

for a smaller $\Delta\mu$ (and thus for a smaller concentration) than the (01-11) facet.

The (0001) facet presents a peculiarity which is due to the $E^{\text{ads}}(\Theta_{hkl})$ function (See Fig. 2 for this facet). Between -3.42 eV and -3.33 eV, there are 3 values of $\Theta_{(0001)}^{\text{eq}}$ satisfying Eq. 5.7

for a given value of $\Delta\mu$ (dotted black line in Figs. 5.3). Assuming that during the first growth steps, there are no ligands on the surfaces and that the ligand coverage increases progressively, we chose to replace this ill-defined region by the value of $\Theta_{(0001)}^{\text{eq}}$ by the solid black line in Fig. 5.3).

From the knowledge of the equilibrium coverage $\Theta_{(0001)}^{\text{eq}}$, one can compute the interface energies for each considered facet at equilibrium from Eq. 5.1 as a function of $\Delta\mu$. Fig. 5.4 reports the interface energies for the three considered facets as a function of $\Delta\mu$.

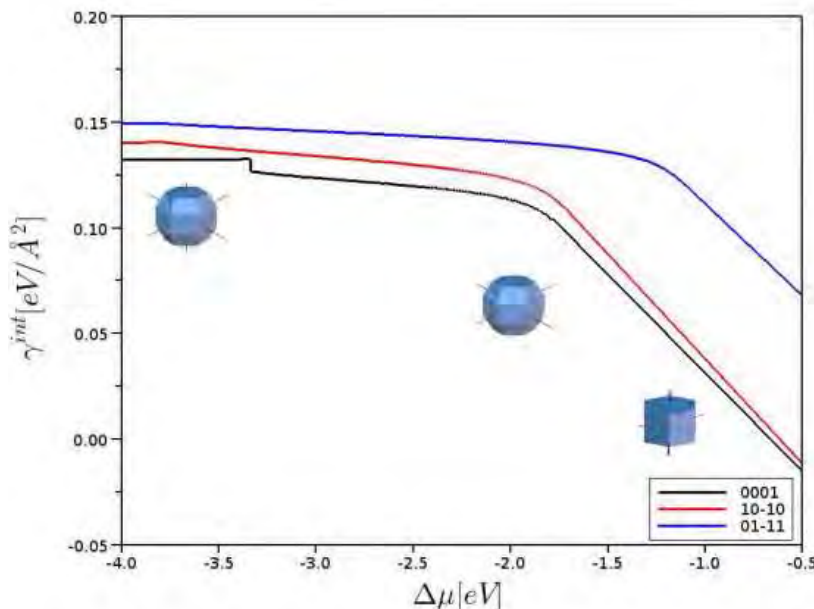


Figure 5.4: Evolution of the interface energy as a function of $\Delta\mu$ for the three considered facets, using the model based on the Langmuir isotherm, and Wulff polyhedra of selected morphologies.

From Fig.5.4, one can clearly see that the differences between the interface energies of the three facets roughly remain constant for $\Delta\mu < -2.0$ eV, giving basically the same Wulff polyhedron. For $\Delta\mu > -2.0$ eV, the differences between the interface energies increase.

Fig.5.4 also displays the corresponding NP morphologies calculated using the Wulff construction. For $\Delta\mu < -2.0$ eV, the morphology is very closed to the ones calculated using the lowest interface energy model, i.e. an ovoid-like polyhedron. For $\Delta\mu > -2.0$ eV, the differences between the interface energies becomes larger and the morphology changes to a prism similarly to the results of the lowest interface energy model. The adsorption isotherm model, as the lowest interface energy mode, is thus not able to explain the different experimental shapes of Co NP stabilized by ligands, i.e. the rod-like and disk-like shapes (exhibiting aspect ratio very different from unity).

5.1.3 Conclusion

The two models presented in this section fail to predict the rod-like and disk-like morphologies of the Co NP observed in experiments. However, these models are commonly used in the literature to predict or explain the morphologies of chemically synthesized NPs. These models are very simple and are based on important assumptions. Among these assumptions, the neglected solvent effects certainly correspond to the biggest assumption. However, the calculation of the

interface energies in the presence of the solvent is clearly out of our computation capabilities using DFT calculations. Other computation techniques (for instance using the empirical potential) that could afford the simulation of the solvent molecules will have the drawback of being unadapted to the description of charge transfer. Besides, the two models assume that the morphologies are driven by equilibrium properties, which supposes that the growth kinetics do not play any role in the final NP morphologies. In order to test this hypothesis, we have developed a kinetic model for the Co NP growth in presence of ligands. This kinetic model is described in the following section.

5.2 Kinetic model

In this model, we describe the NP growth by calculating the Co atom adsorption rate and the ligand adsorption rate on the different NP facets. As for the thermodynamic model, we reduce our study to three facets: (0001), (10-10) and (01-11) and the ligand molecule is CH_3COO .

We describe the NP shape using L_{hkl} , the distances from the NP center to the (hkl) facets, and S_{hkl} which denote the surfaces of the (hkl) facets. Fig. 5.5 schematically displays a NP and reports the quantities L_{hkl} and S_{hkl} . In the following, we will derive the Co adsorptions rate and then the ligands adsorption rate. Finally, the two sets of equations will be solved simultaneously considering in addition the conservation of Co atoms.

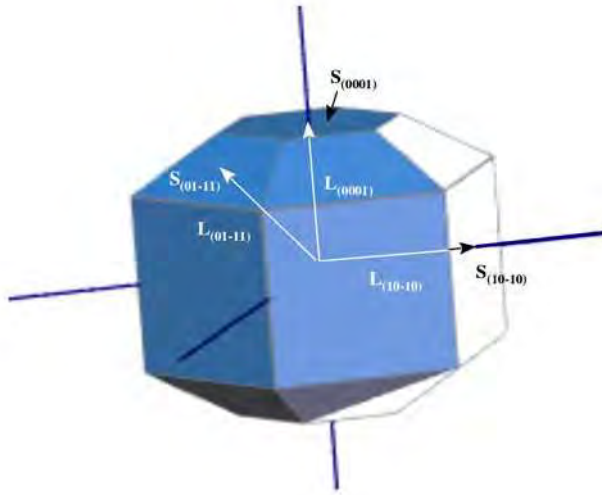


Figure 5.5: Sketch of a Co NP with the notations used in the kinetic model.

5.2.1 Theoretical aspects

5.2.1.1 Cobalt growth

During a time interval Δt , the number N_{hkl} of adsorbed Co atom on the (hkl) facet depends on the rate of adsorption and desorption of a Co atom and on the number of available sites, i.e. the number of sites non-covered by ligands:

$$\frac{dN_{hkl}}{dt} = p_{hkl}^{\text{Co,ads}} (N_{hkl}^{\text{tot}} - 2 \times n_{hkl}^{\text{L}}) - p_{hkl}^{\text{Co,des}} (N_{hkl}^{\text{tot}} - 2 \times n_{hkl}^{\text{L}}) \quad (5.10)$$

where $p_{hkl}^{Co,ads}$ and $p_{hkl}^{Co,des}$ are the rates of a single Co adsorption and desorption, respectively, N_{hkl}^{tot} is the total number of Co adsorption sites of the S_{hkl} surface, and $n_{hkl}(t)$ is the number of ligands adsorbed on the (hkl) facet. Note that, in the case of CH_3COO molecules adsorbed on Co surface, one ligand adsorbs on two Co adsorption sites.

Describing the adsorption/desorption rate by a standard Arrhenius law, the detailed balance of adsorption/desorption rates of the Co atoms states that:

$$\frac{p_{hkl}^{Co,des}}{p_{hkl}^{Co,ads}} = e^{(\mu_{Co}^{NP}(T) - \mu_{Co}^{sol}(T, c_{Co}(t))) / k_B T} \quad (5.11)$$

where $\mu_{Co}^{NP}(T)$ and $\mu_{Co}^{sol}(T, c_{Co}(t))$ are the chemical potentials of Co at temperature T respectively in the NP and in the solution at concentration $c_{Co}(t)$ at time t. The chemical potential of Co in the solution reads:

$$\mu_{Co}^{sol}(T, c_{Co}(t)) = \mu_{Co}^{sol}(T, c_1) + k_B T \ln \frac{c_{Co}(t)}{c_1} \quad (5.12)$$

where c_1 is a reference concentration. We choose c_1 as the concentration at which the Co in the solution is in equilibrium with the Co at the NP surface, at temperature T. So that $\mu_{Co}^{sol}(T, c_1) = \mu_{Co}^{NP}(T)$ and we have simply:

$$\mu_{Co}^{NP}(T) - \mu_{Co}^{sol}(T, c_{Co}(t)) = -k_B T \ln \frac{c_{Co}(t)}{c_1} \quad (5.13)$$

Thus, Eq. 5.10 becomes:

$$\frac{dN_{hkl}}{dt} = p_{hkl}^{Co,ads} \left(1 - \frac{c_1}{c_{Co}(t)} \right) N_{hkl}^{tot} (1 - \Theta_{hkl}(t)) \quad (5.14)$$

Where we have used the definition of the coverage $\Theta_{hkl}(t) = 2n_{hkl}^L(t) / N_{hkl}^{tot}$

The normal growth speed $\frac{dL_{hkl}}{dt}$ reads:

$$\frac{dL_{hkl}}{dt} = \frac{dN_{hkl}}{dt} \frac{d_{hkl}}{N_{hkl}^{tot}} \quad (5.15)$$

where d_{hkl} is the thickness of a monolayer perpendicular to the $[hkl]$ direction. So that finally, using Eq. 5.14,

$$\frac{dL_{hkl}}{dt} = p_{hkl}^{Co,ads} \left(1 - \frac{c_1}{c_{Co}(t)} \right) (1 - \Theta_{hkl}(t)) d_{hkl} \quad (5.16)$$

The growth of a given (hkl) facet thus depends on the concentration of Co in the solution and on the number of available sites on the facet. As expected, at equilibrium, $c_1 = c_{Co}(t)$ and the growth stops. If there is no more available adsorption sites ($\Theta_{hkl}(t) = 1$), the growth stops also. The growth of the facet decreases as the concentration of Co in the solution decreases.

Finally, the total number N_{Co}^{tot} of Co atoms present in the system (NP + solution) must be conserved during the NP growth:

$$\sum_{hkl} dN_{hkl} \left[\frac{c_1}{c_0} - \frac{c_{Co}(t)}{c_1} \right] = 0 \quad (5.17)$$

$$+ N^{\text{tot}} \int_{hkl} \frac{c_0}{dt} c_0 dt = c_0 - c_1$$

where $c_0 = c_{Co}(0)$ is the initial Co concentration in the solution at the beginning of the growth process.

5.2.1.2 Ligands adsorption

During the NP growth, the ligands adsorb and desorb from the Co surface. The number n_{hkl}^L of adsorbed ligands varies as a function of time following:

$$\frac{dn_{hkl}^L}{dt} = \frac{1}{2} \frac{d(\Theta_{hkl}(t)N_{hkl}^{\text{tot}})}{dt} = \frac{N_{hkl}^{\text{tot}}}{2} p_{hkl}^{L,\text{ads}} - p_{hkl}^{L,\text{des}} (1 - \Theta_{hkl}(t)) \Theta_{hkl}(t) \quad (5.18)$$

where $p_{hkl}^{L,\text{ads}}$ and $p_{hkl}^{L,\text{des}}$ are the adsorption and desorption rates of ligand on the (hkl) facet, and N_{hkl}^{tot} is the total number of Co adsorption sites on the (hkl) surface. $\Theta_{hkl}(t)$ is the ligand coverage at time t . Note again that one ligand adsorbs on 2 Co adsorption sites.

The detailed balance of the adsorption and desorption processes of ligands is:

$$\frac{p_{hkl}^{L,\text{ads}}}{p_{hkl}^{L,\text{des}}} = \exp^{-\left(\mu^{\text{ads}}(T, \Theta_{hkl}) - \mu(T, c)\right)/k_B T} \quad (5.19)$$

where $\mu^{\text{ads}}(T, \Theta_{hkl})$ and $\mu(T, c)$ are the chemical potentials of the adsorbed ligands and ligands in solution at concentration c at temperature T . As already mentioned, the chemical potential difference $\mu^{\text{ads}}(T, \Theta_{hkl}) - \mu(T, c)$ can be related to the adsorption energies computed in DFT via:

$$\mu^{\text{ads}}(T, \Theta_{hkl}) - \mu(T, c) = E_{hkl}^{\text{ads}}(\Theta_{hkl}) - \Delta\mu \quad (5.20)$$

Therefore,:

$$\frac{p_{hkl}^{L,\text{ads}}}{p_{hkl}^{L,\text{des}}} = \exp^{-\left(-E_{hkl}^{\text{ads}}(\Theta_{hkl}) + \Delta\mu\right)/k_B T} \quad (5.21)$$

In the following, we assume that the concentration c of ligands in the solution does not change during the NP growth. This is justified by the fact that only a small fraction of ligands in the solution are expected to be captured by the NP surfaces, so that the ligands concentration hardly varies during the growth (see Figure: 5.6).

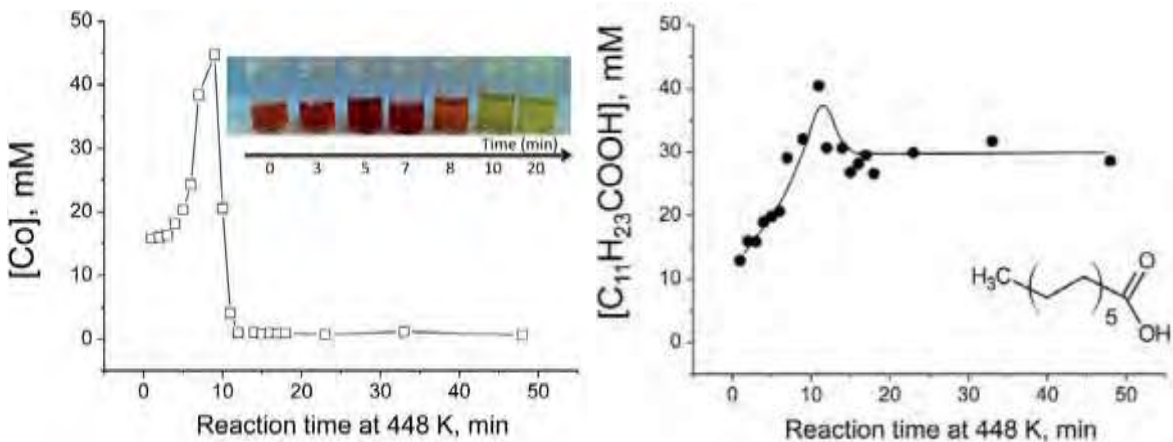


Figure 5.6: Evolution of concentration of Co and ligands as a function of time. Adapted from [5].

Using Eq. 5.21, Eq. 5.18 reads:

$$\frac{d}{dt} \left(\Theta_{hkl}(t) N_{hkl}^{\text{tot}} \right) = N_{hkl}^{\text{tot}} p_{hkl}^{L,\text{ads}} \frac{f}{1 - \Theta_{hkl}(t)} - e^{(E_{hkl}^{\text{ads}}(\Theta_{hkl}) - \Delta\mu)/k_B T} \Theta_{hkl}(t) \quad (5.22)$$

At equilibrium, the number of ligands on the facets does not vary, $d(\Theta_{hkl}(t)N_{hkl}^{\text{tot}})/dt = 0$, so that:

$$1 - \Theta_{hkl}^{\text{eq}} - e^{(E_{hkl}(\Theta_{hkl}) - \Delta\mu)/k_B T} \Theta_{hkl}^{\text{ads}} = 0 \quad (5.23)$$

And we recover the adsorption isotherm Eq. 5.7:

$$\Theta_{hkl}^{eq} = \frac{e^{(-E_{hkl}^{ads}(\Theta_{hkl}^{eq}) + \Delta\mu)/k_B T}}{1 + e^{(-E_{hkl}(\Theta_{hkl}) + \Delta\mu)/k_B T}} \quad (5.24)$$

Eq. 5.22 can be re-written in the following form:

$$\frac{1}{N_{hkl}^{tot}} \frac{d(\Theta_{hkl}(t)N_{hkl}^{tot})}{dt} = p_{hkl}^{L,ads} f_{hkl} [1 - \Theta_{hkl}(t)[1 + e^{(E_{hkl}(\Theta_{hkl}) - \Delta\mu)/k_B T}]] \quad (5.25)$$

During the growth, the total number of sites N_{hkl}^{tot} on a facet increases with time. However, since its derivative with respect to time is expected to be small compared to $\frac{d(\Theta_{hkl}(t))}{dt}$ we neglect the variation of N_{hkl}^{tot} with time.

$$\frac{d\Theta_{hkl}(t)}{dt} = p_{hkl}^{L,ads} f_{hkl} [1 - \Theta_{hkl}(t)[1 + e^{(E_{hkl}(\Theta_{hkl}) - \Delta\mu)/k_B T}]] \quad (5.26)$$

Eqs. 5.26, 5.17 and 5.16 provide a complete set of equations enabling us to calculate the NP morphology evolution. However, these equations depend on the rates $p_{hkl}^{L,ads}$ and $p_{hkl}^{Co,ads}$ of adsorption of the ligand and of the Co on the NP surface. These quantities are a priori unknown. Their calculations would require the use of heavy simulations techniques (such as the nudge elastic band method) able to capture the transitions states. The rates $p_{hkl}^{L,ads}$ and $p_{hkl}^{Co,ads}$ presumably depend on the coverage $\Theta_{hkl}(t)$ and on the temperature and the solvent may not be negligible. Since our goal is here only to test if the growth kinetic may play a role on the NP morphologies, we have investigated different ratio $p_{hkl}^{L,ads}/p_{hkl}^{Co,ads}$ supposing that this ratio does not depend on the coverage $\Theta_{hkl}(t)$.

5.2.1.3 Modelling details

In this section, we solve the Eq. 5.26, 5.17 and 5.16. For each facet, the coverage is initially set to zero ($\Theta_{hkl}(t = 0) = 0$). The NP dimensions L_{0001} , L_{10-10} and L_{01-11} are initialized in order to define the NP volume and size of the facets just after the nucleation regime which obviously can not be described by our approach.

The $p_{hkl}^{Co,ads}$ and $p_{hkl}^{Co,ads}$ both logically depend on the facet orientation. However, the exact expressions for these parameters are unknown. We limited our study to the two following cases:

- "Isotropic" model: $p_{hkl}^{Co,ads} d_{hkl}$ does not depend on the facet orientation (hkl) which means that the initial growth velocity of all surfaces are the same.
- "Attachment energy" model : the $p_{hkl}^{Co,ads}$ depend on the facet orientation and the values are defined following the "Attachment Energy" model (see Chapter 3) section 3.6

We will firstly investigate the "isotropic case" and then the "attachment energy" case will be used to discuss the validity of our conclusions in the isotropic case.

We define a dimensionless time $\tilde{t} = \frac{t}{\tau}$ with $\tau = \frac{Co,ads}{0001}$

$$\left(\frac{c_1}{c_0} - 1 \right) \quad (5.27)$$

and dimensionless lengths:

$$\tilde{L}_{hkl} = \frac{L_{hkl}}{d_{0001}} \quad (5.28)$$

We assume that the parameter λ controlling the ratio $p_{hkl}^{L,\text{ads}}/p_{hkl}^{\text{Co,ads}}$ does not depend on the facet orientation:

$$\lambda = \frac{p_{hkl}^{L,\text{ads}}}{p_{hkl}^{\text{Co,ads}}} \frac{c_1}{1 - \frac{c_1}{c_0}} \quad (5.29)$$

"Isotropic" model We firstly develop the formulation for the isotropic case where the initial growth velocities of all surfaces are the same.

Eq. 5.26, 5.17 and 5.16 now become:

$$\frac{d\Theta_{hkl}(t)}{dt} = \lambda \frac{f}{(E^{\text{ads}})} \left[1 - \Theta_{hkl}(t) [1 + e^{-hkl(\Theta_{hkl}) - \Delta\mu/k_B T}] \right] \quad (5.30)$$

$$\sum_{hkl} \frac{c_1 d}{dt} \frac{c_{Co}(t)}{c_0} = 0 \quad (5.31)$$

$$+ N^{\text{tot}} \frac{\frac{c_0}{dt} \times c_0 dt}{hkl} \frac{c_1}{1 - \frac{c_1}{c_{Co}(t)}} \frac{d\tilde{L}_{hkl}}{dt} = \frac{(1 - \Theta_{hkl}(t))}{1 - \frac{c_1}{c_0}} \quad (5.32)$$

"Attachment Energy" model: The ratio between the growth velocity of the (hkl) surfaces to the (0001) one: $\frac{V_{hkl}}{V_{0001}}$ are calculated in Chapter 3 Sec. 3.6. We recall here: $V_{10-10}/V_{0001} = 1.15$ and $V_{01-11}/V_{0001} = 1.03$

Eq. 5.26, 5.17 and 5.16 now become:

$$\frac{d\Theta_{hkl}(t)}{dt} = \lambda \frac{f}{(E^{\text{ads}})} \left[1 - \Theta_{hkl}(t) [1 + e^{-hkl(\Theta_{hkl}) - \Delta\mu/k_B T}] \right] \quad (5.33)$$

$$\sum_{hkl} \frac{c_1 d}{dt} \frac{c_{Co}(t)}{c_0} = 0 \quad (5.34)$$

$$+ N^{\text{tot}} \frac{\frac{c_0}{dt} \times c_0 dt}{hkl} \frac{c_1}{1 - \frac{c_1}{c_{Co}(t)}} \frac{d\tilde{L}_{hkl}}{dt} = \frac{(1 - \Theta_{hkl}(t)) \times V_{hkl}}{1 - \frac{c_1}{c_0}} \times \frac{V_{hkl}}{V_{0001}} \quad (5.35)$$

Therefore, the parameters necessary for the modelling are the following:

- λ which controls the Co and ligands adsorption rates
- The chemical potential difference $\Delta\mu$
- The ratio $\frac{c_0}{c_1}$ of the initial Co concentration c_0 to the equilibrium concentration c_1 .
- The total number of Co atoms N_{Co}^{tot} , which fix the final sizes of the NP. Note that this model considers only the growth of one single NP and does not describe the concentration

of NP in the solution. N^{tot} is thus the number of available Co atoms per created NP.

- The initial size of the nanoparticles: L_{0001} , L_{10-10} and L_{01-11} .

5.2.2 Results

5.2.2.1 Simple kinetics model: Ligands are more active than Co

We first deal with the case where the ligands adsorb and desorb more quickly than the Cobalt monomer. In this case, the prefactor $\lambda \gg 1$. From 5.26 and 5.16, we obtain that the coverage of ligands on the facet can reach equilibrium after a few steps of the simulation. The equation 5.32 becomes

$$\frac{d\tilde{L}_{hkl}}{d\tilde{t}} = \frac{1 - \frac{c_1}{c_{Co}(t)}}{1 - \frac{c_1}{c_0}} (1 - \Theta_{hkl}^{eq}(t)) \quad (5.36)$$

Thus, the ratio between the growth rate of the three surfaces does not depend on time. By the choice of zero initial seed ($L_{0001} = L_{10-10} = L_{01-11} = 0$), the final form can be predicted using the ratio between the growth rates of these surfaces and depends solely on the relation between the adsorption rates of these surfaces. There is no need to carry out a simulation as a function of time in this case. Figure 5.7 shows the size ratio comparing the other surfaces to the (0001) surface and considering different models. The evolution for the two models is similar, the only difference of ratio comes from the initial growth rates. By increasing the ligand concentration in the solution (i.e. increasing $\Delta\mu$), the evolution can be divided in three regions:

- From $\Delta\mu = -4$ eV to $\Delta\mu = -3.38$ eV, the two aspect ratios increase from 0.86 to 2.11 in the attachment energy model (from 1 to 2.42 in the isotropic model). In this region, comparing to the Θ^{eq} in Fig. 5.3, we see that the growth rate is decreased by the coverage of the (10-10) surface and the (01-11) surface while the (0001) surface is still not covered by ligands. The morphology of the Co NP changes from a spherical form to an elongated form.
- From $\Delta\mu = -3.38$ eV to $\Delta\mu = -3.31$ eV, the aspect ratios decrease rapidly from a rod-like form (2.06 in the attachment energy model and 2.42 in the isotropic model) to a disk-like form. It corresponds to the rapid change of Θ^{eq} of the (0001) surface. The change of $\Delta\mu$ here is about $2 k_B T$ which is equivalent to an increase of ≈ 7.3 times the ligand concentration in the solution at 450 K .
- From $\Delta\mu > -3.31$ eV, the aspect ratios decrease slowly and the NP remains disk-like.

Interestingly, conversely to the thermodynamic models, we now observe a significant modification of the NP morphology with $\Delta\mu$, which is related to the ligand concentration in solution: the NP change from a spherical-like polyhedron to an elongated one and then to a disk-like shape. Even if the obtained elongated form does not exactly resemble the rod-like form observed in experiments, the kinetic model provides a real improvement compared to the thermodynamic ones since the morphologies change drastically with $\Delta\mu$. The fact that we do not observe a rod for intermediate values of $\Delta\mu$ can be attributed to many factors among which (i) the use of the simple form of the kinetic model, and (ii) the use of only three facets in the model.

We will now derive the kinetic model in the general case where the ratio λ is varied from very small to very large values.

5.2.2.2 Initial parameters

When the ligands and the Co atoms have comparable adsorption rates, we must carry out a simulation to determine the final shape of the Co nanoparticles. Here we firstly discuss the role of our initial parameters: The initial sizes L_{0001} , L_{10-10} and L_{01-11} ; The ratio $\frac{c_0}{c_1}$ of initial

concentration and final concentration of Co; The total number of Co atoms N_{Co}^{tot} which fix the final size of the NP. For simplicity, in this section all the results were simulated in the case of the "isotropic" model.

Initial seed size The equation Eq. 5.26 does not depend on the size of the nanoparticle. The two equations 5.17 and 5.16 have only the parameter $\frac{c_1}{c_{Co}(t)}$ that depends on the NP size.

However, this parameter does not depend on the facet orientation. When the seed sizes are small compared to the final sizes of the nanoparticle, the effect of the seed sizes on the final morphology of the NP is very small. Figure 5.8 shows the size of the NP as a function of time for ($\lambda = 1$, $\frac{c_1}{c_{Co}(t)} = 100$, $\Delta\mu = -3.5$ [eV], $N^{tot} = N_0 = 15.24 \times 10^6$) for different seed sizes:

c_0

solid line for seed sizes of 0 and dashed line for seed size of 30 Å in each dimension. The final

morphology depends only slightly on the seed size. From the following we decided to choose

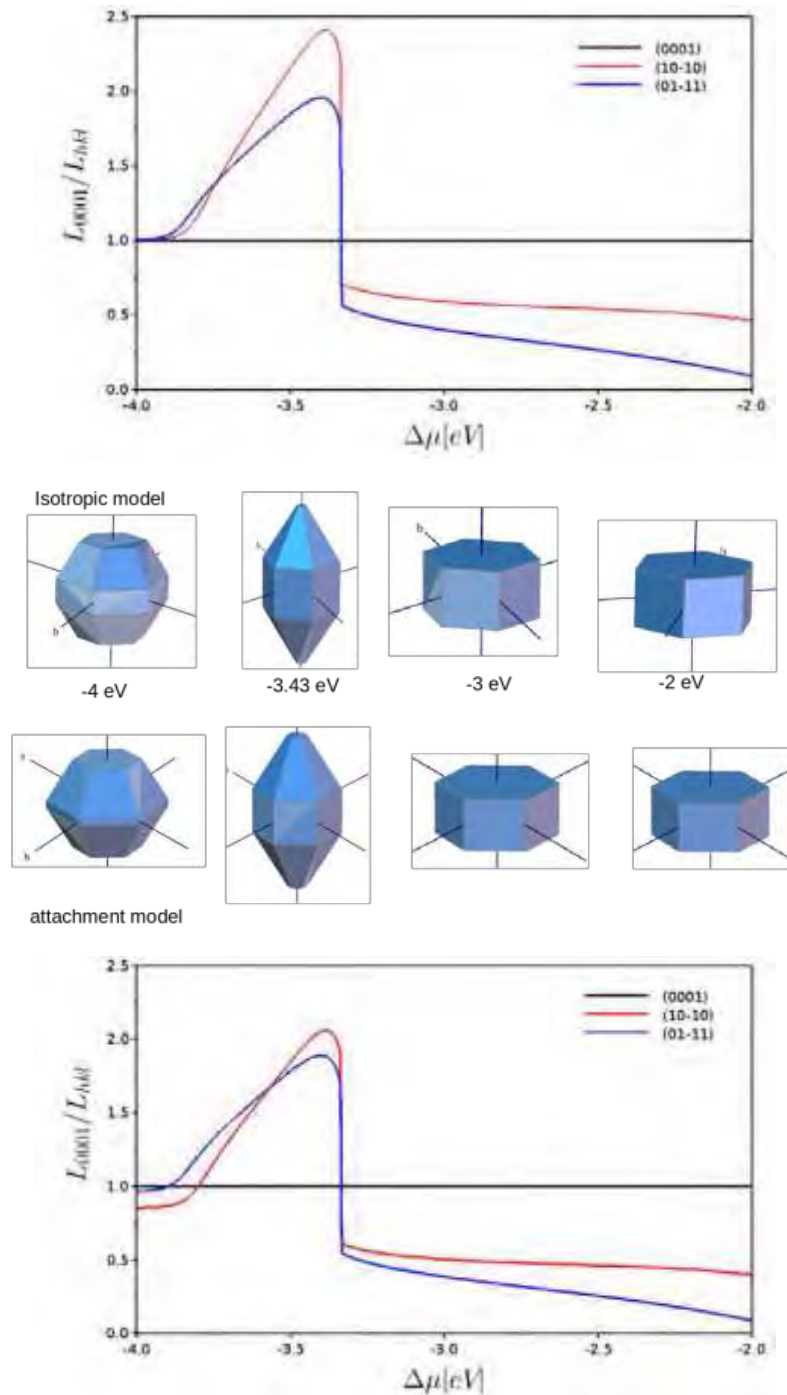


Figure 5.7: Sizes of the NP compared to the reference (0001) surface as a function of $\Delta\mu$, for the two models of Co adsorption. **Top:** Isotropic model for the Co initial growth rate. **Middle:** Schematic views of the NP shapes in the different cases. **Bottom:** Attachment energy model for the Co initial growth rate.

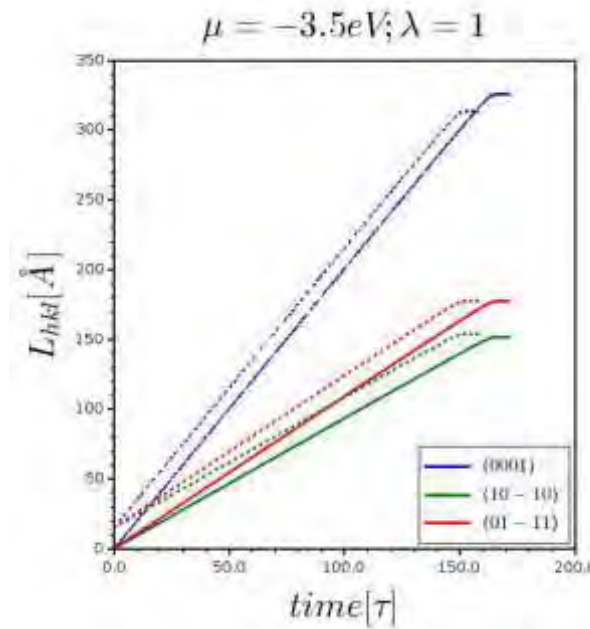


Figure 5.8: Size evolution as a function of time for different seed sizes. Seed size 0 for solid line and 15 Å in each dimension for the dashed line. Here $N_{Co}^{tot} = N_0 = 15.24 \times 10^6$ atoms and $\frac{c_0}{c_1} = 100$.

the initial seed size as 0, and the discussion below are concentrated solely on the growth effect on the morphology.

Ratio $\frac{c_0}{c_1}$ and N_{Co}^{tot} These two parameters determine the final volume of the nanoparticles.

By the conservation of N_{Co}^{tot} , the number of the Co atoms in the system, the final volume of the NPs is:

$$V_{NP}^f = N_{Co}^{tot} \left(1 - \frac{c_1}{c_0}\right) \times V_b \quad (5.37)$$

where V_b is the bulk volume occupied by one atom of Co. Both ratios $\frac{c_0}{c_1}$ and N_{Co}^{tot} affect the size and the final volume of the NPs. All our simulations are carried out until the concentration of Co in the solution is $c_{Co}(t) = 1.000001 \times c_1$. Fig 5.9 shows an example of evolution of Co concentration as a function of time for $\frac{c_0}{c_1} = 100$, $N_{Co}^{tot} = N_0/4$, $\lambda = 1$ and $\mu = -3\text{eV}$.

Figure 5.10 shows the evolution of the NP size with different values of $\frac{c_0}{c_1}$ and N_{Co}^{tot} . These

simulations were done with $\lambda = 1$ and $\Delta\mu = -3.5$ eV. In this particular conditions, the ligands reach the equilibrium coverages after less than a few τ , so we can see the dependency of the growth time as a function of the ratios $\frac{c_0}{c_1}$ and N_{Co}^{tot} .

In Figure 5.10 left, the two cases have the same $\frac{c_0}{c_1} = 100$, the growth time is proportional to the maximum size of the nanoparticles ($\sqrt[3]{\frac{c_1}{N_{Co}^{tot}}}$). In figure 5.10 right, the two cases have the same N_{Co}^{tot} , the growth time is greater for small $\frac{c_0}{c_1}$ due to the choice of N_{Co}^{tot} .

and $\frac{c_0}{c_1}$ controls the growth time of the NP which is an important parameter compared to the time needed for the ligands to reach their equilibrium coverages. In order to compare our results with experiments, we want to fix N_{Co}^{tot} so that the characteristic size of the created NP at the end of the growth is roughly 200 \AA and the ratio $\frac{c_0}{c_1} \gg 1$. From here, we choose $N_{Co}^{\text{tot}} = N_0 = 15.24 \times 10^6$ atoms and $\frac{c_0}{c_1} = 100$ for the following discussions.

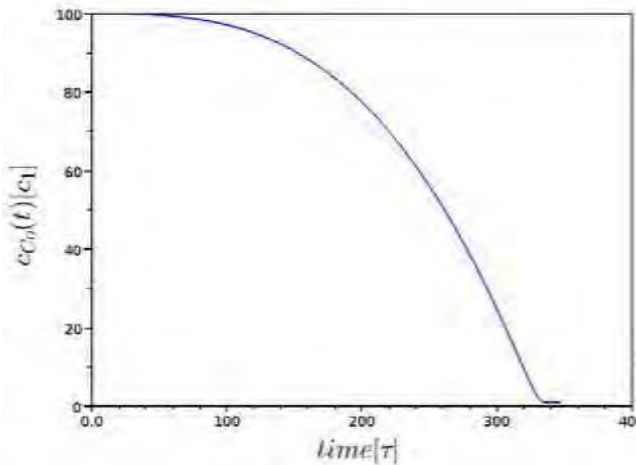


Figure 5.9: Evolution of Cobalt concentration as a function of time for $\frac{c_0}{c_1} = 100$, $N_{Co}^{tot} = N_0/4$, $\lambda = 1$ and $\mu = -3\text{eV}$. Simulation stop at $c_{Co}(t) = 1.000001 \times c_1$.

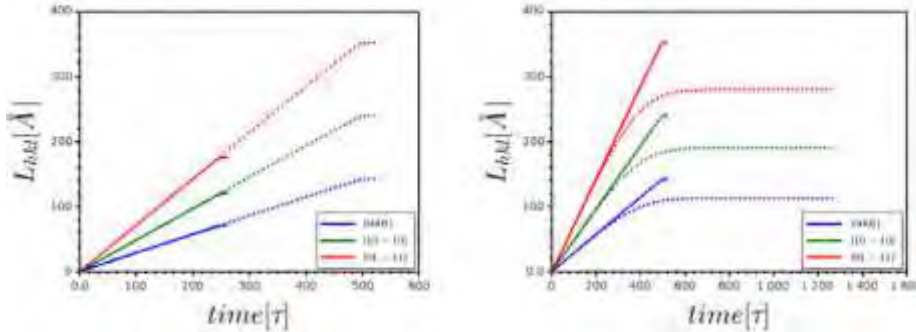


Figure 5.10: Size evolution as a function of time for different $\frac{c_0}{c_1} N_{Co}^{tot}$ for $\lambda = 1$ and $\mu = -3.5\text{eV}$

- Left** $\frac{c_0}{c_1} = 100$ dashed line : $N_{Co}^{tot} = N_0 = 15.24 \times 10^6$; solid line: $N_{Co}^{tot} = N_0/8$. **Right** $\frac{c_0}{c_1} = 100$ solid line: $\frac{c_0}{c_1} = 100$; dashed line : $\frac{c_0}{c_1} = 2$.

5.2.2.3 Role of λ

The ligands coverage is described uniquely in Eq. 5.33 (for the "attachment model") and Eq. 5.30 (for the "isotropic model"). In these equations, λ controls the adsorption rate of ligands while $\Delta\mu$ controls the equilibrium coverage.

Figure 5.11 shows the evolution of the coverages of the (0001) surface at $\Delta\mu = -3$ eV for different values of λ as a function of time. The line stops when the concentration of Co in the solution is $1.000001 \times c_1$. The evolution is about the same for different values of λ . The time needed for reaching the equilibrium coverages is of the same order of $1/\lambda$.

The growth of Co can be divided in 2 modes: the early mode in which the ligands coverage increases from 0 to Θ_{eq} , the later mode in which the ligands coverage reaches Θ_{eq} . For $\lambda = 1$ and $\lambda = 0.1$ the coverage reaches the equilibrium coverage after a few τ . That is the particular case of the "simple kinetics" model present previously in Sec. 5.2.2.1. The growth occurs principally in the later mode. While in the case of $\lambda = 0.001$, the coverage remains very small compared

to the equilibrium coverage. The growth occurs principally in the early mode. Finally, for $\Delta\mu = 0.01$, the time of the 2 modes are comparable.

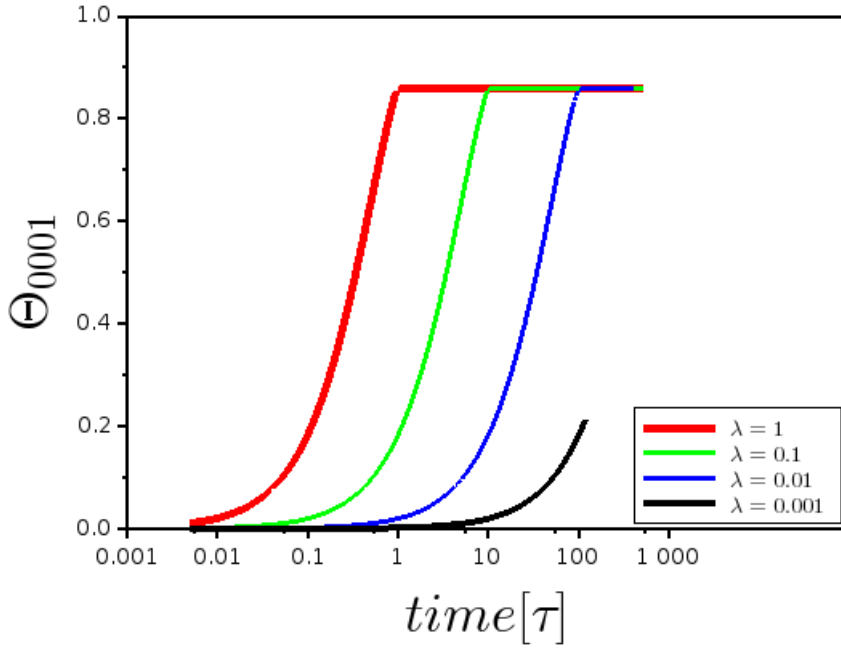


Figure 5.11: coverage evolution as a function of time (log scale) at $\Delta\mu = -3$ eV for different value of λ .

5.2.2.4 Kinetic model: morphology prediction

When the adsorption rate of ligands and the Co incorporation rate are comparable, we must carry out a simulation to determine the final shape of the Co nanoparticles.

Figures 5.12 and 5.13 show the aspect ratios of the final NP shapes in the cases of the isotropic and of the attachment energy models, respectively, as a function of $\Delta\mu$. The reference size is chosen to be the distance to the (0001) surface, $L_{(0001)}$. For these two models, we first considered the case where λ is the same for each facet and we vary it from 0.001 to 1.

One can first notice that the sets of graphs show strong similarities with the graphs presented in the previous section for the simple kinetic model. Three different regions can be distinguished: (1) for $\Delta\mu < -3.8$ eV, (2) for $-3.8 \text{ eV} < \Delta\mu < -3.3$ eV and (3) for $\Delta\mu > -3.3$ eV. In fact, the chemical potential controls the ligand coverage on the surface and indirectly the growth rate of the ligands in the solution. The evolution of the morphology is therefore similar to the case of the simple kinetic model. Both the isotropic model and the attachment energy model present the same aspect, only the relative values of the aspect ratios present some differences.

The dependency of the adsorption rate ratio λ can be divided in three cases:

- When $\lambda > 0.1$, we see that the aspect ratio evolution converges to the extreme case of the simple kinetic model, as expected. The NP shape is spherical for small $\Delta\mu$, rod-like for intermediate values and disk-like for larger values.
- When $0.1 > \lambda > 0.001$, the aspect ratios decrease in the intermediate region but the tendency does not change. The peak of aspect ratio for each line always exists however it is slightly decreased. In fact, the maximum aspect ratio corresponds to the point where the (0001) surface is not covered by ligands but the other surfaces are partially covered. The growth rate of the (0001) surface at the position of the peak is the same for all values of λ but the growth rates of the two other surfaces depends on the ligand coverage. The greater the ligand coverage is, the smaller the growth rate. Thus when λ decreases, the

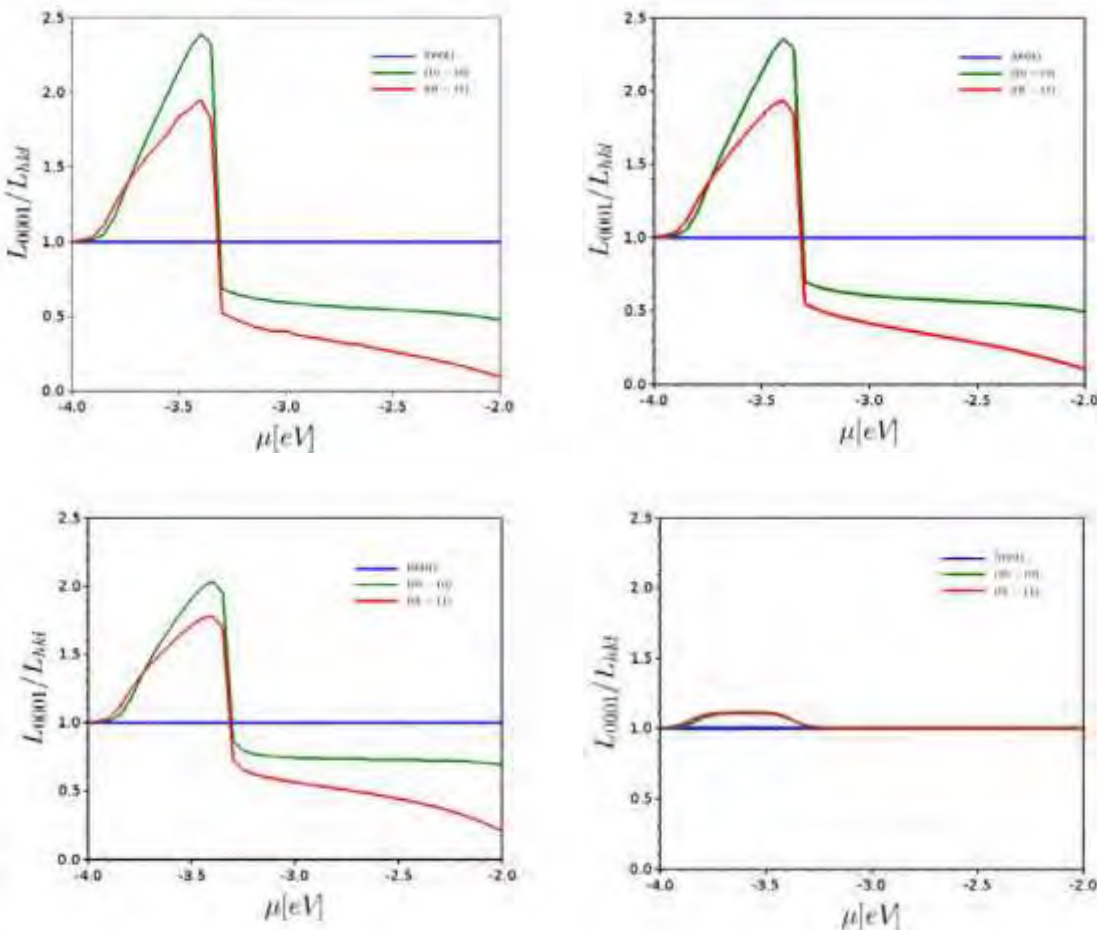


Figure 5.12: Evolution of the NP size as a function of $\Delta\mu$ for the isotropic model. **top:** Left : $\lambda = 1$; Right : $\lambda = 0.1$ - **bottom** Left: $\lambda = 0.01$; Right: $\lambda = 0.001$

ligands do not have enough time to reach the equilibrium coverage and the ratio between these growth rates decrease.

- When $\lambda = 10^{-3}$, the aspect ratios do not change with the chemical potential. It corresponds to the situation where the Co growth does not depend on the presence of ligands. The final morphology reflects the initial growth rate relation between the surfaces.

In summary, for intermediate and large values of the λ ratio, the general kinetic model recovers the simple kinetic model, if λ is the same for every facet. The corresponding morphologies as a function of $\Delta\mu$, which is related to the ligand concentration in solution, are similar to the ones presented in Fig. 5.7: spherical for small values of $\Delta\mu$, elongated for intermediate values of $\Delta\mu$ and disk-like for large values of $\Delta\mu$. For very small values of λ , we observe almost no evolution of the morphology of the NP with $\Delta\mu$. This corresponds to the extreme case where the ligands can not adsorb on the Co surface, and the NP morphology is that of the Co NP in vacuum, which is determined by the model used for the Co adsorption, isotropic or attachment energy.

By varying the λ ratio between 10^{-3} and 1, the only noticeable modification of the morphology is a decrease of the aspect ratio for the elongated morphology which becomes more spherical for small values of λ .

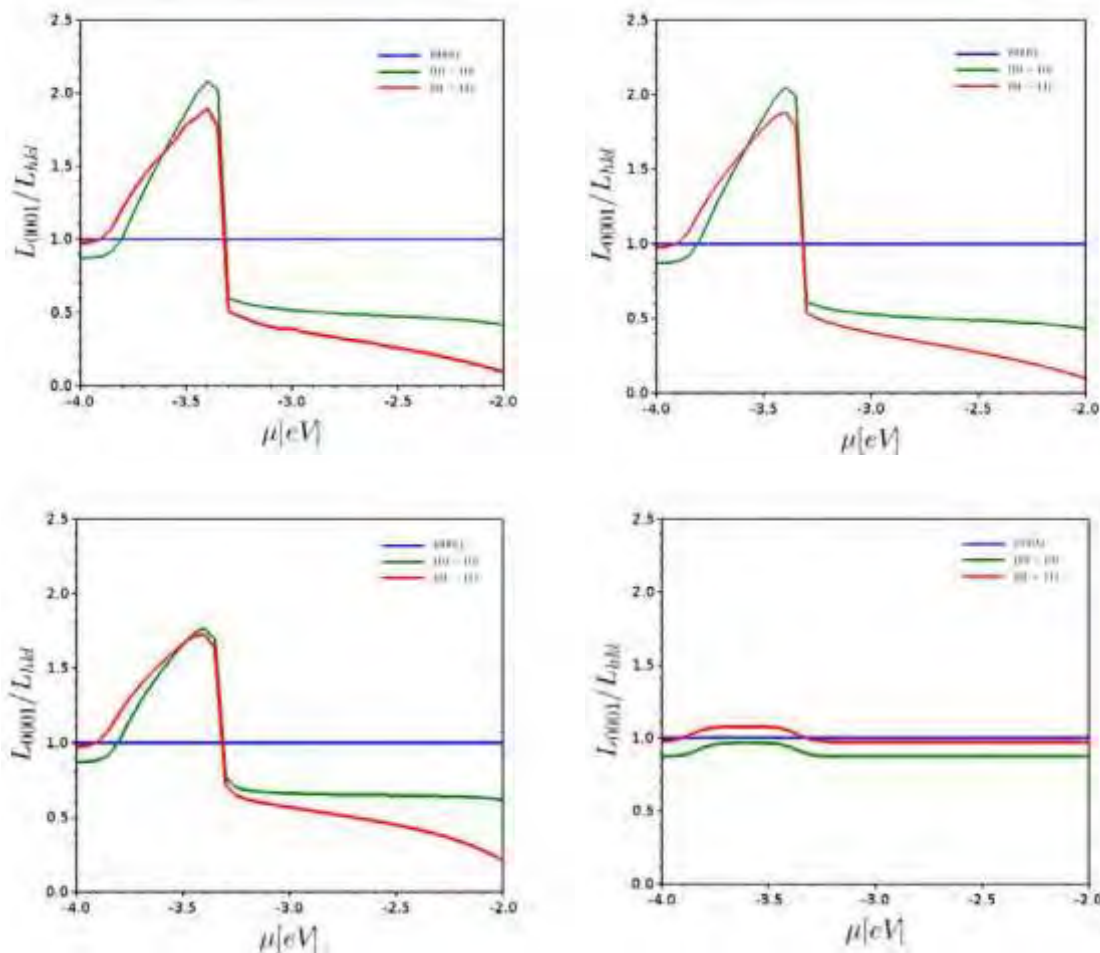


Figure 5.13: Evolution of the NP size as a function of $\Delta\mu$ for the "attachment" model. **top:** Left : $\lambda = 1$; Right : $\lambda = 0.1$ - **bottom** Left: $\lambda = 0.01$; Right: $\lambda = 0.001$

5.2.3 Discussion

In the kinetic anisotropical growth model proposed here, the morphology depends on the growth rate of facets in the three principal surface orientations of hcp cobalt. For each orientation, the growth rate results from the competition between the incorporation rate of cobalt atoms and the surface covering rate by ligand adsorption (up to one monolayer). For a given facet, the Co incorporation rate was defined as the velocity of the increase of the thickness (when a full atomic layer of cobalt atoms were incorporated). This thickening rate depends on two quantities. The first is the number of available sites on the cobalt surface (not covered by ligands). The second quantity is concentration ratio of cobalt monomers in solution at the time t and that at equilibrium (when the growth of NP stops). The surface covering rate also depends on the number of available sites on the surface ($1 - \Theta_{hkl}(t)$) with $\Theta_{hkl}(t)$ varies from 0 to 1. At equilibrium, Θ_{hkl}^{eq} could be defined as the adsorption isotherm as described in Sec. 5.1.2. This kinetic growth was considered as stopped when the concentration of cobalt in solution $c_{Co}(t)$ reaches the equilibrium concentration c_1 .

The competition (between cobalt incorporation and ligand adsorption) was characterized by λ . When λ is close to 1, the time for cobalt monomers to be fully incorporated into the NP is similar to the time for the surfaces of the NP to be covered by ligands at the equilibrium coverage Θ_{hkl}^{eq} . When $\lambda \gg 1$, the surfaces will be covered (Θ_{hkl}^{eq}) far before the concentration of cobalt in solution reaches c_1 . On the opposite side, for $\lambda \ll 1$ ($\lambda = 0.001$ for instance), when cobalt atoms are fully incorporated into the NP, the surface coverages of ligands are still far to reach the Θ_{hkl}^{eq} values (5.11).

When the growth stops, the morphologies predicted by using this kinetic model depends essentially on the chemical potential difference $\Delta\mu$, which reflects the initial concentration of ligands in the solution. Except for small values of λ ($\lambda = 0.001$), the morphology of Co NPs changes from a spherical form in the case of no adsorption of ligands on the surfaces ($\Delta\mu < -3.8eV$) to the rod-like form for intermediate values ($-3.8eV < \Delta\mu < -3.3eV$) and then change to disk-like form for greater values of the chemical potential ($\Delta\mu > -3.3eV$). With small λ ($\lambda = 0.001$), as the NP is mostly uncovered, the morphology is very close to the spherical shape.

In the application of this kinetic model presented here, we limited the size of the NP at about 200 \AA (about 100 layers in the [0001] direction) and the concentration ration to $\frac{c_0}{c_1} = 100$.

Both the "isotropic growth rate" model and the "attachment growth rate" model give similar results. The only difference (in dimension) is due to the accumulation of different rates of the different facet orientations. Even relatively simple, the application of this model has shown several important kinetic aspects not present in the thermodynamics models:

1. The anisotropic shape evolution (from spherical, rod-like to disk-like shape) as a function of the concentration of ligands.
2. The growth kinetic (time for a NP to reach its maximum size) as a function of λ .
3. The evolution of the size as a function of the initial concentration of cobalt c_0 .

Of course, the predicted morphologies are not in perfect agreement with the experimental ones. These differences could be attributed for one part to the difference between the conditions used in simulation and in synthesis. For the other part, it should also be noticed that the assumptions we used have imposed some restrictions such as:

- the solvent effects on the adsorption energies are neglected
- identical λ are used for all facets

- λ does not depend on the coverage $\Theta_{hkl}(t)$
- the ligands are considered to be always in excess.
- the adsorption/incorporation rate (of ligands and Co atoms) are supposed to be constant during the growth
- the diffusion of ligands and cobalt atoms on the surface/in solution has not been taken into account explicitly.

Some of these factors could be easily introduced in our model and would certainly help to improve the agreement between the predicted morphologies and the experimental results.

5.3 Conclusion

In this chapter, I have presented different models for the morphology prediction of Co NPs in presence of the CH_3COO ligand. In the first part, two thermodynamic models were investigated : the lowest interface energy model and the adsorption isotherm model. The applications of these two models have shown an evolution of the NP morphology as a function of ligands concentration. However, these thermodynamic equilibrium shapes failed to predict the rod-like form of the NPs observed in experiments. In order to take into account the kinetic effects on the morphology of the Co NPs, we have derived a model which is based on the competition between the adsorption rate of ligands and the incorporation rate of cobalt atoms. This model, both in its simplified form or in its general form, has the capacity to predict not only a rod-like form, but also the spherical and disk-like shapes depending on the concentration of ligands in solution. This anisotropy of shape is clearly due to the kinetics effects. Our kinetics model, even still relatively simple, seems to be a promising method to explain the variety of forms of Co nanoparticles synthesized in solution.

The knowledge of the relation between the structure and the properties of materials is the key to understand and improve their functional properties. High quality nanoparticles with a narrow size distribution and a well-defined morphology are required to this end. Among the fabrication method, chemical synthesis has the advantage of low cost and flexibility. In this method, the nature of the adsorbate (or ligands), the temperature, the chemical conditions and the kinetics parameters play an important role in the morphological control. However the use of these specific conditions render the growth mechanisms complex and difficult to explain by an unified theory. The existing efforts in predicting nanoparticle morphologies can only investigate the problem case by case.

In the particular case of hcp Co nanoparticles, potential anisotropic magnetic properties induced by the existence of anisotropic morphologies are particular interesting for applications. In recent experiments, it has been shown that the morphology control of Co NP could be obtained by using ligands such as RhB, DHA, R-NH₂ [2, 26] (which contain amine termination) or carboxylate termination such as C₁₁H₂₃COO⁻ [5].

The motivation of my work was therefore to use DFT calculations to investigate the effect of these ligands adsorbed on the metallic surfaces with, as final objective, the building of a model able to predict the morphology of a nanoparticle as a function of the concentration of the adsorbed ligands. All of our DFT calculations were performed using VASP [18, 20, 17, 19], a periodic code package.

In modeling the interaction between surfaces and ligands, the first step is to describe the metallic substrate (their bulk and surfaces properties) and the isolated molecules. To this end, the choice of an efficient exchange and correlation functional is important. Notably, it is necessary to take into account the van der Waals (vdW) interactions in these systems. Contrary to the case of molecules, the use of vdW dispersion interaction in metallic systems is a subject of discussion. We compared the efficiency of PBE, PBE+DFTD and opt86B functionals in taking account the effect of vdW interactions on the surface and bulk properties of fcc Ni and hcp Co. In bulk calculations, in many aspects, PBE shows a clear advantage over the two other functionals regarding cell parameters, cohesive energy and bulk modulus. In surface calculations, the results of the three investigated functionals give contrasted results depending on the studied property. The opt86B functional gives the best agreement with experiments for Co(0001) and Ni(111) for surface energies and relaxations. For work functions and magnetic moments, PBE seems to be the best choice for Co and opt86B is the one for Ni. Given the disparity of these results, we decided to model the metallic surfaces with the PBE functional and to add dispersion forces only between the surface atoms and the molecules.

The surface energies obtained for clean metal surfaces were used in the morphology prediction for hcp Co and fcc Ni nanoparticles without ligands, using the Wulff reconstruction method and the attachment energy model. In the case of Co, the dominating surfaces for the Wulff model are (0001), (01-11) and (10-10), whereas in the attachment energy model, the (01-11) surface dominates, the other surfaces having non-negligible contributions. For the case of Ni, Wulff reconstruction model shows a spherical form with equivalent participation of (111) and (001) facets.

Conclusion

The majority of molecules used in controlling Co NPs morphology contains at least one amine or one carboxylate group. Therefore, we investigated the adsorption of simple ligands CH_3COO^- and CH_3NH_2 on the metallic surfaces and then extend to longer hydrocarbon chains.

The energetic and structural properties of CH_3COO^- , $\text{C}_5\text{H}_{11}\text{COO}^-$, $\text{C}_{11}\text{H}_{23}\text{COO}^-$ and CH_3NH_2 are optimized in order to investigate their interaction with metal surfaces at different coverages.

The first results showed that the adsorption energies of CH_3NH_2 on the Co and Ni surfaces were much smaller than the ones of CH_3COO^- . Among the 3 different chain lengths for the R-COO molecules, as the calculations for CH_3COO^- require less computer resources, we have obtained, for this ligand, a large set of adsorption energies as a function of the coverage for the three investigated surfaces. These adsorption energies were then fitted by a polynomial function, which has a key importance for building the growth models of the nanoparticle in the presence of ligands.

We tested two existing thermodynamic models (the lowest interface energy model and the adsorption isotherm model) and developed a new kinetic model. The thermodynamic models have shown an evolution of the NP morphology as a function of ligands concentration but none of these two models has predicted the rod-like morphology. The principal reason is that the rod-like shape does not correspond to any thermodynamically favored shape. In other words, the criteria of the minimization of the Gibb's free surfaces energy could not be satisfied in the case of nanorods.

In order to take into account the kinetic effects on the morphology of Co NP, we have introduced a model which is based on the competition between the adsorption rate of ligands and the incorporation rate of cobalt atoms. In the application of this model on CH_3COO^- stabilized Co NPs, we have imposed several important parameters: the total number of Co atoms in the solution was fixed as well as the initial concentrations of cobalt atoms (expressed as c_0/c_1 ratio) and of ligands (expressed as $\Delta\mu$). The final results predict a variety of morphologies such as elongated, spherical and disk-like nanoparticles depending on the initial chemical potential of ligands in the solution and the ratio λ . In this model, the ratio λ , which expresses the competition between the adsorption rate of ligands and of the incorporation of Co atoms, could take different values depending the binding strength of a ligand on a given facet of NP. Thus the change of λ could be interpreted as the use of a different ligand type (amine, TOPO or RhB for example). We still need to complete the investigation of this model by a systematic analysis of the influence of each parameter, and then by changing to other ligand/surface systems. To this aim, the key factor is to obtain a smooth function for the adsorption energy as a function of the coverage, for each set of ligands and facets. With such a function, this model could be generalized to predict a variety of nanoparticles morphologies.

This model could also be improved by including more details such as : the solvent effects on the adsorption energies; the dependence of λ on the chemical potential of the solution, on the surface coverage $\Theta_{hkl}(t)$ and on the facet orientation; the diffusion of ligands and monomers on the surface and in solution. These supplementary parameters would potentially help to improve the agreement between the predicted morphologies and the experimental results.

Atomics position of Co surfaces

The surface replication vectors of Co(0001) and positions of the atoms in the cell are respectively showed in Eqs. 3.16 and 3.17. Here i present only the others surfaces. The (1-100) and (10-10) surfaces have the same normal vector and the same replication vector. They are two inequivalent planes of the same direction. Their replication vector in space are shown in Eq. A.1.

$$\begin{aligned} & v_1 = 1 \ 0 \ 0 \quad a \ i \\ & v_2 = 0 \ 1 \ \sqrt{\frac{2}{3}} \quad c \ j \\ & v_3 = 0 \ 0 \ \quad a \ k \end{aligned} \quad (A.1)$$

where a and c are the lattice parameters of Co and i, j, k are the orthogonal unit vectors in the space. Atomic positions of (1-100) and (10-10) are shown respectively in equation A.2 and A.3.

$$\begin{array}{ccccccc} & p_1 & & 0 & 0 & 0 & \\ & p_2 & & 0 & 0.5 & 1/6 & \\ \sqcup & p_3 & & 0.5 & 0 & 1/3 & \\ & & & & & & \\ & & & & & & \\ & \dots & & \dots & \dots & \dots & \\ & p_{4n-3} & & 0 & 0 & n-1 & \\ & p_{4n-2} & & 0 & 0.5 & n-5/6 & \\ & p_{4n-1} & & 0.5 & 0 & n-1/2 & \\ & p_{4n} & & 0.5 & 0.5 & n-1/3 & \end{array} \quad (A.2)$$

$$\begin{array}{ccccccc} & p_1 & & 0 & 0.5 & 0 & \\ & p_2 & & 0 & 0 & 1/3 & \\ \sqcup & p_3 & & 0.5 & 0.5 & 1/2 & \\ & & & & & & \\ & & & & & & \\ & \dots & & \dots & \dots & \dots & \\ & p_{4n-3} & & 0 & 0.5 & n-1 & \\ & p_{4n-2} & & 0 & 0 & n-2/3 & \\ & p_{4n-1} & & 0.5 & 0.5 & n-1/3 & \\ & p_{4n} & & 0.5 & 0 & n-1/6 & \end{array} \quad (A.3)$$

Similar to the two previous surfaces, the (1-102) and (0-112) surfaces have the same replication vectors (Eq. A.4), only the termination layer of the surface is different. Their atomic positions are respectively shown in Eqs. A.5 and A.6.

Appendix A

$$\begin{matrix} & \square & \square & a & 0 & 0 & \square \square & i & \square \\ \square & v_2 & \square = & \square & 0 & \sqrt{c^2 + a^2} & 0 & \square \square & j & \square \\ v_3 & & & 0 & 0.684a & 0.729a & & & k & \end{matrix} \quad (\text{A.4})$$

where a and c are the lattice parameters of Co and i, j, k are the orthogonal unit vectors in the space. The atomic positions of the (1-102) surface are given by:

$$\begin{array}{ccccccc}
 & p_1 & & 0 & 0 & 0 & \\
 \square & \square & \square & & & & \square \\
 \square & p_2 & \square & 0 & 1/3 & 1/6 & \square \\
 \square & p_3 & \square & 1/2 & 1/2 & 1/2 & \square \\
 & \square & \square & & & & \square \\
 & \square & \square & \square & & & \square \\
 & \cdots & = & \cdots & \cdots & \cdots & v_2 \square \\
 \square & p_{4n-3} & \square & 0 & 0 & n-1 & \square \\
 \square & p_{4n-2} & \square & 0 & 1/3 & n-5/6 & \square \\
 & \square & \square & 1/2 & 1/2 & n-1/2 & \square \\
 & p_{4n-1} & \square & 1/2 & 2/3 & n-1/6 & \square \\
 & p_{4n} & & 1/2 & 0 & n-1/3 & \square
 \end{array} \tag{A.5}$$

And the ones for the (10-12) surface are given by:

$$\begin{array}{ccccccc}
 & p_1 & & 0 & 1/3 & 0 & \\
 \square & \square & \square & & & & \square \\
 \square & p_2 & \square & 0 & 1/2 & 1/3 & \square \\
 \square & p_3 & \square & 1/2 & 2/3 & 1/2 & \square \\
 & \square & \square & & & & \square \\
 & \square & \square & \square & & & \square \\
 & \cdots & = & \cdots & \cdots & \cdots & v_2 \square \\
 \square & p_{4n-3} & \square & 0 & 1/3 & n-1 & \square \\
 \square & p_{4n-2} & \square & 0 & 1/2 & n-2/3 & \square \\
 & \square & \square & 1/2 & 2/3 & n-1/2 & \square \\
 & p_{4n-1} & \square & 1/2 & 0 & n-1/6 & \square \\
 & p_{4n} & & 1/2 & 0 & n-1/3 & \square
 \end{array} \tag{A.6}$$

For the (01-11) surface, the replication vectors and the atomic positions are shown respectively in Eqs. A.7 and A.8.

$$\begin{array}{ccccccccc}
 & v_1 & & a & & 0 & & i & \\
 & \square & \square & \square & & \square & & \square & \\
 & v_2 & \square & = & \sqrt{c^2 + a^2} & \sqrt{c^2 + a^2} & 0 & \square & j \\
 & v_3 & \square & & 0.262 & 0.965 & 0 & \square & k \\
 & & & & & 0.965 & 1.766c & 0.940c &
 \end{array} \tag{A.7}$$

where a and c are the lattice parameters of Co and i, j, k are the orthogonal unit vectors in the space. The atomic positions of the (01-11) surface are given by:

$$\begin{array}{ccc}
 & p_1 & \square \\
 \square & & \square \\
 & p_2 & \square \\
 & p_3 & \square
 \end{array}$$

$\begin{array}{ccccccc} \square & 0 & 0 & 0 & 0 & 1/2 & \square \\ \square & 2/3 & 2/3 & 1/12 & 2/3 & 2/3 & 7/12 \\ & & & p_4 & & & v_1 \\ & & & & & & \\ & & & & = & & \\ & & & \dots & \dots & \dots & \\ & & & \square & \square & \square & \\ & & & p_{4n-3} & 0 & 0 & n-1 \\ & & & & 2/3 & 2/3 & n-11/12 \\ & & & p_{4n-2} & & & \\ & & & & & & \\ & & & \square & 0 & 0 & n-1/2 \\ & & & p_{4n-1} & 2/3 & 2/3 & n-5/12 \\ & & & p_{4n} & & & \end{array}$
(A.8)

The replication vectors of the (2-1-10) surface are shown in Eq. A.9. For this surface, there are 2 atoms in each plane. Their positions are shown in Eq. A.10

$$\begin{array}{ccccccccc}
& v_1 & \square & \square & c & 0 & \square & i & \square \\
& & & & & \swarrow & & & \\
& v_2 & \square & = & 0 & a & 3 & 0 & \square \quad j \quad \square \\
& v_3 & & & 0 & 0 & a & & k
\end{array}
\quad (A.9)$$

where a and c are the lattice parameters of Co and i, j, k are the orthogonal unit vectors in the space. Atomic positions for the (2-1-10) surface

$$\begin{array}{ccccccc}
 & p_{1\alpha} & & 0 & 0 & 0 & \\
 \\
 \boxed{} & \boxed{} & \boxed{} & 1/2 & 2/3 & 0 & \boxed{} \\
 \boxed{} & \boxed{} & \boxed{} & 1/2 & 1/6 & 1/2 & \boxed{} \\
 \boxed{} & \boxed{} & \boxed{} & 1/2 & 2/3 & 1/2 & \boxed{} v_1 \\
 \boxed{} & \boxed{} & \boxed{} & \cdots & \cdots & \cdots & \boxed{} \\
 \boxed{} & \cdots & \boxed{} & 0 & 0 & n- & \boxed{} v_2 \boxed{} \\
 \boxed{} & \boxed{} & \boxed{} & 1/2 & 2/3 & n- & \boxed{} v_3 \\
 \boxed{} & \boxed{} & \boxed{} & 1/2 & 1/6 & n-1 & \boxed{} \\
 \boxed{} & \boxed{} & \boxed{} & 0 & 2/3 & n-1 & \boxed{} \\
 p_{2n\alpha} & & & & & /2 & \\
 p_{2n\beta} & & & & & /2 &
 \end{array} \tag{A.10}$$

where the index α and β denote the two different atoms in each layer.

Appendix B

Diffusion of adatom and ligands molecule on the Co surfaces

The diffusion of a Co adatom and of the ligands on the surfaces of Co are important in the kinetic aspects of the growth of the nanoparticle. Here we present the diffusion barriers of a Co adatom and of the CH₃COO molecule of on the Co(0001) and Co(10-10) surfaces. For this purpose, we used the Nudge Electric Band (NEB) [89] [90] method which is implemented in VASP [18, 20, 17, 19]. NEB is a method for finding saddle points and minimum energy paths between two given optimized configurations. For all our calculations, we fixed the initial and final positions of adatoms and molecules to their optimized configurations and created 4 intermediate images between these 2 equilibrium configurations to model the pathways of adatoms or molecules on the surfaces. Each image will find the lowest possible energy while maintaining equal spacing with its neighboring images. The diffusion barrier is then calculated as :

$$E^{diff} = E^{max} - E^{min} \quad (\text{B.1})$$

where E^{max} is the maximum total energy among the different images along the pathway and E^{min} is the minimum one (optimized configuration). Figure B.1 shows an example of the variation of the total energy with different configurations of the adatom for a cell containing 1 adatom on a 2x2 (0001) surface. Figure B.2 and B.3 show respectively the corresponding pathways of the Co adatom on the (0001) and (10-10) surfaces for the case of a 2x2 surface. The diffusion barrier of the adatom on the 2 surfaces are given in Table B.1. We can see that the difference between the diffusion barriers of these two surfaces are of the order of a few meV.

Note that the diffusion barriers are highly sensitive to the size of the simulation cell. The results presented here might not be fully converged with respect to the cell size, nevertheless the comparison between the two surfaces is still meaningful.

For the CH₃COO molecule, the initial and final configurations of the diffusion pathways for the 2 surfaces, (0001) and (10-10), are shown in Fig B.4. The diffusion mode is different: On the (0001) surface, the molecules favor a rotational diffusion whereas on the (0001) surface, the molecules favor a translational diffusion. This difference in diffusion mode explains the large difference between the diffusion barriers of the molecules in the 2 cases (see Table B.1). The diffusion of the molecule on the (0001) facet should therefore be faster than on the (10-10) one.

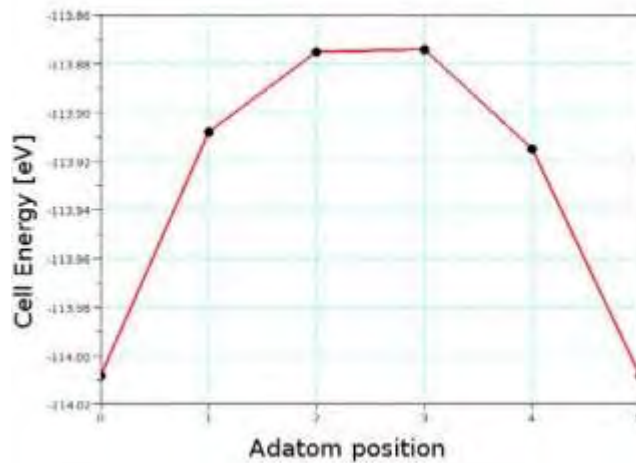


Figure B.1: Total energy for different positions of one adatom on the (0001) surface. Positions 0 and 5 are equilibrium positions, 1-4 are intermediate positions.

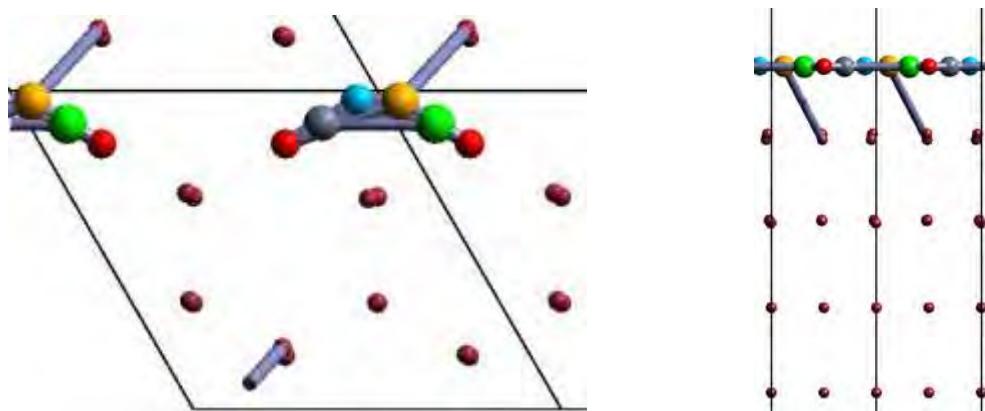


Figure B.2: Diffusion pathway of one adatom on a 2x2 cell of the (0001) surface. **Left:** Top view **Right: side view.** The big red spheres are the optimized positions of the adatom, the intermediate positions are : 1 (grey) 2 (blue) 3 (orange) 4 (green). The bulk layer of Co (small red spheres) are shown as in the optimized configuration.

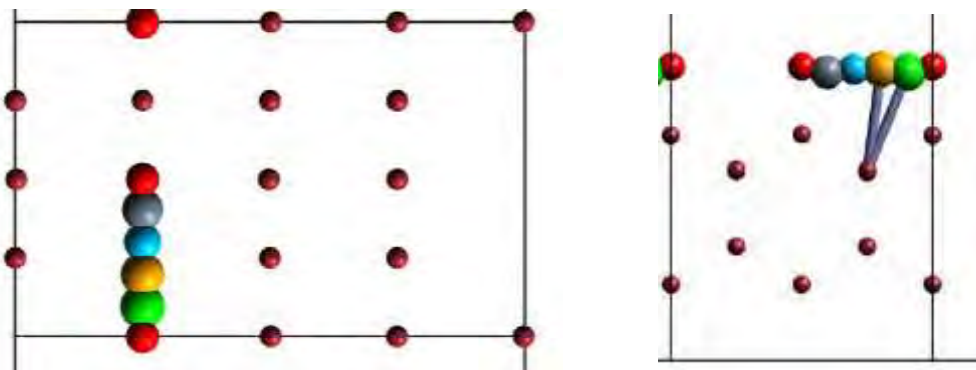


Figure B.3: Diffusion pathway of one adatom on a 2x2 cell of the (10-10) surface. **Left:** Top view **Right: side view.** The big red spheres are the optimized positions of the adatom, the intermediate positions are : 1 (grey) 2 (blue) 3 (orange) 4 (green). The bulk layer of Co (small red spheres) are shown as in the optimized configuration.

surface	modelling cell	diffusion objects	E^{diff} [eV]
0001	2x2	Co adatom	0.132
	4x4	Co adatom	0.118
	2x3	CH ₃ COO	0.221
10-10	2x2	Co adatom	0.134
	4x4	Co adatom	0.122
	2x2	CH ₃ COO	0.413

Table B.1: Diffusion barriers of the Co adatom and the CH₃COO molecule on different surfaces of Co in different cells.

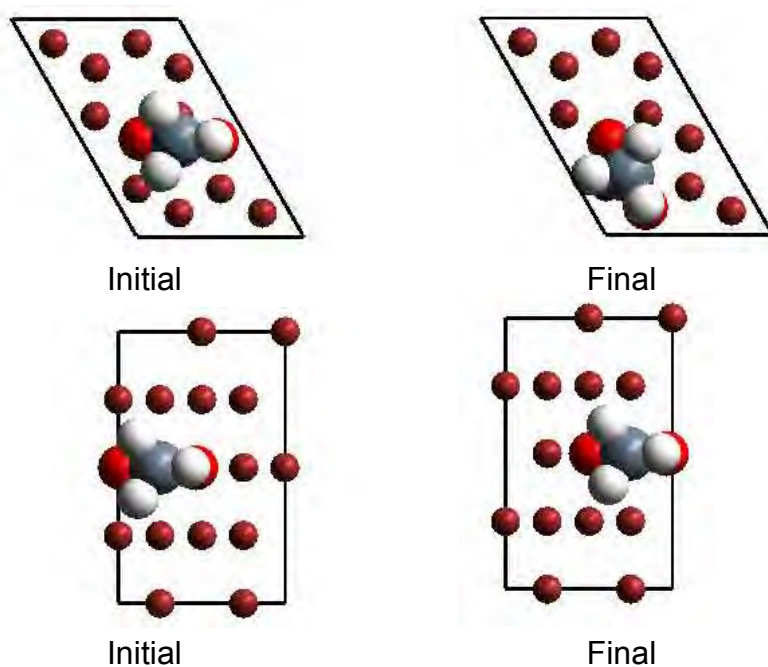


Figure B.4: Initial and final configurations of CH₃COO on the studied surfaces **top** (0001), **bottom** (10-10). The pathway is a rotation for CH₃COO on (0001) and translation for CH₃COO on (10-10)

List of Figures

1	Formes des NPs déterminées par le modèle de construction de Wulff et le modèle de l'énergie d'attachement. De gauche à droite: forme d'équilibre de la NP de Co, forme de la NP de Co par le modèle de l'énergie d'attachement et forme d'équilibre de la NP de Ni.	x
2	Energies d'adsorption de CH_3COO en fonction de θ pour les 3 surfaces étudiées. Les lignes correspondent aux fonctions polynomiales de la forme $a + b \times \theta^3 + c \times \theta^6$ pour chacune de ces 3 surfaces.	xiii
3	Évolution de l'énergie d'interfaces pour les différentes facettes et couvertures en fonction du potentiel chimique du ligand dans la solution. Pour chaque courbe, la légende indique le nom de la facette et la couverture de surface. La ligne verte en gras représente l'énergie d'interface la plus faible pour toute la couverture à chaque potentiel chimique. Les interfaces correspond à l'énergie d'interface minimale sont indiquées dans chaque région. (0001) dominant la surface correspondant à une forme de disque, (10-10) la surface dominante correspond à la forme de bâtonnet.	xv
4	Polyèdres de Wulff construits pour différentes valeurs de $\Delta\mu$ en utilisant les énergies d'interface minimales.	xvi
5	Évolution du Θ^{eq} en fonction du $\Delta\mu$ pour les trois facettes étudiées.	xvii
6	Evolution de l'énergie de l'interface en fonction de $\Delta\mu$ pour les trois facettes considérées, en utilisant le modèle basé sur l'isotherme de Langmuir, et les polyèdres de Wulff de morphologies choisies.	xviii
7	Evolution du rapport d'aspect de la NP en fonction de $\Delta\mu$ pour le modèle "isotrope". Haut: Gauche : $\lambda = 1$; Droite : $\lambda = 0.1$ - Bas Gauche: $\lambda = 0.01$; Droite: $\lambda = 0.001$	xx
8	Formes des NPs pour différentes valeurs de $\Delta\mu$: -4 eV; -3,43 eV; -3 eV; -2 eV à $\lambda = 1$ avec le modèle "isotrope" et le modèle de l'énergie d'attachement.	xi
1.1	Calculated atomic structure of a 5nm diameter PbS nanocrystal passivated with oleate and hydroxyl ligands (from [28]).	6
1.2	Lamer diagram showing the growth steps of nanoparticle in the solution (from [29]).	7
1.3	Example of an early stage Co cluster with carboxylate and amine as ligands (calculated with MOPAC2012.)	8
1.4	TEM images with precursor injection rate in a synthesis of Co NPs: (a) slow addition; (b) intermediate addition; (c) fast addition. [4].	9
1.5	A schematic illustration of the reaction pathways that lead to Pd nanostructures with different shapes. The green, orange, and purple colors represent the (100), (111), and (110) facets, respectively. R is the ratio between the growth rates along the [100] and [111] axes.(Adapted from [43])	10
1.6	Shape of Ag NPs obtained by selectively deposited Ag atoms on a) one, 2) two and c) six faces of a Ag 40 nm side cube seed (Adapted from [54])	11

1.7	High resolution TEM images of hcp-Co nanodisks with (a) c-axis parallel to the substrate, (c) with c-axis perpendicular to the substrate. (Adapted from ref. [2])	12
1.8	TEM images of Co nanoparticles obtained with an addition of different Na(C ₁ H ₂ 3COO) equivalents relative to Co(II): (a) 0 equiv.; (b) 0.5 equiv.; (c) 1.5 equiv. and (d) 2 equiv. (Adapted from [5]).	13
1.9	Stability diagrams for the Co (0001) and (10-10) surfaces with different ligands: in red, CH ₃ COO; in black, C ₂ H ₅ COO; in blue, C ₃ H ₇ COO. (Adapted from [5])	13
1.10	Stability of Co NP facets as a function of the chemical potential in the solution[5].	18
1.11	Example of Langmuir isotherm.	19
1.12	Prediction of PbSn NP shape using adsorption isotherm. left: Interface energy ratio as a function of an arbitrary coverage of the two facets and morphology prediction in each region; right: Isotherm lines at different temperatures linking the surface coverage of 2 facets in the same gaze pressure conditions. [25]	19
1.13	Wulff polyhedra of Fe NPs for different temperatures and gaze activity of H ₂ (10 ⁻⁷ for the first two ones and 1 for the last two), adapted from [53].	20
1.14	Top: Nanoparticle shape. Bottom Free energy as a function of the surface area of the NP and the relative population of NPs as a function of their diameter. [11]	21
1.15	Free energy diagram for nucleation as the variation of nucleus size (extracted from [62])	22
1.16	The morphology prediction of Ag nanoparticles with adsorbent of different chain lengths, as a function of coverage. [10]	25
2.1	Self-consistency scheme: from an initial guessed V_s^{in} , we solve the Kohn Sham equations. Then, we find the electron density functional. Afterwards, V_{ext} , V_{xc} and the coulomb potential of electron are recalculated to compose V_s^{out} . If $V_s^{out} = V_s^{in}$ the problem is solved, if not, an other new V_s^{in} will be introduced in function of V_s^{out} and V_s^{in} then restart a new iteration.	32
3.1	Primitive and unity cells of HCP and FCC structures. (a) triclinic cell of Ni, (b) FCC primitive cell in the unit cell, (c) tetragonal primitive cell of Co, (d) HCP primitive cell in the unit cell.	39
3.2	Left: Co primitive cell energy as a function of the k-points number. Right: Ni primitive cell energy as a function of the k-points number.	39
3.3	Ni (left) and Co (right) cell energy as a function of the cutoff energy.	40
3.4	Co (left) and Ni (right) cell energy as a function of the smearing σ .	40
3.5	Cell energy as a function of the primitive cell volume for Ni with the PBE functional. The results of the fit are given in the inset: lattice parameter a , bulk modulus B and cohesive energy (before isolated atom correction).	42
3.6	Energy of the Co primitive cell as a function of the lattice parameters (left) and of the volume cell (right). Only the red points are taken into account in the fitting curve.	43
3.7	Top: Symmetric configuration. Bottom: asymmetric configuration of a slab.	45
3.8	Total energy of 7 Co layers (top) and 7 Ni layers (bottom) as a function of the number of vacuum layers, calculated with the PBE functional.	47
3.9	Surface energy of Co(0001) (left) and Ni(111) (right) as a function of the number of layers calculated with the PBE functional.	48
3.10	Deviation of the calculated interlayer distances from the interlayer distance in the bulk (in %).	49
3.11	Atomic magnetic moments in each layer for Ni (111) (upper graph) and Co(0001) (lower graph) computed with the three different methods.	50

3.12 Average electrostatic potential in the z–direction for the Co(0001) calculated by different functionals. From top to bottom : PBE, DFTD, opt86B.	51
3.13 Average electrostatic potential in the z–direction for the Ni(111) calculated by different functionals. From top to bottom : PBE,DFTD, opt86B.	52
3.14 Surface energies of Co surfaces (1-100), (10-10), (0-111), (2-1-10), (10-12) and (1-102) as a function of the number of layers in the slab, computed with the PBE functional.	54
3.15 Equilibrium form of a Co NP using the Wulff reconstruction model.	55
3.16 Surface energy (left) and center interlayer distances deviation (right) for Ni(100) as a function of the layer number in the slab, computed with the PBE functional. the red line in the lower graph present the bulk distance.	56
3.17 Equilibrium form of a Ni NP using the Wulff construction model.	57
3.18 (1-100) and (10-10) surface terminations and the corresponding interlayer distances.	57
3.19 Visual form of a Co NP obtained from the attachment energy model.	58
4.1 Left: Total energy of the CH_3COO as a function of the size of the simulation cell. Right: Total energy of the CH_3COO as a function of the cut-off energy.	62
4.2 Relaxed geometry of the investigated molecules. Top from left to right: CH_3NH_2 , CH_3COO , $\text{C}_5\text{H}_{11}\text{COO}$. Bottom $\text{C}_{11}\text{H}_{23}\text{COO}$. H: white; C: grey; O: red; N: blue.	63
4.3 Red rectangle: simulation cell of the interface between Co(0001) and the $\text{C}_{11}\text{H}_{23}\text{COO}$	64
4.4 Possible adsorption sites on the Co(0001) surface: T = Top ; H = hollow; B = bridge. The 2 hollow sites H1 and H2 are not equivalent.	65
4.5 Adsorption of CH_3COO^- on Co(0001) at different coverages. The oxygen atoms are in always in the "Top" position.	66
4.6 Adsorption of CH_3COO^- on Co(10-10)surface at different coverages: (a& b) $\theta = 0.099\text{\AA}^{-2}$ with one O atom in Top position and one in Hollow H1 position; (c&d) $\theta = 0.049\text{\AA}^{-2}$ with all O atoms in Top positions. (e & f) $\theta = 0.066\text{\AA}^{-2}$ Mix of the 2 configurations.	68
4.7 Adsorption energies of CH_3COO as a function of the coverage per surface unit, for each studied facet. The lines correspond to polynomial fits of the form $a + b \times \theta^3 + c \times \theta^6$	70
4.8 Top and side views of the adsorption of CH_3NH_2 on the Co(0001) surface.	73
4.9 Top and side views of the adsorption of CH_3NH_2 on the Ni surfaces.	74
5.1 Evolution of the interface energies for the different facets and coverages as a function of the chemical potential in the solution. For each curve, the legend reports the facet name and the coverage of ligands (molecules/ \AA^2). The bold blue line represents the lowest interface energy for all coverage at each chemical potential. The interfaces with the smallest interface energy are indicated in each region. (0001) surface dominating correspond to a disk-like form, (10-10) dominating surface correspond to rod-like form.	79
5.2 Wulff polyhedra built for different values of $\Delta\mu$ using the lowest interface energies of Fig. 5.1.	80
5.3 Evolution of Θ^{eq} as a function of $\Delta\mu$ for the three considered facets.	81
5.4 Evolution of the interface energy as a function of $\Delta\mu$ for the three considered facets, using the model based on the Langmuir isotherm, and Wulff polyhedra of selected morphologies.	82
5.5 Sketch of a Co NP with the notations used in the kinetic model.	83

5.6 Evolution of concentration of Co and ligands as a function of time. Adapted from [5].	85
5.7 Sizes of the NP compared to the reference (0001) surface as a function of $\Delta\mu$, for the two models of Co adsorption. Top: Isotropic model for the Co initial growth rate. Middle: Schematic views of the NP shapes in the different cases. Bottom: Attachement energy model for the Co initial growth rate.	89
5.8 Size evolution as a function of time for different seed sizes, Seed size 0 for solid line and 15 Å in each dimension for the dashed line. Here $N_{Co}^{tot} = N_0 = 15.24 \times 10^6$ atoms and $\frac{c_0}{c_1} = 100$	90
5.9 Evolution of Cobalt concentration as a function of time for $\frac{c_0}{c_1} = 100$, $N_{Co}^{tot} = N_0/4$, $\lambda = 1$ and $\mu = -3\text{eV}$. Simulation stop at $c_{Co}(t) = 1.000001 \times c_1$	91
5.10 Size evolution as a function of time for different $\frac{c_0}{c_1} N_{Co}^{tot}$ for $\lambda = 1$ and $\mu = -3.5\text{eV}$ Left $= 100$ dashed line : $N^{tot} = N_0 = 15.24 \times 10^6$; solid line: $N^{tot} = N_0/8$. Right $\frac{c_1}{c_0} N_{Co}^{tot} = N_0 = 15.24 \times 10^6$ solid line: $\frac{c_0}{c_1} = 100$; dashed line : $\frac{c_0}{c_1} = 2$	91
5.11 coverage evolution as a function of time (log scale) at $\Delta\mu = -3 \text{ eV}$ for different value of λ	92
5.12 Evolution of the NP size as a function of $\Delta\mu$ for the isotropic model. top: Left : $\lambda = 1$; Right : $\lambda = 0.1$ - bottom Left: $\lambda = 0.01$; Right: $\lambda = 0.001$	93
5.13 Evolution of the NP size as a function of $\Delta\mu$ for the "attachment" model. top: Left : $\lambda = 1$; Right : $\lambda = 0.1$ - bottom Left: $\lambda = 0.01$; Right: $\lambda = 0.001$	94
B.1 Total energy for different positions of one adatom on the (0001) surface. Positions 0 and 5 are equilibrium positions, 1-4 are intermediate positions.	104
B.2 Diffusion pathway of one adatom on a 2x2 cell of the (0001)surface. Left: Top view Right: side view. The big red spheres are the optimized positions of the adatom, the intermediate positions are : 1 (grey) 2 (blue) 3 (orange) 4 (green). The bulk layer of Co (small red spheres) are shown as in the optimized configuration.	104
B.3 Diffusion pathway of one adatom on a 2x2 cell of the (10-10) surface. Left: Top view Right: side view. The big red spheres are the optimized positions of the adatom, the intermediate positions are : 1 (grey) 2 (blue) 3 (orange) 4 (green). The bulk layer of Co (small red spheres) are shown as in the optimized configuration.	104
B.4 Initial and final configurations of CH_3COO on the studied surfaces top (0001). bottom (10-10). The pathway is a rotation for CH_3COO on (0001) and translation for CH_3COO on (10-10)	105

List of Tables

1	Energies de surface de Co en eV/ \AA	ix
2	Energies de surface de Ni en eV/ \AA	ix
3	Les énergies d'adsorption et les transferts de charge de CH_3COO^- sur les différentes surfaces de Co à différents taux de recouvrement. Le transfert de charge est une valeur moyenne calculée avec toutes les molécules dans la supercellule. Lorsque deux valeurs sont présentes, elles correspondent aux deux modes d'adsorption.	xii
2.1	C_6 coefficients and Van der Waals radii R_0 used in the DFT-D2 method[13]	35
3.1	Energies of isolated atoms. The size of the box is larger than the cutoff distance of the Grimme dispersion term so that PBE and PBE+DFTD give the same results.	42
3.2	Lattice parameter a , bulk modulus B , cohesive energy and atomic magnetic moment for Ni with different functionals.	43
3.3	Lattice parameters a and c/a , bulk modulus B , cohesive energy E_0 and magnetic moment of Cobalt with different functionals.	43
3.4	surface energy of Co (0001) and Ni(111) calculated by different functionals.	48
3.5	Calculated and experimental deviation of the interlayer distances Δd_{12} , Δd_{23} , and Δd_{34} , from the corresponding bulk values (in %).	49
3.6	Calculated and experimental work functions Φ in eV.	50
3.7	Surface energies of all the investigated Co surfaces computed with the PBE functional, in eV/ \AA^2 and in J/m ² .	55
3.8	Surface energies of Ni surfaces computed with the PBE functional, in eV/ \AA^2 and in J/m ² .	57
3.9	Attachment energies and relative growth velocities of Co surfaces in the attachment energy model. Note that the surfaces (1-100)—(10-10) have the same directions but different terminations, so only average velocities are presented for these surfaces. The same is true for (1-102) — (10-12).	58
4.1	Energy of the computed molecules in vacuum and covalent bond lengths. The experimental values are taken from the corresponding average bond length. C-C distance was the value of $\text{CH}_2\text{-CH}_2$ bond for $\text{C}_5\text{H}_{11}\text{COO}^-$ and $\text{C}_{11}\text{H}_{23}\text{COO}^-$.	63
4.2	Adsorption energy of the CH_3COO^- molecule and Co-O distance calculated with different functionals.	66
4.3	Bader charge analysis of the CH_3COO^- molecule adsorbed on Co(0001) for a surface coverage of 0.031 \AA^{-2} and in vacuum.	67
4.4	Bader charge analysis of the CH_3COO^- molecule with one O atom in Top position and one in Hollow H1 position on Co(10-10) for a surface coverage of 0.66 \AA^{-2} and in vacuum.	67

4.5 Adsorption energies and net charge transfer of CH ₃ COO on the different surfaces of Co at different coverages. The charge transfer is averaged over the ones of the different molecules in the supercell. When two values are present, they correspond to the two adsorption modes.	69
4.6 Adsorption energies of C ₅ H ₁₁ COO on the different surfaces of Co at different coverages.	71
4.7 Energy adsorption of C ₁₁ H ₂₃ COO on the different surfaces of Co at different coverages.	71
4.8 Adsorption energies of CH ₃ COO on different surfaces of Ni at different coverages.	72
4.9 Adsorption energies of CH ₃ NH ₂ on the different surfaces of Co for different coverages.	72
4.10 Adsorption energies of CH ₃ NH ₂ on the different surfaces of Ni for different coverages.	73
B.1 Diffusion barriers of the Co adatom and the CH ₃ COO molecule on different surfaces of Co in different cells.	105

Bibliography

- [1] Xia Younan, Xiong Yujie, Lim Byungkwon, Skrabalak, and Sara E. Shape-controlled synthesis of metal nanocrystals: Simple chemistry meets complex physics? *Angewandte Chemie International Edition*, 48(1):60–103, 2009.
- [2] Miguel Comesana-Hermo, Diana Ciuculescu, Zi-An Li, Sven Stienen, Marina Spasova, Michael Farle, and Catherine Amiens. Stable single domain co nanodisks: synthesis, structure and magnetism. *J. Mater. Chem.*, 22:8043–8047, 2012.
- [3] LaMer, Victor K., and Dinegar Robert H. Theory, production and mechanism of formation of monodispersed hydrosols. *Journal of the American Chemical Society*, 72(11):4847–4854, 1950.
- [4] Nikos Liakakos, Benoît Cormary, Xiaojian Li, Pierre Lecante, Marc Respaud, Laurent Maron, Andrea Falqui, Alessandro Genovese, Laure Vendier, Spyros Koïnis, Bruno Chaudret, and Katerina Soulantica. The big impact of a small detail: Cobalt nanocrystal polymorphism as a result of precursor addition rate during stock solution preparation. *Journal of the American Chemical Society*, 134(43):17922–17931, 2012. PMID: 23043267.
- [5] Kahina Ait Atmane, Carine Michel, Jean-Yves Piquemal, Philippe Sautet, Patricia Beauquier, Marion Giraud, Mickael Sicard, Sophie Nowak, Remi Losno, and Guillaume Viau. Control of the anisotropic shape of cobalt nanorods in the liquid phase: from experiment to theory... and back. *Nanoscale*, 6:2682–2692, 2014.
- [6] Andrei Y. Khodakov, Wei Chu, and Pascal Fongarland. Advances in the development of novel cobalt fischer tropesch catalysts for synthesis of long chain hydrocarbons and clean fuels. *Chemical Reviews*, 107(5):1692–1744, 2007. PMID: 17488058.
- [7] Sang Wook Kim, Seung Uk Son, Su Seong Lee, Taeghwan Hyeon, and Young Keun Chung. Colloidal cobalt nanoparticles: a highly active and reusable pauson-khand catalyst. *Chem. Commun.*, pages 2212–2213, 2001.
- [8] Wulff G. *Zeitschrift fur Krystallographie und Mineralogie*, 34(5/6):449–530, 1901.
- [9] I.M. Lifshitz and V.V. Slyozov. The kinetics of precipitation from supersaturated solid solutions. *Journal of Physics and Chemistry of Solids*, 19(1):35 – 50, 1961.
- [10] Xin Qi, Tonnam Balankura, Ya Zhou, and Kristen A. Fichthorn. How structure-directing agents control nanocrystal shape: Polyvinylpyrrolidone-mediated growth of ag nanocubes. *Nano Letters*, 15(11):7711–7717, 2015. PMID: 26509492.
- [11] Amanda S. Barnard and Yu Chen. Kinetic modelling of the shape-dependent evolution of faceted gold nanoparticles. *J. Mater. Chem.*, 21:12239–12245, 2011.

- [12] Fatah Chiter, Van Bac Nguyen, Nathalie Tarrat, Magali Benoit, Hao Tang, and Corinne Lacaze-Dufaure. Effect of van der waals corrections on dft-computed metallic surface properties. *Materials Research Express*, 3(4):046501, 2016.
- [13] Stefan Grimme. Semiempirical gga-type density functional constructed with a long-range dispersion correction. *'Journal of Computational Chemistry'*, 27(15):1787–1799, 2006.
- [14] M. Dion, H. Rydberg, E. Schröder, D. C. Langreth, and B. I. Lundqvist. Van der waals density functional for general geometries. *Phys. Rev. Lett.*, 92:246401, Jun 2004.
- [15] Oleg A. Vydrov and Troy Van Voorhis. Nonlocal van der waals density functional made simple. *Phys. Rev. Lett.*, 103:063004, Aug 2009.
- [16] John P. Perdew, Kieron Burke, and Matthias Ernzerhof. Generalized gradient approximation made simple. *Phys. Rev. Lett.*, 77:3865–3868, Oct 1996.
- [17] G. Kresse and D. Joubert. *Physical Review B*, 59:1758, 1999.
- [18] G. Kresse and J. Hafner. *Physical Review B*, 47:558, 1993.
- [19] G. Kresse and J Furthmuller. *Physical Review B*, 54:11169, 1996.
- [20] G. Kresse and J Furthmuller. *Computational Materials Science*, 6:15–50, 1996.
- [21] R Tran, Z Xu, B Radhakrishnan, D Winston, W Sun, KA Persson, and SP Ong. Data from: Surface energies of elemental crystals, 2016.
- [22] C. Kittel. *Introduction to Solid State Physics*. Wiley, 2004.
- [23] Wei Liu, Victor G Ruiz, Guo-Xu Zhang, Biswajit Santra, Xinguo Ren, Matthias Scheffler, and Alexandre Tkatchenko. Structure and energetics of benzene adsorbed on transition-metal surfaces: density-functional theory with van der waals interactions including collective substrate response. *New Journal of Physics*, 15(5):053046, 2013.
- [24] J. E. Lennard-Jones. On the determination of molecular fields. *Proc. R. Soc. Lond. A*, 106(738):463–477, 1924.
- [25] Clive R. Bealing, William J. Baumgardner, Joshua J. Choi, Tobias Hanrath, and Richard G. Hennig. Predicting nanocrystal shape through consideration of surface-ligand interactions. *ACS Nano*, 6(3):2118–2127, 2012. PMID: 22329695.
- [26] Victor F. Puntes, Daniela Zanchet, Can K. Erdonmez, and A. Paul Alivisatos. Synthesis of hcp-co nanodisks. *Journal of the American Chemical Society*, 124(43):12874–12880, 2002. PMID: 12392435.
- [27] Lu An Hui, Salabas E. L, and Schuth Ferdi. Magnetic nanoparticles: Synthesis, protection, functionalization, and application. *Angewandte Chemie International Edition*, 46(8):1222–1244, 2007.
- [28] Danylo Zherebetskyy, Marcus Scheele, Yingjie Zhang, Noah Bronstein, Christopher Thompson, David Britt, Miquel Salmeron, Paul Alivisatos, and Lin-Wang Wang. Hy-

- droxylation of the surface of pbs nanocrystals passivated with oleic acid. *Science*, 344(6190):1380–1384, 2014.
- [29] Jin Chang and Eric R. Wacławik. Colloidal semiconductor nanocrystals: controlled synthesis and surface chemistry in organic media. *RSC Adv.*, 4:23505–23527, 2014.

- [30] David Thompson. Michael faraday's recognition of ruby gold: the birth of modern nanotechnology. *Gold Bulletin*, 40(4):267–269, 2007.
- [31] Lucio Colombi Ciacchi. Nucleation and growth of platinum clusters in solution and on biopolymers. *Platinum Metals Rev.*, 47(3):98, 2003.
- [32] Yujie Xiong, Isao Washio, Jingyi Chen, Martin Sadilek, and Younan Xia. Trimeric clusters of silver in aqueous agno₃ solutions and their role as nuclei in forming triangular nanoplates of silver. *Angewandte Chemie International Edition*, 46(26):4917–4921, 2007.
- [33] McLean John A., Stumpo Katherine A., and Russell David H. Size-selected (2 - 10 nm) gold nanoparticles for matrix assisted laser desorption ionization of peptides. *Journal of the American Chemical Society*, 127(15):5304–5305, 2005. PMID: 15826152.
- [34] Li Xi, Kuznetsov Aleksey E., Zhang Hai-Feng, Boldyrev Alexander I., and Wang Lai-Sheng. Observation of all-metal aromatic molecules. *Science*, 291(5505):859–861, 2001.
- [35] Eirini Zacharaki, Maria Kalyva, Helmer Fjellvåg, and Anja Olafsen Sjåstad. Burst nucleation by hot injection for size controlled synthesis of *E*-cobalt nanoparticles. *Chemistry Central Journal*, 10(1):1–11, 2016.
- [36] F. Baletto, C. Mottet, and R. Ferrando. Microscopic mechanisms of the growth of metastable silver icosahedra. *Phys. Rev. B*, 63:155408, Mar 2001.
- [37] F. Baletto, R. Ferrando, A. Fortunelli, F. Montalenti, and C. Mottet. Crossover among structural motifs in transition and noble-metal clusters. *The Journal of Chemical Physics*, 116(9):3856–3863, 2002.
- [38] Francesca Baletto and Riccardo Ferrando. Structural properties of nanoclusters: Energetic, thermodynamic, and kinetic effects. *Rev. Mod. Phys.*, 77:371–423, May 2005.
- [39] Ajayan P. M. and Marks L. D. Quasimelting and phases of small particles. *Phys. Rev. Lett.*, 60:585–587, Feb 1988.
- [40] Charles L. Cleveland and Uzi Landman. The energetics and structure of nickel clusters: Size dependence. *The Journal of Chemical Physics*, 94(11):7376–7396, 1991.
- [41] A. I. Kirkland, D. A. Jefferson, D. G. Duff, P. P. Edwards, I. Gameson, B. F. G. Johnson, and D. J. Smith. Structural studies of trigonal lamellar particles of gold and silver. *Proceedings of the Royal Society of London A: Mathematical, Physical and Engineering Sciences*, 440(1910):589–609, 1993.
- [42] V. Germain, J. Li, Z. L. D. Ingert, Wang, and M. P. Pilani. *J. Phys. Chem. B*, 19(107):8717, 2003.
- [43] Y. Xiong and Y. Xia. Shape-controlled synthesis of metal nanostructures: The case of palladium. *Advanced Materials*, 19(20):3385–3391, 2007.
- [44] Benjamin Wiley, Yugang Sun, Brian Mayers, and Younan Xia. Shape-controlled synthesis of metal nanostructures: The case of silver. *Chemistry – A European Journal*, 11(2):454–463, 2005.
- [45] Sara E. Skrabalak, Jingyi Chen, Leslie Au, Xianmao Lu, Xingde Li, and Younan Xia. Gold nanocages for biomedical applications. *Adv Mater*, 19(20):3177–3184, Oct 2007. 18648528[pmid].

- [46] T. Wang, C. Lee, and L.D. Schmidt. Shape and orientation of supported pt particles. *Surface Science*, 163(1):181 – 197, 1985.
- [47] M. Rosa Axet, Karine Philippot, Bruno Chaudret, Martiane Cabié, Suzanne Giorgio, and Claude R. Henry. Tem and hrtem evidence for the role of ligands in the formation of shape-controlled platinum nanoparticles. *Small*, 7(2):235–241, 2011.
- [48] H. H. Huang, X. P. Ni, G. L. Loy, C. H. Chew, K. L. Tan, F. C. Loh, J. F. Deng, and G. Q. Xu. Photochemical formation of silver nanoparticles in poly(n-vinylpyrrolidone). *Langmuir*, 12(4):909–912, 1996.
- [49] Israel Cano, Miguel A. Huertos, Andrew M. Chapman, Gerd Bunkowsky, Torsten Gutmann, Pedro B. Groszewicz, and Piet W. N. M. van Leeuwen. Air-stable gold nanoparticles ligated by secondary phosphine oxides as catalyst for the chemoselective hydrogenation of substituted aldehydes: a remarkable ligand effect. *Journal of the American Chemical Society*, 137(24):7718–7727, 2015. PMID: 26034996.
- [50] F. Bonet, K. Tekaia-Elhsissen, and K. Vijaya Sarathy. Study of interaction of ethylene glycol/pvp phase on noble metal powders prepared by polyol process. *Bulletin of Materials Science*, 23(3):165–168, 2000.
- [51] Y. Gao, P. Jiang, D. F. Liu, H. J. Yuan, X. Q. Yan, Z. P. Zhou, J. X. Wang, L. Song, L. F. Liu, W. Y. Zhou, G. Wang, C. Y. Wang, S. S. Xie, J. M. Zhang, and D. Y. Shen. Evidence for the monolayer assembly of poly(vinylpyrrolidone) on the surfaces of silver nanowires. *The Journal of Physical Chemistry B*, 108(34):12877–12881, 2004.
- [52] Alicia M. Jackson, Jacob W. Myerson, and Francesco Stellacci. Spontaneous assembly of subnanometre-ordered domains in the ligand shell of monolayer-protected nanoparticles. *Nature Materials*, 3(5):330–336, 2004.
- [53] Guntram Fischer, Romuald Poteau, Sébastien Lachaize, and Iann C. Gerber. Surfaces of a colloidal iron nanoparticle in its chemical environment: A dft description. *Langmuir*, 30(39):11670–11680, 2014. PMID: 25259402.
- [54] Xiaohu Xia and Younan Xia. Symmetry breaking during seeded growth of nanocrystals. *Nano Letters*, 12(11):6038–6042, 2012. PMID: 23121517.
- [55] Younan Xia, Xiaohu Xia, and Hsin-Chieh Peng. Shape-controlled synthesis of colloidal metal nanocrystals: Thermodynamic versus kinetic products. *Journal of the American Chemical Society*, 137(25):7947–7966, 2015. PMID: 26020837.
- [56] Hsin-Chieh Peng, Jinho Park, Lei Zhang, and Younan Xia. Toward a quantitative understanding of symmetry reduction involved in the seed-mediated growth of pd nanocrystals. *Journal of the American Chemical Society*, 137(20):6643–6652, 2015. PMID: 25941798.
- [57] N.A. Spaldin. *Magnetic Materials: Fundamentals and Applications*. Cambridge University Press, 2010.
- [58] H. Freundlich. eine darstellung der chemie der kolloide und verwandter gebiete. *Kapillarchemie*. Leipzig: Academische Bibliotek, 1909.
- [59] Stephen Brunauer, P. H. Emmett, and Edward Teller. Adsorption of gases in multimolecular layers. *Journal of the American Chemical Society*, 60(2):309–319, 1938.

- [60] M. TEMKIN and V. PYZHEV. Kinetics of the synthesis of ammonia on promoted iron catalysts. *Jour. Phys. Chem. (U.S.S.R.)*, 13:851–867, 1939.
- [61] Amanda S. Barnard. Clarifying stability, probability and population in nanoparticle ensembles. *Nanoscale*, 6:9983–9990, 2014.
- [62] J.W. Mullin. *Crystallization (Fourth Edition)*. Butterworth-Heinemann, Oxford, fourth edition edition, 2001.
- [63] M. Kahlweit. Ostwald ripening of precipitates. *Advances in Colloid and Interface Science*, 5(1):1 – 35, 1975.
- [64] Murielle A. Watzky, , and Richard G. Finke. *Journal of the American Chemical Society*, 119(43):10382–10400, 1997.
- [65] Dongsheng Li, Michael H. Nielsen, Jonathan R. I. Lee, Cathrine Frandsen, Jillian F. Banfield, and James J. De Yoreo. Direction-specific interactions control crystal growth by oriented attachment. *Science*, 336(6084):1014–1018, 2012.
- [66] Peng Xiaogang, Manna Liberato, Wickham Juanita, Scher Erik, Kadavanich Andreas, and Alivisatos A. P. *Nature*, 404(6773):59–61, 2000.
- [67] A S Barnard. Modelling of nanoparticles: approaches to morphology and evolution. *Reports on Progress in Physics*, 73(8):086502, 2010.
- [68] W. Kohn and L. J. Sham. Self-consistent equations including exchange and correlation effects. *Phys. Rev.*, 140:A1133–A1138, Nov 1965.
- [69] P. Hohenberg and W. Kohn. Inhomogeneous electron gas. *Phys. Rev.*, 136:B864–B871, Nov 1964.
- [70] P. E. Blöchl. Projector augmented-wave method. *Phys. Rev. B*, 50:17953–17979, Dec 1994.
- [71] D. M. Ceperley and B. J. Alder. Ground state of the electron gas by a stochastic method. *Phys. Rev. Lett.*, 45:566–569, Aug 1980.
- [72] Frank Herman, John P. Van Dyke, and Irene B. Ortenburger. Improved statistical exchange approximation for inhomogeneous many-electron systems. *Phys. Rev. Lett.*, 22:807–811, Apr 1969.
- [73] A. D. Becke. Density functional calculations of molecular bond energies. *The Journal of Chemical Physics*, 84(8):4524–4529, 1986.
- [74] John P. Perdew and Wang Yue. Accurate and simple density functional for the electronic exchange energy: Generalized gradient approximation. *Phys. Rev. B*, 33:8800–8802, Jun 1986.
- [75] Chengteh Lee, Weitao Yang, and Robert G. Parr. Development of the colle-salvetti correlation-energy formula into a functional of the electron density. *Phys. Rev. B*, 37:785–789, Jan 1988.
- [76] John P. Perdew, J. A. Chevary, S. H. Vosko, Koblar A. Jackson, Mark R. Pederson, D. J. Singh, and Carlos Fiolhais. Atoms, molecules, solids, and surfaces: Applications of the generalized gradient approximation for exchange and correlation. *Phys. Rev. B*, 46:6671–6687, Sep 1992.

- [77] Yingkai Zhang and Weitao Yang. Comment on “generalized gradient approximation made simple”. *Phys. Rev. Lett.*, 80:890–890, Jan 1998.
- [78] Michael Filatov and Walter Thiel. Tests of a density functional with laplacian terms: activation barriers and bond-stretching energies. *Chemical Physics Letters*, 295(5–6):467 – 474, 1998.
- [79] Becke A. Density functional thermochemistry. iii the role of exact exchange. *The Journal of Chemical Physics*, 98(7):5648–5652, 1993.
- [80] A. D. Becke. Correlation energy of an inhomogeneous electron gas: A coordinate space model. *The Journal of Chemical Physics*, 88(2):1053–1062, 1988.
- [81] P. J. Stephens, F. J. Devlin, C. F. Chabalowski, and M. J. Frisch. Ab initio calculation of vibrational absorption and circular dichroism spectra using density functional force fields. *J. Phys. Chem.*, 98(45):11623–11627, 1994.
- [82] Jiří Klimeš, David R Bowler, and Angelos Michaelides. Chemical accuracy for the van der waals density functional. *Journal of Physics: Condensed Matter*, 22(2):022201, 2010.
- [83] G. Kresse and D. Joubert. From ultrasoft pseudopotentials to the projector augmented-wave method. *Phys. Rev. B*, 59:1758–1775, Jan 1999.
- [84] Hendrik J. Monkhorst and James D. Pack. *Physical Review B*, 13:5188, 1976.
- [85] J. Lahtinen, J. Vaari, T. Vaara, K. Kauraala, P. Kaukasoina, and M. Lindroos. *Surface Science*, 425:90–100, 1999.
- [86] Alexandre Tkatchenko, Robert A. DiStasio, Roberto Car, and Matthias Scheffler. Accurate and efficient method for many-body van der waals interactions. *Phys. Rev. Lett.*, 108:236402, Jun 2012.
- [87] Hartman P. and W. G. Perdok. On the relations between structure and morphology of crystals. i. *Acta. Cryst.*, 8, 1955.
- [88] Frank H. Allen, Olga Kennard, David G. Watson, Lee Brammer, A. Guy Orpen, and Robin Taylor. Tables of bond lengths determined by x-ray and neutron diffraction. part 1. bond lengths in organic compounds. *J. Chem. Soc., Perkin Trans. 2*, pages S1–S19, 1987.
- [89] Graeme Henkelman and Hannes Jónsson. Improved tangent estimate in the nudged elastic band method for finding minimum energy paths and saddle points. *The Journal of Chemical Physics*, 113(22):9978–9985, 2000.
- [90] Graeme Henkelman, Blas P. Uberuaga, and Hannes Jónsson. A climbing image nudged elastic band method for finding saddle points and minimum energy paths. *The Journal of Chemical Physics*, 113(22):9901–9904, 2000.